2809644248

REFERENCE ONLY

UNIVERSITY OF LONDON THESIS

Degree PhD Year 2007 Name of Author ELLIS, Andrew Shaw

COPYRIGHT
This is a thesis accepted for a Higher Degree of the University of London. It is an unpublished typescript and the copyright is held by the author. All persons consulting this thesis must read and abide by the Copyright Declaration below.

COPYRIGHT DECLARATION
I recognise that the copyright of the above-described thesis rests with the author and that no quotation from it or information derived from it may be published without the prior written consent of the author.

LOANS
Theses may not be lent to individuals, but the Senate House Library may lend a copy to approved libraries within the United Kingdom, for consultation solely on the premises of those libraries. Application should be made to: Inter-Library Loans, Senate House Library, Senate House, Malet Street, London WC1E 7HU.

REPRODUCTION
University of London theses may not be reproduced without explicit written permission from the Senate House Library. Enquiries should be addressed to the Theses Section of the Library. Regulations concerning reproduction vary according to the date of acceptance of the thesis and are listed below as guidelines.

A. Before 1962. Permission granted only upon the prior written consent of the author. (The Senate House Library will provide addresses where possible).

B. 1962-1974. In many cases the author has agreed to permit copying upon completion of a Copyright Declaration.

C. 1975-1988. Most theses may be copied upon completion of a Copyright Declaration.

D. 1989 onwards. Most theses may be copied.

This thesis comes within category D.

☐ This copy has been deposited in the Library of UCL

☐ This copy has been deposited in the Senate House Library, Senate House, Malet Street, London WC1E 7HU.

Bound By
Blissett Bookbinc
020 8992 396
www.blissetts.c

Modelling chute delivery of grains in a food-sorting process

Andrew Shaw Ellis

Department of Mathematics
University College London
University of London

A thesis submitted for the degree of
Doctor of Philosophy

Supervisor
Prof. F. T. Smith F.R.S.

March 2007

ProQuest LLC
789 East Eisenhower Parkway
P.O. Box 1346
Ann Arbor, MI 48106-1346

I, Andrew Shaw Ellis, confirm that the work presented in this thesis is my own. Where information has been derived from other sources, I confirm that this has been indicated in the thesis.

Abstract

The whole of the thesis is motivated by a particular problem from the food-sorting industry in which grains of food, typically rice, flow down chutes. As they fall down the chute, the grains form a rapidly moving mono-layer. This project starts with a discrete model treating individual grains based on partcle dynamics without air resistance. Single grains and then many grains are addressed, and the methodology used includes large computations describing the particle paths, velocities and other key features accompanied by analysis. Much of the thesis thereafter is concerned with the development of a continuum model for the chute flow of grains, inspired by the clusters and voids seen in the above computations and based on analogies with the Lighthill-Whitham model of traffic flow. The crucial difference here is that the flow is not uni-directional and so a multi-valued flow-density relation is required. The introduction of such a law yields complex and rich flow behaviours. The mathematical interest is in solving hyperbolic and parabolic partial differential equations, incorporating shocks and fans into analytical and numerical solutions of the governing equation, in asymptotic methods used in analysis of particular limits, especially those relating to clashing or separation of grains, and in seeking steady state solutions for the density profile. Finally, air effects are studied. In particular, local viscous or inviscid effects in the gaps between grains are investigated, followed by the subsequent interaction effects on many grains.

Acknowledgements

First, I would like to convey my deepest gratitude to my supervisor, Prof F. T. Smith FRS, for his constant help, advice, and patient support throughout the course of my PhD. I also thank him for sharing with me his great enthusiasm for and his profound knowledge of applied mathematics.

I must also thank many others for their help during the preparation of this thesis. In particular, to Sortex Ltd. for their support, financial and otherwise, with a special thanks to Dr. Mark Honeywood and Dr. Gabriel Hamid for many hours of useful discussions. Thanks also go to the Smith Institute, especially to Dr. Tim Boxer for his kind advice throughout. Prof. Ben Heydecker of UCL Centre for Transport Studies was always ready with helpful advice. I am also much obliged to my other colleagues and postgraduate friends at UCL.

On a more personal note, I thank my parents Charles and Susan, and my brothers Christopher, Simon and Jonathan who are there for me always. Finally, I would like to express my sincere indebtedness to my wife, Joanna, for her continual patience, kindness and love.

Contents

List of Figures

List of Tables

Chapter 1

Introduction

The present study involves modelling, analysis, computations and experimental work and is related to multi-particle interactions, granular flow, traffic flow and fluid dynamics. These and the layout of the thesis are described later in the chapter after the aim and direct motivation from industry are described.

The aim of this thesis is to find a suitably accurate mathematical model for the nearly two-dimensional, gravity-driven, rapid flow of a monolayer of grains down an inclined chute. This is directly motivated by a problem from the food-sorting industry, in particular from a company that manufactures machines for the sorting of food, Sortex Ltd. Many food stuffs can be sorted with these machines, including rice, coffee beans, carrots, peas and strawberries. The majority of machines manufactured by Sortex however are employed in the sorting of rice grains. The attention of the project, therefore, is focused solely on rice.

In the particular food-sorting process developed by Sortex, grains fall from a hopper and are subsequently moved along by a vibrator tray. At the end of the tray the grains fall on to an inclined chute, down which they are accelerated due to gravity. They quickly form an apparent two-dimensional monolayer upon the chute. Shortly after the grains have fallen from the bottom of the chute they pass an optical system that can detect defective grains. A grain is considered to be defective if it is, for example, of the wrong size, shape or colour. Foreign bodies, such as small shards of glass, can also be detected. If the optical system detects a defective grain, a powerful jet of air is fired from at least one ejector in an array of ejectors, and the grain is knocked into a reject bucket by the force of the impact. A schematic diagram of the process is shown in figure 1.1. Studies of the ejector and jet properties are in the theses by Westwood and Wilson [56], [63].

The chute is approximately $30cm$ wide and a metre in length. The grains exit the chute with a vertical velocity of the order of $4 - 5ms^{-1}$. The dimensions of a typical grain of rice are a width of $1 - 3mm$ and a length of $5 - 7mm$. The mass has a magnitude of roughly $10^{-5}kg$.

Particular difficulties arise as the grains fall off the chute, since they are not uniformly distributed. In fact, the distribution of grains at the bottom of the chute is typically clustered and inhomogeneous. As a consequence, the air jet can, and usually does, remove other grains of rice surrounding the reject grain. These grains may not themselves be defective. This erroneous ejection of surrounding grains is a source of inefficiency in the food-sorting process; the grains in the reject bucket sometimes must be sorted through again to reduce waste.

Currently, the optical system can be configured to yield an increased sorting performance, but if a high level of sorting is required a chute with channels must be used. These 'channelised' chutes align the grains with the ejectors and improve the uniformity of the product feed. There is however a concomitant reduction in the mass of grains that can be sorted in a given time (known as the 'throughput').

Understandably, Sortex would like to remove this problem as much as possible whilst maintaining a high throughput of grains in these machines. Such a development in chute design would take the industry forward and perhaps make Sortex world leaders (or help maintain their position as world leaders) in the food-sorting industry.

The remit of this project, therefore, is to try to find a suitable mathematical model for a chute flow of grains in order to increase knowledge and understanding of the underlying physics so that the above ejection problem can be reduced as much as possible.

An interesting aspect of this thesis is in the modelling itself. For such a chute

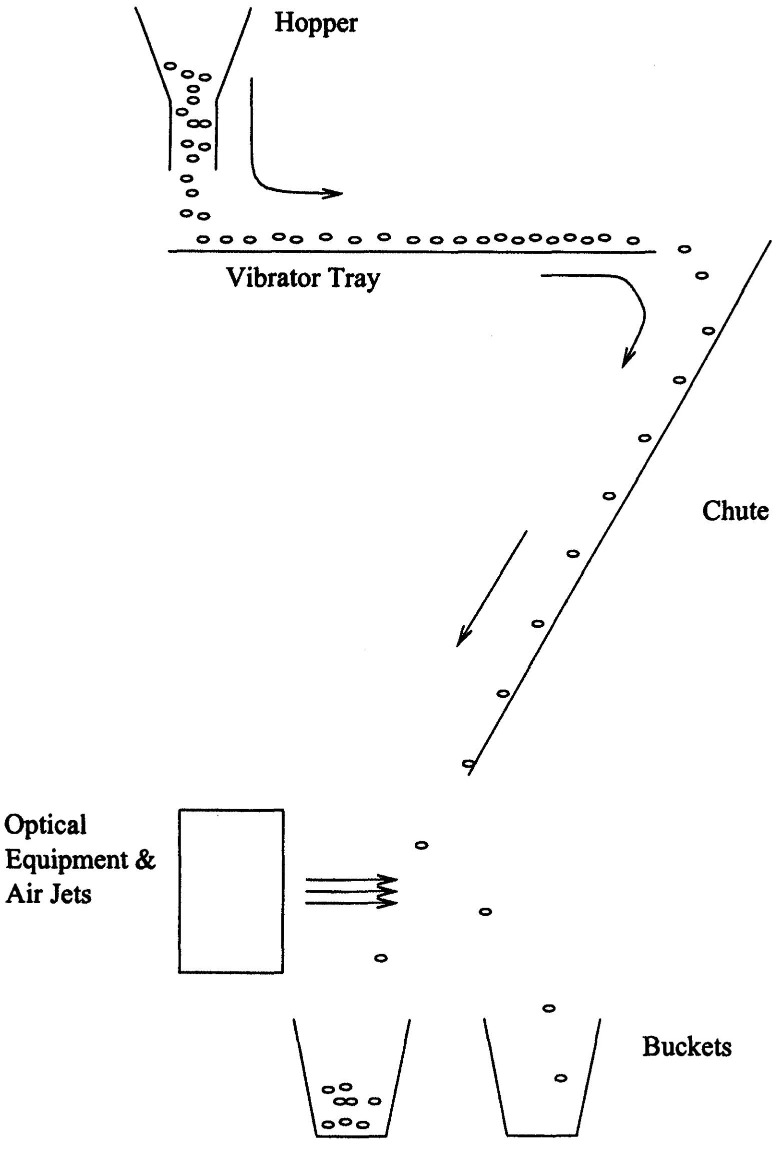

Figure 1.1: A schematic side-view diagram of the food-sorting process. The picture is not to scale.

flow of grains, which perhaps can be thought of as a rapid, sparse granular flow or alternatively as a suspension flow, there is no 'grand theory of everything' to apply. That is to say, there is no analogue to, for example, the Navier-Stokes equations that applies to all granular or particle-laden flows which we can study in an appropriate limit; rather, we must model the process from first principles.

A standard approach in granular mechanics is to postulate some so-called 'constitutive relations' that are crucial to the granular flow [6], [8], [26], [29], [47], [50]. These studies often address the particle forces alone, neglecting the multiphase nature of granular materials, especially for rapid flows [8]. The constitutive relations typically focus on the shear forces and stress tensors obtained from the particle-particle collisions, and the notion of granular temperature is often introduced as an analogue to kinetic theories of ideal gases. Particle collisions can be dealt with by either hard disk models or soft particle molecular dynamics simulations [40], [55]. The former model collisions using Newton's law of restitution [46]; the latter try to obviate problems associated with inelastic collapse by using a 'spring-dashpot' model. 'Inelastic collapse' is the name given to the phenomenon of a particle undergoing an infinite number of collisions in a finite time [9], [40], [65], and occurs only in hard disk models. Inelastic collapse can cause difficulties when one is attempting to model granular phenomena with hydrodynamic analogies [11], [18].

Together with the theory, computational simulations often are of use when studying granular flows [39], [53]. Modern computations can be massive (up to nearly ten thousand particles [54]) and often demonstrate that pattern formations arise within granular flows. This can be due to the development of clustering or of shear-banding [16]. The observation of patterns in computational work has been of great significance [41]. In the pharmaceutical industry for instance drugs are mixed in rotating drums. Obviously a homogeneous mixture is required so that the dosage is constant within each tablet. Computational simulations show that after a certain number of revolutions, shear-banding can spontaneously occur, leading to an inhomogeneous mixture. This structure will then disappear, only to return later. We can see consequently that a computational model of the flow is of great importance in this case.

Usually problems in granular mechanics deal with phenomena such as avalanches, lahars (landslides), pharmaceutical processes, powders in rotating drums, chute flows and so on [16], [41], [47]. In particular, there are some well developed theories of chute flows [6], [19], [26], [39], [50]. Typically, even for sparser rapid granular flows, enduring particle contacts are significant and the flows can be many particles deep. The rapid monolayer which we study is believed to be atypical for a granular flow. Enduring contacts are not thought to be as significant here. For this reason, a conventional granular flow theory as described above may not be appropriate for a model of this chute flow.

On the other hand, suspension flows tend to be concerned with sparser grain flows where the interstitial fluid is important for the grain dynamics [12], [23], [30], [61], [62], such as in the study of aeolian or fluvial transport [59]. These studies are concerned with issues such as entrainment, which are believed to be less important aspects of chute flows, such as those of interest to us. One major aspect of the chute monolayer is that the dynamics is thought to be driven by the frequent, binary impacts of the grains. Hence the Sortex problem seems to lie between the arenas of suspension flows and granular flows.

Mathematical modelling of discrete phenomena by partial differential equations is a technique successfully employed in studies of traffic and pedestrian flows [17], [21], [22], [38], [42], [57], [58]. In fact, research on granular phenomena and research on traffic problems have a large overlap: see for example [64]. Perhaps the most well known theory is the celebrated Lighthill and Whitham model of traffic flow [38], [57], [58]. This theory explains well experienced behaviours of traffic, including density waves in traffic, shock waves as vehicles approach congestion and traffic jams at intersections. Another example is Hughes' description of pedestrian flows [21], [22]. He uses a Lighthill-Whitham type model for pilgrims crossing the Jamarat bridge in Mecca. His work suggests a method of safely placing barriers in order to prevent the crushing of pilgrims, which has in the past led to a number of deaths. It is the theory of Lighthill and Whitham that we try to develop for the chute flow later in this thesis.

Prior to developing this model, however, we first study the simpler problem of a single grain falling through a chute. This is done in chapter 2. The aim of this chapter is to determine whether an analytical model can be utilized for a simple particulate problem with a substantial number of collisions. We find that indeed it can. In this case to obtain a continuous approximation we assume that the particle collisions with the wall are asymptotically perfectly elastic and that the chute is narrow. Also in this chapter, a short calculation is presented which shows that at the bottom end of the chute the boundary layer around a falling grain is of the order of the grain size. Thus we might expect air effects to become a significant aspect of the flow.

Having investigated the one particle problem, chapter 3 deals with a large computational simulation of the many-grain flow. Initially, a simple computational model is introduced. The trajectories of the particles are governed by simple ballistic laws. Conservation of momentum and Newton's law of restitution are used to determine the velocities at collisions. Collision detection is considered in this chapter and we use a method similar to that of Louge [39], rather than an event-driven algorithm of the type discussed by Sigurgeirsson et al. [53]. The velocities of the grains are assumed to have only horizontal velocity fluctuations, hence there is no vertical interaction between particles. Air effects and friction are also ignored and only binary collisions are allowed. The effect of changing the coefficient of restitution is investigated. An encouraging comparison between the results and data from Sortex is observed, despite the simplifications. Following this, a commercially available code, PFC2D, is used to investigate more complex effects, such as vertical interactions and the effects of chute geometry, and the combination of the two. In all the computations we find that clusters and voids are a key feature, especially for those which neglect vertical interactions.

Chapter 4 discusses possible analytical models for the chute flow. We mention that statistical physics approaches seem to be attractive, especially when the chute flow is compared to an ideal gas. Analogues to kinetic theories have been used for chute flows in the past for conventional granular flow problems [50]. However, some of the assumptions of statistical mechanics are readily broken in practice. In particular, the mean free path is of the order of the particle size and there is a continual input of energy into the system. A simple statistical analysis is attempted, however, but it appears not to be of great value. Furthermore, some of the assumptions of the analysis also fail, and so this model is abandoned. We note in passing that mean field theory, lattice-gas automata and random walk theory may be appropriate statistical techniques of value. A full study of statistical methods is beyond the scope of this thesis, as we prefer to concentrate on the continuum modelling.

In chapter 5 we develop a theory for a chute flow based on an analogy with the Lighthill and Whitham model of traffic flow. As the model is developed from first principles, it is sensible to start relatively simply. We therefore consider only a one-dimensional model. However, the one-dimensional computational simulation of chapter 3 does produce encouraging results, so we hope that the continuum model may do so also. We write down a conjectured partial differential equation for the density of regions of particles which move left and right across the chute. The density is a function of time and position across the chute. As time increases, the particles are considered to fall down the chute. The partial differential equation is a hyperbolic kinematic wave equation. As such, discontinuities arise in the solution. We aim to include these discontinuities in a description of the clusters and voids which arise on the chute. Of course, a two-dimensional model would be one improvement to make. We show the two-dimensional equations in brief and show that the one-dimensional solution would emerge anyway, as the grains fall down the chute.

One novel aspect of the present model is that the wave-speed and the flux are multi-valued 'functions' of the density; for a particular value of the density there is a positive and a negative value of the flux. This allows the regions of particles to move leftward or rightward across the chute. Since the wave-speed is defined to be the rate of change of the flux with respect to the density, it too is multi-valued. In traffic models, by contrast, the flow is usually uni-directional and so those models do not have the multi-valuedness feature. The formation of clusters and voids relates mathematically, and directly, to the branch switches between the positive and negative values of the flux. The inclusion of the branch switches in the model gives rise to many interesting features. The flux-density relation is known as the 'fundamental diagram' or 'fundamental curve'. The strengths and weaknesses of the proposed fundamental diagram are then discussed.

After postulating the model, we solve the ensuing partial differential equation for certain simple initial conditions. The solutions are found by a method of characteristics. Shocks and expansion fans must sometimes be incorporated into the solution, and we also discuss these. Remarks are made about conservation of mass and conditions on the entropy.

More general solutions are then sought in chapter 6, focusing in this chapter particularly on one-way flows in which solutions remain always on one branch of the fundamental diagram. In order to find general solutions numerically an artificial viscous dissipation term is added. That changes the character of the equation from a hyperbolic to a parabolic one. The discontinuities are consequently 'smoothed out'. This is a standard method in traffic flow theory [43], [57]. The parabolic equation is referred to throughout the thesis as 'the continuum equation'. A finite difference scheme is employed to find solutions which replicate closely those found from the inviscid analysis in chapter 5.

We then extend the analysis to seek solutions that do not mimic the (fairly simple) analytical results of chapter 5. In particular, an asymptotic solution valid at small time is compared to the results from the numerics. There is a satisfactory agreement between the two.

Chapter 6 concludes with an examination of the steady states of the one-way flow. A special case in which the densities at each boundary are nearly equal is examined analytically. Other general solutions are difficult to compute accurately as inaccuracies seem to be introduced at the point in the scheme where the direction of the upwind differencing changes sign.

In chapter 7 two-way flows are examined for which the grains can move to and fro across the chutes. This necessitates the incorporation of branch-switching in the solutions to the continuum equation. For such solutions to be found we argue that, as a consequence of the introduction of the viscous dissipation term, the fundamental diagram must be changed near its endpoints. Explicitly, local viscous regions in the neighbourhood of the endpoints of the fundamental diagram permit solutions to smoothly switch branches. These local viscous effects are investigated analytically first at the low density branch switch and second at the high density branch switch.

In the former case, a similarity equation valid at small time is derived. The equation is solved by a Runge-Kutta technique, but a series solution is required through zero density since a singularity exists there. Smooth behaviour through the branch switch is found to exist. An alternative method is to find solutions that are asymptotically close to an exact solution of the equation. Crucially, this reveals that a large region of low density can evolve, mimicking the formation of a void on the chute. Furthermore, analysis shows that a separating region must have zero density at its minimum, as may be expected from physical intuition. Some solutions lead to an asymmetric density profile and these have minima which can move temporally. This observation has ramifications for the steady state solutions discussed later.

For the large density case, a small viscous layer is introduced which is valid for order one times. This yields a partial differential equation for the local density. The equation is inverted and solved by a finite difference method. Smooth curves which emulate the evolution of a cluster are shown to exist.

Steady states for the two-way flow are then examined. A simplified but representative version of the fundamental diagram is used to capture the main features of the flow. The continuum equation is written in terms of polar co-ordinates so that branch switching may be incorporated while avoiding problems associated with the bi-valued fundamental diagram. A few steady states are found, but the number of restrictions on the initial condition prevents us from finding very many significantly different steady states. It is demonstrated that the problem is not over-prescribed, despite the number of restrictions on the initial condition. We observe that apparent steady states can be found in which sinusoidal-type solutions can be joined to constant solutions. These relate to the asymmetric minima mentioned above, which move. We find, however, that such solutions have a $t^{\frac{1}{2}}$ growth at order one times at the 'junctions' and thus do not form valid steady state solutions, in the sense of a steady state being a large-time limit. Hence they are ultimately dismissed. Some steady states can be found analytically.

In chapter 8 an investigation of air effects on the grain flow is undertaken. We start with an analysis of the viscous effects between two grains, the separation between grains being small relative to their length. The viscous effects prevent the grains from touching, in line with the results in [44]. Following this, the interaction effects between many grains separated by small lubricating layers is researched. The stability of the array is investigated. Inviscid effects between two flat grains are then investigated. In this case grains are now able to touch. However, the interaction between many grains separated by small inviscid layers seems to have the same qualitative behaviour as the viscous case, with both yielding algebraic growth of small disturbances, and hence relatively weak instability.

The main body of the thesis then finishes with concluding remarks in chapter 9.

Finally, there are seven appendices: four of the appendices examine in more detail points made in the text; one discusses related experimental work involving the author concerning a measure of chute performance; another appendix concerns an argument for determining the boundary conditions at the chute walls in the inviscid model by a method of characteristics; the final appendix presents in summary form the industrial recommendations for Sortex Ltd.

Chapter 2

One particle in a chute

One aim of this thesis is to find a suitable mathematical model for a chute flow of grains. However, it is sensible to start with a *very simple* case to see if this yields an analytical solution before undertaking the full problem.

We therefore consider in this chapter the trajectory of only one particle falling down a chute under gravity. As it falls, the particle bounces from side to side off the walls. The aim is to find the equations that govern its motion after each bounce. We obtain a set of difference equations which provide an iterative scheme for calculating the particle's motion. Taking the limit of the coefficient of restitution tending to unity then produces differential equations for the motion. The solution of this continuous approximation can be compared to the numerics from the iterative scheme and thus the validity of the differential equations can be tested.

For the sake of simplicity at this stage, there are many assumptions in the current model, the main ones being as follows. First, it is assumed that the chute is vertical; second, that the grains are round and we assume that consequently no rotation is induced at a collision; third, that there is no frictional or drag force between the grain and the chute; fourth, drag forces or other air effects are not included until section 2.3. A more realistic collision model would have to reconsider these and perhaps other points.

To start with, then, we have the following simple equations of Newtonian particle motion,

$$m\ddot{y} = -mg, \tag{2.1}$$

and

$$m\ddot{x} = 0. \tag{2.2}$$

Here y is the distance down the chute, x is the distance across the chute, g is the acceleration due to gravity ($g \approx 9.8\,ms^{-2}$ as the chute is assumed to be vertical in the current chapter) and t is the time between collisions. A dot denotes differentiation with respect to time. Equations (2.1) and (2.2) give the solutions

$$y_{n+1} = -\frac{1}{2}gt^2 + v_n^+ t + y_n, \tag{2.3}$$

and

$$x_{n+1} = u_n^+ t + x_n, \tag{2.4}$$

where u and v are the moduli of the horizontal and vertical velocity components respectively. The subscript n represents a quantity at the instant of the n^{th} bounce, a superscript plus sign indicates a quantity immediately after a collision and a superscript minus sign indicates a quantity immediately before a collision.

At the collision the velocities are assumed to change as follows:

$$v_n^+ = v_n^-, \tag{2.5}$$

and

$$u_n^+ = \hat{e}u_n^-, \tag{2.6}$$

where $\hat{e}$ is the coefficient of restitution and takes a constant value between 0 and 1. Equation (2.6) is Newton's empirical law of restitution [46]. If $\hat{e} = 1$ then the collision is perfectly elastic and the particle conserves all its energy. Energy is lost in a collision if $\hat{e} \neq 1$ and so in this case a particle will return with its relative velocity reduced in magnitude. In particular, if $\hat{e} = 0$, the collision is imperfect, the particle loses all its energy during the collision and it coalesces with the chute wall. Note that there is no minus sign in (2.6) because for the moment we are only considering the modulus of the horizontal velocity. The horizontal velocity is always considered to be positive and the modulus signs have been dropped. The vertical velocity component remains unchanged at a collision.

The time between each collision is the time taken to cross the chute:

$$t = \frac{x_{n+1} - x_n}{u_n^+} = \frac{\alpha}{u_n^+}, \tag{2.7}$$

where α has been defined as $\alpha = x_{n+1} - x_n$, and is the chute width.

Thus, on substitution into (2.3), we obtain:

$$y_{n+1} = -\frac{1}{2} g \left(\frac{\alpha}{u_n^+}\right)^2 + v_n^- \left(\frac{\alpha}{u_n^+}\right) + y_n. \tag{2.8}$$

Clearly, we can also obtain an equation for the vertical velocity of the particle immediately prior to a collision,

$$v_{n+1}^- = -\frac{g\alpha}{u_n^+} + v_n^- . \tag{2.9}$$

As there is no acceleration in the horizontal direction, the horizontal velocity immediately prior to the $(n+1)^{th}$ collision is equal to the horizontal velocity immediately after the n^{th} collision. Hence

$$u_{n+1}^- = u_n^+ . \tag{2.10}$$

Therefore the set of discrete difference equations governing the behaviour of the particle in the chute is:

$$u_{n+1}^- = \hat{e} u_n^- , \tag{2.11}$$

$$v_{n+1}^- = -\frac{g\alpha}{u_{n+1}^-} + v_n^- , \tag{2.12}$$

and

$$y_{n+1} = -\frac{1}{2} g \left(\frac{\alpha}{u_{n+1}^-}\right)^2 + v_n^- \left(\frac{\alpha}{u_{n+1}^-}\right) + y_n. \tag{2.13}$$

Here α is the horizontal distance between each collision, corresponding to the width of the chute. Given the initial values of $(u^- v^-, y^-)$ as (U_0, V_0, Y_0) respectively we find that after m collisions the general solutions are given by

$$u_m^- = U_0 \hat{e}^m, \tag{2.14}$$

$$v_m^- = -\frac{g\alpha}{U_0} \left(\hat{e}^{-m} + \hat{e}^{-m+1}\right) + V_0, \tag{2.15}$$

and

$$y_m^- = -\frac{1}{2}g\left(\frac{\alpha}{U_0}\hat{e}^{-m}\right)^2 + \left(-\frac{g\alpha}{U_0}\left[\hat{e}^{-m+1} + \hat{e}^{-m+2}\right] + V_0\right)\left(\frac{\alpha}{U_0}\hat{e}^{-m+1}\right) + Y_0. \quad (2.16)$$

2.1 Obtaining the differential equations and their solutions

Here we consider the case of near-perfect collisions, for which we require $\hat{e} \simeq 1$, together with a narrow chute so that α is small. So we can expand $\hat{e}$ as

$$\hat{e} = 1 - \alpha E$$

say, in the limit

$$\alpha \to 0,$$

where E is an $O(1)$ constant.

Subtracting u_n^- from both sides of equation (2.11) and employing the above expansion we obtain:

$$\frac{u_{n+1}^- - u_n^-}{\alpha} = -Eu_n^-.$$

If we take the limit as $\alpha \to 0$ and write $\alpha \equiv \delta h$ (the later being a small incremental distance in the horizontal) then we simply see the above as

$$\frac{du}{dh} = -Eu. \quad (2.17)$$

Similarly, equation (2.12) is seen to become

$$\frac{dv}{dh} = -\frac{g}{u}. \quad (2.18)$$

Finally,

$$\frac{dy}{dh} = -\frac{1}{2}\frac{g\alpha}{u^2} + \frac{v}{u}. \quad (2.19)$$

The boundary conditions are

$$u = u_0 \text{ at } h = 0, \quad (2.20a)$$

$$v = v_0 \text{ at } h = 0, \quad (2.20b)$$

and

$$y = 0 \text{ at } h = 0. \tag{2.20c}$$

The solutions to the continuous differential equations derived above are straightforward and are as follows.

$$u = u_0 e^{-Eh}, \tag{2.21}$$

$$v = v_0 + \frac{g}{u_0 E}\left(1 - e^{Eh}\right), \tag{2.22}$$

and

$$y = \frac{v_0 u_0 E + g}{u_0^2 E^2} e^{Eh} - \frac{g\,(\alpha E + 2)}{4E^2 u_0^2} e^{2Eh} + \frac{g\,(\alpha E - 2) - 4u_0 v_0 E}{4u_0^2 E^2}. \tag{2.23}$$

Now it is possible to remove the factor of g from the solution (2.23) if we make the following transformation:

$$\begin{pmatrix} u_0 \\ v_0 \end{pmatrix} = \sqrt{\alpha g} \begin{pmatrix} u_{0c} \\ v_{0c} \end{pmatrix}, \tag{2.24}$$

where u_{0c} and v_{0c} are the quantities to be used in a calculation. Consequently the solutions are now written as

$$u = \sqrt{\alpha g}\, u_{0c} e^{-Eh}, \tag{2.25}$$

$$v = \sqrt{\alpha g}\, v_{0c} + \frac{\sqrt{g}}{\sqrt{\alpha} u_{0c} E}\left(1 - e^{Eh}\right), \tag{2.26}$$

and

$$y = \frac{\alpha v_{0c} u_{0c} E + 1}{\alpha u_{0c}^2 E^2} e^{Eh} - \frac{(\alpha E + 2)}{4E^2 \alpha u_{0c}^2} e^{2Eh} + \frac{(\alpha E - 2) - 4\alpha u_{0c} v_{0c} E}{4\alpha u_{0c}^2 E^2}. \tag{2.27}$$

2.2 Comparison between the results from the continuous and discrete equations.

We now compare the solutions of the ordinary differential equations (2.25), (2.26) and (2.27) with the results from the difference equations (2.11), (2.12) and (2.13) in order to test the validity of the continuum approach. In truth, the difference equations are the equations which 'correctly' describe the behaviour of the particle and the ordinary differential equations are a continuous approximation to this.

We plot the solutions for u and v as functions of y from the differential equations for typical parameters. We also calculate numerically the position and velocity of the grain at each collision using the iterative scheme implied by the discrete equations. The data is used to plot u_n^- and v_n^- as functions of y_n. The solutions are then compared graphically to assess the validity of the continuous approximation. To put this on a firmer quantitative basis, the error between the two methods is calculated after the final collision.

To find u and v as functions of y from the continuum approach, h must first be eliminated from the solutions. We can write h as a function of y and substitute this into the solutions for u and v for typical parameters. (By typical parameters we mean simple representative values of u_{0c}, v_{0c} and α.)

We observe that equation (2.27) is quadratic in e^{Eh}. Thus the solution is

$$\begin{aligned} e^{Eh} &= \frac{4\alpha\left(v_{0c}u_{0c}E+1\right)}{2\left(2+\alpha E\right)} \\ &\mp \frac{\sqrt{16\left(\alpha v_{0c}u_{0c}E+1\right)^2+4\left(2+\alpha E\right)\left(\left(\alpha E-2\right)-4\alpha v_{0c}u_{0c}E-4E^2\alpha u_{0c}^2 y\right)}}{2\left(2+\alpha E\right)}. \end{aligned} \tag{2.28}$$

Now if we choose $u_{0c} = \frac{1}{\sqrt{\alpha}}$, $v_{0c} = -\frac{1}{\sqrt{\alpha}}$ as typical values for the non-dimensional velocities at $h = 0$ (because of (2.24), so that the dimensional velocities are $O(1)$ in magnitude, which seems to be approximately correct, at least for an initial investigation), and if we put $E = 1$, (2.28) reduces to

$$e^h = \mp\frac{\sqrt{(2+\alpha)\left((2+\alpha)-4y\right)}}{(2+\alpha)}. \tag{2.29}$$

Since $e^h > 0$ the positive root must be taken here.

Substituting into equations (2.25) and (2.26) for u and v we obtain the solutions as functions of y:

$$u = \frac{\sqrt{g}\,(2+\alpha)}{\sqrt{(2+\alpha)\left((2+\alpha)-4y\right)}} \tag{2.30}$$

and

$$v = -\frac{\sqrt{g\,(2+\alpha)\left((2+\alpha)-4y\right)}}{(2+\alpha)}. \tag{2.31}$$

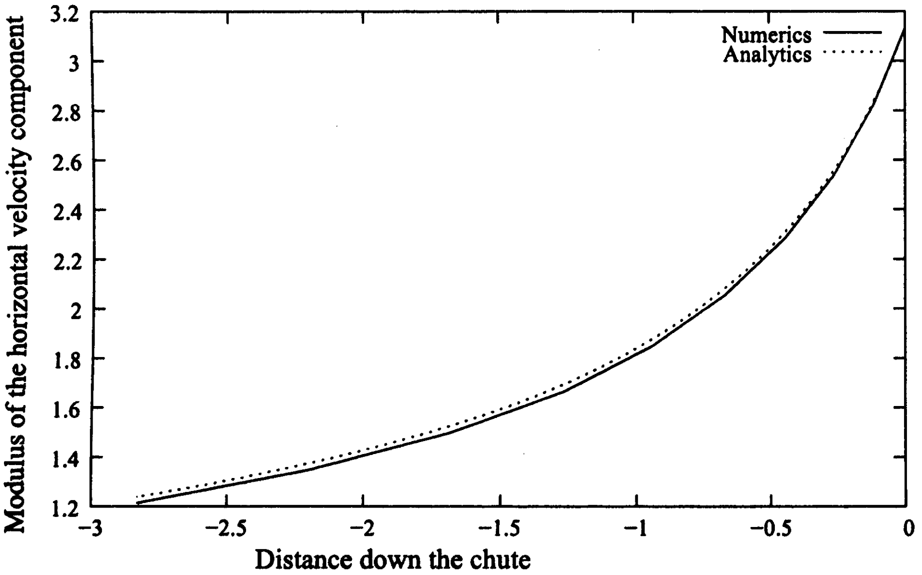

Figure 2.1: Graph showing the difference between the analytical solution for u with $\alpha = 0.1$ and the numerics after ten bounces. The solid line is the solution from the iterative scheme and the dotted line is the solution from the differential equation.

Figure 2.1 shows the continuous and discrete solutions of $u(y)$ for $\alpha = 0.1$. (For the discrete solutions $u(y)$ is actually a plot of u_n versus y_n). This involves only ten impacts, but there is clearly a good match between the two results. In fact the error between the value of u from the differential equation and the value from the discrete equation (which can be considered to be the 'true' value) at the end of the computation is only 2.08%.

Figure 2.2 shows the solutions for $v(y)$ from the two methods for $\alpha = 0.1$. Again, a good match between the results is observed. The error between the two values at the end of the simulation is 2.04%.

2.3 Some brief remarks on air effects

If drag is included between the grain and the air (we still assume that there are no frictional or drag forces between grain and chute), the governing equation for the

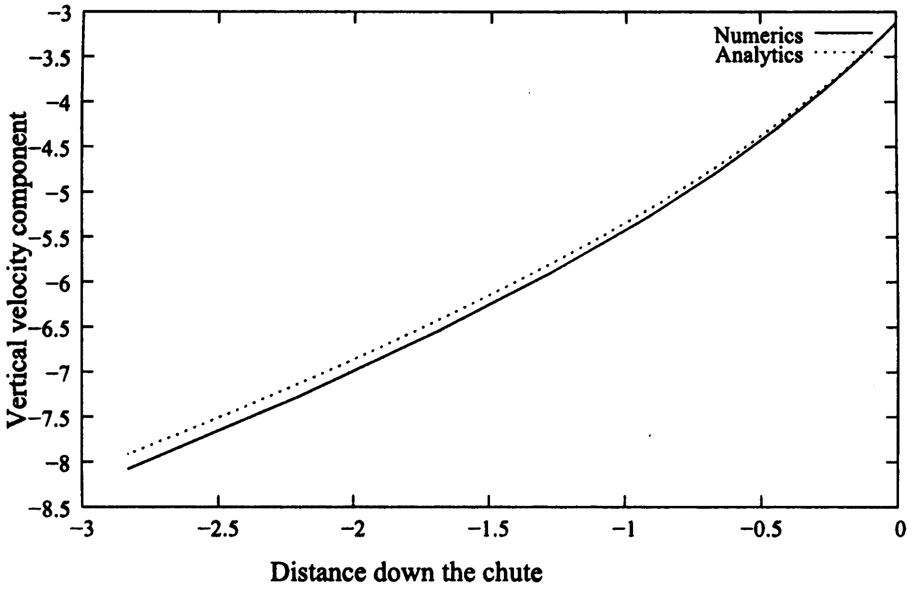

Figure 2.2: Graph showing the difference between the analytical solution for v with $\alpha = 0.1$ and the numerics after ten bounces. The solid line is the solution from the iterative scheme, whereas the dotted line is the solution from the differential equation.

particle's motion in the vertical direction (2.1) is modified to

$$m\ddot{y} = mg - \lambda m\dot{y}^2 \tag{2.32}$$

where λ is a positive constant that determines the magnitude of the drag force. This is the amplitude-squared law of drag, which assumes a sufficiently large flow rate or grain-based Reynolds number. Our concern will tend towards this case of higher flow rates. An alternative for lower grain-based Reynolds number is a linear term, $-\lambda_2 m\dot{y}$ say [32]. It has also been assumed here that $|\dot{x}| \ll |\dot{y}|$, which seems sensible for the current industrial application as observation does indeed indicate that horizontal velocities are significantly less than vertical velocities in the chute. We mention finally here that we have not considered the x-momentum equation but we anticipate that similar terms would arise there.

To continue, then, the particle will fall at terminal velocity when the drag balances with gravity and the acceleration is zero. An expression for terminal velocity can thus be found by putting $\ddot{y} = 0$ to obtain

$$\dot{y} = \sqrt{\frac{g}{\lambda}}. \tag{2.33}$$

Denoting the terminal velocity as v_e, we see

$$\lambda = \frac{g}{v_e^2}. \tag{2.34}$$

The governing equation therefore becomes

$$\ddot{y} = g - \frac{g}{v_e^2}\dot{y}^2. \tag{2.35}$$

This is a classical problem of Newtonian dynamics but let us note below the details a little. To solve the above equation, let $q = \dot{y}$ to obtain

$$\int \frac{v_e^2}{v_e^2 - q} dq = \int 2g dy + c, \tag{2.36}$$

where c is a constant of integration. Integrating reveals

$$-v_e^2 \ln \left| v_e^2 - q \right| = 2gy + c. \tag{2.37}$$

If the particle starts at rest at $y = 0$ then $c = -v_e^2 \ln \left|v_e^2\right|$. Hence

$$q = v_e^2\left(1 - e^{-\frac{2gy}{v_e^2}}\right), \tag{2.38}$$

i.e.

$$\frac{\dot{y}^2}{v_e^2} = 1 - e^{-\frac{2gy}{v_e^2}}. \tag{2.39}$$

For terminal velocity to be reached, we require $2gy >> v_e^2$ so that $\frac{\dot{y}^2}{v_e^2} \rightarrow 1$ then. The limiting case is $2gy = v_e^2$. Typical values in the industrial setting (see chapter 1) are roughly $y \sim 1m$ and $g \sim 10ms^{-2}$, so $v_e = O(4.5)ms^{-1}$.

Further, the chute-based global Reynolds number of the flow is $Re = \frac{LV}{\nu}$ where L is the chute length, V is the terminal velocity and $\nu = 1.5 \times 10^{-4} m^{-2} s$ is the viscosity of air. Thus $Re \sim 3 \times 10^4$ and therefore the dimensional boundary layer thickness $\delta = O(Re^{-\frac{1}{2}}L) \sim 5mm$. This means that the global boundary layer thickness is of the order of the grain size, and so we might expect air effects to be a significant aspect of the chute flow.

On the other hand the grain-based or local Reynolds number of the flow is $Re_g = \frac{L_g V}{\nu}$ where L_g is the length of a rice grain, for instance. That is $L_g \sim 5 \times 10^{-3} m$. Thus the local Reynolds number is $Re_g \sim 150$, which is a moderate value, lying somewhere between the large or small regimes. The local dimensional boundary layer thickness is $\delta_g = O\left(Re_g^{-\frac{1}{2}} L_g\right) \sim 0.4mm$, which nominally is small relative to the grain size. Air effects will be dealt with at the end of the thesis in chapter 8.

2.4 Summary

We have seen that the problem of a bouncing grain falling down a chute, which is an inherently discrete process, can yield to a continuum approach. This encourages a view that an analytical model may be of use for a simple particulate problem and we hope that the same will be true for the fully developed chute flow. However, before tackling the problem of finding a suitable continuum model for the chute flow (which is begun in earnest in chapter 5) we wish to examine more thoroughly the physical processes at work on the chute. In order to do this, a computational simulation of the flow is developed in the next chapter.

Finally we have demonstrated in this relatively short chapter that air effects may be a significant aspect of the flow, since the boundary layer thickness is of the order of the grain size. We shall return to a study of the air effects in chapter 8.

Chapter 3

Computational simulations of chute flow

Prior to developing continuum or statistical models of the chute flow, we wish to gain more understanding of the physical and impact processes occurring on the chute. In order to do this, we directly compute in the present chapter the trajectories of all the particles in a representative large group as they fall down the chute. We aim to find the velocities and positions of the particles as they exit the chute, and in some sense solve the complete problem. It is then possible to compare these numerics with the data provided by Sortex. Asking if the computational model exhibits any of the observed behaviour seen in reality may enable us to see if the model has captured any of the important processes which occur upon the chute. Thus we may obtain some insight into the physics of chute flow.

3.1 Binary collision model

We start with the most basic of models. We assume that there is no air resistance, that there is no friction between the particles and the chute and between particles, that all particles are spherical and of equal mass, that no rotation is induced at collisions, that restitution acts only in the normal direction, and that only collisions between pairs of part (called binary collisions). Therefore the positions and velocities of the i^{th} particle at the $(n+1)^{th}$ time-step are given by the following simple ballistic equations (cf. chapter 2):

$$x_{i,n+1} = u_{i,n}t + x_{i,n}, \tag{3.1}$$

$$y_{i,n+1} = -\frac{1}{2}gt^2 + v_{i,n}t + y_{i,n}, \tag{3.2}$$

$$u_{i,n+1} = u_{i,n}, \tag{3.3}$$

and

$$v_{i,n+1} = -gt + v_{i,n}. \tag{3.4}$$

In the above, x, y, u and v are the horizontal and vertical co-ordinates and the horizontal and vertical velocity components respectively; t is a fixed time-step and $g = 9.81\ ms^{-2}$ is the acceleration due to gravity. Note that equation (3.3) simply states that the horizontal velocity is unchanged at each time-step since there is no acceleration in the horizontal direction.

If we find that a collision occurs (see test below) within a time-step then the velocities of the colliding particles must be changed accordingly. To find the correct equations we consider a collision between the i^{th} and j^{th} particles. Conservation of momentum yields:

$$u_{i,n} + u_{j,n} = \bar{u}_{i,n} + \bar{u}_{j,n} \tag{3.5}$$

and

$$v_{i,n} + v_{j,n} = \bar{v}_{i,n} + \bar{v}_{j,n}, \tag{3.6}$$

where a bar denotes a quantity after a collision. Newton's empirical law of restitution [46] also applies at collisions. If two particles collide so that the line between particle centres (i.e. the normal direction to the point of contact) forms an angle θ to the horizontal, restitution states that in the normal direction

$$(\bar{u}_{i,n} - \bar{u}_{j,n})\cos(\theta) + (\bar{v}_{i,n} - \bar{v}_{j,n})\sin(\theta) = \hat{e}\,(u_{j,n} - u_{i,n})\cos(\theta) + \hat{e}\,(v_{j,n} - v_{i,n})\sin(\theta), \tag{3.7}$$

and in the tangential direction the velocities do not change so,

$$(\bar{u}_{i,n} - \bar{u}_{j,n})\sin(\theta) - (\bar{v}_{i,n} - \bar{v}_{j,n})\cos(\theta) = (u_{i,n} - u_{j,n})\sin(\theta) - (v_{i,n} - v_{j,n})\cos(\theta) \tag{3.8}$$

That is to say, the speed of retreat of the particles along the normal direction to the point of contact is the speed of approach along the normal direction to the point of contact reduced by a factor $\hat{e}$, known as the coefficient of restitution, which takes a constant value on the interval $[0, 1]$. This is a consequence of energy loss at collisions in general (due to heat exchange during impacts, and so on). If $\hat{e} = 1$ then energy is conserved at a collision and the speed of separation is equal to the speed of approach. Otherwise energy is lost in a collision and particles separate less quickly. In the case $\hat{e} = 0$ all energy is lost and the particles stick together, or coalesce.

Solving equations (3.5) and (3.7) and equations (3.6) and (3.8) simultaneously gives

$$\begin{aligned}\bar{u}_{i,n} = \frac{1}{4}\left[(1+\hat{e})\left(u_{j,n} - (u_{i,n} - u_{j,n})\cos(2\theta) - (v_{i,n} - v_{j,n})\sin(2\theta)\right) + \right.\\ \left.(3-\hat{e})\,u_{i,n}\right] \quad (3.9)\end{aligned}$$

$$\begin{aligned}\bar{u}_{j,n} = \frac{1}{4}\left[(1+\hat{e})\left(u_{i,n} + (u_{i,n} - u_{j,n})\cos(2\theta) + (v_{i,n} - v_{j,n})\sin(2\theta)\right) + \right.\\ \left.(3-\hat{e})\,u_{j,n}\right] \quad (3.10)\end{aligned}$$

$$\begin{aligned}\bar{v}_{i,n} = \frac{1}{4}\left[(1+\hat{e})\left(v_{j,n} + (v_{i,n} - v_{j,n})\cos(2\theta) - (u_{i,n} - u_{j,n})\sin(2\theta)\right) + \right.\\ \left.(3-\hat{e})\,v_{i,n}\right] \quad (3.11)\end{aligned}$$

and

$$\begin{aligned}\bar{v}_{j,n} = \frac{1}{4}\left[(1+\hat{e})\left(v_{i,n} - (v_{i,n} - v_{j,n})\cos(2\theta) + (u_{i,n} - u_{j,n})\sin(2\theta)\right) + \right.\\ \left.(3-\hat{e})\,v_{j,n}\right] \quad (3.12)\end{aligned}$$

as the new velocities following the collision during the n^{th} time-step.

3.2 Computational algorithm

The equations of section (3.1) which govern the particle dynamics on the chute are now used in a computation to produce a first simulation of the flow for many particles. In particular, we can plot the particle trajectories and find the distribution of particle positions and velocities as the particles exit the chute. A brief overview of the algorithm is as follows.

1. Specify the initial conditions.
2. Advance the particles to their new positions and find their new velocities using equations (3.1) - (3.4).
3. Check for collisions.
4. If particles are found to be colliding, change their velocities in accordance with equations (3.9) - (3.12).
5. Go back to 2). Or
6. Stop when particles have exited the chute and save their positions and velocities.

We expand on this description in a little more detail as follows. Initially, particles are placed evenly on a horizontal line at the top of the chute. The particles are disks of one millimetre. They are given arbitrary horizontal velocity fluctuations, but the vertical velocity component is chosen initially to be zero. In the first cases, the horizontal velocities are of the form $u_{i,0} = (-1)^i * 0.01 \sin(x_{i,0})$, but later we choose random values. There are 150 particles in each simulation.

The algorithm for detecting collisions works in the following way. At each time-step the distance between particle centres is calculated for all possible particle pairs. If this distance is less than the particle diameter the particles are deemed to be colliding. Note that this means the particles are actually overlapping (albeit only slightly) at a collision, which is unphysical. To avoid this problem a method was tried in which a variable time-step was used in order to exactly determine the time at which the particles just touch. However, that typically required a continual reduction in the time-step. If the initial time-step is small then after a few such reductions the computer reads the time-step as being identical to zero and so the exact point

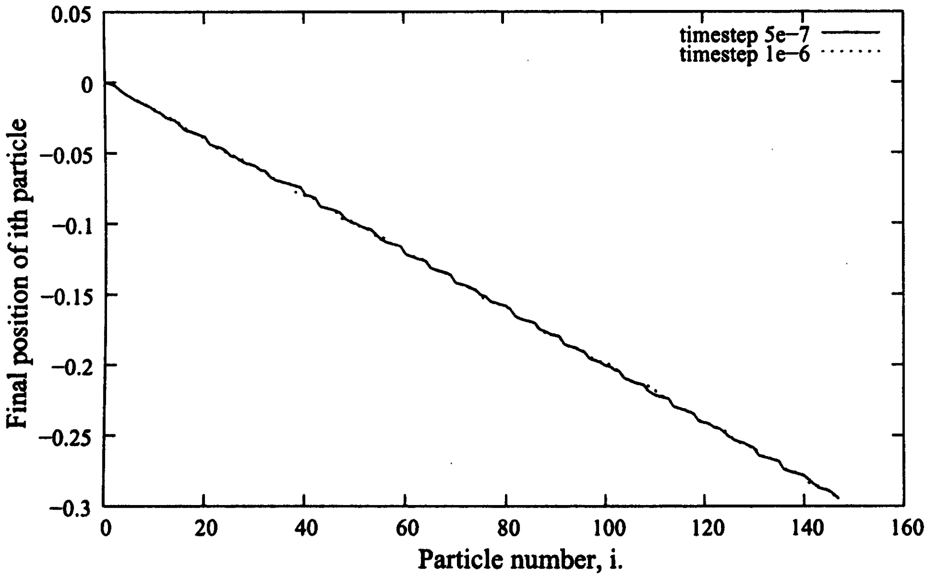

Figure 3.1: Plot showing the final particle distributions for two different time-steps. We see only a small difference between the results and therefore state that the 'overlap' weakness is reduced if the fixed time-step is small. The particles have dropped down the entire chute (i.e. $1m$).

of collision cannot be located. Instead, we require the time-step to be fixed and it is hoped so small that no collisions are accidentally missed by advancing too far. Choosing a small time-step also minimises the overlap problem. We checked that the results are robust to this (seemingly small) flaw by running the program for a particular fixed time-step, then re-running the program again with the same initial conditions but with a smaller fixed time-step and checking that the results have not changed significantly. When this is done, see figure 3.1 below, we see negligible change in the results.

Others have used similar algorithms in the study of granular flows. See, for example, a computer simulation of Louge [39] which investigates a theory of Jenkins' [26] concerning the boundary conditions for flat, frictional granular flows. Louge also has to negotiate the problem of overlap. He ran his simulation until each particle has experienced an average of ten collisions. The time-step is then readjusted so that the mean overlap does not exceed a given tolerance. This is optimised by running simulations with decreasing values of the tolerance until all results of interest become insensitive to further reductions.

On the other hand, researchers such as Sigurgeirsson and Stuart [53] avoid the problem entirely by using an event-driven algorithm. In this method the time to possible next collisions is calculated and the computation is advanced by the smallest time. Thus the exact point of collision is located and there is no risk of missing collisions. However, for this method to be used it must always be possible to determine the time to the next collision. We fear that this may not always be the case, especially for more complex models which may include non-linear effects. As we wish to write a program that would be able to deal with quite complex cases we opt for the former method.

A fundamental test of the code, where we check some results against a simple analytical case, is discussed in Appendix A.

3.3 Preliminary results

We start with an investigation of the effect of changing the coefficient of restitution $\hat{e}$. In simulations for this study, periodic initial conditions were chosen for the horizontal velocity fluctuations. Such an initial condition is found to provoke, or seems to provoke, the clustering phenomenon, explained below.

We examine figures 3.2 - 3.4 illustrating the particle trajectories on the chute for varying values of the coefficient of restitution for the same periodic initial conditions, i.e. $u_{i,0} = (-1)^i * 0.01 \sin(x)$. Each line is a path of a particular particle on the chute. The chute has been chosen to have a width of $0.3m$ and a length of $1m$, as in the Sortex machines (chapter 1).

It seems that as the coefficient of restitution is reduced the distribution of particles may become ever more inhomogeneous: the particles apparently form into clusters, separated by voids, by the time they exit the chute. A suggested mechanism for this is as follows. As particles collide they lose energy. The energy loss is directly

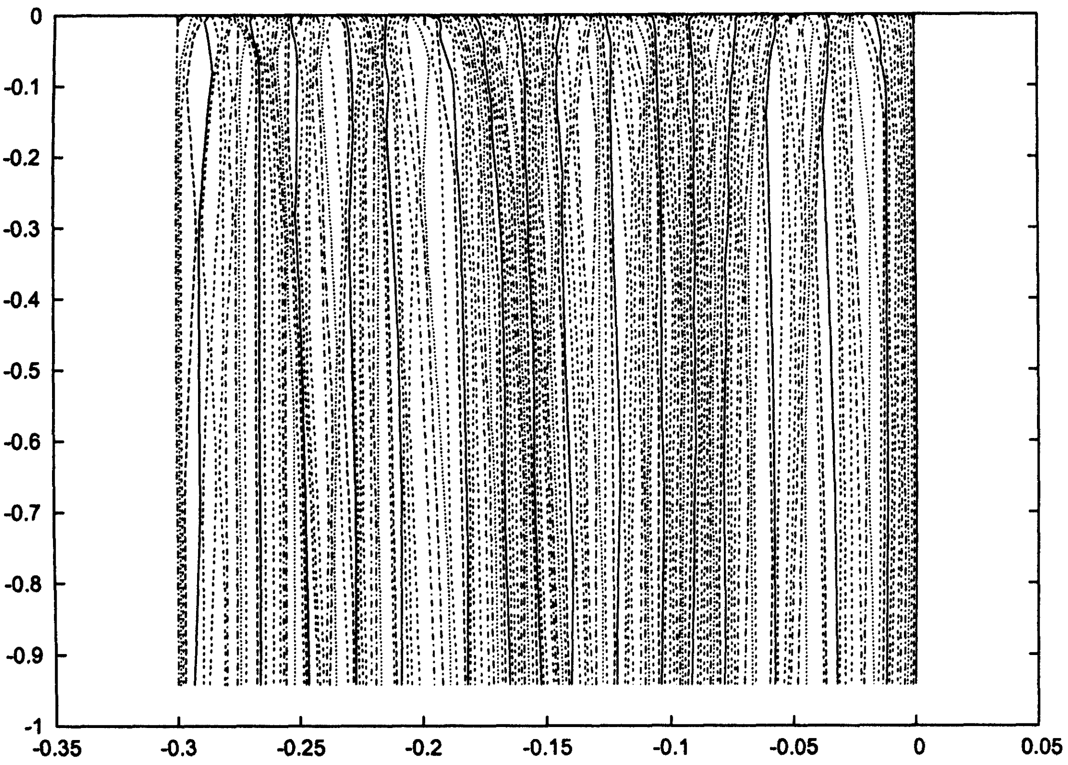

Figure 3.2: Particle trajectories for $\hat{e} = 0.9$. The picture is an 'energetic' one with many collisions. The final distribution is much more uniform here than in other cases.

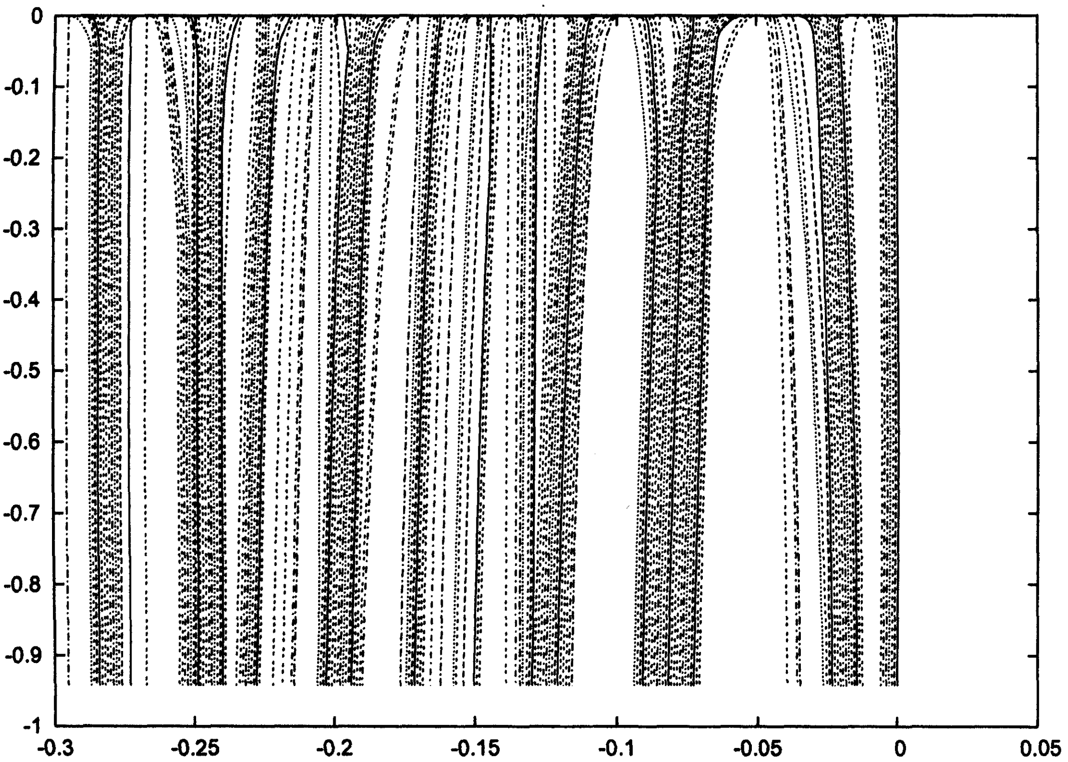

Figure 3.3: Particle trajectories for $\hat{e} = 0.4$. Notice that seemingly particles quickly form into large coalesced masses and the final distribution is highly inhomogeneous and clustered.

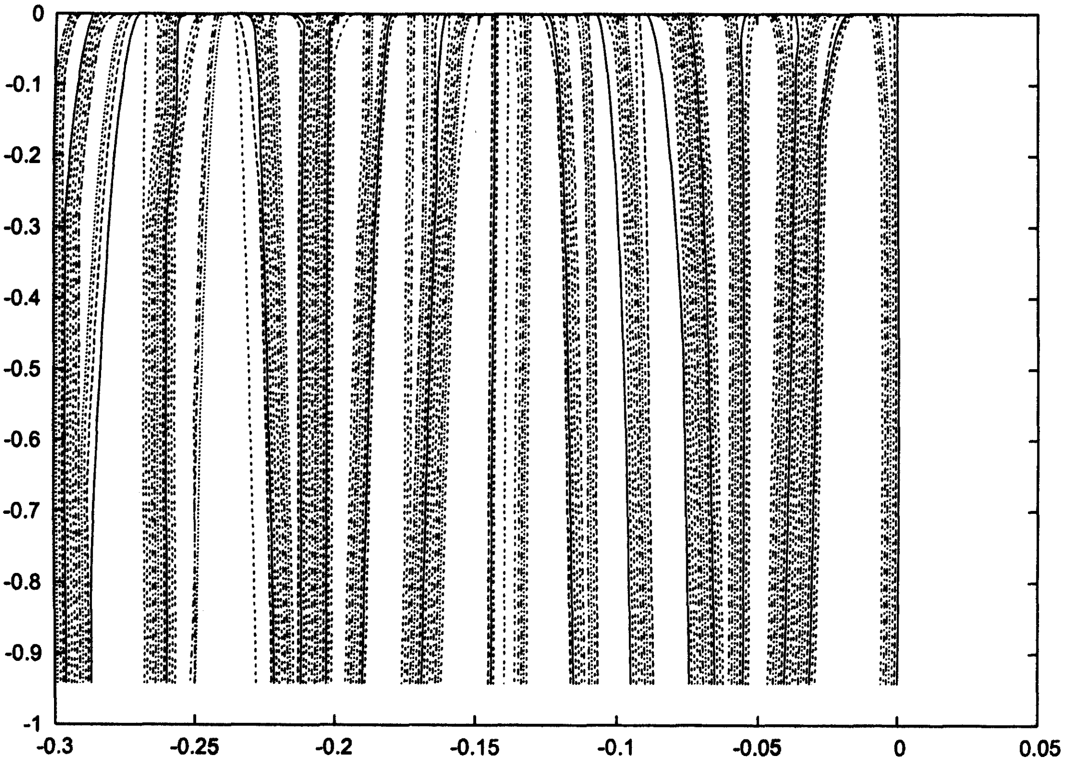

Figure 3.4: Particle trajectories for $\hat{e} = 0.1$. The picture is much the same as in the previous case except there are slightly more apparent clusters and, on average, fewer particles in each one.

related to the coefficient of restitution; as $\hat{e} \to 0$, energy loss increases. Consequently particles separate with a much reduced velocity. Another particle may collide with one of the particles in this pair; there would now be three particles in a small region separating slowly. Thus groups begin to form. After many collisions this might lead to the apparent clusters seen in the figures. If $\hat{e}$ is larger it may take a longer time to form these groups, as not as much energy is lost in each collision, and so the particle distribution might be more homogeneous as the particles exit the chute. If, however, $\hat{e}$ is very small the particles will tend to fall in small coalesced groups; two particles will collide and in effect form a coalesced pair. Almost all the horizontal velocity component will be lost, (if the particle velocities are initially opposite and small in magnitude, which is true for neighbouring particles in the current simulation) and the pair will fall almost vertically through the chute. From here on these two particles will not have a sufficiently large horizontal velocity component to experience further collisions with other particles. Hence for very small coefficients of restitution we tentatively suggest the possible clustering may be less pronounced than for medium values. Further investigation of the apparent clustering phenomenon is presented in Appendix B.

We must also be aware of the issue of 'inelastic collapse' in the model, i.e. the phenomenon of a particle undergoing an infinite number of collisions in a finite time [29], [40]. (The classic example is the case of a bouncing ball: the height of the top of the bounce becomes smaller and smaller with increasing time but only asymptotically approaches zero). Inelastic collapse occurs as a consequence of using a 'hard-disk' model. The assumption was made that the particles were rigid when the collisional rule was given in equations (3.7) and (3.8). However, Zhou and Kadanoff [65] have shown this only to be a significant issue when $\hat{e} < 7 - 4\sqrt{3} \approx 0.072$ for one-dimensional systems and our model, for the moment at least, considers particle collisions only on horizontal lines. Since the coefficient of restitution for grain-grain collisions in reality is seen to be around $0.25 - 0.5$ we need not be concerned about this. (Of course, there are alternative models for dealing with particle contact collisions, such as the so-called 'spring-dashpot' system [40], [47]).

The conjectured clustering phenomenon also leads us to ask about what may happen if there are more than two bodies involved in a collision. This may at first seem likely in a large group of particles. Hence we develop our own empirical law for three-body collisions (although other authors have considered this, e.g. Constantin, Grossman and Mungan [9]). We consider three particles, particles 1, 2 and 3. We split the three-body collision into a series of binary collisions until the particles escape (again this may be an infinite number of collisions if inelastic collapse occurs instead; so we remain outside this regime). However, the results are found to be dependent on order - a sequence starting with particle 1 hitting particle 2 does not yield the same result, in general, as collisions where the first collision is between particles 2 and 3. Thus we find the result for both sequences and take the average of the final velocities as our empirical law. However, when simulations are run it is found that in practice three-particle collisions are extremely rare and are thus of negligible effect, and so there is no great need for the inclusion of our new empirical law in the code. The reason for this could be that the horizontal velocity fluctuations within a proposed cluster are so small that the particles tend to fall together just as one coalesced mass. Figure 3.5 shows the typical reduction in horizontal velocity fluctuations from the initial values. At first, the amplitude of the velocity fluctuations has a magnitude up to the order of 0.01, but at the bottom of the chute the amplitude is roughly half this value, on average. One small flaw with the averaging approach, described above, is that it could enhance energy loss. A better approach in the future may be to randomly select between the two options each time.

We now move on to examine the final particle distributions for varying initial density and compare them with Sortex images. To produce images from the author's code, the initial condition is changed so that particles start with random horizontal velocity fluctuations. The particles are evenly spaced along a line at the top of the chute. We plot the final positions and then re-run the simulation for another batch of particles. We plot the final position of these particles exactly one particle diameter above those of the previous batch, and so on. Thus this picture is not a 'true' image of many particles coming off the chute and, importantly, there is no

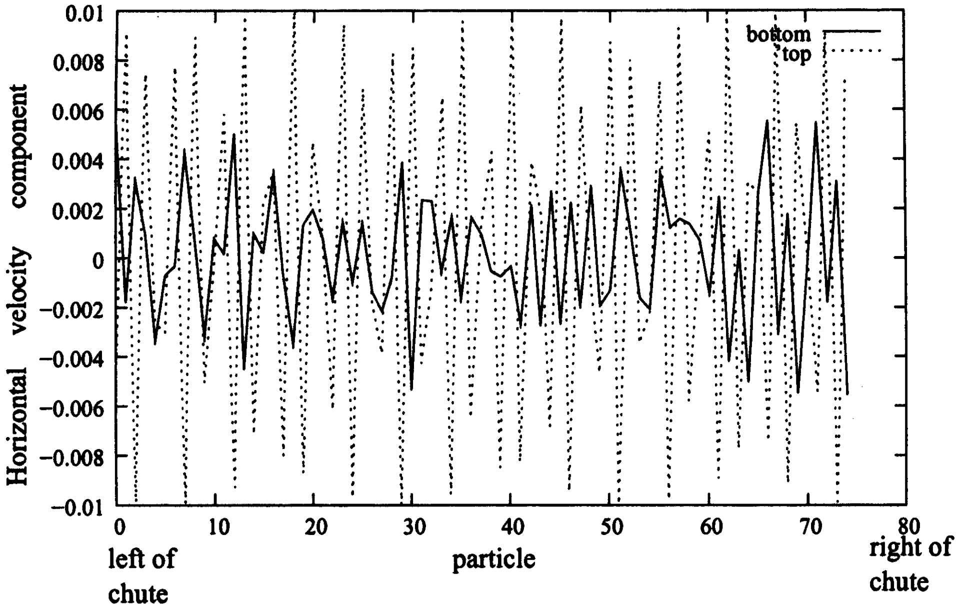

Figure 3.5: Graph showing reduction in amplitude of horizontal velocity fluctuations for $\hat{e} = 0.5$. The solid line is the horizontal velocity component of each particle as they exit the chute, the dashed line shows the initial horizontal velocity fluctuations at the top of the chute.

vertical interaction between each batch, which is perhaps an over-simplification.

However, Sortex images are actually produced in somewhat the same way. Sortex engineers take an image of one line of particles as the particles exit the chute and then take another image and scan that above the previous one, and so on. Therefore, even in a Sortex image, one is not looking at particles falling off the chute, but rather a sequence of snap-shots of particles as they come off the chute. Hence these Sortex images and the computer generated images from the present code make for a reasonably fair comparison. (Although there is no vertical interaction between the lines of images that make up the Sortex 'photograph', this interaction has existed upon the chute and therein lies an important difference between our computation and reality). In the code we vary the density by first sending down 150 particles evenly spaced on a line, then we change to 100 and finally only 50 grains.

Observe that the densities used in the computation do not directly correspond to the densities in each of the corresponding Sortex images. Rather the comparisons are only meant as a guide; they show at most a very informal if encouraging agreement between the present model and the real-life Sortex results, and indeed they could be illusory. That is to say, we are not discussing flows of the same density, we are only comparing examples of dense flows from simulation and experiment, then comparing sparser flows, and so on. Such a comparison, however, is over-simplistic as we compare a distribution *of points* to a distribution of *finite sized* grains; this is a weak point and in view of this all comparisons must be made cautiously.

Some general agreement between the model and Sortex images is possibly observed. The density distributions appear to be inhomogeneous in all cases. In the high density case there appear to be few voids and the size of each void seems roughly to be of the correct magnitude as seen in the Sortex image. The number of such voids in our picture and the Sortex image also seems to be of the same order. There also appear to exist regions of very high density where grains are tightly packed together and this also is perhaps a common feature of both images.

In the medium density picture we again see apparently the same common general features described above. The conjectured voids perhaps are slightly larger and

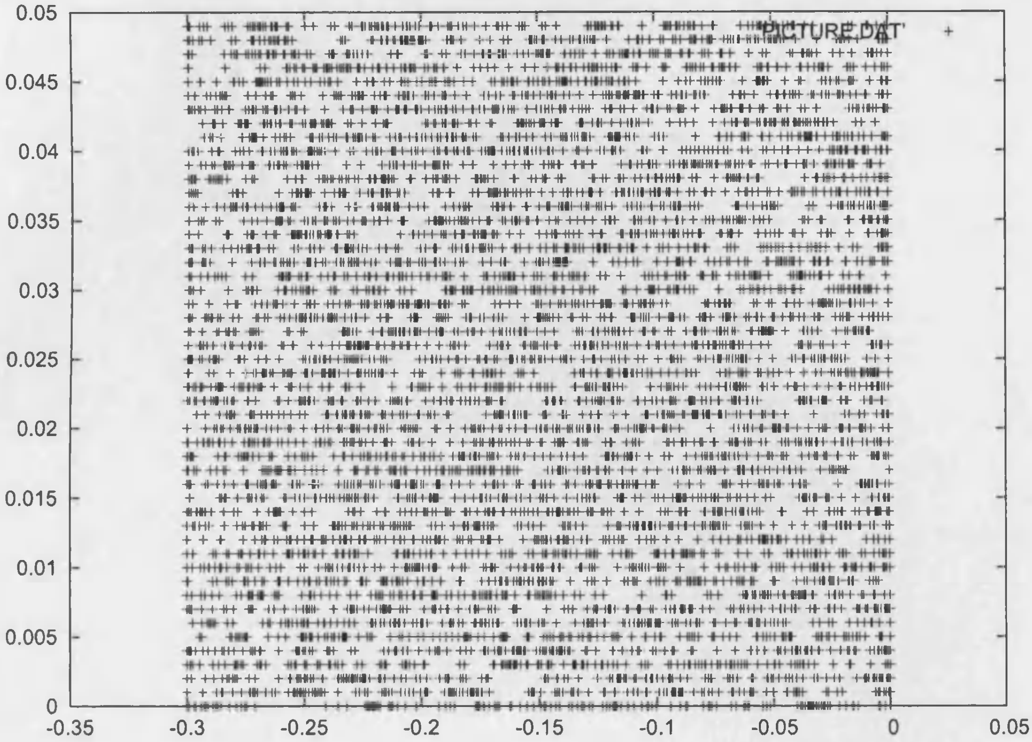

Figure 3.6: Computer generated image of high density flow. Each point represents the centre of a grain.

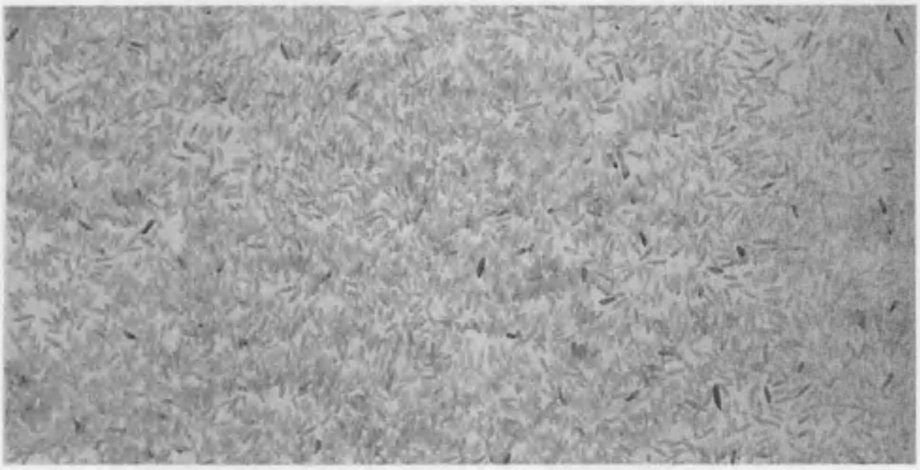

Figure 3.7: Sortex image of high density flow.

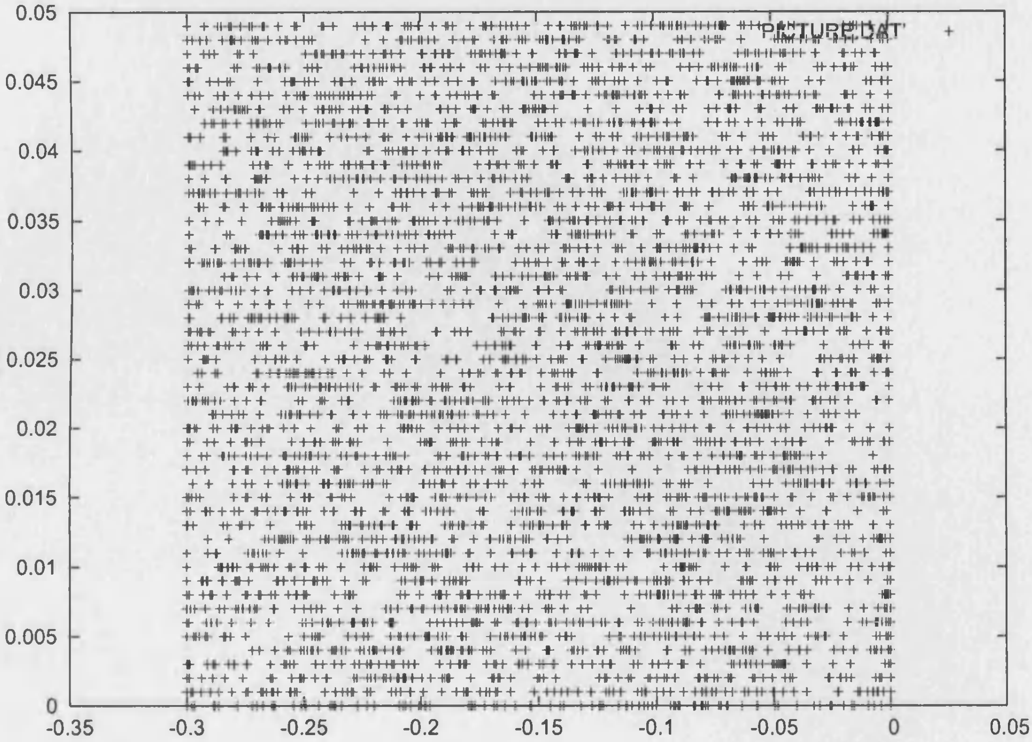

Figure 3.8: Computer generated image of medium density flow. Each point represents the centre of a grain.

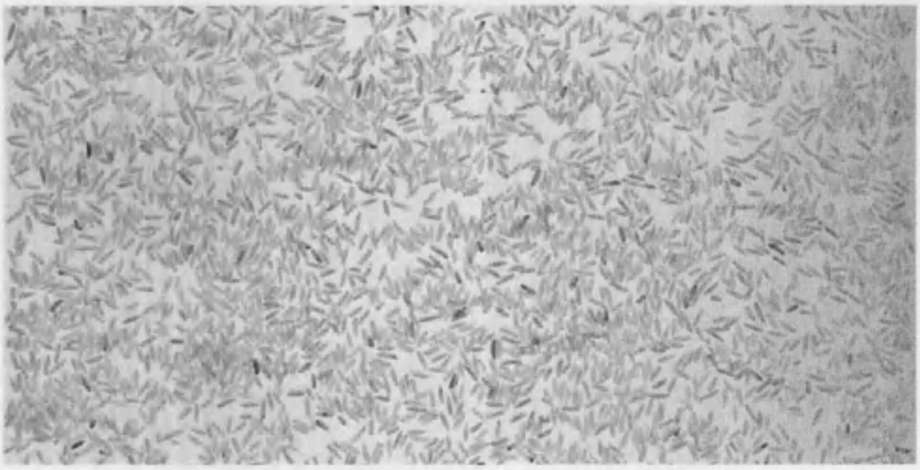

Figure 3.9: Sortex image of medium density flow.

Figure 3.10: Computer generated image of low density flow. Each point represents the centre of a grain.

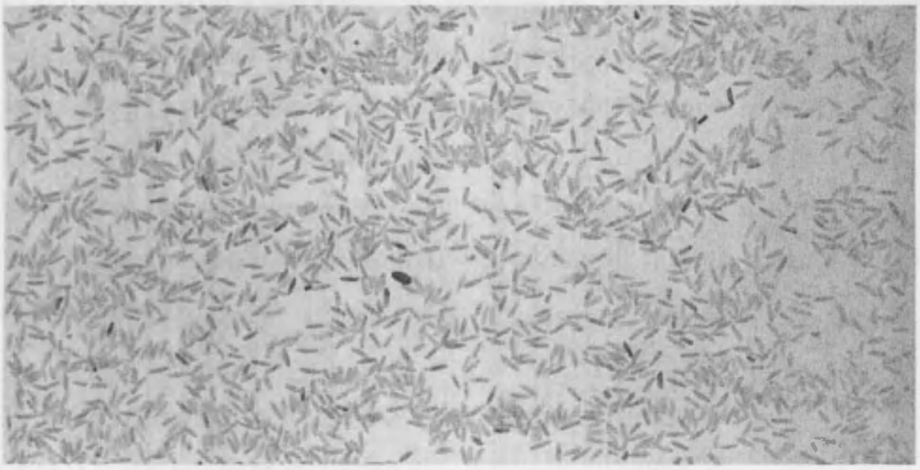

Figure 3.11: Sortex image of low density flow.

perhaps slightly more numerous, but in general the picture appears not to have changed much.

The low density case is again potentially encouraging if no more. Some isolated grains are appearing in the picture, the possible clusters do not seem to be as tightly packed and the possible voids appear to be larger and frequently occurring.

In conclusion, the model appears to capture perhaps the creation of inhomogeneous density distributions by the physics of clustering and energy loss. This seems to be a potentially important feature of chute flows. Indeed, we are not the first to make this observation, see [2], [29], [47] and references therein. Questions of inelastic collapse and many-particle contacts have arisen and seem to be relatively unimportant for the parameter regime of interest to Sortex (at least in one dimension). Finally, the model, albeit simplistic (as described in a previous paragraph), shows some possibly encouraging agreement with reality.

We should re-emphasise that a question remains about how the distributions of rice differ from a random placement of grains on a plane. The question is of significance to Sortex. Indeed, the author undertook a preliminary investigation of the issue whilst working at Sortex, of which a brief summary can be found in appendix C and more detailed reports can be obtained on request. The investigations were an initial attempt to tackle the issue, a complete analysis of which is outside the realm of the present thesis. We reiterate here the weakness of comparing computational distributions of *points* with experimental distributions of *finite-sized* grains and (although subsequently in section 3.4.1, see figure 3.17, computational results with finite sized discs are presented) we state again that all comparisons must be made cautiously.

3.4 Inclusion of more complex effects

It is desirable to include more complex effects in the simulation, such as interactions in the vertical and effects due to the chute geometry. In particular, we wish to have a physically realistic computational simulation with which we can investigate pertinent aspects of the flow. Recall from chapter 1 that the wish is to reach a uniform flow which will reduce the erroneous ejection of grains surrounding a reject particle. Methods of statistically measuring the clustering (in order to determine if there is any improvement to the flow) were investigated by the author during a period of experimental work undertaken at Sortex Ltd. and these investigations are discussed in appendix C.

To enable us to accurately model the full flow, we utilize a commercially available code (from Itasca) called 'PFC2D'. This code allows easy simulation of complex granular phenomena using a programming language called 'FISH' alongside useful internal routines. With this code it is relatively simple to include wall/grain friction, change the grain density, alter wall shape and investigate other relevant properties. First, this code is used to replicate the earlier results found from the simulations using the author's code, before an investigation of more complex effects is undertaken.

A number of parameters must be set in the PFC2D code for both the wall properties and the ball properties. For the walls and the balls, the normal and tangential shear stiffness is arbitrarily set at a value of $1 \times 10^8 N\ m^{-1}$ to ensure that they are sufficiently stiff. This is the recommended value in PFC2D for a wall. The balls are also set to have an arbitrary density of $1000 kg\ m^{-3}$, i.e. about the density of water. This may or may not be suitable for rice. Friction between balls is set to zero and the acceleration due to gravity is chosen as $8.5 m\ s^{-2}$ as the chute typically slopes at an angle of 60^o to the horizontal. The coefficient of restitution between balls has to be set by choosing a critical damping ratio. In order to make sure that this ratio corresponds to a value of $\hat{e} \sim 0.4$, as in the author's computations, we must set the 'notension' function to 'on' and pick the normal viscous damping parameter as 0.35. Finally, in each experiment the balls start along a horizontal line at the top of the chute with initial velocities specified as described below.

3.4.1 Results

As mentioned above, we initially employ the commercial code to run a simulation of the same type as that in the author's code in order to compare with previous results.

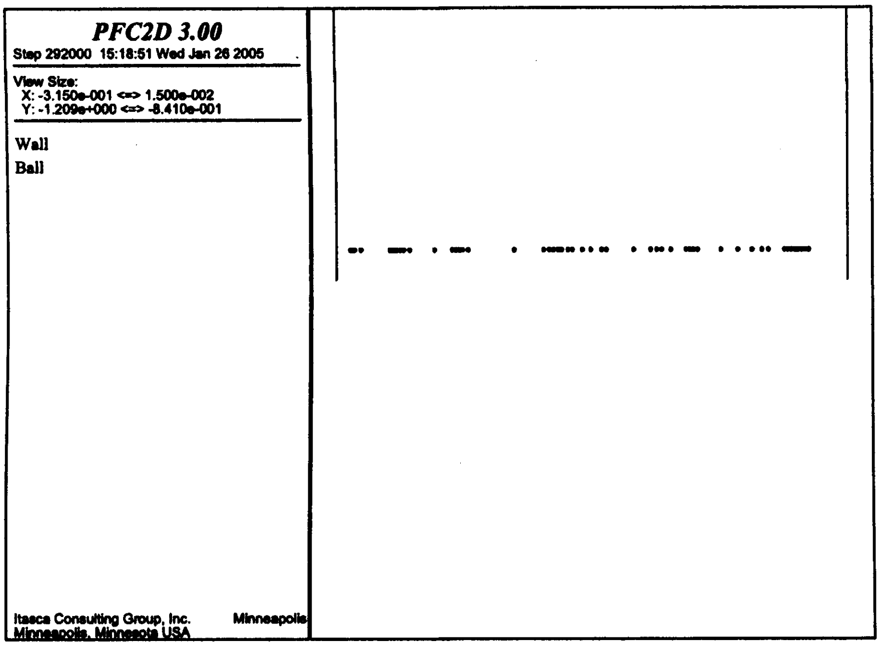

Figure 3.12: The above figure shows the end result of a simulation in which particles enter the chute with horizontal velocity fluctuations only (as in the author's code). They then fall under gravity and collisions also occur. We observe a clustered structure which is very similar to the results previously produced.

That is to say, we run a simulation in which one line of particles falls through a chute with only random horizontal velocity fluctuations. Again, friction, air effects and so on are neglected. There are fifty particles in the simulation.

Figure 3.12 shows the end result of one simulation. The picture is qualitatively the same as before, with a clustered structure being observed.

Having confirmed that the PFC2D code seems to yield results consistent with the established code, we move on to include more complex effects in the model. Vertical velocity fluctuations are now included in the initial condition. The vertical velocity fluctuations are random in magnitude, but the velocity is always downward (i.e. we exclude particles moving up the chute). Further to this, a second 'batch' of particles enters the chute after an arbitrary time delay.

As a consequence of the vertical velocity fluctuations, particle interaction between

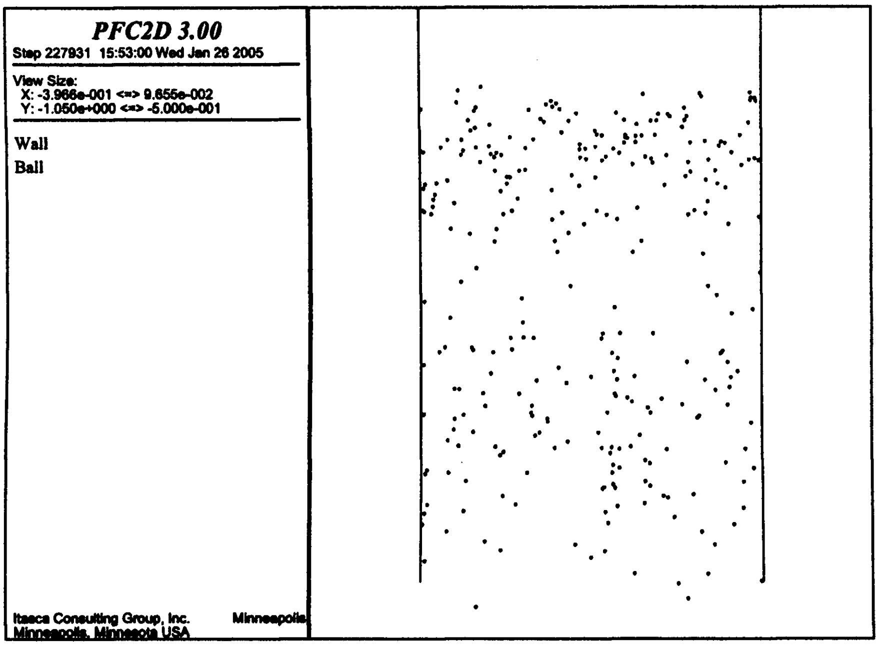

Figure 3.13: In the above figure, vertical velocity fluctuations have been included in the initial condition. Further to this, a second 'batch' of particles enters the chute after a time delay. As a consequence of the vertical velocity fluctuations particle interaction between the two batches occurs resulting in situations with the above character. Only the lower half of the chute is shown.

the two batches occurs. The faster particles from the second batch catch up the slower particles from the first batch and (more) collisions take place. This may be why there appears to be more clustering toward the top of the distribution. There also appears to be a banded structure: a slight gap is perceived between the fast and the slow particles. We observe that a clustered structure is still apparent and the distribution of grains is not homogeneous, see figure 3.13.

The effect of chute geometry is now introduced into the simulation. Four different chute shapes are examined: a straight chute, a chute that widens, a chute that tapers and a chute that has a bend. Only a pair of particles with random horizontal velocity fluctuations are placed in the chutes at first. (Vertical velocity fluctuations are again neglected for this simulation).

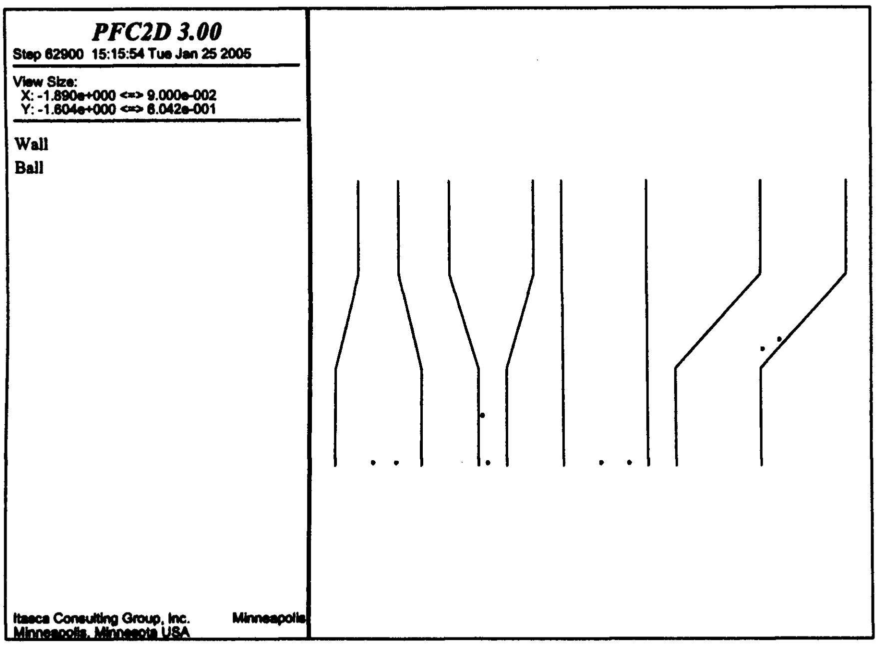

Figure 3.14: We now move on to a preliminary investigation of chute-shape effects. First, we simply place a pair of particles at fixed positions with random horizontal velocities into four chutes of different shape. The first chute has a part where it widens and the end result appears to be very similar to the straight chute. The second chute narrows part way down. This seems to create a vertical displacement of the particles. Third is the straight chute for which the results have already been studied more fully. Finally, there is a chute with a bend. Here the particles are seen to be much further up the chute than in the preceding examples.

Figure 3.14 shows the final positions of the two particles. In the chute which has a widening the results are much the same as for the straight chute. The second chute, which tapers, seems to create a vertical displacement of the particles. In the chute with the bend it appears that the particles take much longer to fall through the chute as the particle pair is still near the middle of the chute at the time when the other particles are exiting.

Next, many particles are placed in these chutes. In this simulation vertical velocity fluctuations have again been neglected. Note that as the first chute is narrow at

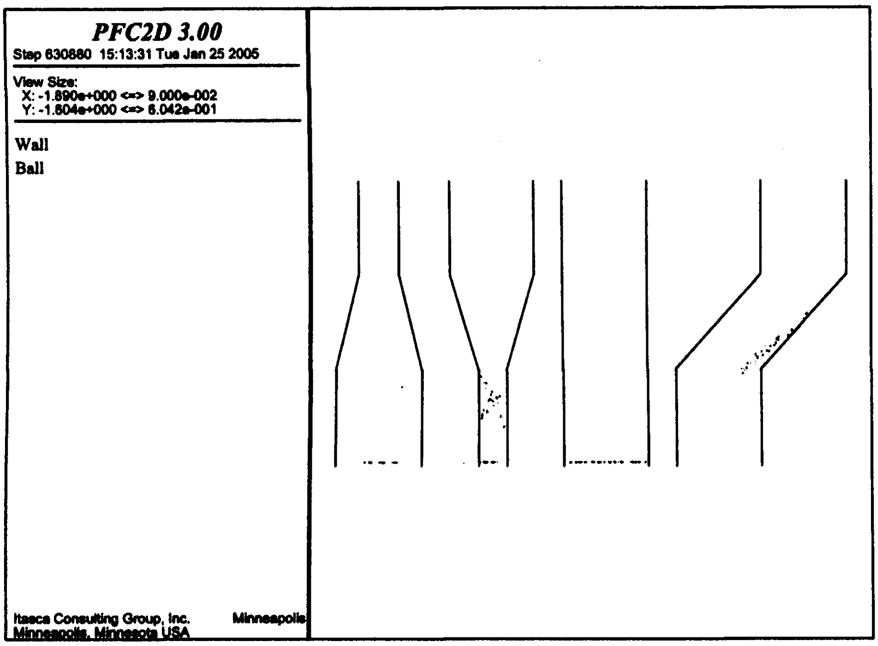

Figure 3.15: Many particles are placed in the chutes. The different particle behaviours are discussed in the text.

the top only half as many particles can enter this chute. The end result is again qualitatively similar to the straight chute except that there are fewer particles and all of them are in a region near the centre of the chute. The second shape, namely the tapered chute, splits the grains into two groups. The particles that start at the centre cluster together, as usual, through collisions with neighbouring particles. They then fall straight through the middle region of the chute without colliding with the walls and thus go ahead of the other particles. These other particles are involved with collisions at the walls that slow their fall and cause them to move toward the centre of the chute. This causes them to be displaced vertically. Here they undergo further particle-particle collisions. Hence a second cluster of particles evolves higher up the chute. In the fourth chute all particles hit the sloping right-hand wall which slows their fall and disperses them slightly. See figure 3.15 for clarification.

For the final investigation concerning the chute geometry we include vertical velocity fluctuations (cf. figure 3.13). The effect of this seems to be a vertical dispersion

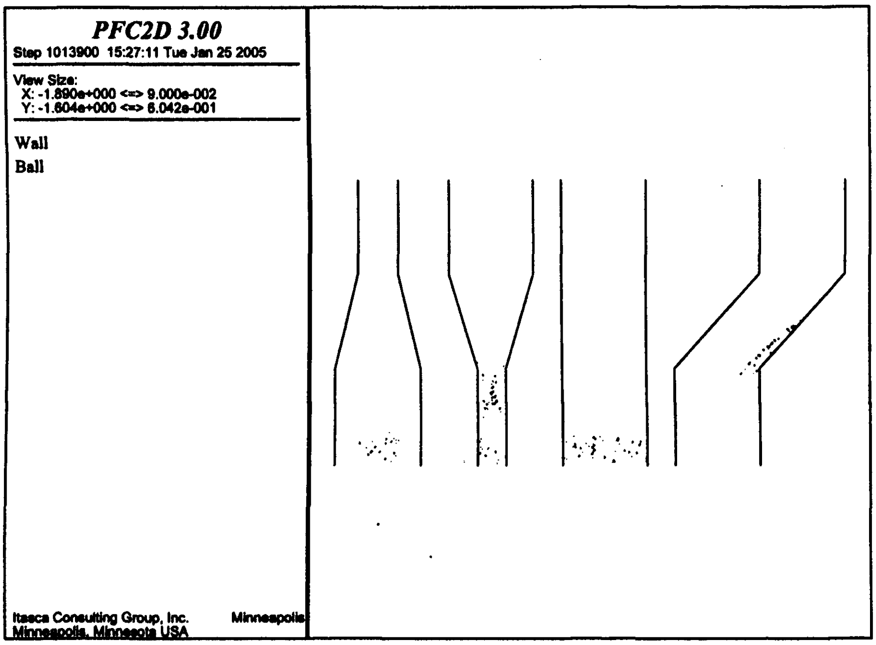

Figure 3.16: In the final computation on chute shape effects, vertical velocity fluctuations are added. The different behaviours are described in the text..

of the particles in the widening chute, in the straight chute and in the tapered chute. For the chute with the bend, the vertical velocity fluctuations seem not to significantly alter the previously observed behaviour. We refer to figure 3.16.

In the above simulations we have quite systematically introduced more complexity into the computational simulations. We at first included vertical velocity fluctuations, then added the effects of changing the chute shape, and then combined the two. We find that clustering is a key feature of all the flows, especially those that neglect vertical velocity fluctuations. A brief investigation of chute shape effects demonstrated that none of the changes in geometry appeared to give significantly more uniform distributions.

As a final experiment, we return to the straight chute and this time allow sixteen batches of interacting grains to fall down the chute. Both horizontal and vertical velocity fluctuations are included. There are now 944 particles in total. This simulation is perhaps most similar to a chute flow on a Sortex machine. Figure 3.17

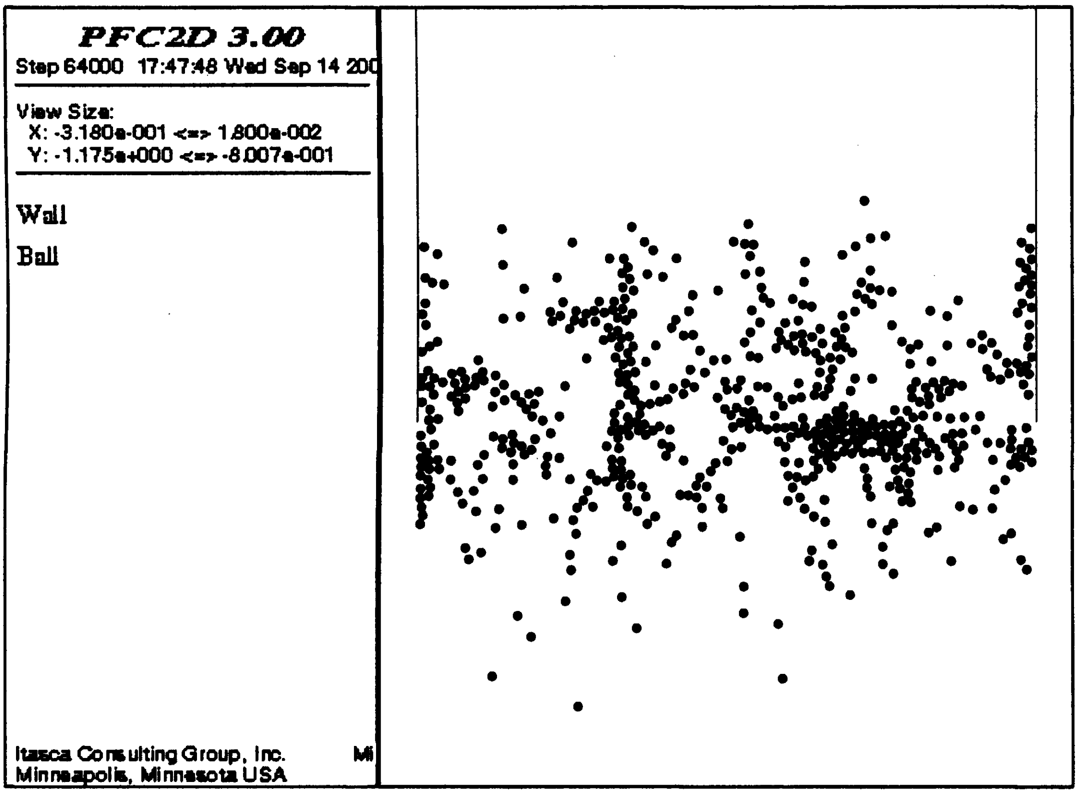

Figure 3.17: A final simulation in which 16 batches of interacting grains fall through the chute. Only the final portion of the chute is depicted and the particles are shown as they exit the chute.

shows the particles as they exit the chute. The main features to note are the possibly clustered nature of the particles (some of the apparent clusters are quite large and dense) and the fact that particles seem to form high density regions near the walls. Returning to the comments made at the end of section 3.3, it may perhaps be more useful to compare this figure, showing a distribution of *finite-sized discs*, to the experimental results in figures 3.7, 3.9 and 3.11, which show distributions of *finite-sized rice grains*.

3.5 Summary

In this chapter, computational simulations of chute flow have been studied. Initially a simple code developed by the author was used to demonstrate that clustering is a key feature of flows in the absence vertical velocity fluctuations. These results appeared to agree qualitatively with results from Sortex machines.

Next, a commercially available code PFC2D was used to include more complicated effects. This included the introduction of vertical velocity fluctuations. Clustering was still seen to be a key feature, although perhaps to a slightly lesser extent than previously.

An investigation into chute shaping effects was also undertaken. None of the adaptations to the shape appeared to significantly improve the uniformity of the particle distributions.

Chapter 4

Analytical models of chute flow

In the previous chapter we employed computational simulations of chute flows of grains in order to deepen our knowledge of the important physical processes. We observed that clustering is a key feature and that a fairly simple simulation, neglecting vertical interactions, appeared to capture the crucial aspects of the flow. We now wish to develop in this chapter accurate analytical models of the grain flow which will also demonstrate the appropriate behaviour. There are two main avenues of study when tackling particulate flow problems analytically: one is statistical mechanics, and the other continuum mechanics.

4.1 Statistical mechanics

Statistical mechanics seems (initially at least) to be a desirable method of studying granular and particle-laden flows. The idea of following every particle's motion to determine the physical properties of a system, as in computational methods (e.g. in chapter 3), is perhaps very inelegant by comparison. Rather, using probabilistic methods has historically been seen to be a very powerful method of describing many complex systems macroscopically, consider for example the kinetic theory of gases. Indeed, discussing granular flows using kinetic theory has been attempted with some success in the past [50].

It must be noted however that there are some important differences between an ideal gas and a granular flow, differences which some scientists would argue make this approach untenable [15]. First, particulate systems are highly inelastic and energy is lost at each collision. Second, the mean free path of a particle in a typical flow is of the order of particle size. Third, the rice-grain case is itself different from the traditional granular case (the latter flow is characterised by a rapidly moving monolayer without enduring contacts). Finally, in our system, the particles are continually accelerating due to gravity and hence there is a continual input of energy. Thus some assumptions of the kinetic theory of gases and statistical mechanics are readily broken in practice.

Yet the use of probabilistic methods and statistics remains very appealing and there have been suggestions that the study of lattice gas cellular automata may be a powerful way forward here [45]. In the latter *particles* are followed along a lattice as opposed to *particle distributions* in Lattice-Boltzmann methods. We do not however examine these methods in this thesis.

It is possible, nevertheless, to examine here a very simple probabilistic method of determining the final velocity distribution of the particles as they exit the chute. Suppose that two particles, particle 1 and particle 2, undergo a series of N collisions with each other. Let $\alpha = \frac{1-\hat{e}}{2}$ and $\beta = \frac{1+\hat{e}}{2}$. Using equations (3.9) and (3.10) it is possible to show that after one collision

$$\bar{u}_{1,1} + \bar{u}_{2,1} = (\alpha + \beta)\,(u_{1,0} + u_{2,0}) \tag{4.1}$$

and

$$\bar{u}_{1,1} - \bar{u}_{2,1} = (\alpha - \beta)\,(u_{1,0} - u_{2,0})\,. \tag{4.2}$$

(Recall that velocities are denoted $u_{i,n}$ where i is the particle number and n is the collision number). Therefore after N collisions:

$$\bar{u}_{1,N} + \bar{u}_{2,N} = (\alpha + \beta)^N\,(u_{1,0} + u_{2,0}) \tag{4.3}$$

and

$$\bar{u}_{1,N} - \bar{u}_{2,N} = (\alpha - \beta)^N\,(u_{1,0} - u_{2,0})\,. \tag{4.4}$$

Hence the final velocity of the first particle after N collisions is

$$u_{1,N} = \frac{(\alpha+\beta)^N}{2}\left(u_{1,0}+u_{2,0}\right) + \frac{(\alpha-\beta)^N}{2}\left(u_{1,0}-u_{2,0}\right) \tag{4.5}$$

which, in terms of $\hat{e}$, can be written as

$$u_{1,N} = \frac{\left(1-\hat{e}^N\right)}{2}u_{1,0} + \frac{\left(1+\hat{e}^N\right)}{2}u_{2,0}. \tag{4.6}$$

The above is true only if particle 1 continually collides with particle 2. However, particle 1 will in reality collide with other particles. These particles will be in a small neighbourhood of particle 1. So qualitatively we may expect their behaviour to be roughly the same, as seen from the computation. That is to say, we expect the velocity fluctuations of neighbouring particles in a small region to be of the same order. Thus we assume that all collisions that particle one undergoes can be approximated as if particle one has been continually colliding with only one other particle. In general we can write the final velocity of the i^{th} particle as

$$u_{i,N_i} = \frac{\left(1-\hat{e}^{N_i}\right)}{2}u_{i,0} + \frac{\left(1+\hat{e}^{N_i}\right)}{2}u_{i+1,0}. \tag{4.7}$$

Therefore, provided we can find an approximation for N_i, the expected number of collisions for the i^{th} particle as it falls through the chute, we can obtain an expression for the average velocity distribution as the particles exit the chute.

Now we state that

$$N_i = \int_0^{\tau} P_i\left(t\right) dt \tag{4.8}$$

where $P_i\left(t\right) dt$ is the probability that the i^{th} particle undergoes a collision within a time dt. Also τ is the length of time a particle spends on the chute. The problem is now reduced to finding a suitable expression for $P_i\left(t\right)$, which is a probability density function.

If we try, as a first approximation, $P_i\left(t\right) = \rho$, the packing density, generally poor results are seen except in areas where the particle density is sparse and each particle has undergone few collisions. See figure 4.1 for example. Moreover, the model lacks spatial symmetry: each particle acts only on the particle to its left and is acted on by the particle to its right, which does not seem to be sensible.

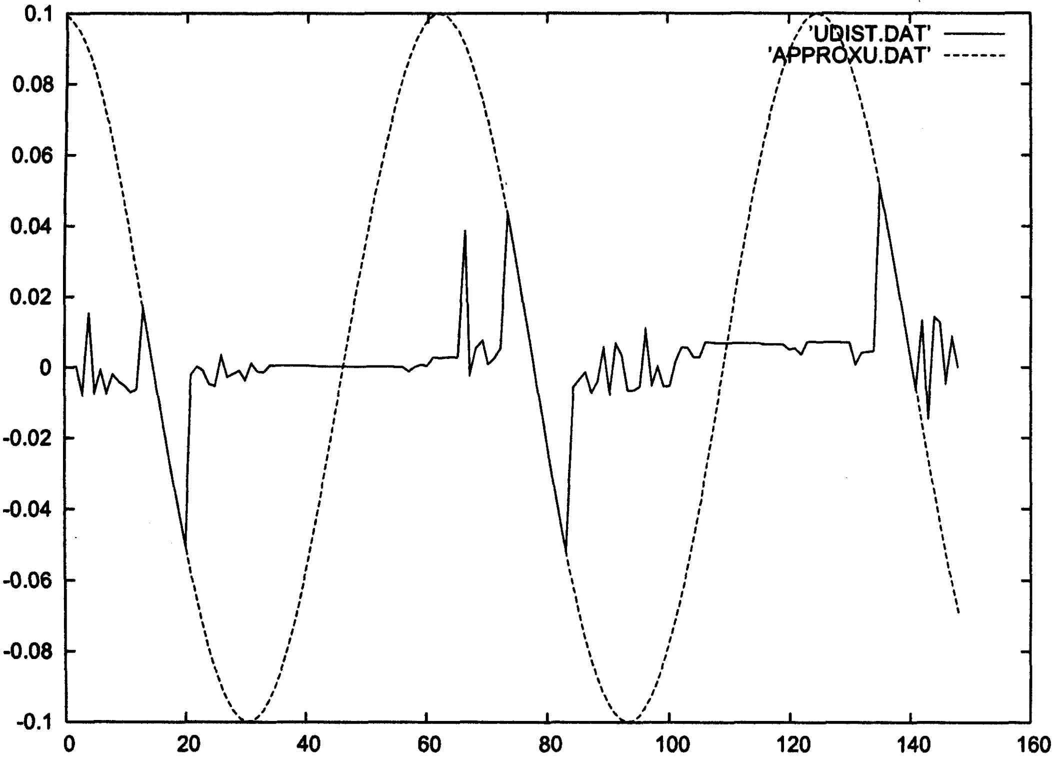

Figure 4.1: Graph showing difference between first approximation for velocity distribution at the bottom of the chute (dashed line) and the actual distribution (solid line). The initial distribution was $u_i = 0.1 * cos\,(0.1i)$. Agreement is only seen in regions where the density was seen to be sparse. (The y-axis is the velocity of the particle, the x-axis is the particle number).

Note also that the above approximation would be poor for the case of random velocities in the initial conditions. This is owing to the assumption that neighbouring particles have velocities of the same order. Clearly, in the random case, there would be no reason for this. Since Sortex suggest that random velocity fluctuations are the most sensible initial conditions the assumption is violated and this approach, it is felt, has to be abandoned.

Another statistical approach is that of mean field theory. The idea here is to fix the number of particles and their initial velocities and run the computer simulation M times for random initial positions. We can then ensemble average over the M different sets of initial conditions to extract $\langle \mathbf{v}(\mathbf{x}) \rangle$, their average velocities. This is given by

$$\langle \mathbf{v}(\mathbf{x}) \rangle = \frac{\sum \mathbf{v} \text{ within } \left(\mathbf{x} + d^2\mathbf{x}\right)}{M \text{ realisations}}. \tag{4.9}$$

We can then say that $\langle \mathbf{v}(\mathbf{x}) \rangle$ is the velocity of the mean field which can now be treated as a continuum. We must check that total momentum is conserved. Interactions of particles with the continuum must then be included to obtain a set of differential equations governing its motion.

An alternative is to fix the number of particles and their velocities and average over M configurations to find the average positions. If we do this, however, we find the average particle distribution is simply a uniform distribution of particles spread evenly across the bottom of the chute. This seems to miss all the rich behaviour of clustering found in the computation. Therefore the mean-field approach is discontinued here.

Finally, if a representative particular trajectory is examined its path is reminiscent of a random walk - it continually moves downward, but it changes its horizontal direction at seemingly random intervals. It is a possibility, therefore, that the statistics of random walks may be a useful tool for tackling the problem in the future.

4.2 Continuum mechanics

Continuum models also offer a powerful way to tackle particulate flow problems such as suspension flows [12], [23], [30], [61], traffic and pedestrian flows [21], [22], [38] and aspects of granular flows e.g. [19]. Here the particulate nature of the problem is essentially ignored, or can be overlooked, by addressing larger macro-scale behaviour and assuming that quantities such as density are continuous. It is then possible to write hydrodynamic-like equations that govern the overall particulate motion. Some of these models have been used with great success. For example, Hughes [21] used a continuum theory of pedestrian flows to suggest a method of safely placing barriers to try to prevent tragic events as pilgrims cross the bridge of Jamarat in Mecca, and Lighthill and Whitham [38] used a continuum theory of kinematic waves to describe traffic flow. Their results are very interesting and explain well experienced phenomena such as traffic jams at traffic lights and density waves in moving vehicular flow.

However, not everyone agrees that continuum models are sensible. Some may argue that it is not sensible to ignore the particulate nature of such flows as one may miss some important local or global physics of the flow in doing so. Importantly, Du, Li and Kadanoff [11] have shown that hydrodynamical descriptions of particles can break down in certain one-dimensional systems, as equipartition of energy is violated. Their colleagues, nonetheless, have been developing a useful description of granular hydrodynamics in two dimensions [18].

In this thesis we choose to use a continuum method to describe the chute flow analytically. In fact, we try to develop the Lighthill-Whitham theory of traffic flow to produce a description of a chute flow. This is undertaken in the next chapter and is expanded further in chapters 6 and 7.

Chapter 5

The 'inviscid' continuum model

In this chapter, we propose a continuum model for a chute flow of grains. An argument is presented for extending the Lighthill-Whitham model of traffic flow to cover the chute flow. Strengths and weaknesses of the argument are described. In particular, the continuum model we propose requires the introduction of a fundamental relation between the flux q and the density ρ, and the physical mechanism underlying the particular fundamental diagram requires discussion and appraisal. We follow through the implications of the present flux-density relation in detail. We cannot deny that the model omits many factors, and as such is incomplete, as would be any first model.

The continuum model which we develop below and in subsequent chapters is based around ideas generated from Lighthill and Whitham's study of traffic flow [38] using the theory of kinematic waves explained by Whitham [57], [58]. It is assumed that **the density of rice grains ρ forms a continuum.** Obviously this is not the case in reality as only discrete grains of rice exist, but the continuum view may provide a useful macroscopic description of the rice flow. In particular, this assumption may be justified in certain circumstances, outlined below.

As a consequence of the physics of the chute flow (for example, random jostling, random collisions and clustering) and with support from the computational results presented in chapter 3, it is argued that a state can evolve where grains form into large coalesced masses. Each mass moves as if it is one body with a particular velocity distribution and each has a large number of particles in it. The density of each mass may be different in each case. As there are large numbers of particles, the density of each mass could take any value. When the chute flow is in this state there are sudden jumps in density between each cluster and there can also be voids, as supported by the results in chapter 3. These aspects can be explained by the shocks or expansion fan structures found in the continuum model. The analysis here starts at some point down the chute where the clustered (shock-fan) structure has evolved, or rather is about to evolve, and the continuum model is justified. Furthermore, here a smooth piecewise continuous density distribution at the start will break within a finite time (or distance down the chute) into a shock-wave or fan, as in Whitham [57], [58]. Hence the model mimics the change of a smooth initial density distribution into a non-smooth one. Finally, we shall see that discontinuous cases can be the simplest cases for analysis and hence form a suitable starting point.

It is further assumed that grains **move essentially along horizontal lines (the x direction) with a flow rate** q which descend the chute under gravity. In reality, vertical interactions could be an important mechanism in the flow, but calculations with the 1D horizontal-line assumption achieve physically reasonable results according to chapter 3, in particular section 3.3. The one-dimensional model is found to contain rich and complex behaviour which may serve to guide or encourage the use of a 2D model later. We shall present below, in passing, the 2D equations and shall observe that the 1D solution would emerge anyway as the grains fall down the chute.

By conservation of mass the continuity equation is:

$$\rho_t + q_x = 0 \tag{5.1}$$

where a subscript t denotes $\frac{\partial}{\partial t}$ and a subscript x denotes $\frac{\partial}{\partial x}$. If q is taken to be dependent only on ρ, (5.1) becomes

$$\rho_t + q_\rho \rho_x = 0. \tag{5.2}$$

We make this assumption to keep the wave problem simple as a first approximation; this may also be justified on physical grounds (see below) and the strength of the assumption is addressed in section 5.2. Also, if

$$q_\rho \equiv \frac{dx}{dt} \tag{5.3}$$

then (5.2) states that the total derivative

$$\frac{d\rho}{dt} = 0. \tag{5.4}$$

Now let us call $q_\rho \equiv c(\rho)$, the wavespeed. Hence the density is constant along straight lines (the 'characteristics') given by

$$x = c(\rho)\, t + x_0 \tag{5.5}$$

where x_0 is a constant of integration representing an initial position for x. The resultant equation for the flow is

$$\rho_t + c(\rho)\, \rho_x = 0. \tag{5.6}$$

Therefore, an initial density distribution $\rho = f(x)$ at $t = 0$ determines in principle how the density evolution with time via the characteristics. To determine $c(\rho)$ we claim that q is related to the density ρ by $q = Q(\rho)$ say and then $c(\rho) = Q'(\rho)$ where the prime denotes differentiation with respect to the argument. (We shall shortly discuss the validity of choosing a particular $q = Q(\rho)$ relation). We must also initially specify q along each characteristic. The values (ρ, q) in the initial condition thus determine a unique value of c which in turn determines the gradient of the characteristic. The flux and the density are then constant along the characteristic, that is to say, both q and ρ are propagated along the characteristics. The initial conditions in the current chapter are piecewise-constant as these provide a fairly basic starting point for the analysis.

As an aside, we remark that one improvement would be to make the model two-dimensional. Briefly, the 2D equation would be

$$\rho_t + c_1(\rho)\rho_x + c_2(\rho)\rho_y = 0. \tag{5.7}$$

Examining the orders of magnitude in the equation as $y \to \infty$ and seeking a solution independent of y reveals equation (5.6), i.e. the 1D model.

We propose below a particular $Q(\rho)$ relation for the chute flow. Immediately following this, the validity of the proposition is discussed with regard to its strengths and weaknesses. Note that, borrowing from traffic flow theories, the $Q(\rho)$ curve is known as the fundamental diagram or fundamental curve.

If $\rho = 0$ there can be no flow, so then $q = 0$ trivially. Further, it is argued that there is no flow for a maximum value ρ_M of the density, corresponding to a 'jamming' of grains across the chute where each grain is touching the neighbouring grain or wall and hence, within some interval of x at least, there is no room for any grain to move relatively across the chute. In between q takes a single maximum at some value of the density ρ_F. However, the rice can travel in both directions (unlike the traffic flow case) and hence q can also take negative values (of the same magnitude by virtue of symmetry) for each value of ρ. That is to say, there are two branches of the fundamental diagram, one which describes leftward moving grains, and the other rightward moving grains, and so the flux-density relation is necessarily double-valued. Finally, the $Q(\rho)$ curve on each branch is expected to pass through inflexion points relatively near the cusps, which lie at the zero-q end of the branches, as explained in the following paragraph. See also figure 5.1. Where the positive branch and the negative branch approach the maximum and minimum values of ρ, the curves meet at a cusp, as we shall soon see.

The reasoning for the cusps and hence inflexion points is so that the wavespeed remains finite and smooth as the solution passes through the endpoints and switches branches. To see this consider putting $\rho = f(\mu)$ where $\mu = \frac{x}{t}$ is a similarity variable. The governing equation becomes

$$(c - \mu)f' = 0 \tag{5.8}$$

so $\mu = c$ is allowed (as too, then, are expansion fans). Next, at the high density endpoint (the reasoning applies equally to the zero density endpoint) consider having locally

$$q = \pm\beta(\rho_m - \rho)^n \tag{5.9}$$

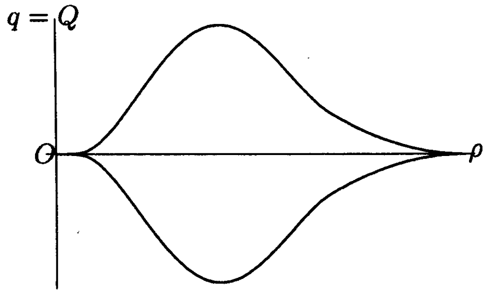

Figure 5.1: Sketch of the fundamental diagram, including the cusps at $q = 0$ and inflexion points relatively nearby.

with the unknown power $n > 0$ and the constant β being non-zero. Then

$$c = \mp\beta n(\rho_m - \rho)^{n-1}, \tag{5.10}$$

so

$$\mu = \mp\beta n(\rho_m - \rho)^{n-1}. \tag{5.11}$$

Rearranging yields

$$\rho = \rho_m - \left(\frac{|\mu|}{\beta n}\right)^{\frac{1}{n-1}}. \tag{5.12}$$

Consequently if $\frac{1}{n-1} = M$ with M an even integer then the wave-speed smoothly varies as the density passes through a maximum. In particular, if $n = \frac{3}{2}$ we see that $M = 2$ and the density $\rho = \rho_m - \left(\frac{|\mu|}{\beta n}\right)^2$, which would be expected to be the most general case. Similar reasoning for a cusp also applies at the low density end. The fundamental curve's upper branch is therefore concave upwards at its endpoints. Accordingly, for there to be a maximum q in between, inflexion points must be produced between the maximum and the end points. Including an inflexion point also allows mass-conserving shock-fan structures, as we shall see later, which allow physically acceptable descriptions of clashing and separating regions to develop. We should refer also in passing to the discussion of viscous effects on branch switching in chapter 7.

Concerning strengths and weaknesses, and in particular the present proposed fundamental diagram, in pedestrian and traffic flows there are obvious physical reasons why people or cars slow down with increased density (over-crowding, driver nervousness and so on) whereas it is difficult to argue totally why, for example, a densely packed region of grains may move more slowly than a sparser region as in the cases here. This difficulty could be countered, perhaps tentatively, that when the density is low the grains may have small horizontal velocities because collisions are unlikely and so there is slim chance of any horizontal velocities being induced. At large densities, however, collisions are likely to be more numerous and thus grain speeds would reduce. In the extreme case of a blockage the grains would come to a complete stop and may become packed at the jammed density. Thus a situation arises in which the density influences the flux, or vice-versa, and the view that $q = Q(\rho)$ appears to be justified (at least as a first approximation). Further, owing to these simple arguments a shape of such a fundamental curve, similar to the one proposed above, seems to be suggested. Alternatively, we could argue that such a choice of fundamental diagram is appropriate for certain physical situations, such as with colliding or separating grains on a chute. It may be of significance here that at a collision the grains can be considered to instantaneously change velocity at the point of touching, and so the flux of the grains is zero when the density is maximal, exactly as in the present proposed fundamental diagram. Other situations, such as with a highly dense region moving on an otherwise empty chute should be covered by another fundamental diagram, but such a situation may be unlikely to develop in practice because high densities seem more likely to arise when grain speeds are slow. It is also worth mentioning that as clusters and voids were the key feature of the computational results in chapter 3, and as collisions and separations are believed to be the crucial mechanism behind the formation of clusters and voids, then this aspect of the flow may be the most pertinent part to consider in an initial model. Some of the above criticisms may also apply to the theory when it is applied to traffic flow (for example a densely packed region of cars on an otherwise empty highway will not in reality have $q = 0$, they may accelerate away and diffuse). Given the above setting we continue with the present 1D formulation, perhaps especially relevant to colliding and separating grains (rather than being appropriate for an entire chute flow), and examine the outcome.

Interesting aspects arise in the model because $Q(\rho)$ is smoothly varying on each branch and so the characteristics generally intersect or diverge within a finite time if ρ and q vary on each characteristic. Intersections are a significant feature since at intersections the density would be implied as multivalued. Such an apparent contradiction is resolved by the formation of a 'shock' (see Whitham [57]). On one side of the shock the density takes one value, ρ_1 say, and on the other side a different value ρ_2 yielding macroscopically a sudden jump across the shock. The shock wave travels with velocity

$$U = \frac{q_2 - q_1}{\rho_2 - \rho_1} \tag{5.13}$$

which is the gradient of the chord between (ρ_1, q_1) and (ρ_2, q_2) on the fundamental curve.

Diverging characteristics create an area devoid of information about the density potentially but lead to an 'expansion fan'. The aim in what follows is to employ the shock wave and expansion fan structures as mechanisms to obtain inhomogeneous density distributions upon the chute and provide some further explanation of clusters and voids when grains are colliding or separating.

5.1 Analytical solutions of the continuum model

In this section a number of simple analytical solutions to the continuum equation are illustrated. In this way, we see that it is possible to build increasingly complex solutions to the continuum model which have desired features such as clusters and voids. These have been seen to be potentially crucial from the preceding computations in chapter 3. In theory it is possible to determine any solution analytically by examining the characteristics, together with the shocks and fans.

5.1.1 Shock waves

Let us consider an example in which there are two adjacent regions of constant density, one with density ρ_1 and the other with density ρ_2. The corresponding values of the flux are q_1 and q_2 respectively. If we allow $\rho_1 < \rho_2 < \rho_F$ then $0 < q_1 < q_2 < q_F$.

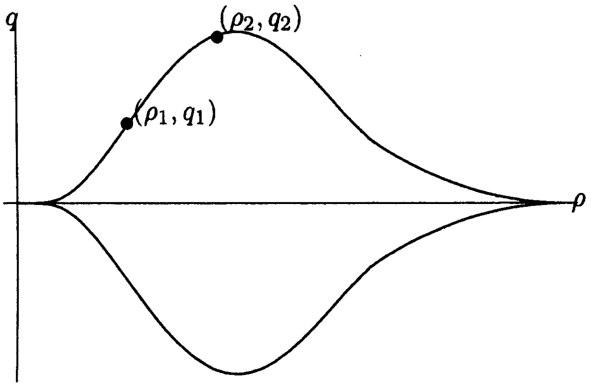

Figure 5.2: This figure highlights the values of ρ_1, q_1, ρ_2, q_2 for the example of the shock wave outlined in subsection 5.1.1. The respective slopes are c_1 and c_2.

Recall that ρ_F and q_F are the respective values of the density and the flux at the extrema of the fundamental curve (here extrema is used in the calculus sense of the word). It is possible to choose this arrangement such that $c_1 > c_2$: see figure 5.2 for clarity. (Recall that $c = \frac{dq}{d\rho}$ and that c is the gradient of each characteristic. Hence the gradient of each characteristic is equal to that of to the tangent to the fundamental curve at the corresponding value of (ρ, q)). Furthermore, if the region of density ρ_1 is allowed to lie 'underneath' the region of density ρ_2, as depicted in figure 5.3, then the characteristics are seen to intersect in the $x - t$ plane. As has already been stated, the density will be multivalued at such an intersection since the density is a different constant along each intersecting characteristic. This is physically unacceptable. The solution is to replace the intersecting points with a shock, i.e. a sudden jump in the density. In this way, we see that the correct $x - t$ diagram for this case is as in figure 5.4, in which two regions of constant density are separated by a shock. The corresponding evolution of the density profile is as in figure 5.5. Both regions are moving rightward (as $q > 0$) and there is a translating shock between the two regions.

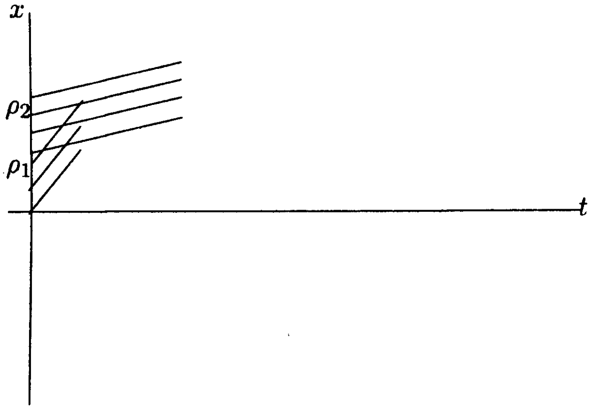

Figure 5.3: The characteristics in the first example described in subsection 5.1.1 appear to intersect in the $x - t$ plane. This is physically unacceptable.

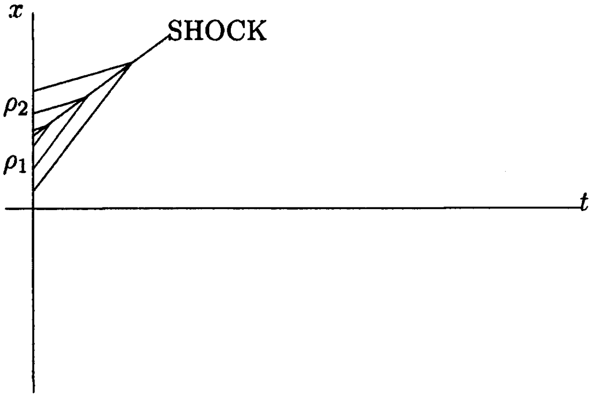

Figure 5.4: The solution (continuing from figure 5.3) is to replace the intersecting points by a shock wave; a sudden jump in the value of the density.

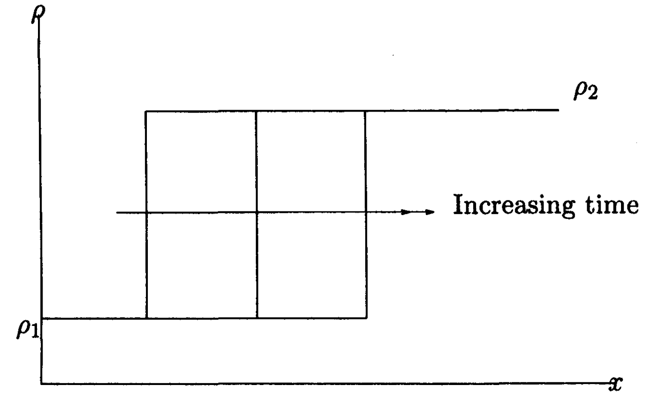

Figure 5.5: The corresponding density profile is shown above as it evolves over time. The two regions translate rightwards, separated by a shock.

5.1.2 Expansion fans

Again let us consider an example in which there are two adjacent regions of constant density, one with density ρ_1 and the other with density ρ_2, where the corresponding values of the flux are q_1 and q_2 respectively. However, now we suppose that $q_1 > 0$, $q_2 < 0$ and $\rho_1 < \rho_2 < \rho_{IL}$. Here ρ_{IL} and q_{IL} respectively are the values of the density and flux at the inflexion point on the left. Similarly, ρ_{IR} and q_{IR} are the values of the density and flux at the inflexion point on the right. Thus $c_1 > 0$, $c_2 < 0$ and $|c_1| > |c_2|$, see figure 5.6. (If $\rho_{IL} < \rho_1 < \rho_2 < \rho_F$ then the solution is a little more complex as we shall see in a later example in subsection 5.1.3). The region with density ρ_1 is allowed to lie above the region with density ρ_2, as in figure 5.7. Observe that such an arrangement corresponds to the two regions moving apart since $q > 0$ in the upper region and $q < 0$ in the lower region. In the $x - t$ diagram, there is seen to be a region devoid of characteristics. Consequently, there appears to be no information about the density evolution here, yet we know that the regions are separating. The problem can be resolved by the introduction of an expansion fan.

An expansion fan is a region of characteristics which all start from the same point, but their gradient continuously changes from the value of the gradient of the characteristic in the upper region to the gradient of the characteristic in the lower

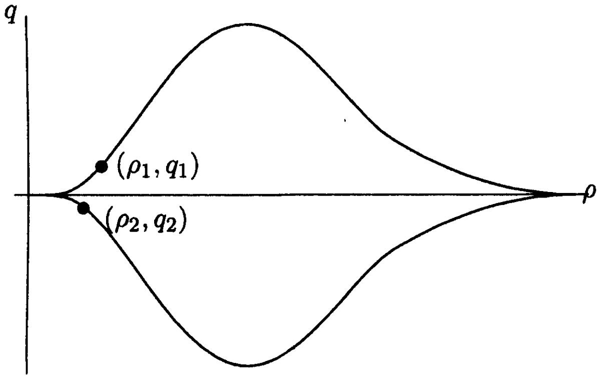

Figure 5.6: This figure highlights the values of ρ_1, q_1, ρ_2, q_2 for the example of the 'fan' outlined in subsection 5.1.2.

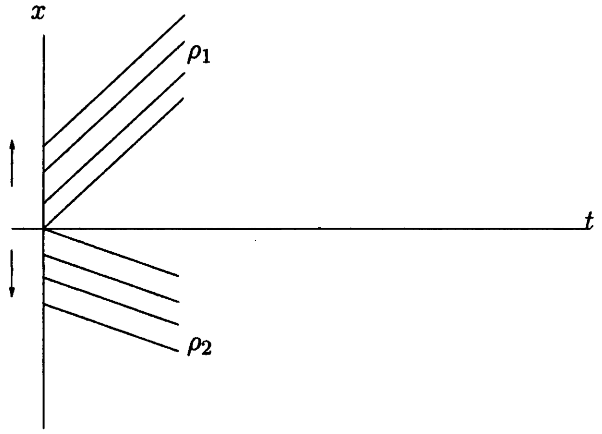

Figure 5.7: A plot of the $x - t$ plane reveals a region devoid of any characteristics, and hence any information about the density. Yet we know that the regions are separating.

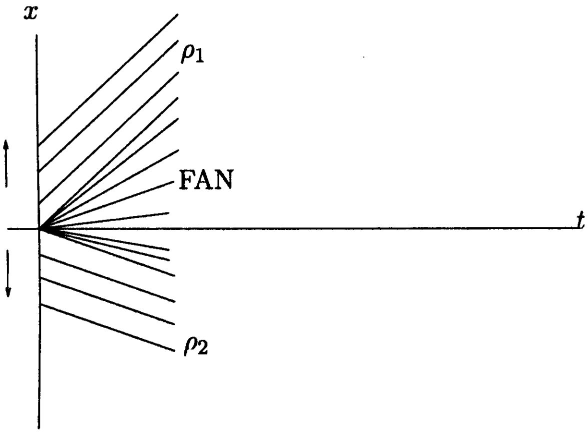

Figure 5.8: Continuing from figure 5.8, it is seen that the problem can be resolved by the introduction of an expansion fan.

region. Hence the void region is now replaced by a 'fan' of characteristics whose gradients decrease monotonically. As the gradient varies through this fan, so must the density. See figure 5.8. The continual change in the gradient corresponds to moving from the point (ρ_1, q_1) on the upper branch of the $q(\rho)$ curve to the point (ρ_2, q_2) via the cusp at $(0, 0)$. Notice that the characteristic at the centre of the fan has zero slope and thus the point of zero density is stationary.

Therefore the fan in this case corresponds to a gradual decrease in the density and a reduction in flux to a stationary central point with zero density, this is followed by a gradual increase in the density accompanied by an increase in magnitude of the flux, which is now negative.

The expansion fan has allowed the density to *switch* branches. The physical interpretation of this is indeed a separation of the two regions. Figure 5.9 illustrates the evolution of the corresponding density profile to highlight the physics.

Expansion fans can similarly be used to describe parts of clashing regions. Consider two regions of constant density with $\rho_2 > \rho_1 > \rho_{IR}$ and $q_1 > 0$ and $q_2 < 0$. Now $c_1 < 0$ and $c_2 > 0$ since ρ_1 and ρ_2 lie toward the large density end of the fundamental diagram, as in figure 5.10. Allowing the ρ_1 region to lie underneath the ρ_2 region will result in an $x - t$ plot of the characteristics that is qualitatively

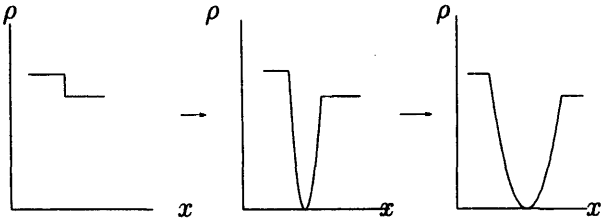

Figure 5.9: The corresponding evolution of the density profile shows that the expansion fan has captured the physical process of separation.

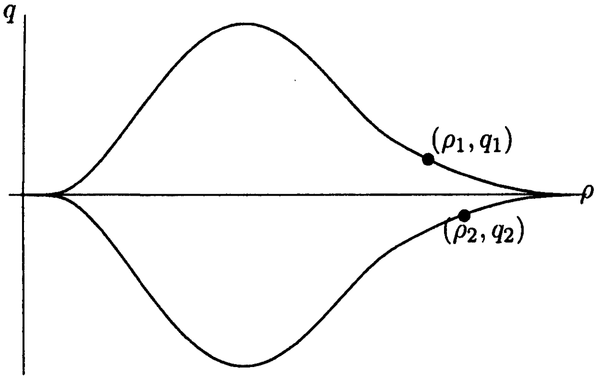

Figure 5.10: This figure highlights the values of ρ_1, q_1, ρ_2, q_2 for the example of a fan in a colliding region.

similar to that in the example above. Such an arrangement corresponds to clashing of grains. Again there will be a region devoid of characteristics where an expansion fan can be introduced.

However, in this example, monotonically decreasing the gradient of the characteristics in the fan corresponds to moving along the fundamental diagram from (ρ_2, q_2) to (ρ_1, q_1) via the cusp located at $(\rho_M, 0)$. Observe that the characteristic at the centre of the fan has zero slope and thus the point of maximal density is stationary.

Thus, moving through the fan from ρ_2 to ρ_1 allows the density to switch branches from the lower branch to the upper branch while passing through a point of maximum density. Hence the fan describes a region where the density smoothly increases to the maximum and then smoothly decreases out again to a region of constant density. That is to say, the fan describes a 'hump' of large density at the location where

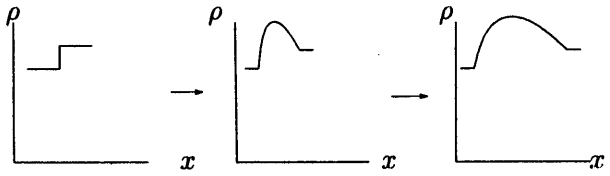

Figure 5.11: The corresponding evolution of the density profile makes the point that the expansion fan has captured the physical process of collision.

we know that grains are colliding. Figure 5.11 shows the evolution of the density profile to highlight this point.

The expansion fan structures can be described analytically [57]. The characteristics satisfy equation (5.5) which is

$$x = c\,(\rho)\,t + x_0. \tag{5.14}$$

Each characteristic in the fan crosses the x-axis at the same point, hence x_0 is the same constant for each one. Therefore we can rearrange (5.5) to find the gradient of each characteristic in the fan as

$$c(\rho) = \frac{x - x_0}{t}. \tag{5.15}$$

Therefore the complete solution for the wave speed is

$$c = \begin{cases} c_1, & c_1 < \frac{x-x_0}{t}, \\ \frac{x-x_0}{t}, & c_2 < \frac{x-x_0}{t} < c_1, \\ c2, & \frac{x-x_0}{t} < c_2. \end{cases} \tag{5.16}$$

5.1.3 Shock-Fan-Shock structures

In both of the above examples we have seen that the expansion fan structures appear to describe well the physics of separating and colliding grains and that a shock can describe a sudden jump in the density. Hence the shock and fan structures seem to be able to allow the sort of behaviour in the continuum model that has been observed in other methods, such as the computations in chapter 3.

We now examine some more complex examples that include a mixture of shocks and fans.

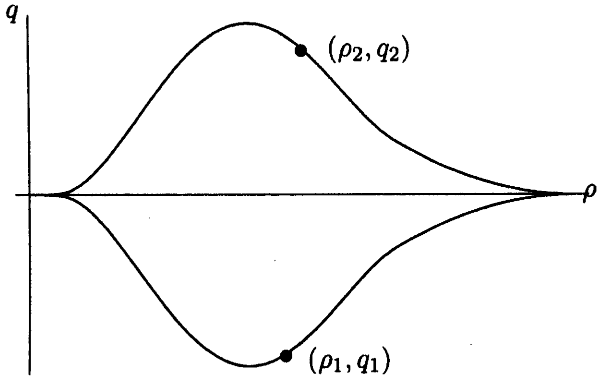

Figure 5.12: This figure highlights the values of ρ_1, q_1, ρ_2, q_2 for an example including a mix of shocks and fan in a colliding region.

Consider two regions of constant density, the upper region with $\rho_F < \rho_1 < \rho_{IR}$ and $q_1 < 0$ and the lower region with $\rho_F < \rho_2 < \rho_{IR}$ and $q_2 > 0$. Thus $c_1 > 0$ and $c_2 < 0$. See figure 5.12 .

If the characteristics are plotted in the $x - t$ plane there will again be a region devoid of characteristics which we intuitively expect to describe a clashing region.

One simply might expect the resolution of this problem to be again an expansion fan between (ρ_1, q_1) and (ρ_2, q_2), but the solution this time is a little more involved, as follows. Since ρ_1 and ρ_2 are to the left of the inflexion point ρ_{IR} they are located on points of the fundamental curve that are concave. Consequently, the characteristics in an expansion fan would not monotonically decrease from c_1 to c_2. Hence an expansion fan cannot be immediately plotted.

Instead, consideration indicates that there must be a shock from ρ_1 to ρ_{T-} and a shock from ρ_2 to ρ_{T+}, where ρ_{T-} is the point where a chord drawn from (ρ_1, q_1) is tangent to the fundamental curve. Similarly, ρ_{T+} is the point where a chord drawn from (ρ_2, q_2) is tangent to the fundamental curve. Both ρ_{T-}, $\rho_{T+} > \rho_{IR}$, clearly. See figure 5.13 . An expansion fan can now be drawn between ρ_{T-} and ρ_{T+}. Observe that such a shock-fan-shock structure will still conserve mass and satisfy the appropriate entropy conditions: see section 5.3.

The plot of the characteristics in the $x - t$ diagram for this situation is shown in

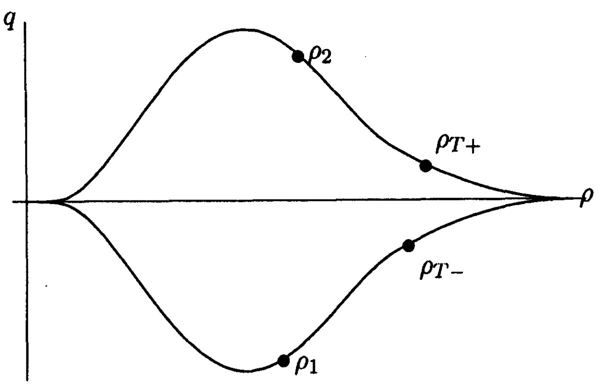

Figure 5.13: This figure displays the values of ρ_1, q_1, ρ_2, q_2, ρ_{T-}, ρ_{T+} for an example including a mix of shocks and fan(s) in a colliding region.

figure 5.14 and figure 5.15 depicts the time evolution of the density profile. There is a region of constant density moving leftward, then a shock to a fan where there is a high density region, then there is a shock down to a region of constant density moving rightward. It is possible to see how these structures could build a picture of the grains on the chute similar to those seen in the Sortex images in figure 3.6, for example.

'Shock-Fan-Shock' structures, as we shall call them, can arise in other situations. Consider ρ_1, ρ_2 given in the above example, but now with ρ_2 lying in the upper region and ρ_1 lying in the lower region. At first sight, it seems that the characteristics are intersecting and so the solution ought to be a shock. However, if a line were drawn through the intersecting points, the gradient would not be equal to the gradient of the chord between (ρ_1, q_1) and (ρ_2, q_2); the chord would not have the required speed U (and hence such a shock would not conserve mass - see section 5.3).

Examining the above arrangement more carefully, we see that the two regions are separating. Therefore the solution is required to switch branches via the cusp at the origin. The problem is avoided by the introduction of two shocks to the points ρ_{T2-} and ρ_{T2+}. The point ρ_{T2-} is the place on the fundamental curve where the gradient c_{T2-} is tangent to a chord drawn from ρ_1 such that $\rho_{T2-} < \rho_{IL}$. Similarly, the point ρ_{T2+} is the place on the fundamental curve where the gradient c_{T2+} is

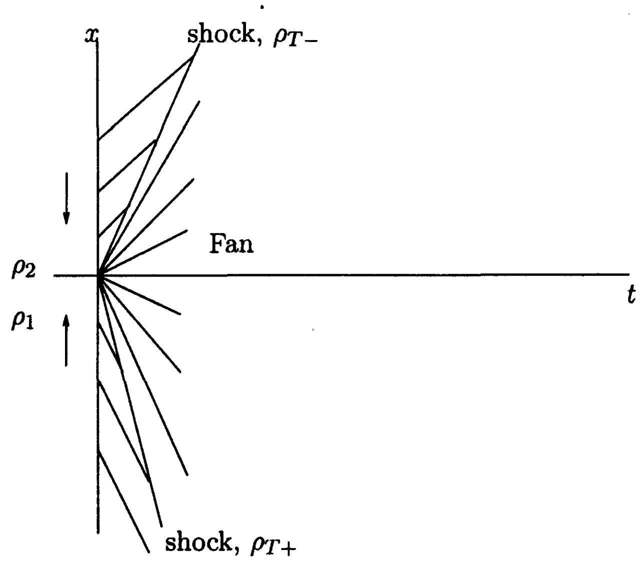

Figure 5.14: The figure shows the characteristics for the shock-fan-shock structure described in the text.

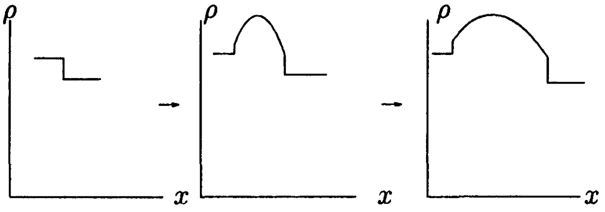

Figure 5.15: The corresponding evolution of the density profile is shown for figure 5.14.

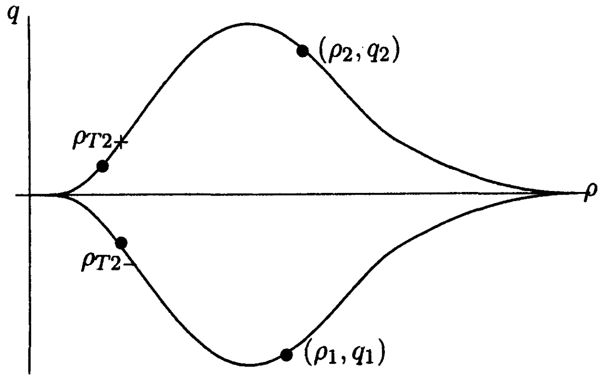

Figure 5.16: This figure highlights the values of ρ_1, q_1, ρ_2, q_2, ρ_{T2-}, ρ_{T2+} for an example including a mix of shocks and fan in a separating region.

tangent to a chord drawn from ρ_1 such that $\rho_{T2+} < \rho_{IL}$. See figure 5.16 for details. An expansion fan can now be drawn between ρ_{T2-} and ρ_{T2+} that switches branches through the cusp at zero density. Figure 5.17 shows the characteristics.

The time evolution of the density profile for this example is sketched in figure 5.18. There is a region of constant density moving leftward adjacent to a leftward-translating shock down to small densities. Then there is a fan through zero density that is next to a rightward-moving shock that jumps to large densities. We reiterate that it is possible to see how these structures could build a picture of the grains on the chute similar to those seen in the Sortex images such as figure 3.6.

5.1.4 Merging shocks

In this example there are three density regions moving downwards and separating. One possible set of initial conditions for this to occur is shown in figure 5.19. This seemingly results in the characteristics overlapping from each region so two separate shock waves must pass through the points of overlap between these regions (as seen in figure 5.20). A consequence of this is that the two shock waves merge and the region of density ρ_2 ceases to exist. Ultimately only two regions of discrete density exist, one with density ρ_1 and the other with density ρ_2, and there is a sudden jump in density between the two parting regions.

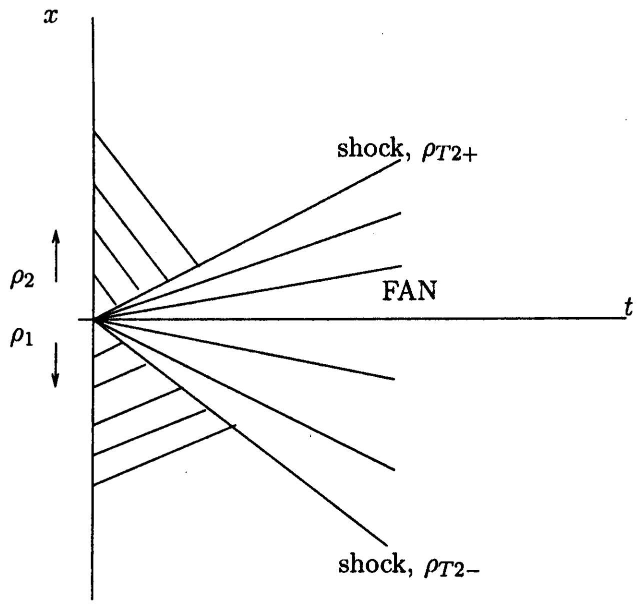

Figure 5.17: The figure shows the characteristics for the shock-fan-shock structure in the case of separating grains described in the text.

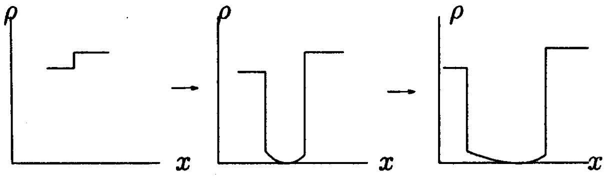

Figure 5.18: A sketch of the time evolution of the density profile for the example of a shock-fan-shock structure when grains are separating.

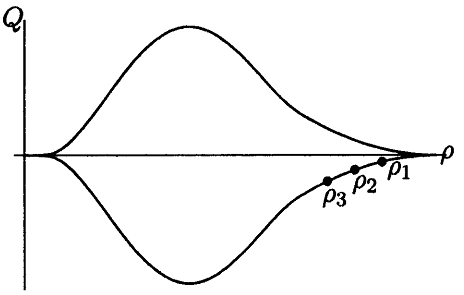

Figure 5.19: Plot showing positions of (q, ρ) co-ordinates for example 5.1.4.

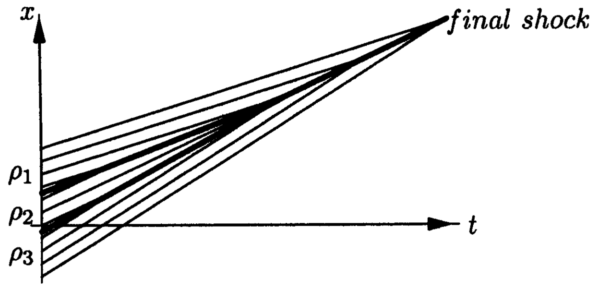

Figure 5.20: Sketch of the characteristics for example 5.1.4: all regions are moving downwards and separating from each other. Initially shock waves (indicated by heavy lines) exist between each region, but as time increases the ρ_2 region is reduced in size. Eventually this region is 'swallowed up' entirely, the shocks merge and we are left with two discrete density regions that are moving apart.

5.1.5 Another example with three discontinuous regions

It is useful to consider another example with three discontinuous density regions to show the complexity of possible solutions. Let us consider three regions of differing density with ρ_1, ρ_2 and ρ_3 as given in figure 5.21. These are chosen such that $\rho_{IL} < \rho_1 < \rho_F$ with corresponding $q_1 > 0$; $\rho_2 > \rho_{IR}$ with corresponding $q_2 > 0$; and $\rho_3 > \rho_{IR}$ with corresponding $q_3 < 0$. We also draw attention to the point ρ_{T+} which is the point where a chord drawn from (ρ_1, q_1) is tangent to the fundamental curve on the upper branch. Observe that $\rho_{IL} < \rho_{T+} < \rho_{IR}$ and the chord is the shock s_1.

These three regions are allowed to lie in the $x - t$ plane such that the region of density ρ_3 lies above the region of density ρ_2, which in turn lies above the region of density ρ_1. Thus we observe that there is an area of colliding grains between ρ_3 and ρ_2 and consequently an expansion fan is required here. A fan is also required at the bottom of the ρ_2 region to a density with value ρ_{T+}. This is required to satisfy the entropy condition, see section 5.3. The characteristic with density ρ_{T+} coincides with the shock s_1 where there is a jump down to density ρ_1. Consequently the $x - t$ plane is as shown in figure 5.22 and a schematic representing the evolution of the density profile is shown in figure 5.23.

We mention here that there is some further analysis in appendix D concerning

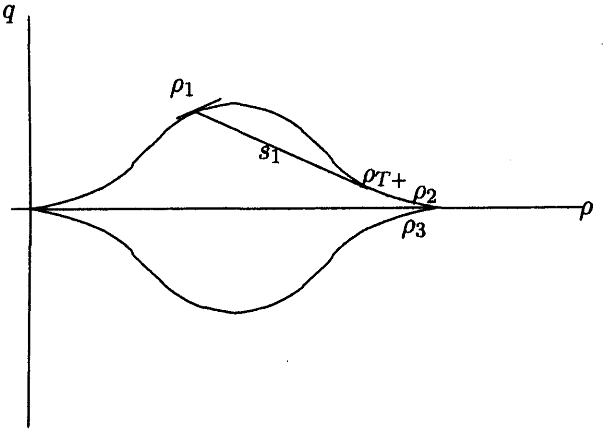

Figure 5.21: The important values of ρ_1, ρ_2, etc. are shown on the fundamental diagram for example 5.1.5.

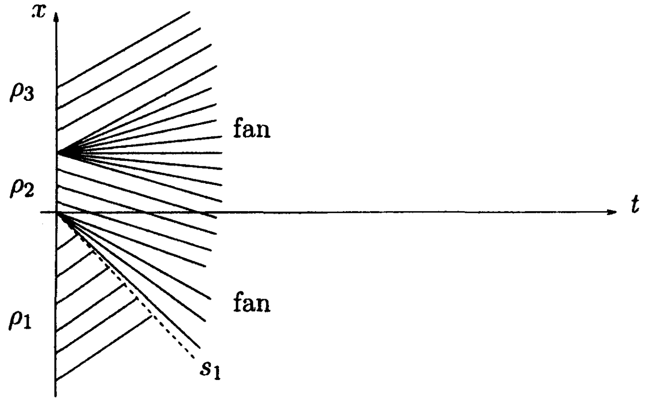

Figure 5.22: This figure shows the construction of the $x - t$ diagram for example 5.1.5. The region of ρ_1 lies at the bottom. There is a shock, s_1, and a fan between the ρ_1 and ρ_2 regions. A now familiar expansion fan structure occurs in the colliding region between ρ_2 and ρ_3.

Figure 5.23: This figure shows a sketch of the the evolution of the density profile corresponding to figure 5.22. Density is on the vertical axis, position across the chute is along the horizontal axis. A shock exists between ρ_1, on the left of the chute, and the small fan to the region of density ρ_2. A 'hump' of high density exists in the colliding region between ρ_2 and ρ_3. As time increases the two fans spread out. The shock on the left persists for all time.

how to determine the characteristics at the chute walls.

5.2 Appraisal

If the fundamental diagram proposed at the beginning of this chapter is taken to give the flux-density law for a chute flow of grains the above sections show that the inherent discontinuities in the model (the shocks and fans and combinations of the two) can perhaps describe the formation of clusters, voids and sudden jumps in the density during collisions and separations. Hence we can construct descriptions of significant parts of a chute flow including regions of colliding or separating grains. However, we do not claim that the fundamental diagram must describe the *entire* chute flow. The approach has also been an empirical one: we have seen that the results can describe some situations seen on chutes in reality, although the original physical arguments *per se* remain open to question.

5.3 Remarks on mass conservation and entropy

The shock wave must travel with velocity (5.13) as a consequence of mass conservation. The supporting argument from LeVeque, which properly determines the shock speed from the properties 'within' the shock, rather than from approaching the shock externally, as in Whitham's analysis [57], [34] is as follows. The integral form of the conservation law is used to determine the shock speed at any time in terms of the states $\rho_1(t)$ and $\rho_2(t)$ immediately to the left and right of the shock, respectively. Suppose that the shock speed is a constant U over a very short time interval from t_1 to $t_1 + \Delta t$; the integral form of the conservation law (5.1) states that

$$\int_{x_1}^{x_1+\Delta x} \rho\left(x, t_1 + \Delta t\right) dx - \int_{x_1}^{x_1+\Delta x} \rho\left(x, t_1\right) dx = \int_{t_1}^{t_1+\Delta t} q\left(\rho\left(x_1, t\right)\right) dt - \int_{t_1}^{t_1+\Delta t} q\left(\rho\left(x_1 + \Delta x, t\right)\right) dt. \tag{5.17}$$

Since ρ and q are essentially constant along each edge $x_1 + \Delta x$ and $t_1 + \Delta t$ this becomes

$$\Delta x \rho_2 - \Delta x \rho_1 = \Delta t q\left(\rho_1\right) - \Delta t q\left(\rho_2\right) + O\left(\Delta t^2\right). \tag{5.18}$$

If the shock speed is U then $\Delta x = -U\Delta t$ (if $U < 0$); therefore

$$-U\Delta t \rho_2 + U\Delta t \rho_1 = \Delta t q\left(\rho_1\right) - \Delta t q\left(\rho_2\right) \tag{5.19}$$

and hence

$$U = \frac{q\left(\rho_2\right) - q\left(\rho_1\right)}{\rho_2 - \rho_1}, \tag{5.20}$$

which is identical to equation (5.13). Therefore all the solutions outlined above do indeed conserve mass.

The presence of shocks can also be determined by Oleinik's entropy condition. See again LeVeque [34] and Morgan, Baines and Sweby [42]. The condition is as follows. If R is defined to be

$$R \equiv \frac{q(\rho_+) - q(\rho)}{\rho_+ - \rho}, \tag{5.21}$$

where ρ_+ is the value of the density on the right-hand side of the discontinuity, and if L is defined to be

$$L \equiv \frac{q(\rho_-) - q(\rho)}{\rho_- - \rho}, \tag{5.22}$$

where ρ_- is the value of the density on the left-hand side of the discontinuity, then if

$$R \leq U \leq L \tag{5.23}$$

is satisfied for all $\rho \in [\rho_-, \rho_+]$ then the entropy condition is satisfied and the discontinuity is a shock.

It can be verified that Oleinik's entropy condition is in fact satisfied for all the shocks in the previous examples, including those in the shock-fan-shock structures developed above also satisfy the entropy condition [42].

Chapter 6

The 'viscous' continuum model for grains in one-way flow

6.1 Introduction

The preceding chapter showed that if mass is conserved on the chute then equation (5.6) must be satisfied. After postulating a form of the relation between the density and the flow rate we proceeded to solve the equation using a method of characteristics. The structure of the characteristics sometimes led to the need for shock waves and expansion fans, which resulted in inhomogeneous density distributions. Only examples that have discontinuous initial conditions have so far been investigated.

Obviously we wish to find the long-term density distributions for an arbitrary set of initial conditions, and in particular we would like to solve the problem for a continuous initial density distribution. However, owing to the shock wave and expansion fan structures, it is difficult to do this in general, both analytically and computationally.

In the present chapter, we attempt to find such solutions; in particular, we consider those which remain always on one branch of the fundamental diagram. That is to say, this chapter concerns only those situations in which grain movement is uni-directional. Solutions which require a branch switch, i.e. in which grains move both to and fro, are dealt with in chapter 7. We seek numerical solutions there by considering the continuum equation in polar co-ordinates.

First in this chapter we try to find uni-directional solutions by solving the continuum equation with a simple finite difference scheme. Those solutions which emulate inviscid results such as translating shocks and expansion fans are sought. Following this we analyse an asymptotic solution valid at small times for a smooth initial condition. The chapter ends with a search for steady state solutions which remain on one branch.

6.2 Viscous model and numerical scheme

One standard way to compute general solutions to equations of the above form, whilst avoiding any problems associated with the inclusion of shocks and fans, is to add an artificial viscous dissipation term $\nu\rho_{xx}$, with ν a small parameter. This changes the nature of the partial differential equation from a hyperbolic equation to a parabolic one, and also all discontinuities can be 'smoothed out' in principle. Indeed, this is the conventional method used in traffic flow problems [43], [57]. Whitham [57] discusses at length the validity of such an approach and shows that in the limit of the viscosity ν tending to zero the solutions do in fact asymptote toward the familiar shock and fan structures seen for the inviscid equation. Furthermore, in traffic flow problems there are outright physical arguments to include a viscous smoothing of the shocks, such as the notion of driver awareness.

In addition to the possible computational benefit, physical arguments for including viscous dissipation involve in particular the inclusion of air effects. As grains approach each other in collisions effects of air cushioning could perhaps reduce the importance of impacts in the model and thus make the density distribution more homogeneous. In fact, air effects are investigated in detail in chapter 8. Another line of argument is that including a viscous dissipation term is comparable to including the next term in a Taylor expansion of the flux. Thus the flux is now identical to $q - \nu\rho_x$. The consequences of introducing viscous dissipation into the continuum model during collisions and separations in a two-way flow are thoroughly examined in chapter 7.

It suffices to say for now that we modify equation (5.6) to

$$\rho_t + c\rho_x = \nu \rho_{xx}, \tag{6.1}$$

where ν is a small positive constant, in order to find some general solutions for the density in a one-way flow. Equation (6.1) is of central importance here and is referred to frequently throughout the rest of the thesis. We shall refer to this equation hereinafter as the 'continuum equation'. We state again that if ν is small, which is the case of most concern, solutions to the continuum equation (6.1) may approximate well solutions to the inviscid equation (5.6).

As an aside, we briefly mention (echoing a similar remark in chapter 5) here that if the work were extended to 2D then the relevant equation would be

$$\rho_t + c_1(\rho)\rho_x + c_2(\rho)\rho_y = \nu\left(\rho_{xx} + \rho_{yy}\right) \tag{6.2}$$

and again examining the orders of magnitude as $y \to \infty$ and seeking a solution independent of y would yield the 1D equation (6.1) above.

Equation (6.1) is solved numerically by a finite difference scheme as follows. The derivative with respect to time is discretized as

$$\frac{\rho_i - \bar{\rho}_i}{\delta t} \tag{6.3}$$

where ρ_i is the value of the density at the i^{th} spatial station at the current time, $\bar{\rho}_i$ is the density at the i^{th} spatial station at the previous (known) time, and δt is the time step.

Upwind or downwind differencing is used for the spatial first derivative, depending on the sign of $c(\rho)$ at the i^{th} station:

$$\rho_x \approx \frac{\rho_{i+1} - \rho_i}{\delta x}, \text{ if } c(\bar{\rho}_i) < 0, \tag{6.4a}$$

$$\rho_x \approx \frac{\rho_i - \rho_{i-1}}{\delta x}, \text{ if } c(\bar{\rho}_i) > 0, \tag{6.4b}$$

where δx is the step length in the spatial direction; we take δt significantly smaller than δx. Each term in the spatial derivatives is evaluated at the known time level.

Finally the second derivative with respect to x is discretized as

$$\frac{\rho_{i+1} - 2\rho_i + \rho_{i-1}}{(\delta x)^2}. \tag{6.5}$$

This results in equations of the form

$$\underline{\underline{\mathbf{M}}}\rho = \frac{\bar{\rho}}{\delta t} \tag{6.6}$$

where $\underline{\underline{\mathbf{M}}}$ is a tri-diagonal matrix. By substituting the discretized forms of the derivatives into (6.1) it is specifically found that the elements on the lower diagonal are given by

$$-\frac{1}{(\delta x)^2} \tag{6.7a}$$

if $c(\bar{\rho}_i) < 0$, or

$$\left(-\frac{c(\bar{\rho}_i)}{\delta x} - \frac{1}{(\delta x)^2}\right) \tag{6.7b}$$

if $c(\bar{\rho}_i) > 0$; the elements on the diagonal are given by

$$\left(-\frac{1}{\delta t} - \frac{c(\bar{\rho}_i)}{\delta x} + \frac{2}{(\delta x)^2}\right) \tag{6.8a}$$

if $c(\bar{\rho}_i) < 0$, or

$$\left(-\frac{1}{\delta t} + \frac{c(\bar{\rho}_i)}{\delta x} + \frac{2}{(\delta x)^2}\right) \tag{6.8b}$$

if $c(\bar{\rho}_i) > 0$; and the elements on the upper diagonal are given by

$$\left(\frac{c(\bar{\rho}_i)}{\delta x} - \frac{1}{(\delta x)^2}\right) \tag{6.9a}$$

if $c(\bar{\rho}_i) < 0$, or

$$-\frac{1}{(\delta x)^2} \tag{6.9b}$$

if $c(\bar{\rho}_i) > 0$. The matrix $\underline{\underline{\mathbf{M}}}$ is inverted by Gaussian elimination and each ρ_i can subsequently be found. Thus the scheme is of the implicit type. This can be repeated over many time steps to find each particular solution.

6.3 Solutions to the continuum model

The author has demonstrated that the code can be used to reproduce well known results for particular expressions for the wave speed c (such as $c = 0$ giving the heat equation, $c = \rho$ giving Burgers' equation, and so on), and these tests can be obtained on request. We can therefore be reasonably confident that the code provides accurate solutions. Thus we move on to find numerical solutions to the continuum model of interest here, i.e. those which remain on one branch. Thus we specify boundary conditions for $\rho(x_L, t)$, $\rho(x_R, t)$ at the left x_L and right x_R boundaries respectively and an initial condition $\rho(x, 0)$ across the chute at $t = 0$.

An appropriate flux-density relation must first be specified for the continuum model. We propose two versions: both are equally valid for the one-way flows with which this chapter is concerned, but the second one leads to simpler analysis in section 6.4. The first one is

$$q = \begin{cases} \pm\rho^4, & 0 \leq \rho < 1, \\ \pm\left(c_1\rho^4 + c_2\rho^3 + c_3\rho^2 + c_4\rho + c_5\right) & 1 \leq \rho < 10, \\ \pm\left(\rho_M - \rho\right)^2, & 10 \leq \rho < \rho_M. \end{cases} \tag{6.10}$$

where for now $\rho_M = 15$; c_1, c_2, ...c_5 are constants chosen to ensure that the function matches smoothly and also that there is a maximum (or minimum on the lower branch) at an arbitrary point in the interval $\rho \in [0, \rho_M]$, and $\pm$ obtains the upper or lower branch respectively. The fundamental diagram for this density-flux law is shown in figure 6.1; it captures the main features required that were elucidated at the start of chapter 5. As we consider only uni-directional grain movement we choose the positive branch without loss of generality. This law is used in the computational analysis immediately below with which we try to emulate the inviscid solutions.

The second flux-density relation, used below in the asymptotic analysis of section 6.4 for the sake of simplicity, is

$$q = \pm\gamma\rho^{\frac{3}{2}}e^{-\rho}, \quad \text{so} \quad c = \pm\gamma\rho^{\frac{1}{2}}e^{-\rho}\left(\frac{3}{2} - \rho\right), \tag{6.11}$$

where $\gamma = 1$ for convenience and we choose the positive (upper) branch. The fundamental diagram is shown in figure 6.2. Clearly there is no maximum density here, but one-way solutions require no branch switch anyway. Otherwise, the fundamental diagram displays the required features elucidated upon in chapter 5.

Initially, the code is used in an attempt to emulate some of the analytical results

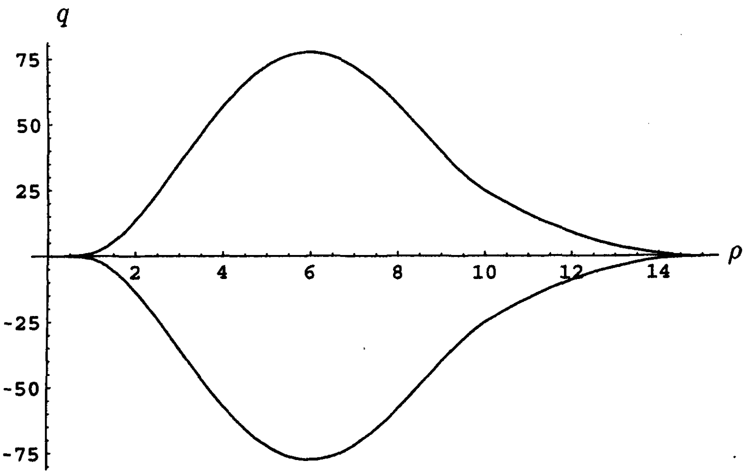

Figure 6.1: The fundamental diagram used in the computation.

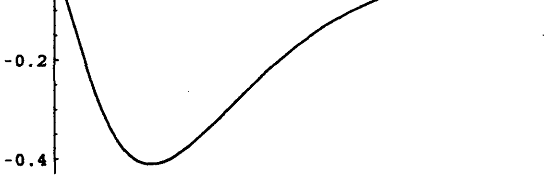

Figure 6.2: The fundamental diagram used in the asymptotic analysis of section 6.4.

seen in chapter 5. Recall that these solutions were for discrete, discontinuous input, as these formed a simple starting point for the analysis. We attempt to approximate such initial conditions in the code, although of course it is not particularly desirable to start the computation with discontinuous input.

6.3.1 Emulating a translating shock

For the first example we try to mimic the translating shock type of solution seen in subsection 5.1.1. We repeat that the solution in 5.1.1 is for the inviscid hyperbolic equation (5.6), whereas the numerical solutions we seek here are for the parabolic p.d.e. (6.1). If, however, ν is taken to be sufficiently small, the numerical solutions to (6.1) may approximate well the inviscid solutions to the hyperbolic equation. (The effect of $\nu\rho_{xx}$ is to smooth out the discontinuities in the hyperbolic equation; if ν is sufficiently small then there is sufficient smoothing to allow the computation to run and thus produce seemingly 'sharp' solutions, while avoiding any associated problems with discontinuities). In this example, $\nu = 0.0001$.

The initial condition used for this example is

$$\rho(x,0) = \begin{cases} 2, & x \leq 4, \\ e^{-25(x-5)^2} + 2, & 4 < x \leq 5, \\ 3, & x > 5. \end{cases} \tag{6.12}$$

and the boundary conditions are

$$\rho(0,t) = 2, \tag{6.13a}$$

$$\rho(15,t) = 3. \tag{6.13b}$$

Hence there are two regions of constant density, both with $q > 0$ (i.e. the density is fixed on the upper branch), and there is a smooth transition between the two regions; this approximates the discontinuous input leading to a translating shock type of solution in subsection 5.1.1.

Figure 6.3 shows the solution obtained at times $t = 0.5$, 1, and 1.5. As time increases, the 'jump' between the two near-constant regions steepens considerably

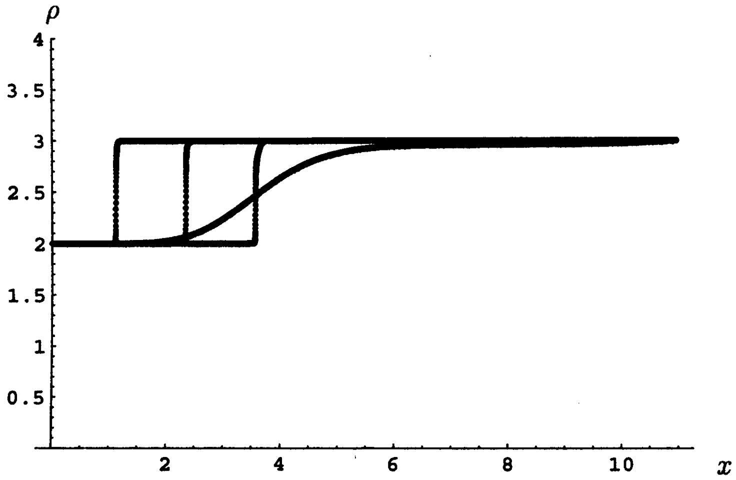

Figure 6.3: Figure showing the solution at $t = 0.5,\ 1,$ and 1.5 for the example in subsection 6.3.1. The initial condition is the smoothest thick black line. As time increases, the 'jump' between the two near-constant regions steepens considerably and translates leftward, mimicking a translating shock. The solution is shown at times $t = 0.5,\ 1,$ and 1.5.

and translates leftward, mimicking well a translating shock. (For the analogous inviscid problem with discontinuous input, it is easy to determine that a leftward translating shock is the correct solution).

6.3.2 Emulating an expansion fan

For the second example, we try to replicate an expansion fan type of solution seen in subsection 5.1.2. Again we put $\nu = 0.0001$. The initial condition is

$$\rho(x,0) = \begin{cases} 13, & x \leq 2.5, \\ 2e^{-1000(x-2.5)^2} + 11, & 2.5 < x \leq 3, \\ 11, & x > 3. \end{cases} \tag{6.14}$$

The boundary conditions are

$$\rho(0,t) = 13, \tag{6.15a}$$

$$\rho(5,t) = 11. \tag{6.15b}$$

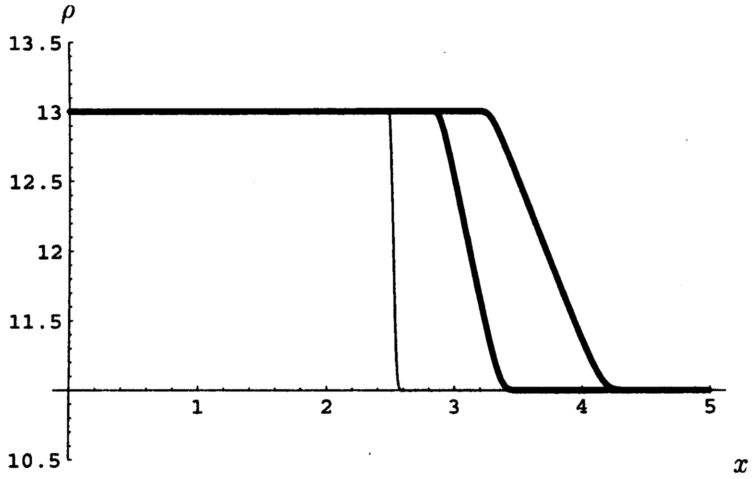

Figure 6.4: The figure shows the initial condition and two solutions, one at $t = 0.1$ and the other at $t = 0.2$. As time increases, the 'jump' between the two near-constant regions flattens considerably and spreads rightwards across the chute, mirroring well an expansion fan.

Hence initially there are two regions of constant density, each now with $q < 0$ (i.e. the density is on the lower branch), and a smooth, yet steep, transition between the two regions, approximating the discontinuous input leading to an expansion fan type of solution in subsection 5.1.2.

Figure 6.4 shows the initial condition and the solution obtained at times $t = 0.1$ and 0.2. As time increases, the 'jump' between the two near-constant regions flattens considerably and spreads rightwards across the chute, resembling an expansion fan. (Again, in the analogous inviscid problem with discontinuous input, it is easy to determine that such an expansion fan is the correct solution).

6.3.3 Solutions involving a branch switch and further comments

It is desirable to seek solutions involving a branch switch in order to replicate some of the more complex solutions seen in chapter 5, such as those in subsection 5.1.3. Moreover, it might allow us to model collisions or separations or allow us to find general solutions to the continuum model. With the current code, however, the sign of the flux q must be specified artificially in the initial condition and q cannot be changed as ρ changes. It is impossible, therefore, to include both branches of the fundamental diagram in the scheme, where we solve solely for $\rho(x,t)$.

In chapter 7 we return to the branch-switch problem, after first considering necessary adaptations to the fundamental diagram in the light of the viscous dissipation term, and attempt to solve the continuum equation in polar co-ordinates to allow the solution to freely move around the fundamental diagram. In the remainder of the current chapter other uni-directional solutions are sought. In the next section, an asymptotic solution to the continuum equation for a smooth initial condition is examined, which is valid at small times. Following this, steady states are sought. The steady state can be regarded approximately as the density profile as the grains reach the bottom of the chute.

6.4 An asymptotic solution to the continuum equation

Here we find an asymptotic and a numerical solution for the non-constant smooth initial condition $\rho(x,0) = x$ and the boundary conditions $\rho(x=0,t) = 0$ and $\rho(x = x_1, t) = x_1$, and then we make comparisons. Strictly, the asymptotic part is for asymptotically small time, but it is anticipated to be useful for comparisons with the numerical part over a finite range of early times. The motivation for so-doing is to find a solution which remains on one branch which does not mimic the discontinuous input used in the inviscid model, thus extending the types of solution obtained. The subsections 6.4.1 - 6.4.4 below cover the core, the inner layer, the outer layer and the resulting comparison in turn. For this analysis the flux-density law is as given in equation (6.11).

6.4.1 Core expansion

First consider an expansion in the core (where x is of order unity) for asymptotically small time. Let

$$\rho = \rho_0(x) + t\rho_1(x) + t^2\rho_2(x) + \dots ; \tag{6.16}$$

we refer to the end of this subsection for a note on why non-integer powers have been neglected. The initial condition

$$\rho(x,t=0) = x \tag{6.17}$$

gives

$$\rho_0 = x. \tag{6.18}$$

In the above c has also been expanded as

$$c = \bar{c}_0 + t\bar{c}_1 + ... \tag{6.19}$$

Substituting the expansion for ρ into equation (6.11) results in

$$c = \bar{c}_0 + t\bar{c}_1 + ... = \gamma\left(\rho_0 + t\rho_1\right)^{\frac{1}{2}} e^{(\rho_0 + t\rho_1)} \left(\frac{3}{2} - (\rho_0 + t\rho_1)\right) + ... \tag{6.20}$$

so

$$\bar{c}_0 = \gamma\rho_0^{\frac{1}{2}} e^{-\rho_0} \left(\frac{3}{2} - \rho_0\right). \tag{6.21}$$

Hence

$$\left(\rho_1 + 2t\rho_2\right) + \left(\bar{c}_0 + t\bar{c}_1\right)\left(\rho_0' + t\rho_1'\right) = \nu\left(\rho_0'' + t\rho_1''\right) + O\left(t^2\right) \tag{6.22}$$

upon substitution into equation (6.1). At $O(1)$ in equation (6.22) we see

$$\rho_1 + \bar{c}_0\rho_0' = \nu\rho_0'' \tag{6.23}$$

hence

$$\rho_1 = -\gamma x^{\frac{1}{2}} e^{-x} \left(\frac{3}{2} - x\right) \tag{6.24}$$

after substituting for ρ_0 and $\bar{c}_0$. Observe that $\rho_1(x)$ does not satisfy the boundary condition $\rho_1(x = x_1, t) = 0$. Therefore, in the core we have

$$\rho = x - \gamma x^{\frac{1}{2}} e^{-x} \left(\frac{3}{2} - x\right) t + O\left(t^2\right). \tag{6.25}$$

It is worth recording that only integer powers of t are involved in the core. For, if $\rho = \rho_0(x) + t^r\rho_r(x) + ...$ with r non-integer instead of (6.16), then $c = \bar{c}_0 + t^r\bar{c}_r + ...$ (with $\bar{c}_r \propto \rho_r$) and so substitution into (6.1) yields $\rho_r = 0$. Hence the term ρ_r is absent, in effect, as is $\bar{c}_r$.

6.4.2 Inner-layer expansion

At small time an inner layer must be introduced so that the left-hand boundary condition at $x = 0$ is satisfied for all time. (Although equation (6.25) satisfies the left-hand boundary condition up to $O\left(t^2\right)$, it does not do so at higher orders). Balancing terms in equation (6.1), with the local $c(\rho)$ behaviour going as $\rho^{\frac{1}{2}}$, we obtain the orders

$$\frac{\rho}{t} + \gamma \rho^{\frac{1}{2}} \frac{\rho}{x} = \nu \frac{\rho}{x^2}. \tag{6.26}$$

Noting that γ and ν are order one constants (in fact, we have chosen $\gamma = 1$ earlier and when we compare the asymptotic result to the numerical result we choose $\nu = 1$.) and that $\rho \sim x$, we guess that the first and the third terms must balance in order to introduce an effect distinct from that in the core. Hence the inner variable is chosen to be

$$\eta = \frac{x}{t^{\frac{1}{2}}}. \tag{6.27}$$

Now the expansion implied is

$$\rho = g_0(\eta) + t^{\frac{1}{2}} g_1(\eta) + t^{\frac{5}{4}} g_2(\eta) + \dots\,. \tag{6.28}$$

It can be seen that these powers must be chosen by putting $\rho = g_0 + t^n g_1 + t^m g_2$ with $0 < n < m$ and substituting into equation (6.1). After finding the derivatives in terms of η by using the chain rule and a little further manipulation we arrive at

$$\begin{aligned} n t^{n-1} g_1 + m t^{m-1} g_2 - \frac{\eta}{2t}\left(t^n g_1' + t^m g_2'\right) & \\ + t^{\frac{n}{2}} g^{\frac{1}{2}} \left(1 + \frac{t^{m-n} g_2}{2 g_1}\right) t^{-\frac{1}{2}} \left(t^n g_1' + t^m g_2'\right) & \\ = \frac{\nu}{t}\left(t^n g_1'' + t^m g_2''\right). & \end{aligned} \tag{6.29}$$

Here a prime denotes differentiation with respect to η and we have also found the local $c(\rho)$ relation, $c \sim \rho^{\frac{1}{2}}$, to be

$$c = t^{\frac{n}{2}} g_1^{\frac{1}{2}} + t^{m-\frac{n}{2}} \frac{g_2}{2} g_1^{-\frac{1}{2}} \tag{6.30}$$

and $g_0 = 0$ as we see that this is a valid solution to (6.29) if the leading order terms are included. At $O\left(t^{n-1}\right)$ an ordinary differential equation for g_1 is thus obtained:

$$\nu g_1'' + \frac{\eta}{2} g_1' - n g_1 = 0 \tag{6.31}$$

and we can see that if $n = \frac{1}{2}$ then $g_1 = \text{Constant} \times \eta$ is one solution and that this matches as required with the core. At the next order the terms of order t^{m-1} and $t^{\frac{3n}{2}-\frac{1}{2}}$ must balance. Since $n = \frac{1}{2}$ we obtain $m = \frac{5}{4}$.

Therefore, substituting (6.28) into equation (6.1), we ultimately reach

$$\begin{aligned}\frac{1}{2}t^{-\frac{1}{2}}g_1 + \frac{5}{4}t^{\frac{1}{4}}g_2 - \frac{\eta}{2t^{\frac{1}{2}}}g_1' - \frac{t^{\frac{1}{4}}\eta}{2}g_2' & \\ + t^{-\frac{1}{2}}\left(t^{\frac{1}{4}}g_1^{\frac{1}{2}} + \frac{tg_2}{2}g_1^{-\frac{1}{2}}\right)\left(t^{\frac{1}{2}}g_1' + t^{\frac{5}{4}}g_2'\right) & \\ = \frac{\nu}{t}\left(t^{\frac{1}{2}}g_1'' + t^{\frac{5}{4}}g_2''\right). & \qquad (6.32)\end{aligned}$$

By including terms of $O\left(t^{-\frac{1}{2}}\right)$ we find that we are required to solve

$$\nu g_1'' + \frac{\eta}{2}g_1' - \frac{1}{2}g_1 = 0 \qquad (6.33)$$

subject to

$$g_1(0) = 0 \qquad (6.34)$$

and, to match with the core where $\rho_0 = x$,

$$t^{\frac{1}{2}}g_1(\eta \to \infty) \sim \rho_0. \qquad (6.35)$$

Note again that one solution is

$$g_1 = B\eta \qquad (6.36)$$

where B is a constant. To find the other solution first differentiate equation (6.33) with respect to η to yield

$$g_1''' + \frac{\eta}{2\nu}g_1'' = 0. \qquad (6.37)$$

Multiplying by an integrating factor $e^{\frac{\eta^2}{4\nu}}$ and integrating once gives

$$g_1'' = Ae^{-\frac{\eta^2}{4\nu}} \qquad (6.38)$$

where A is a constant of integration. Hence

$$g_1' = A\int_{\infty}^{\eta} e^{-\frac{\bar{\eta}^2}{4\nu}}d\bar{\eta}. \qquad (6.39)$$

The lower bound can be chosen at liberty and so we pick infinity for convenience. The full solution to equation (6.33) is, therefore,

$$g_1 = A\int_0^{\eta} I d\tilde{\eta} + B\eta \tag{6.40}$$

where

$$I \equiv \int_{\infty}^{\tilde{\eta}} e^{-\frac{\bar{\eta}^2}{4\nu}} d\bar{\eta}. \tag{6.41}$$

Note that at $\eta = 0$, $g_1 = 0$ as required, and also that, from (6.35),

$$t^{\frac{1}{2}} g_1 (\eta \to \infty) = Bt^{\frac{1}{2}}\eta + At^{\frac{1}{2}} \int_0^{\infty} \int_{\infty}^{\tilde{\eta}} e^{-\frac{\bar{\eta}^2}{4\nu}} d\bar{\eta} \sim x \tag{6.42}$$

must be satisfied, i.e.

$$t^{\frac{1}{2}} g_1 (\eta \to \infty) = Bx + At^{\frac{1}{2}} \int_0^{\infty} \int_{\infty}^{\tilde{\eta}} e^{-\frac{\bar{\eta}^2}{4\nu}} d\bar{\eta} \sim x. \tag{6.43}$$

Consequently, we must choose A=0, so that an $O\left(t^{\frac{1}{2}}\right)$ term is not driven into the core, and we must also choose $B = 1$; the necessary absence of non-integral powers of t in the core was shown just after (6.25). Therefore

$$g_1 = \eta. \tag{6.44}$$

Moving on to $O\left(t^{\frac{1}{4}}\right)$ in equation (6.32) we find that we are required to solve

$$\nu g_2'' + \frac{\eta}{2} g_2' - \frac{5}{4} g_2 = \eta^{\frac{1}{2}}. \tag{6.45}$$

First, for the particular integral, try

$$g_{2PI} = \lambda \eta^{\frac{5}{2}}. \tag{6.46}$$

Substituting into equation (6.45) reveals

$$g_{2PI} = \frac{4}{15\nu} \eta^{\frac{5}{2}}. \tag{6.47}$$

For the complementary functions

$$\nu g_2'' + \frac{\eta}{2} g_2' - \frac{5}{4} g_2 = 0 \tag{6.48}$$

must be solved. The general solution is subject to the boundary conditions

$$g_2(0) = 0 \tag{6.49}$$

and

$$t^{\frac{5}{4}} g_2(\eta \to \infty) = 0, \tag{6.50}$$

so that an $O\left(t^{\frac{5}{4}}\right)$ term is not driven into the core; again see just after (6.25).

Just below we provide a numerical solution to this equation, by employing the Runge-Kutta method. A second method of solution, found by a general integral transform of the form:

$$g_{2CF} = \int_C e^{w\eta} \phi(w)\, dw \tag{6.51}$$

is presented in appendix E. A third method of solution, kindly noted by Professors Kerr and Please, can be found by making the substitution

$$g_2(\eta) = e^{-\frac{\eta^2}{8\nu}} h(\eta). \tag{6.52}$$

The subsequent differential equation is that of a Parabolic Cylinder Function, which can be rescaled into one of the standard forms of Abramowitz and Stegun [1]. Known properties of these functions can then be used to obtain the required behaviour.

First, we examine a series solution to equation (6.48) in order to show that a $\eta^{\frac{1}{2}}$ + h.o.t solution can exist at large η before we go on to search for it with the Runge-Kutta scheme. It is possible that the $\eta^{\frac{1}{2}}$ term alone, when added to g_1, might show the right trends as the solution passes from layer to core. The $g_2'(0)$ condition in the Runge-Kutta scheme must be changed until the solution is sufficiently close to the $\eta^{\frac{1}{2}}$ growth at large η.

Put

$$g_{2CF} \sim A_0 \eta^{\frac{5}{2}} + A_1 \eta^n + \ldots \tag{6.53}$$

into equation (6.48) to obtain

$$\frac{15\nu}{4} A_0 \eta^{\frac{1}{2}} + \nu A_1 n(n-1)\eta^{n-2} + \frac{A_1 n}{2}\eta^n - \frac{5}{4} A_1 \eta^n + \ldots = 0. \tag{6.54}$$

Balance the first, third and fourth terms to get $n = \frac{1}{2}$. Then

$$\frac{15\nu A_0}{4} = A_1 \tag{6.55}$$

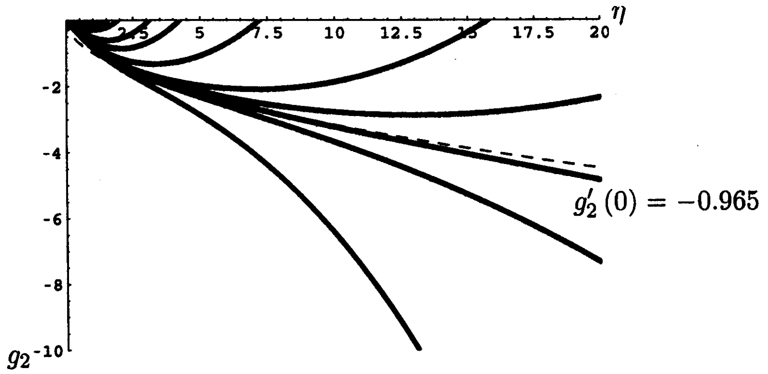

Figure 6.5: Plotted above are numerical solutions (solid black lines) to equation (6.45) for many different initial conditions for g_2'. The dashed line is a plot of $-\eta^{\frac{1}{2}}$, the series solution. We see that if we choose $g_2'(0) = -0.965$ in the computation then the solution asymptotes to the series solution.

must be satisfied so equation (6.54) holds true up to $O\left(\eta^{\frac{1}{2}}\right)$. Matching the $\eta^{\frac{5}{2}}$ term with the particular integral (6.47), in order to satisfy the boundary condition (6.50), gives

$$A_0 = -\frac{4}{15\nu} \tag{6.56}$$

and

$$A_1 = -1; \tag{6.57}$$

so

$$g_{2GS} \sim -\eta^{\frac{1}{2}} + \ldots . \tag{6.58}$$

Now solve equation (6.45) by a Runge-Kutta scheme. The initial conditions are

$$g_2(0) = 0 \tag{6.59}$$

and the value for $g_2'(0)$ that gives a solution which asymptotes to $-\eta^{\frac{1}{2}}$ is chosen. We use the numerical scheme 25.5.18 in Abramowitz and Stegun [1]. We require the separatrix, in effect.

Figure 6.5 reveals that if $g_2'(0) = -0.965$ is chosen then the solution asymptotes to the series solution (6.58). Consequently the solution for g_2 is given by the numerical scheme with the initial conditions $g_2(0) = 0$ and $g_2'(0) = -0.965$. Unfortunately this solution cannot be written in a neat closed form.

6.4.3 Outer-layer expansion

Since the core expansion does not satisfy the right-hand boundary condition $\rho(x_1) = x_1$ an outer-layer expansion must also be introduced near $x = x_1$. In this region the similarity variable

$$\xi = \frac{x - x_1}{t^{\frac{1}{2}}} \tag{6.60}$$

is appropriate and ρ is expanded as

$$\rho = x_1 + t^{\frac{1}{2}}\xi + tF_0(\xi) + t^2 F_1(\xi) + \ldots \tag{6.61}$$

We need to find an expression for the wave speed c near the point $x = x_1$. Substituting a Taylor expansion for c about $x = x_1$ reveals that

$$c = \frac{3}{2}x_1^{\frac{1}{2}}e^{-x_1} - x_1^{\frac{3}{2}}e^{-x_1} + O(t). \tag{6.62}$$

Also c is expanded as

$$c = \hat{c}_0 + t\hat{c}_1 + \ldots; \tag{6.63}$$

so

$$\hat{c}_0 = \frac{3}{2}x_1^{\frac{1}{2}}e^{-x_1} - x_1^{\frac{3}{2}}e^{-x_1}. \tag{6.64}$$

Once again, if the relevant expansions are substituted into equation (6.1) we reach

$$\begin{aligned} \frac{1}{2}t^{-\frac{1}{2}} + F_0 + 2tF_1 - \frac{\xi}{2t}\left(t^{\frac{1}{2}} + tF_0' + t^2F_1'\right) \\ + \left(\hat{c}_0 + t\hat{c}_1\right)\left(\frac{1}{t^{\frac{1}{2}}}\right)\left(t^{\frac{1}{2}} + tF_0' + t^2F_1'\right) \\ = \frac{\nu}{t}\left(tF_0'' + t^2F_1''\right). \end{aligned} \tag{6.65}$$

At $O\left(t^{-\frac{1}{2}}\right)$

$$\frac{\xi}{2} - \frac{\xi}{2} = 0 \tag{6.66}$$

is immediately satisfied. More interestingly, at $O(1)$, the solution to

$$\nu F_0'' + \frac{\xi}{2}F_0' - F_0 = \hat{c}_0 \tag{6.67}$$

must be found subject to

$$F_0(0) = 0 \tag{6.68}$$

and, in view of the core in subsection 6.4.1

$$F_0 \sim -\rho_1 \text{ as } \xi \longrightarrow -\infty. \tag{6.69}$$

First we note that one complementary function is $F_0 = \xi^2 + 2\nu$. Also observe that a particular integral is $F_{O_{PI}} = -\hat{c}_0$. The other complementary function can be found by putting

$$F_0 = \left(\xi^2 + 2\nu\right) H \tag{6.70}$$

and solving for the resultant equation for H:

$$H'' + \frac{\xi\left(\xi^2 + 10\nu\right)}{2\nu\left(\xi^2 + 2\nu\right)} H' = 0. \tag{6.71}$$

Use an integrating factor,

$$IF = \int \frac{\xi\left(\xi^2 + 10\nu\right)}{2\nu\left(\xi^2 + 2\nu\right)} d\xi = \int \frac{\xi^3}{2\nu\left(\xi^2 + 2\nu\right)} d\xi + \int \frac{5\xi}{\xi^2 + 2\nu} d\xi. \tag{6.72}$$

Evaluating the integrals leads to

$$IF = \frac{\xi^2 + 2\nu}{4\nu} + 2\ln\left|\xi^2 + 2\nu\right|. \tag{6.73}$$

Consequently, after integrating once, we find that

$$H' = A \frac{e^{-\left(\frac{\xi^2+2\nu}{4\nu}\right)}}{\left(\xi^2 + 2\nu\right)^2} \tag{6.74}$$

where A is a constant of integration. Now try a solution of the form

$$H = \frac{C\xi}{\xi^2 + 2\nu} e^{-\frac{\xi^2}{4\nu}} + D\mathrm{Erf}\left(\frac{\xi}{2\sqrt{\nu}}\right) \tag{6.75}$$

where C and D are constants. By substitution it is seen that equation (6.74) can be satisfied if

$$C = \frac{2\nu D}{\sqrt{\pi\nu}} \tag{6.76}$$

and

$$D = \frac{Ae^{-\frac{1}{2}}\sqrt{\pi\nu}}{8\nu^2}. \tag{6.77}$$

Hence, the general solution for F_0 is

$$F_0 = A\left[\xi\frac{e^{-\frac{1}{2}}e^{-\frac{\xi^2}{4\nu}}}{4\nu} + \frac{\left(\xi^2+2\nu\right)\sqrt{\frac{\pi}{e}}\mathrm{Erf}\left(\frac{\xi}{2\sqrt{\nu}}\right)}{8\nu^{\frac{3}{2}}}\right] + B\left(\xi^2+2\nu\right) - \hat{c}_0. \tag{6.78}$$

Using the matching condition (6.69) we see that

$$-x_1^{\frac{1}{2}}e^{-x_1}\left(\frac{3}{2}-x_1\right) = \lim_{\xi\to-\infty}\left(\frac{A\left(\xi^2+2\nu\right)\sqrt{\frac{\pi}{e}}\left(-\frac{1}{2\sqrt{\nu}}\right)}{8\nu^{\frac{3}{2}}} + B\left(\xi^2+2\nu\right) - \hat{c}_0\right). \tag{6.79}$$

To prevent the right hand side from diverging we choose

$$\frac{A}{16\nu^2}\sqrt{\frac{\pi}{e}} = B; \tag{6.80}$$

so we are left with

$$x_1^{\frac{1}{2}}e^{-x_1}\left(\frac{3}{2}-x_1\right) = \hat{c}_0 \tag{6.81}$$

which we know to be true already from equation (6.64).

Finally, the initial condition (6.68) gives

$$A = \frac{8\hat{c}_0\nu\sqrt{e}}{2+\sqrt{\pi}} \tag{6.82}$$

and so

$$\begin{aligned}F_0 = \frac{8\hat{c}_0\nu\sqrt{e}}{2+\sqrt{\pi}}&\left[\xi\frac{e^{-\frac{1}{2}}e^{-\frac{\xi^2}{4\nu}}}{4\nu} + \frac{\left(\xi^2+2\nu\right)\sqrt{\frac{\pi}{e}}\mathrm{Erf}\left(\frac{\xi}{2\sqrt{\nu}}\right)}{8\nu^{\frac{3}{2}}}\right]\\ &+ \frac{\hat{c}_0\sqrt{e}}{2\nu\left(2+\sqrt{\pi}\right)}\sqrt{\frac{\pi}{e}}\left(\xi^2+2\nu\right) - \hat{c}_0.\end{aligned} \tag{6.83}$$

Thus we have now determined (at least) the leading order terms for the expansions in the inner, core and outer layers.

6.4.4 Comparison with finite difference solution

It is now possible to compare the asymptotic solution to a numerical finite difference solution obtained as in section 6.2.

Figure 6.6 shows the density as a function of position at a fixed small positive time t. Although a very close agreement is seen between the two solutions the result

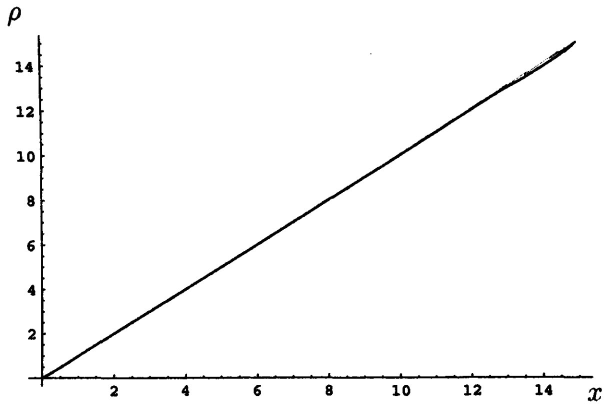

Figure 6.6: Plotted above is ρ as a function of x at a fixed time, $t = 0.1$. The solid black line and the solid grey line are the numerical and two term asymptotic solutions, respectively. See also figures 6.7 and 6.8.

is not necessarily conclusive since neither solution has deviated very far at all from the initial condition.

One alternative approach is to plot the value of the derivative of the density with respect to position at the origin for varying time, as in figure 6.7. A reasonably close agreement is seen for small time, exactly as one would expect. Figure 6.8 shows a close-up of the small time region and again a fairly close agreement is seen between the two results. The difference between the finite difference result and the small-time asymptotic result may be due to the value of $g_2'(0)$ coming from a Runge-Kutta scheme only to an accuracy of three decimal places. (The numerical accuracy of the finite difference scheme has been established by finding the solution on a number of different grids. It appears to remain the same for each grid, as we would hope).

Alternatively, figure 6.9 shows the percentage error between the value of $\left.\frac{d\rho}{dx}\right|_{x=0}$ from the numerical scheme and from the two-term asymptotic result up to $t = 0.01$. The error is fairly small. Therefore, we can be reasonably confident that we have found an asymptotic solution to equation (6.1) for a particular example in which the initial condition does not replicate any of the inviscid solutions obtained earlier and which remains on one branch for all time.

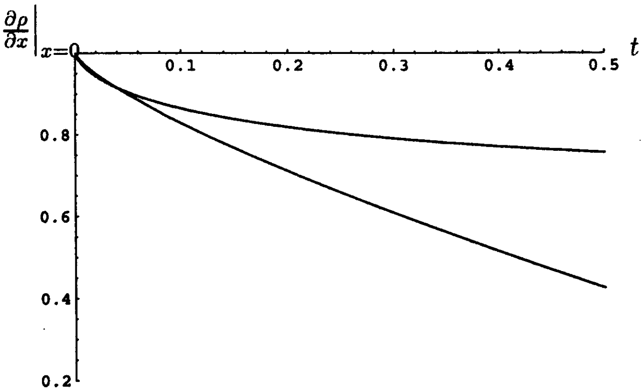

Figure 6.7: An alternative check between the numerical and the small-time-asymptotic result is to plot the derivative of the density with respect to x at the origin for a range of times. Above, the dashed line gives the values of $\left.\frac{\partial\rho}{\partial x}\right|_{x=0}$ from the numerical scheme and the solid line gives the values from the asymptotic scheme. (See also the close-up in figure 6.8). The agreement is seen to be fairly close for approximately $t \leq 0.05$, exactly as one would expect (or hope) for small time asymptotics.

6.5 Steady state solutions

Steady states are sought now for solutions which remain on one branch of the fundamental curve. Steady states may be related to the final density profile obtained near the end of the chute before ejection takes place and they are thus of interest to Sortex.

First, a particular steady state is sought in which the density at the left boundary $\rho_L \approx \rho_R$, where ρ_R is the density at the right boundary. This case yields to analysis and hence numerical solutions can be verified. Other steady states are then sought, but we find that the numerics can be unreliable, the reasons for which are considered.

6.5.1 Seeking a steady state with $\rho_L \approx \rho_R$

First, a steady state is computed in which the densities at the boundaries (ρ_L and ρ_R) are asymptotically close, specifically $\rho_L = \rho_R - \epsilon$ with ϵ small. In this case an

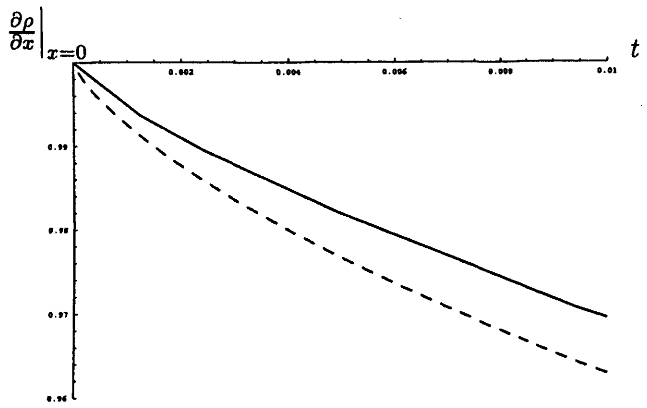

Figure 6.8: Here a close-up in the small time region of the value of $\frac{\partial\rho}{\partial x}\Big|_{x=0}$ for varying time is shown. Again, the dashed line gives the values from the numerical scheme and the solid line gives the values from the asymptotics. There is reasonable close agreement between the two solutions. A possible source for the discrepancy is discussed in the text. Note that the computation was calculated on a grid with the spatial step-length and temporal step-length given by $\delta x = 10^{-3}$ and $\delta t = 10^{-6}$ respectively.

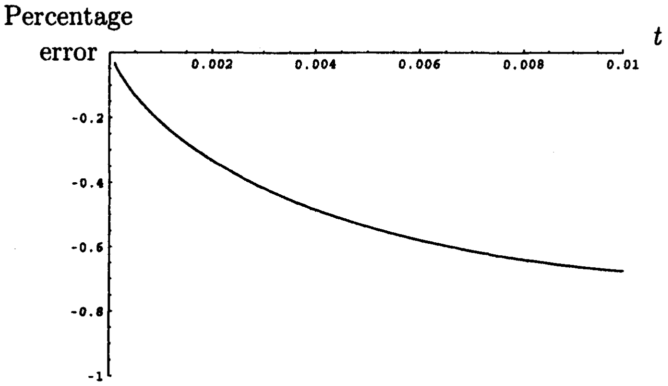

Figure 6.9: The percentage error between the value of $\frac{d\rho}{dx}\Big|_{x=0}$ for the asymptotic result and the numerical result is shown up to $t = 0.01$. It is relatively small (less than 1%) throughout.

approximate analytical solution can be found, thus providing a way to check the subsequent numerical results. The approximate analytic solution is as follows.

As ρ_L and ρ_R are asymptotically close, the wave-speed c can be assumed to be constant along the range $[\rho_L, \rho_R]$. That is, $c = c(\rho_L) \equiv c_0$ with c_0 constant. Hence from (6.1) the equation for the steady states is given by

$$c_0 \frac{d\rho}{dx} = \nu \frac{d^2\rho}{dx^2}. \tag{6.84}$$

This is easily solved to obtain

$$\rho = A + Be^{\frac{c_0}{\nu}x} \tag{6.85}$$

where A and B are constants of integration. The boundary conditions are

$$\rho(x_L) = \rho_L \tag{6.86a}$$

and

$$\rho(x_R) = \rho_R. \tag{6.86b}$$

This yields

$$A = \rho_L - \frac{(\rho_L - \rho_R)e^{\frac{c_0}{\nu}x_L}}{e^{\frac{c_0}{\nu}x_L} + e^{\frac{c_0}{\nu}x_R}} \tag{6.87a}$$

and

$$B = \frac{(\rho_L - \rho_R)}{e^{\frac{c_0}{\nu}x_L} + e^{\frac{c_0}{\nu}x_R}}. \tag{6.87b}$$

The steady state is also computed by a Runge-Kutta method. A basic fourth-order accurate scheme [14] is used to solve (6.84) with

$$\frac{d\rho}{dx} = g \tag{6.88a}$$

and

$$\frac{dg}{dx} = \frac{c_0}{\nu} g \tag{6.88b}$$

where $\nu = 1$, $c_0 = -1$ and for the present computational run $\delta x = \frac{\rho_R - \rho_L}{1000}$.

In figure 6.10 the analytical result and the result from the Runge-Kutta scheme are plotted. The discrepancy between the solutions is seen to be small. Thus we can be reasonably certain that a steady state to the continuum equation has been found.

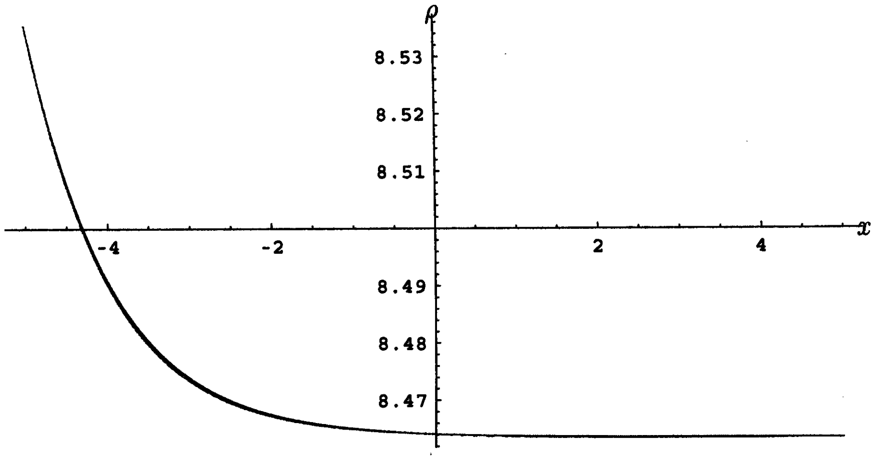

Figure 6.10: This figure shows a steady state for the case when $\rho_L \approx \rho_R$ and c_0 remains approximately constant. Both the analytic solution and the Runge-Kutta solution are plotted. Virtually no difference is observed between the solutions.

6.5.2 Other steady states

An attempt to find other steady state solutions that always remain on one branch was also made. Time-marching solutions from the finite difference scheme were computed to large times and compared to numerical solutions of the steady state equation (6.84), found by a trapezoidal method. The difference between the results from each scheme, however, was marked. An error seems likely to have arisen in the finite difference scheme at the change in sign of the windward differencing. For reasons of brevity, we do not include the computations but they can be obtained from the author on request. Perhaps the results could be re-examined in the future with use of a compact differencing scheme. Such steady states could evolve in principle, nevertheless, as outlined below.

The continuum equation (6.1) can be integrated in x to give

$$\frac{d}{dt}\int_{x_L}^{x_R} \rho dx + [q]_{x_L}^{x_R} = \nu[\rho_x]_{x_L}^{x_R}, \tag{6.89}$$

where $\int_{x_L}^{x_R} \rho dx$ is identical to the total mass. The flux $q - \nu\rho_x$ is non-zero at the boundaries, in general, since these solutions remain on one branch and do not have $\rho = \rho_M$ at the boundaries. (We shall see that this is not so in the two-way case, investigated in section 7.5 in the next chapter). Consequently, $\frac{d}{dt}\int_{x_L}^{x_R} \rho dx \neq 0$ in general. Therefore in principle the mass can evolve with time, starting from its initial value and approaching the steady state value. Therefore, a steady state may evolve in such cases. (Again, we shall see in the next chapter in section 7.5 that this is not so for the case of multivalued fluxes and the steady state there may not be reached). In passing, we mention that (6.89) provides a method of checking mass conservation numerically in time by using the calculated total flux at the boundaries.

6.6 Summary

In this chapter we have attempted to find solutions to the viscous continuum model that remain on one branch for all time, for which the grain movement is uni-directional. The motivation was to extend from the inviscid solutions found in the preceding chapter to more general cases which do not start with discontinuous input. In order to find such solutions, an artificial viscous dissipation term was added, which has the effect of smoothing out the discontinuities. Thus numerical solutions may then be found more easily. Importantly, this results in a parabolic equation and the flux now changes to $q - \nu\rho_x$.

First a finite difference scheme was employed to find solutions which replicate those in the preceding chapter. This is possible, provided that the parameter ν is small. Second, an asymptotic solution, valid at small time, was found for a smooth initial condition that did not replicate the initial conditions for the inviscid equation. Third, we examined steady state solutions for this uni-directional case. A steady state was obtained for the case of the densities at the two boundaries being asymptotically close, but other steady states were more difficult to compute. This is possibly due to an error arising at the change of sign of the windward differencing in the finite difference scheme.

In the next chapter, we wish to extend this still further and obtain solutions to the viscous continuum model for which the grains are able move to and fro. As the fundamental diagram then is not single-valued, this necessitates finding the solution by expressing the density and the flux in different terms, such as polar co-ordinates. Prior to finding such steady states we first investigate the requirement of changing the fundamental diagram; in particular, local viscous laws at the endpoints are investigated. Changes in the local curvature of the fundamental diagram allow the solution to switch branches more easily.

Chapter 7

The 'viscous' continuum model for grains in two-way flow

7.1 Introduction

The solutions of the continuum equation (6.1) have been limited so far to the inviscid case, for which the initial conditions were restricted to discontinuous input, or to the case when solutions remain on one branch. We now aim to compute solutions for cases involving colliding and separating grains, which need to switch between branches on the $Q(\rho)$ curve. In order to avoid problems associated with the double-valued fundamental diagram we solve for the density and q (no longer the flux) as functions of polar co-ordinates.

Prior to doing this we re-investigate the nature of the fundamental diagram. In particular, in chapter 5 we determined that the two branches of the fundamental diagram must meet at cusps at the endpoints. Such geometry/discontinuity is required if the wavespeed is to change smoothly during the branch switch *in the inviscid model*, but in the viscous parabolic governing equation such discontinuities are found to be incompatible with the viscous dissipation term. Consequently, the local $q \sim \rho^{\frac{3}{2}}$ relation should be altered for the viscous case.

We wish to determine whether the new $q = Q(\rho)$ relation produces physically sensible results or not. Even though the $q = Q(\rho)$ law may not have been determined itself by a complete physical argument, we may nevertheless gain some insight into the behaviour of the system. Guessing such laws, examining the outcome and subsequently discussing the validity of the particular fundamental diagram is in the tradition of traffic flow theory. In fact, many different fundamental diagrams exist as empirical models of traffic flow and there is discussion in the literature about which one is best [7]. As this is a novel approach for chute flows, there is currently no such discussion in the literature; so we shall choose this law, however arbitrary it may seem, and examine its implications. Obviously, we do not claim that this is *'the law'* for chute flow, but it is rather a first model for the viscous case.

On changing the fundamental diagram locally at the endpoints, we suggest below that the local behaviour near the origin (or maximum) must be $q \sim \rho^{\frac{1}{2}}$ (or $q \sim (\rho_M - \rho)^{\frac{1}{2}}$) and then we examine if a valid solution exists. To repeat, although this may not necessarily be driven by physics it may yield some understanding of the behaviour of the system. The suggested behaviour above can actually be put on surer ground by considering that as the solution passes through a minimum, as it may do in separating regions, $\rho \sim x^2$. Balancing terms in equation (6.1) thus reveals immediately that $q \sim x$, i.e. $q \sim \rho^{\frac{1}{2}}$ as just above. A similar relation applies near a maximum.

Therefore in sections 7.2 and 7.3 the consequences of this new law in the vicinity of the $\rho = 0$ and $\rho = \rho_M$ cusps respectively are considered. In the former case we find a similarity solution valid at small time, and in the latter case, for small viscosity, a local viscous region is introduced. In both cases the new viscous fundamental diagram indeed allows physically sensible solutions to evolve. Steady states and solutions at large time are then sought in terms of polar co-ordinates in sections 7.4 and 7.5.

7.2 Viscous separation

7.2.1 Similarity equation and local behaviour.

We find a similarity equation valid at small time to examine the local behaviour of the solution near the origin. This is near a density minimum; analogous work applies near a maximum. Branch-switching at the origin physically relates to grain separation. We have $q \sim \rho^{\frac{1}{2}}$, so $c = q' = \frac{1}{2}\rho^{-\frac{1}{2}}$ and substituting into the (6.1) we obtain the ordering

$$\frac{\rho}{t} \pm c_0 \rho^{-\frac{1}{2}} \frac{\rho}{x} \sim \frac{\rho}{x^2}$$

where c_0 is an order one constant arising from the local form of the flux-density law. Balancing terms in ρ we see that $x \sim t^{\frac{1}{2}}$ and hence $\rho \sim t$. This is acceptable since the density is small in a separating region. Therefore the similarity variable $\eta = \frac{x}{t^{\frac{1}{2}}}$ and the form $\rho = tf(\eta)$ hold locally.

Substituting into the continuum equation (6.1) we have $\frac{\partial \rho}{\partial t} = f - \frac{x}{2}t^{-\frac{1}{2}}f'$, $\frac{\partial \rho}{\partial x} = t^{\frac{1}{2}}f'$, and $\frac{\partial^2 \rho}{\partial x^2} = f''$ where a prime denotes differentiation with respect to η. (Positive c_0 is chosen when the flux q is greater than zero. Here locally $f' > 0$. Conversely, the negative c_0 is chosen when the flux q is less than zero, where $f' < 0$ locally). Also putting

$$c \sim \pm c_0 \rho^{-\frac{1}{2}} = \pm \frac{c_0}{t^{\frac{1}{2}} f^{\frac{1}{2}}},$$

we obtain

$$\nu f'' - \left(\pm \frac{c_0}{f^{\frac{1}{2}}} - \frac{\eta}{2} \right) f' - f = 0 \tag{7.1}$$

as the nominal small-time equation near the density extremum. As the purpose here is to describe separating grains we examine the case when the density passes through a minimum. It is shown in the next subsection that $f = 0$ necessarily at a minimum. Thus equation (7.1) is to be solved in subsection 7.2.3 subject to $f(k) = f'(k) = 0$, where $\eta = k$ is the location of the minimum. Also f is expected to grow proportionally to η^2 at large $|\eta|$.

7.2.2 Core behaviour

Approximating the behaviour away from the extremum, in the core, we put

$$c \sim \pm c_0 \rho^{-\frac{1}{2}}$$

and expand

$$\rho = \rho_0(x) + t\rho_1(x) + t^2\rho_2(x)$$

and on substitution into (6.1) we obtain

$$\rho_1 + 2t\rho_2 \pm c_0(\rho_0 + t\rho_1)^{-\frac{1}{2}}\left(\rho_0' + t\rho_1'\right) = \nu\left(\rho_0'' + t\rho_1''\right) + O(t^2).$$

Now if we assume that, for some positive constant λ,

$$\rho_0 \approx \lambda x^2,$$

which is the most general form for a minimum (separating grains) local to the origin, then at leading orders we find

$$\rho_1 = 2\lambda^{\frac{1}{2}}\left(\lambda^{\frac{1}{2}}\nu \mp c_0\right), \tag{7.2}$$

and

$$\rho_2 = \frac{-c_0^2 \pm c_0\nu\lambda^{\frac{1}{2}}}{x^2}. \tag{7.3}$$

Therefore approximately

$$\rho = \lambda x^2 + 2t\lambda^{\frac{1}{2}}\left(\lambda^{\frac{1}{2}}\nu \mp c_0\right) - t^2\frac{c_0^2 \mp c_0\nu\lambda^{\frac{1}{2}}}{x^2} + O(t^3). \tag{7.4}$$

Hence if $x^2 \sim t$ then the three leading terms become $O(t)$ and the series is no longer asymptotic. This reinforces the earlier similarity equation in section 7.2.1 where the similarity variable is $\eta = xt^{-\frac{1}{2}}$. Moreover, if $\lambda = c_0^2\nu^{-2}$ then the $O(t)$ and the $O(t^2)$ terms are zero and so the expansion may still be valid. Therefore a simple crossover between branches may be possible with $\lambda = c_0^2\nu^{-2}$.

If we can find a solution to equation (7.1) that is valid for all η then it may be possible to have a $\rho^{\frac{1}{2}}$ law in the viscous case. We shall discuss how it might correspond to the physics of separation. First of all,

$$f = \Gamma\eta^2 \tag{7.5}$$

is an exact solution if

$$\Gamma = \left(\frac{c_0}{\nu}\right)^2.$$

Other solutions are found below in the form

$$f = \Gamma\eta^2 + \epsilon\tilde{f} \tag{7.6}$$

with ϵ small, as studied in subsection 7.2.5, and in numerical form as described next.

7.2.3 Solving equation (7.1) by a Runge-Kutta method

There are two cases to be examined here. One is where the minimum of f is zero, in which case we need a series solution through the minimum so the numerical scheme does not blow up. The second case is where the minimum has f non-zero: the series in this case is not regular. The latter might be dismissed by a physical argument (the density must be zero at the centre of a separating region) but an analysis is presented for completeness. The series are helpful in the subsequent numerical study.

First put $f = F^2$ so equation (7.1) becomes

$$\nu FF'' + F'\left(\nu F' \mp c_0 + \frac{1}{2}(k+s)F\right) - \frac{1}{2}F^2 = 0 \tag{7.7}$$

where we have defined $s \equiv \eta - k$ and $f' = 0$ at $\eta = k$. Above a prime denotes differentiation with respect to s.

We mention here that having k non-zero allows the minimum, which cannot then be at the origin, to move with speed $\dot{x} = \frac{k}{2}t^{-\frac{1}{2}}$. Thus the solution has a fixed minimum point at $x = 0$ only if $k = 0$ (we shall see later that this corresponds to the exact solution $f = \Gamma\eta^2$). We are free to choose k in the local problem; it is actually determined by the global solution across the whole chute. Since $t \ll 1$ slower movements correspond to $k \to 0$, in effect, and faster movements can be roughly approximated by $|k|$ becoming large.

Expand

$$F = F_0 + sF_1 + s^2F_2 + ... \tag{7.8}$$

which implies that

$$F' = F_1 + 2sF_2 + ...$$

Now $f' = 0$ at $\eta = k$ implies that $2FF' = 0$ at $s = 0$ which results in

$$F_0F_1 = 0.$$

Therefore, if $F_0 \neq 0$ we must have $F_1 = 0$. (We shall continue with this choice for now, but we shall soon see that we must re-expand (7.8) with $F_1 \neq 0$ and $F_0 = 0$). Hence the expansion (7.8) becomes

$$F = F_0 + s^2F_2 + s^3F_3 + O(s^4) \tag{7.9}$$

Substituting (7.9) into equation (7.7) results in

$$\begin{aligned} &\nu \left(F_0 + s^2F_2 + s^3F_3\right)\left(2F_2 + 6sF_3\right) \\ &\quad + \left(2sF_2 + 3s^2F_3\right)\left(\nu\left(2sF_2 + 3s^2F_3\right) \mp c_0 + \frac{1}{2}(k+s)\left(F_0 + s^2F_2 + s^3F_3\right)\right) \\ &\quad\quad - \frac{1}{2}\left(F_0 + s^2F_2 + s^3F_3\right)^2 = 0 + O(s^4) \end{aligned} \tag{7.10}$$

so at leading order we obtain

$$2\nu F_0F_2 - \frac{1}{2}F_0^2 = 0 \tag{7.11}$$

giving

$$F_0 = 0 \text{ or } F_2 = \frac{F_0}{4\nu}. \tag{7.12}$$

So this leads to either $F_0 = 0$, implying that $f = 0$ at the minimum, or to a series for the case when $f = F_0$ at the minimum.

Second, then, is the case where $f = 0$ at the minimum, so that $F_0 = 0$. We must re-expand

$$F = sF_1 + s^2F_2 + s^3F_3 + s^4F_4 + O(s^5) \tag{7.13}$$

about $s = 0$. On substitution into equation (7.7) we see

$$\begin{aligned} &\left(sF_1 + s^2F_2 + s^3F_3 + s^4F_4\right)\left(2F_2 + 6sF_3 + 12s^2F_4\right) \\ &+ \left(F_1 + 2sF_2 + 3s^2F_3 + 4s^3F4 - \frac{c_0}{\nu} + \frac{(s+k)}{2\nu}\left(sF_1 + s^2F_2 + s^3F_3 + s^4F_4\right)\right) * \\ &\quad \left(F_1 + 2sF_2 + 3s^2F_3 + 4s^3F_4\right) - \frac{1}{2\nu}\left(sF_1 + s^2F_2 + s^3F_3 + s^4F_4\right)^2 = 0 + O(s^5) \end{aligned} \tag{7.14}$$

where we have chosen c_0 to be positive since the gradient of f is positive and so we must be on the upper branch of the $Q(\rho)$ curve. At leading order we obtain

$$F_1\left(F_1 - \frac{c_0}{\nu}\right) = 0 \tag{7.15}$$

implying

$$F_1 = \frac{c_0}{\nu} \tag{7.16}$$

if $F_1 \neq 0$. (The $F_1 = 0$ case is considered in the section incorporating equations (7.29) to (7.32) below, it relates to the case in which $f \neq 0$ at the centre of a separating region and is ultimately dismissed). At $O(s)$,

$$4F_1F_2 + \frac{k}{2\nu}F_1^2 = 0 \tag{7.17}$$

so

$$F_2 = -\frac{k}{8\nu}F_1. \tag{7.18}$$

At $O(s^2)$,

$$9F_1F_3 + 6F_2^2 + \frac{3k}{2\nu}F_2F_1 = 0 \tag{7.19}$$

which eventually leads to

$$F_3 = \frac{k^2}{96\nu^2}F_1. \tag{7.20}$$

Finally, at $O(s^3)$,

$$F_4 = -\frac{1}{16F_1}\left(20F_2F_3 + \frac{F_1F_2}{2\nu} + \frac{k}{\nu}F_2^2 + \frac{2F_1F_3k}{\nu}\right) \tag{7.21}$$

resulting in

$$F_4 = -\frac{1}{256}\left(\frac{k^3F_1}{6\nu^3} - \frac{kF_1}{\nu^2}\right). \tag{7.22}$$

So

$$F = \frac{c_0}{\nu}\left(s - s^2\frac{k}{8\nu} + s^3\frac{k^2}{96\nu^2} - s^4\frac{1}{256}\left(\frac{k^3}{6\nu^3} - \frac{k}{\nu^2}\right) + O(s^5)\right). \tag{7.23}$$

Similarly, we need to find the series solution to the left of $s = 0$. Substituting $s = -L$ changes equation (7.7) to

$$FF'' + \left(F' + \frac{c_0}{\nu} - \frac{(k-L)}{2\nu}F\right)F' - \frac{F^2}{2\nu} = 0 \tag{7.24}$$

where a prime now denotes differentiation with respect to L. We now expand F as

$$F = -LF_1 + L^2F_2 - L^3F_3 + L^4F_4 + \dots . \tag{7.25}$$

Comparing terms in like powers of L results in the series solution

$$F = -\frac{c_0}{\nu}\left(L + L^2\frac{k}{8\nu} + L^3\frac{k^2}{96\nu^2} + L^4\frac{1}{256}\left(\frac{k^3}{6\nu^3} - \frac{k}{\nu^2}\right) + \dots\right) \tag{7.26}$$

to the left of the minimum. In fact, any number of terms in the series can be deduced.

We can now use the above series in s (equation (7.23)) to march from the minimum to the right to some positive value $s = a$, say (i.e. $\eta = k + a$) to give us f and f' here. (Recall $f = F^2$ and $f' = 2FF'$). Similarly we can use the series in L (equation (7.26)) to find the values of f and its first derivative at some $L = b,\ b > 0$ which is to the left of the minimum ($\eta = k - L$). Hence we have the starting conditions for two Runge-Kutta schemes; one starting at $\eta = k + a$ and solving equation (7.1) shooting forward to some large positive η, and the other starting at $\eta = k - b$ and solving equation (7.1) shooting backward to some large negative η. To solve equation (7.1) by a Runge-Kutta scheme we put

$$f' = g \tag{7.27}$$

and

$$g' = \frac{1}{\nu}\left(\left(\pm\frac{c_0}{f^{\frac{1}{2}}} - \frac{\eta}{2}\right)g - f\right) \tag{7.28}$$

and use the numerical method 25.5.18 in Abramowitz and Stegun [1]. Note we choose $+c_0$ if $f' > 0$ and $-c_0$ if $f' < 0$ because $c_0 > 0$ on the upper branch where locally at the origin $f' > 0$ and vice versa.

Third, we return to the option where the minimum $f \neq 0$ i.e. $F_0 \neq 0$ and $F_1 = 0$. Recall equation (7.9) is the pertinent expansion in this case, which led to equation (7.10) and at leading order $F_2 = \frac{F_0}{4\nu}$ in (7.12). We shall see that the series in this option is not regular and furthermore it results in the unphysical condition that $f \neq 0$ at the centre of a separating region, and this option is therefore ultimately dismissed. Continuing to $O(s)$ with this choice results in

$$6\nu F_0F_3 \mp 2F_2c_0 + F_2F_0k = 0. \tag{7.29}$$

Thus

$$F_3 = -\frac{F_0 k}{24\nu^2} \pm \frac{2c_0}{24\nu^2}. \tag{7.30}$$

Note that for $f' > 0$, $c_0 > 0$ and vice versa. The shape of the solution is concave upwards; to the right of the minimum f has a positive slope. Hence

$$F_3 = -\frac{F_0 k}{24\nu^2} + \frac{2c_0}{24\nu^2}. \tag{7.31}$$

Therefore, the expansion to the right of the minimum is

$$F = F_0\left(1 + \frac{s^2}{4\nu} + s^3\left(-\frac{k}{24\nu^2} + \frac{c_0}{12\nu^2 F_0}\right)\right). \tag{7.32}$$

Again, the series must also be found to the left of the minimum. As before it is possible to make the substitution $s = -L$ and consequently we are required to solve equation (7.24) once more, this time with the expansion

$$F = F_0 + L^2 F_2 - L^3 F_3 + \ldots. \tag{7.33}$$

Similarly, comparing like powers of L and noting that to the left f has negative slope forcing $c_0 < 0$ leads to the series solution

$$F = F_0\left(1 + \frac{L^2}{4\nu} - L^3\left(-\frac{k}{24\nu^2} - \frac{c_0}{12\nu^2 F_0}\right)\right). \tag{7.34}$$

Writing this in powers of s reveals

$$F = F_0\left(1 + \frac{s^2}{4\nu} + s^3\left(-\frac{k}{24\nu^2} - \frac{c_0}{12\nu^2 F_0}\right)\right). \tag{7.35}$$

The central point here is that the third term in (7.32) differs from the third term in (7.35) in the sign of c_0. The series about the minimum is therefore not regular if $F_0 \neq 0$, which is unacceptable as we are seeking a smooth solution. An inner-inner region would be required if the series solution were non-regular, within which more knowledge of the local physics would be required, possibly concerning 'jump conditions' for example. This solution also has f non-zero at the minimum and so can be dismissed by physical arguments. Altogether therefore the minimum must occur with $f = 0$ and series (7.23) and (7.26) can be used in conjunction with a Runge-Kutta method, as explained above, to find solutions of (7.1). These correspond to the density to being zero at the centre of a separating region, agreeing perhaps with physical intuition.

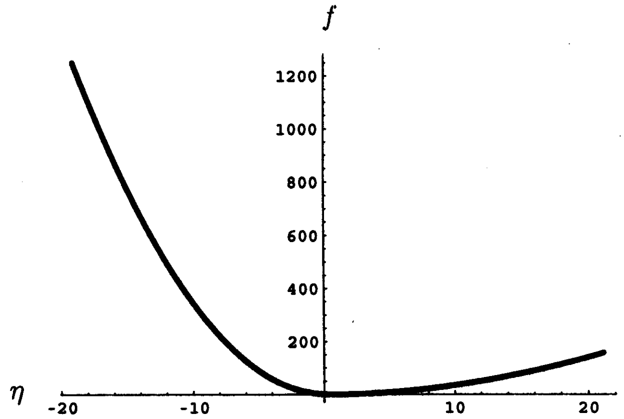

Figure 7.1: A solution to equation 7.1 where the minimum occurs at $(\eta, f) = (1, 0)$. A series solution has been used to enable passage through the minimum. See enlargement in figure 7.2. The step size in this example is $h = 0.001$.

7.2.4 Solutions

The first solution we find is for the values $a = b = 0.1$ and $k = 1$, corresponding to the minimum being located at $(\eta, f) = (1, 0)$. A series expansion is used to find the solution between $\eta = [0.9, 1.1]$ and then two Runge-Kutta schemes are used to shoot forwards or backwards from the end points of the series. Figure 7.1 shows that the density relatively rapidly increases to large values to the left of the minimum yet increases to a smaller value to the right of the minimum: the density distribution is asymmetric either side of the minimum. Figure 7.2 shows an enlargement of the solution near the minimum, highlighting the series solution through the minimum and showing that it matches well with the solutions from the Runge-Kutta schemes. Four terms have been used in the series expansion in this case. Although this may seem a surprisingly small number, when the number of terms in the series is changed to check the numerical accuracy the solution remains virtually the same. The solution $f \sim \eta^2$ to equation (7.1) in the limit $\eta \rightarrow \pm\infty$ can be used to check if the numerical solutions display the correct behaviour. Thus figure 7.3 shows a plot of the solution divided by η^2, and as η increases to large positive and negative values the curve in figure 7.3 apparently tends to a constant as expected.

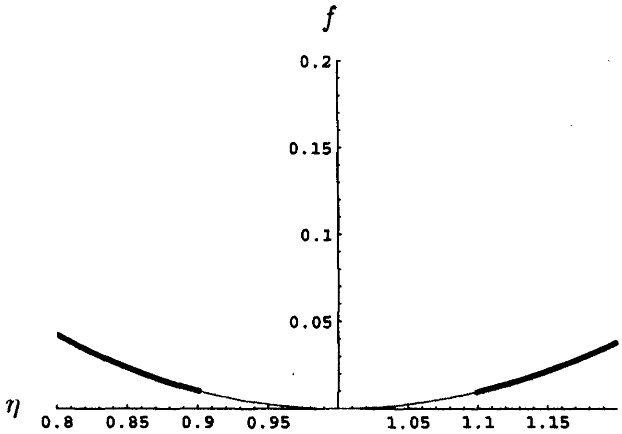

Figure 7.2: Closely examining the minimum in figure 7.1 reveals the series solution (thin line) is seen to match well with the numerical solution (heavy line). In this case, the series solution goes to $O\left(s^4\right)$.

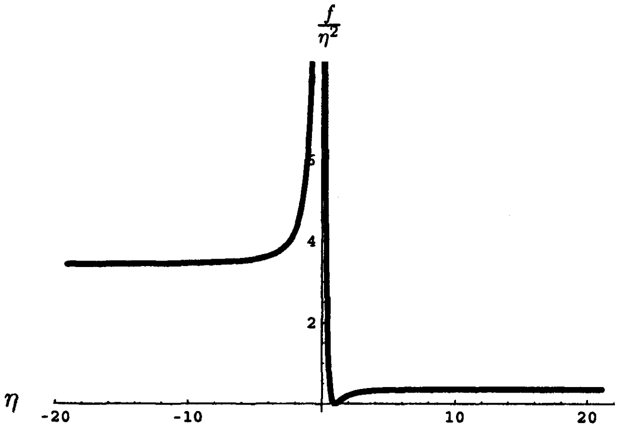

Figure 7.3: Above we plot $\frac{f}{\eta^2}$ and see that this appears to tend to a constant for large values of η. Therefore the numerical solution appears to asymptote to η^2 at large η as expected.

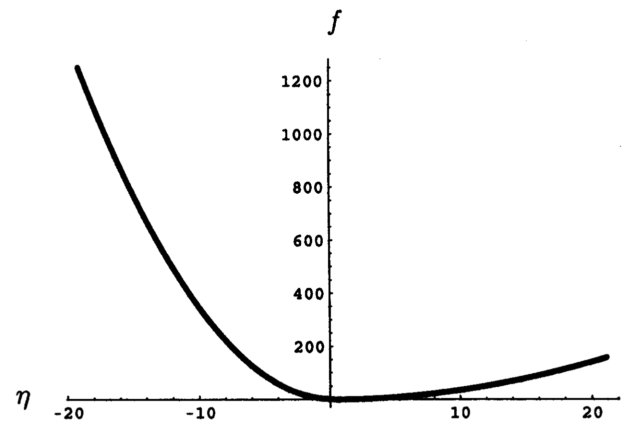

Figure 7.4: Plotted above is the full solution for three different step lengths; $h = 0.0001$, $h = 0.001$, and $h = 0.01$. All three appear to coincide virtually exactly. Figure 7.5 shows an enlargement of the solutions near the origin.

The numerical accuracy of the above solution was further checked. The step-length was made shorter or longer to check the grid-dependence of the solution. Also the number of terms in the series expansion was changed, and the interval of η in which the series is applied, to make sure the solution is not dependent on either. Finally, the length of the series can be changed to further ensure the result has no dependence on this as well. Figures 7.4 to 7.10 investigate these aspects, and the solution does indeed remain virtually the same in all cases.

A number of other solutions can be found where the minimum is located at different points. These solutions have quantitatively different behaviour from the one found above. For example, the solution shown in figure 7.11 has the minimum placed at $(\eta, f) = (0, 0)$. Again, a four-term series expansion is used to find the solution through the minimum and then the Runge-Kutta scheme is used to find the solutions from the end-points of the series which are located at $\eta = -0.1$ and $\eta = 0.1$. In this case, the analytical solution is exactly $f = \Gamma\eta^2$ with $\Gamma = c_0^2\nu^{-2}$ which is symmetric about the origin: see figure 7.13. Therefore this case corresponds to the situation where grains separate into regions of equal density.

Another example is to find the solution when the minimum is placed at $(\eta, f) = (-2, 0)$, as shown in figure 7.14. Again we see an asymmetric solution; to the left

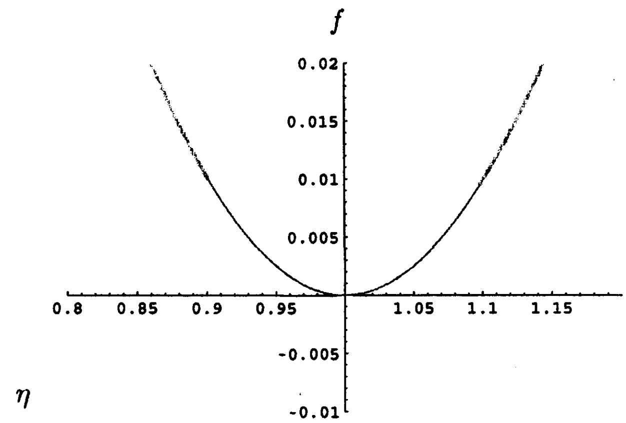

Figure 7.5: This plot shows the solution near the minimum for three different step lengths; $h = 0.0001$, $h = 0.001$, and $h = 0.01$. All three coincide and consequently all three match well with the series expansion through the minimum.

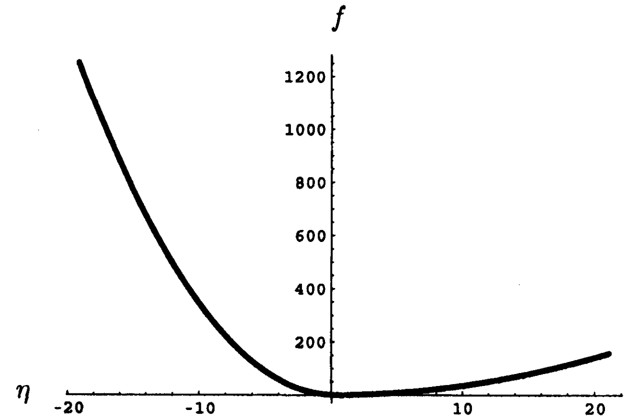

Figure 7.6: Plotted above is the full solution for three different lengths of the series expansion. A series expansion is used to find the solution between $\eta = [0.9, 1.1]$, $\eta = [0.99, 1.01]$ and $\eta = [0, 2]$ in each case. All three appear to coincide virtually exactly. Figures 7.2, 7.7 and 7.8 show an enlargement of the solutions near the origin.

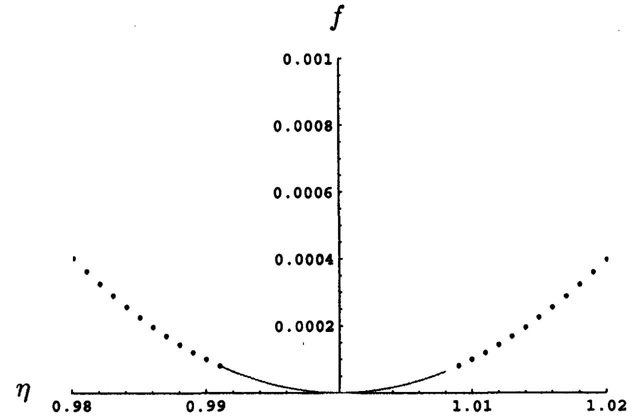

Figure 7.7: Shown above is an enlargement of the solution near the minimum when a series expansion with four terms is used between $\eta = [0.99, 1.01]$.

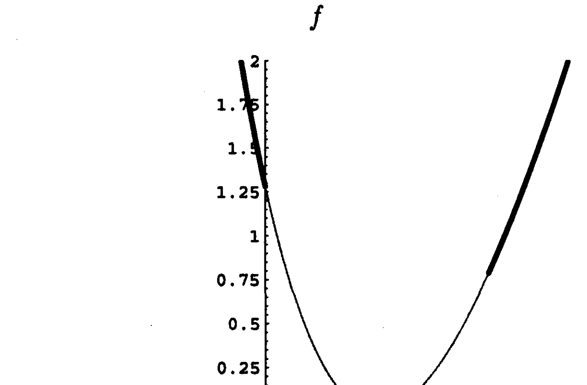

Figure 7.8: Shown above is an enlargement of the solution near the minimum when a series expansion with four terms is used between $\eta = [0, 2]$.

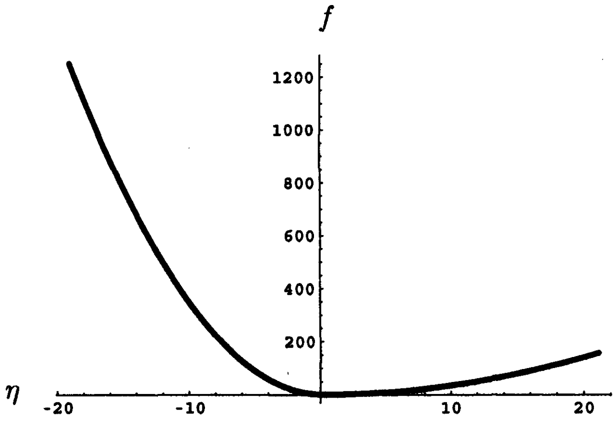

Figure 7.9: Plotted above is the full solution for two cases: one with a two-term series expansion and the other with a four-term series expansion. Both solutions are virtually the same. Figure 7.10 shows an enlargement of the two-term solution near the origin.

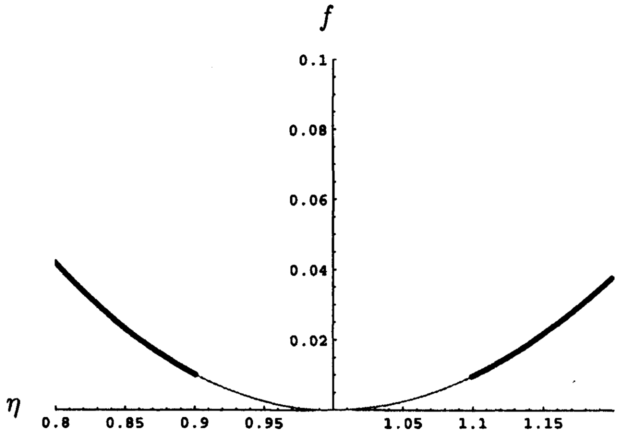

Figure 7.10: Shown above is a close-up of the solution near the minimum when a series expansion with two terms is used between $\eta = [0.9, 1.1]$. c.f. figure 7.2

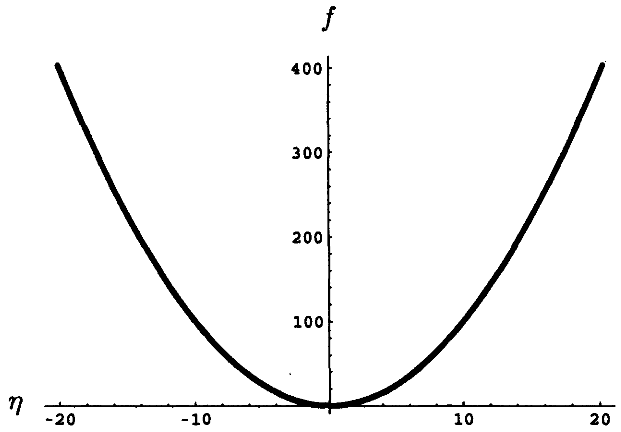

Figure 7.11: The solution to (7.1) for when the minimum is located at the origin. A step size of $h = 0.001$ was used and a four term series expansion was used to find the solution through the minimum. An enlargement of this region is shown in figure 7.12. The grains separate into two regions of equal density.

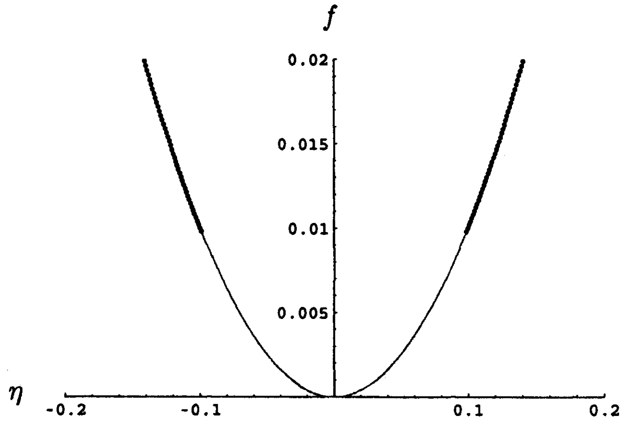

Figure 7.12: Once more, the series expansion allows the solution to pass through the minimum.

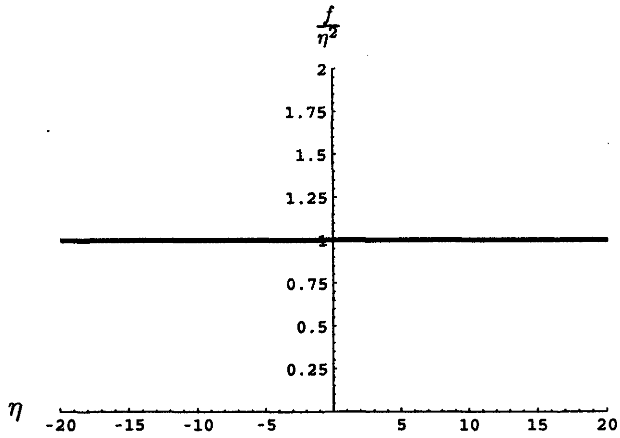

Figure 7.13: The solution in figure 7.11 is divided by η^2 and is equal to a constant everywhere. This is the exact solution, $f = \Gamma\eta^2$ with $\Gamma = c_0^2\nu^{-2} = 1$.

of the minimum f increases only to relatively small values, whereas to the right of the minimum the solution increases relatively rapidly to large values of f. We pay particular note to the way in which the curve seems to tend to a small constant for a large distance to the left of the minimum before beginning to increase. This can be explained analytically as in 7.2.5 later. Once more the series expansion is shown enlarged, in figure 7.15, and is seen to sensibly take the solution through the minimum and match well with the solutions from the Runge-Kutta schemes. Also figure 7.16 shows that the numerical solution does indeed display the expected behaviour as $\eta \rightarrow \pm\infty$.

Before a physical interpretation of the results is given, and before conclusions are drawn about the local viscous $c(\rho)$ law for grains separating at low density, we move on to seek analytical solutions.

7.2.5 Analytical solution

A solution is now sought in the form

$$f = \Gamma\eta^2 + \epsilon\tilde{f} + \dots , \tag{7.36}$$

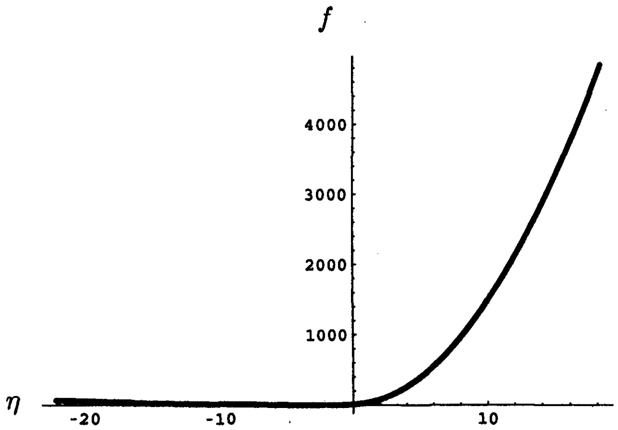

Figure 7.14: The solution to (7.1) when the minimum is located at $(\eta, f) = (-2, 0)$. Again we see an asymmetric solution; to the left of the minimum f increases only to relatively small values, whereas to the right the solution rapidly increases to large values of f. The solution appears to have a large region where f remains constant, a feature to which reference is made in section 7.2.5. For the above solution a step size of $h = 0.001$ was again used, as was a four term series expansion through the minimum. The solution near the minimum is enlarged in figure 7.15.

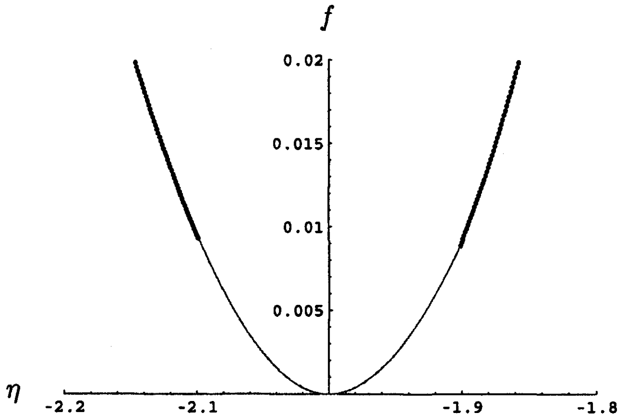

Figure 7.15: An enlargement near the minimum of the solution in figure 7.14 is shown. The thin line is the series expansion through the minimum and the thicker lines are the solutions from the Runge-Kutta schemes.

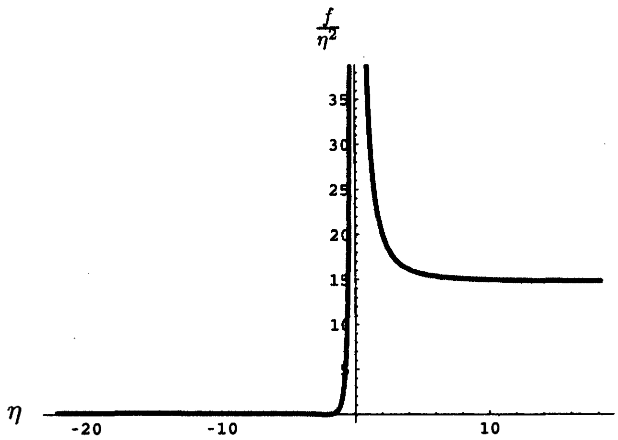

Figure 7.16: The solution divided by η^2 tends to a constant for large values of η, as expected from looking at equation (7.1) in this limit.

which from (7.1) yields

$$\nu\left(2\Gamma+\epsilon\tilde{f}''\right)-\left(\pm c_0\left(\Gamma\eta^2\right)^{-\frac{1}{2}}\left(1-\frac{\epsilon\tilde{f}}{2\gamma\eta^2}\right)-\frac{\eta}{2}\right)\left(2\Gamma\eta+\epsilon\tilde{f}'\right)$$
$$-\left(\Gamma\eta^2+\epsilon\tilde{f}+..\right)=0. \quad (7.37)$$

Thus, at leading order, the equation

$$2\Gamma\nu-\left(\pm\frac{c_0\Gamma^{-\frac{1}{2}}}{|\eta|}-\frac{\eta}{2}\right)(2\Gamma\eta)-\Gamma\eta^2=0 \quad (7.38)$$

has to be satisfied, resulting in

$$\Gamma=\left(\frac{c_0}{\nu}\right)^2 \quad (7.39)$$

where we have used the fact that $\left(\eta^2\right)^{\frac{1}{2}}=|\eta|$. The result (7.39) agrees with what we had earlier in (7.5).

At $O(\epsilon)$ the differential equation

$$\nu\tilde{f}''-\left(\frac{\nu}{\eta}-\frac{\eta}{2}\right)\tilde{f}'+\left(\frac{\nu}{\eta^2}-1\right)\tilde{f}=0 \quad (7.40)$$

is obtained. Since for small η the equation can be approximated as

$$\nu\tilde{f}''-\frac{\nu}{\eta}\tilde{f}'+\frac{\nu}{\eta^2}\tilde{f}=0, \quad (7.41)$$

it can be seen by substitution that locally

$$\tilde{f} \approx A\eta + B\eta\ln\eta \quad \text{for small} \quad \eta. \tag{7.42}$$

Consequently,

$$f \approx \Gamma\eta^2 + \epsilon\left(A\eta + B\eta\ln\eta\right). \tag{7.43}$$

Notice that if $\eta = O(\epsilon)$ then the first term is $O\left(\epsilon^2\right)$, as is the second term to within a logarithm. The value of B depends on the behaviour in an inner region studied below, where two types (I, II) of solution are found. Type I leads clearly to the requirement $B = 0$ and we have that mainly in mind. If B is non-zero on the other hand then ϵ in (7.36) can be replaced by $\frac{\epsilon}{\ln\epsilon}$, to account for the change $\ln\eta \rightarrow \ln\epsilon + O(1)$ in the logarithmic term when η becomes $\epsilon\xi$ with $\xi \sim 1$ in the inner region, and the following working remains unaltered.

Type I. In the inner region

$$\eta = \epsilon\xi \quad \text{and} \quad f = \epsilon^2 F(\xi) + \ldots \tag{7.44}$$

with ξ, F of order unity and

$$\frac{df}{d\xi} = \epsilon F' \quad \text{and} \quad \frac{d^2 f}{d\xi^2} = F'', \tag{7.45}$$

giving, from equation (7.1),

$$\nu F'' - \left(\pm\frac{c_0}{\epsilon F^{\frac{1}{2}}} - \frac{\xi}{2}\right)\epsilon F' - \epsilon^2 F = 0 \tag{7.46}$$

where a prime denotes differentiation with respect to ξ. Consequently, at leading order the nonlinear ordinary differential equation

$$\nu F'' \pm \frac{c_0}{F^{\frac{1}{2}}} F' = 0 \tag{7.47}$$

must be solved.

Integrating once gives

$$\nu F' \mp c_0 F^{\frac{1}{2}} = k_1 \tag{7.48}$$

where k_1 is a constant of integration. Then we multiply by $\frac{d\xi}{dF}$ and solve the resulting equation,

$$\nu = \left(k_1 \pm 2c_0 F^{\frac{1}{2}}\right)\frac{d\xi}{dF}, \tag{7.49}$$

for ξ as a function of F and invert.

Consider

$$\nu \int \frac{dF}{k_1 \pm 2c_0 F^{\frac{1}{2}}} \equiv I.$$

Letting $u = \pm F^{\frac{1}{2}}$ and then making the substitution $s = k_1 + 2c_0 u$ gives

$$I = \pm \frac{\nu}{2c_0^2} \int 1 - \frac{k_1}{s} ds.$$

Hence, the solution for ξ is

$$\xi + k_2 = \frac{\nu}{2c_0^2}\left(k_1 \pm 2c_0 F^{\frac{1}{2}} - k_1 \ln\left|k_1 \pm 2c_0 F^{\frac{1}{2}}\right|\right) \tag{7.50}$$

where k_2 is another constant of integration.

It can be seen from (7.50) that at large $|\xi|$ the asymptote $F \sim d_1\xi^2 + d_2\xi\ln\xi + O(\xi)$ is self-consistent, with $d_1 = \left(\frac{c_0}{\nu}\right)^2$ and $d_2 \propto k_1$. The contribution d_2 or k_1 here plays a key role.

We are now required to invert this solution to find $F(\xi)$ and then match F with the outer region where the $f(\eta)$ solution is valid. Two solution types are found: one (I) in which the shape of the solution is parabolic, and the other (II) in which the log branch can be included and the solution has a large region where F tends to a constant.

Type I has $k_1 = 0$ and the solution for F simply follows as

$$F = \left(\frac{c_0}{\nu}\right)^2 (\xi + k_2)^2. \tag{7.51}$$

Continuing to match this solution with the outer-layer of (7.43) yields

$$\epsilon^2 \left(\frac{c_0}{\nu}\right)^2 (\xi + k_2)^2 \sim \Gamma\eta^2 + \epsilon A\eta \tag{7.52}$$

with $B = 0$. That is,

$$\left(\frac{c_0}{\nu}\right)^2 \eta^2 + 2\epsilon\eta k_2 \left(\frac{c_0}{\nu}\right)^2 + \epsilon^2 \left(\frac{c_0}{\nu}\right)^2 k_2 \sim \Gamma\eta^2 + A\epsilon\eta + \ldots \tag{7.53}$$

Therefore,

$$\left(\frac{c_0}{\nu}\right)^2 \eta^2 = \Gamma\eta^2, \tag{7.54}$$

which we know to be true already since $\Gamma = \left(\frac{c_0}{\nu}\right)^2$. Also, from the order epsilon term,

$$A = 2k_2\Gamma \tag{7.55}$$

and the $\epsilon^2\Gamma k_2$ term must balance with the undetermined $O\left(\epsilon^2\right)$ term on the right-hand side.

Hence,

$$f = \Gamma\eta^2 + \epsilon\left(2k_2\Gamma\eta\right) + O\left(\epsilon^2\right) \tag{7.56}$$

and

$$F = \epsilon^2\Gamma\left(\frac{\eta}{\epsilon} + k_2\right)^2. \tag{7.57}$$

This solution is therefore seen to correspond to an origin shift.

Let us now consider what happens if k_1 is non-zero. Recall from equation (7.50) that ξ grows like $F^{\frac{1}{2}}$ for large F. In order for ξ to be a smooth function of F valid for all ξ the solution in the small F region must connect the two branches of the $+\sqrt{F}$ and $-\sqrt{F}$ curve. Therefore there must somewhere exist a turning point with $\frac{d\xi}{dF^{\frac{1}{2}}}$ infinite. Since

$$\frac{d\xi}{dF^{\frac{1}{2}}} = \frac{2c_0^2}{\nu}\left(\pm 2c_0 \mp \frac{2c_0k_1}{k_1 \pm 2c_0F^{\frac{1}{2}}}\right) \tag{7.58}$$

is to be infinite, at such a turning point

$$F^{\frac{1}{2}} = \mp\frac{k_1}{2c_0}. \tag{7.59}$$

However, for this value of $F^{\frac{1}{2}}$, $\xi\left(F\right)$ is singular. In consequence a solution with a minimum of F at finite ξ does not exist if k_1 is non-zero and if $B = 0$. So $k_1 = 0$ for this particular shape of the $\xi\left(F\right)$ curve. See figure 7.17.

Type II. An altogether different type of solution, which includes a log branch, is valid if the shape of the $\xi\left(F\right)$ curve is of the form of that sketched in figure 7.18. We now wish to see if the log branch in the inner region allows a single-valued solution. The log branch is to send f toward zero at the end away from the inner region (where ξ is large and negative), and then it is possible to match this with f as $\eta \sim \epsilon^{-1}$ into an outer region.

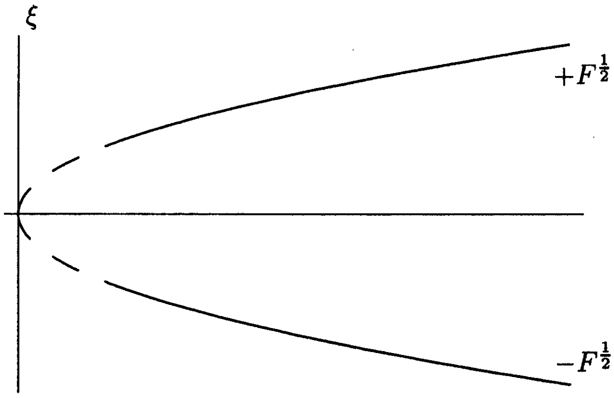

Figure 7.17: Sketched above is $\xi(F^{\frac{1}{2}})$. For a smooth solution the $\pm F^{\frac{1}{2}}$ branches (solid lines) must be connected and so there must exist a turning point with $\frac{d\xi}{dF} = \infty$. This cannot be satisfied if $k_1 \neq 0$ and $B = 0$.

In this case $c_0 > 0$ since $F' > 0$. Hence equation (7.50) can be written as

$$\xi = \frac{\nu}{2c_0^2}\left(-\hat{k}_1 + 2cF^{\frac{1}{2}} + \hat{k}_1 \ln\left|-\hat{k}_1 + 2c_0F^{\frac{1}{2}}\right|\right) - k_2 \tag{7.60}$$

where $\hat{k}_1 = -k_1$ and $\hat{k}_1 > 0$. Therefore, as $F^{\frac{1}{2}} \longrightarrow \frac{\hat{k}_1}{2c_0}$, $\xi \longrightarrow -\infty$ with $\frac{d\xi}{dF^{\frac{1}{2}}} \longrightarrow \infty$. That is to say, the inclusion of the log branch allows a long flat inner-region where F (essentially the density) tends to a constant. The solution is sketched in figure 7.18.

The solution in the inner region must now be matched with the outer solution as $\eta \longrightarrow O\left(\epsilon^{-1}\right)$. We match with $\eta = O\left(\epsilon^{-1}\right)$ because the inner solution has a long, flat region with $\xi \longrightarrow -\infty$ as has just been demonstrated. Far to the left, after the region of small density, f starts to increase to large values (as this makes sense physically for a separating region). Consequently, $f' < 0$ here and so $c_0 < 0$. Therefore, the $-c_0$ case is chosen and putting $\zeta = \epsilon\eta$ is appropriate, corresponding to $\xi = \epsilon^{-2}\zeta$. As the solution leaves the inner region and enters the $\eta = O\left(\epsilon^{-1}\right)$ region $f = \epsilon^2 F$ must still be satisfied. Let $f \sim \epsilon^2 \tilde{F}(\zeta)$ in this region.

Note also that scale ϵ^{-1} has been chosen because the solution must increase to large values far to the left with $\tilde{F}$ parabolic, to match with the parabolic behaviour in the outer region. If ϵ^{-1} is chosen then equation (7.62) below is satisfied, which

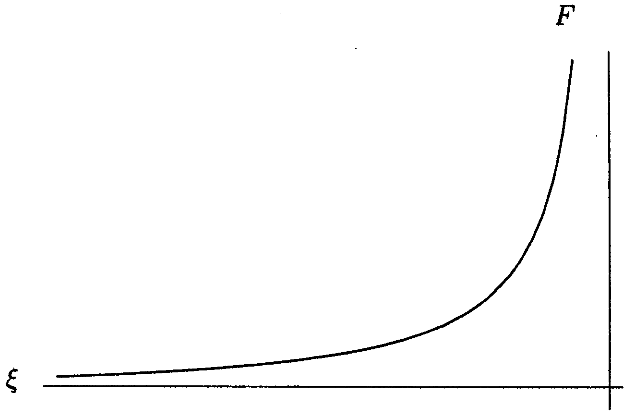

Figure 7.18: Sketched above is F as a function of ξ. It is possible for F to tend to a constant at one end if the log term is included. This may then match with f as $\eta \rightarrow O(epsilon^{-1})$.

eventually results in a quadratic solution for $\tilde{F}$ as required. Thus equation (7.1) can be written as

$$\epsilon^4 \nu \tilde{F}'' - \left(-\frac{c_0 \epsilon^2}{\tilde{F}^{\frac{1}{2}}} - \frac{\zeta \epsilon^2}{2} \right) \tilde{F}' - \epsilon^2 \tilde{F} = 0 \tag{7.61}$$

where a prime denotes differentiation with respect to ζ.

At leading order the solution to

$$\left(\frac{c_0}{\tilde{F}^{\frac{1}{2}}} + \frac{\zeta}{2} \right) \tilde{F}' - \tilde{F} = 0 \tag{7.62}$$

must be found. Multiplying by $\frac{d\zeta}{dF}$ and a little rearranging gives

$$\tilde{F}^{-\frac{1}{2}} \frac{d\zeta}{d\tilde{F}} - \frac{\zeta}{2\tilde{F}^{\frac{3}{2}}} = c_0 \tilde{F}^{-2}. \tag{7.63}$$

Integrating once yields

$$\tilde{F}^{\frac{1}{2}} \zeta = -c_0 + C\tilde{F} \tag{7.64}$$

after a minimal amount of manipulation; C is a constant of integration. The resulting equation is simply a quadratic for $\tilde{F}^{\frac{1}{2}}$ and the standard formula reveals

$$\tilde{F}^{\frac{1}{2}} = \frac{\zeta \pm \sqrt{\zeta^2 + 4Cc_0}}{2C}. \tag{7.65}$$

Squaring shows that

$$\tilde{F} = \frac{\zeta^2 + 2Cc_0 \pm \zeta\sqrt{\zeta^2 + 4Cc_0}}{2C^2}. \tag{7.66}$$

The solution must now match with $\Gamma\eta^2$ as $\zeta \to -\infty$ and with $\frac{\hat{k}_1^2}{4c_0^2}$ as $\zeta \to 0^-$. As $\zeta \to -\infty$ we must choose the positive square root so the solution is non-trivial. The matching condition then results in

$$\epsilon^2 \frac{\zeta^2}{C^2} = \Gamma\eta^2 + ... \tag{7.67}$$

Since $\zeta = \epsilon\eta$ then,

$$\epsilon^4 \frac{\eta^2}{C^2} = \Gamma\eta^2 + ... \tag{7.68}$$

Therefore C can be found by matching with the (as yet undetermined) $O\left(\epsilon^4\right)$ on the right-hand side of (7.68). As $\zeta \to 0^-$, matching requires that

$$\epsilon^2 \frac{\hat{k}_1^2}{2c_0^2} = \epsilon^2 \frac{c_0}{C^2} \tag{7.69}$$

so

$$\hat{k}_1 = \frac{\sqrt{2c_0^3}}{C}. \tag{7.70}$$

A solution of type II is allowed, then, and the constants can be found by matching as above. In fact, a numerical example of this type of solution was seen in figure 7.14.

7.2.6 Physical interpretation of solutions and conclusions.

By modifying the fundamental diagram to include a *representative* local viscous law we see that physically sensible solutions are obtained for the case of separating grains at low density for small times and order one viscosity.

In the solutions presented above the condition $f = 0$ must be satisfied at the centre of the separating region. That is, the density must always be zero in the centre of the separating region. This agrees perhaps with physical intuition and also fits well with results from the idealised inviscid case.

Furthermore, the solutions can be asymmetric about the origin. This corresponds to grains moving apart, possibly at different speeds, into regions of differing density. It is important that the continuum model allows this kind of solution as it was seen in numerical simulations where clusters of different sizes develop.

We found both analytically and numerically that a large region of low density can evolve between two separating regions: see figure 7.14 and the discussion at the end of section 7.2.5. Again, one would expect this to occur for some cases of separating regions and also we recall that numerical simulations had some large regions that were devoid of grains.

Finally, an origin shift of the centre of the separating region was possible i.e. the grains do not have to separate about a fixed point, which is also a physically sensible result.

Consequently, it seems reasonable to conclude for cases of separating grains that the $q \sim \rho^{\frac{3}{2}}$ law from the inviscid case can be changed locally to a viscous $q \sim \rho^{\frac{1}{2}}$ law.

The question of whether the same be done for colliding grains at the other end of the $Q(\rho)$ curve in the neighbourhood of $\rho = \rho_m$ is investigated in the next section.

7.3 Viscous clashing

7.3.1 Introduction

Cases which drive the solution to the high density end of the $Q(\rho)$ curve and the branch switch there are now considered. We investigate the possibility of introducing a similar viscous $Q(\rho)$ law at the high density endpoint. The earlier stated qualifications about the empiricism of the approach also apply here. Branch-switching at the high density endpoint physically corresponds to colliding grains.

A viscous region of small size $\epsilon \ll 1$ is therefore introduced in the neighbourhood of $\rho = \rho_M$, where ρ_M denotes the maximum (jammed) density. Here $q = \pm\epsilon\,(\rho_M - \rho)^{\frac{1}{2}}$ locally. This matches into the inviscid part of the curve where $q = \pm(\rho_M - \rho)^{\frac{3}{2}}$ locally: if $\rho \sim \rho_M - \epsilon$ then $q \sim \epsilon^{\frac{3}{2}}$ in both regions and therefore they match. Also $c = q' \sim \epsilon^{\frac{1}{2}}$. These power laws are chosen by the same reasoning as in section 7.1.

In the inviscid analysis, the wavespeed c is close to zero in the vicinity of ρ_M. The $\rho = \rho_M$ point itself is stationary. The flux q is also small in this neighbourhood. Hence, if a particular region has an initial density close to ρ_M the characteristics will not travel far from this point. Therefore the viscous part is valid for a small region near $\rho = \rho_M$; so $x << 1$. We wish also to find solutions for order one time. (N.B. in the separating case a solution valid for order one viscosity and small time was found. Conversely, we seek here solutions valid for all time but only small viscosity). Therefore we choose the scalings $t \sim 1$ and $x << 1$ alongside $\rho \sim \epsilon$, $q \sim \epsilon^{\frac{3}{2}}$ and $c \sim \epsilon^{\frac{1}{2}}$.

Balancing these terms in the continuum equation (6.1),

$$\rho_t + c\rho_x = \nu\rho_{xx}, \tag{7.71}$$

yields in terms of orders of magnitude

$$\frac{\epsilon}{t} + \frac{\epsilon^{\frac{3}{2}}}{x} = \frac{\nu\epsilon}{x^2}. \tag{7.72}$$

Therefore $x \sim \epsilon^{\frac{1}{2}}$ and $\nu \sim \epsilon$.

Note that $\nu \sim \epsilon$ is clearly a central case. If ϵ were smaller, then the $q \sim \rho^{\frac{3}{2}}$ law would hold true for almost all (q, ρ) and we have seen in previous computations that this poses a difficulty.

7.3.2 Derivation of the equation for the high density viscous region

Given the above scalings, we now put

$$x = \nu^{\frac{1}{2}}X, \tag{7.73a}$$

$$\rho = \rho_M - \nu P, \tag{7.73b}$$

$$c = \nu^{\frac{1}{2}}C, \tag{7.73c}$$

$$q = \nu^{\frac{3}{2}}Q, \tag{7.73d}$$

where X, P, C and Q are all order one. It is important to note that $c = \frac{dq}{d\rho} = \frac{dq}{dQ}\frac{dP}{d\rho}\frac{dQ}{dP}$, i.e. $c = -\nu^{\frac{1}{2}}\frac{dQ}{dP}$ and therefore $C = -\frac{dQ}{dP}$. Now $\frac{\partial}{\partial x} = \nu^{-\frac{1}{2}}\frac{\partial}{\partial X}$ and $\frac{\partial^2}{\partial x^2} = \nu^{-1}\frac{\partial^2}{\partial X^2}$. So equation (7.71) becomes

$$P_t + CP_X = P_{XX}. \tag{7.74}$$

Letting q be a representative linear combination of the viscous and inviscid laws results in

$$q = \pm \left(A\epsilon \left(\rho_M - \rho\right)^{\frac{1}{2}} + B \left(\rho_M - \rho\right)^{\frac{3}{2}} \right), \tag{7.75}$$

where A and B are (positive) constants. Hence

$$c = \pm \left(-A\frac{\epsilon}{2} \left(\rho_M - \rho\right)^{-\frac{1}{2}} - \frac{3}{2}B \left(\rho_M - \rho\right)^{\frac{1}{2}} \right), \tag{7.76}$$

i.e.

$$C = \pm \left(-\frac{A}{2}P^{-\frac{1}{2}} - \frac{3B}{2}P^{\frac{1}{2}} \right). \tag{7.77}$$

Choosing $A = 2$ and $B = \frac{2}{3}$ without loss of generality (the validity of this is quickly outlined in appendix F) gives

$$P_t \mp \left(P^{-\frac{1}{2}} + P^{\frac{1}{2}} \right) P_X = P_{XX}. \tag{7.78}$$

As a consequence of the multi-valued wavespeed, we do not solve (7.78) but instead invert and solve the equation for $Q\left(x,t\right)$ with $P = P\left(Q\right)$. Since the $P = P\left(Q\right)$ relation is single-valued and general solutions may be found more easily. This approach, and the approach of section 7.3.4, is reminiscent to that of Li et al. [37] in which the authors examine the intrusion of normal pressure gradients in near-wall dynamics of transitional-turbulent boundary layers.

We have

$$C = \mp \left(P^{-\frac{1}{2}} + P^{\frac{1}{2}} \right). \tag{7.79}$$

Therefore

$$Q = \pm \left(2P^{\frac{1}{2}} + \frac{2}{3}P^{\frac{3}{2}} \right) + \text{constant}. \tag{7.80}$$

Since $Q = 0$ at $\rho = \rho_M$, i.e. at $P = 0$, the constant is equal to zero. Consequently, since we take positive Q on the upper branch and negative Q on the lower branch,

$$2P^{\frac{1}{2}} + \frac{2}{3}P^{\frac{3}{2}} = \left|Q\right|, \tag{7.81}$$

a relation which needs to be inverted. Let $\lambda\sinh\theta = P^{\frac{1}{2}}$. Then

$$3\lambda\sinh\theta + \lambda^3\sinh^3\theta = \frac{3}{2}\left|Q\right|. \tag{7.82}$$

We require the left-hand side to be equal to $A\sinh 3\theta \equiv 3A\sinh\theta + 4A\sinh^3\theta$. This requires $\lambda = A$ and $\lambda^3 = 4A$. Therefore $A^3 - 4A = 0$ implying that $A = 0$ or $A = 2$. Taking $A = 2$ to avoid triviality yields

$$2\sinh 3\theta = \frac{3}{2}\left|Q\right|. \tag{7.83}$$

Therefore, after a little manipulation,

$$P = 4\sinh^2\left(\frac{1}{3}\sinh^{-1}\left[\frac{3}{4}\left|Q\right|\right]\right). \tag{7.84}$$

Writing the partial derivatives in (7.74) as $P_t = Q_t P_Q$, $P_X = Q_X P_Q$ and $P_{XX} = Q_{XX}P_Q + (Q_X)^2 P_{QQ}$ and further noting that $C = -Q_P$, gives

$$a_1 Q_t - Q_X = a_1 Q_{XX} + a_2 (Q_X)^2 \tag{7.85}$$

as the equation for $Q(X,t)$, where a_1 and a_2 are P_Q and P_{QQ} respectively. Explicitly

$$a_1 = \frac{\operatorname{sgn}(Q)}{\sqrt{1+\frac{9Q^2}{16}}}\sinh\left(\frac{2}{3}\sinh^{-1}\left[\frac{3}{4}\left|Q\right|\right]\right) \tag{7.86}$$

and

$$a_2 = -\frac{9Q\operatorname{sgn}(Q)}{16\left(1+\frac{9Q^2}{16}\right)^{\frac{3}{2}}}\sinh\left(\frac{2}{3}\sinh^{-1}\left[\frac{3}{4}\left|Q\right|\right]\right) + \frac{1}{2\left(1+\frac{9Q^2}{16}\right)}\cosh\left(\frac{2}{3}\sinh^{-1}\left[\frac{3}{4}\left|Q\right|\right]\right). \tag{7.87}$$

Observe that a_1 and a_2 have discontinuous higher derivatives. In terms of $P(X)$, P and at least its first two derivatives are continuous.

7.3.3 Numerical solution of equation (7.85)

Equation (7.85) is discretized as

$$a_1\left(\frac{Q_i - \bar{Q}_i}{\delta t}\right) - \left(\frac{Q_{i+1} - Q_{i-1}}{2\delta X}\right) = a_1\left(\frac{Q_{i+1} - 2Q_i + Q_{i-1}}{\delta X^2}\right) + a_2\left(\frac{\bar{Q}_{i+1} - \bar{Q}_{i-1}}{2\delta X}\right)^2 \tag{7.88}$$

where a_1 and a_2 are evaluated at the known time-step, as is the $(Q_x)^2$ term. A bar denotes the quantity at the known time-step, while absence of a bar denotes a quantity at the unknown time-step. The subscript i denotes the quantity at each spatial grid-point. The solution is then found by a usual finite-difference method.

Solutions are found on a number of grids to ensure they are accurate. The grid sizes used are $(\delta X, \delta t) = (10^{-1}, 10^{-3})$, $(10^{-2}, 10^{-5})$ and $(10^{-3}, 10^{-7})$. Figure 7.19 shows a solution for the above three grid sizes. There is excellent agreement between all three. All other solutions are found on a grid of $(\delta X, \delta t) = (10^{-2}, 10^{-5})$.

Figure 7.20 shows solutions for the case in which two regions collide symmetrically about a central point located at $x = 0.25$. Note in all solutions that we plot $\rho_m - P$ versus X to show the *local* change in the density through the clashing region. The viscosity has a value of $\nu = 0.001$. As time increases the hump shape spreads across the domain tending to produce a region of maximum (jamming) density. The boundary conditions in this case are consistent with a continual input of grains at a fixed density. The solutions were found for times of $t = 0.1$, 1.0 and 10.0.

Figure 7.21 shows solutions in which two regions collide asymmetrically about a particular point. Again the boundary conditions are consistent with a continual input of grains at a fixed density. The viscosity in this example has a value of $\nu = 0.1$. Solutions are plotted at times of $t = 0.1$, 1.0 and 10.0. Again a hump forms and spreads across the chute over time. In this case the growth of the hump is not isotropic; the density increases to higher values more rapidly to the left of the initial point of collision.

The boundary conditions used just are tentative however, namely $Q(X_L, t) = Q_L$, $Q(X_R, t) = Q_R$, with Q_L, Q_R arbitrary non-zero constants. In the next section we find the correct boundary conditions which correctly match solutions to equation (7.85) into an inviscid expansion fan.

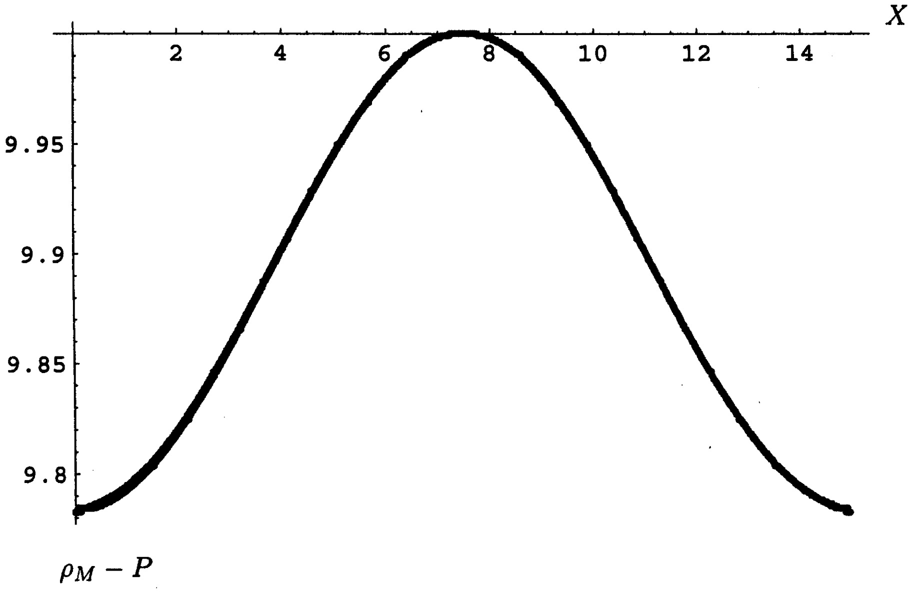

Figure 7.19: The plot shows the local deviation in the density ($\rho_M - P$) near the maximum at a time $t = 0.1$ for a number of different grids. The grid sizes used are $(\delta X, \delta t) = (10^{-1}, 10^{-3})$, $(10^{-2}, 10^{-5})$ and $(10^{-3}, 10^{-7})$. There is good agreement between all three curves. Recall that here, and in figures 7.20 and 7.21, $P \equiv \frac{(\rho_M - \rho)}{\nu}$ and $X \equiv \frac{x}{\nu^{\frac{1}{2}}}$ with ν small. Here $\nu = 0.001$.

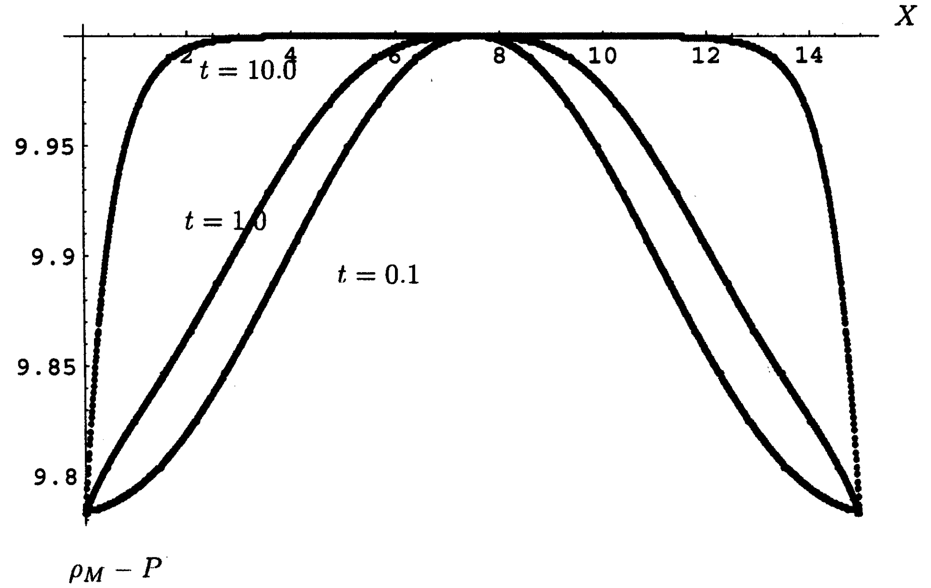

Figure 7.20: This figure shows local deviation of the density against position for a solution to equation (7.85) for various times. The initial condition was for grains to be continually colliding symmetrically about a particular point. A hump of large density appears and this spreads and increases over time. Here $\nu = 0.001$.

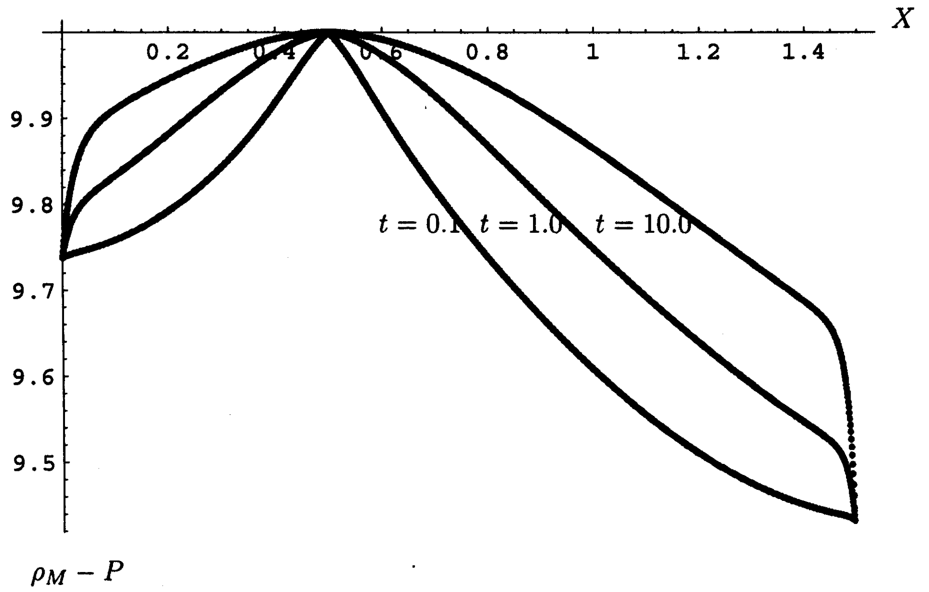

Figure 7.21: Another solution to equation (7.85) for various times is plotted above. In this example the initial condition was for grains to continually collide asymmetrically about a particular point. Again, a hump appears and spreads over time but the density increases to higher values more rapidly to the left of the initial point of collision. Here $\nu = 0.1$.

7.3.4 Finding the appropriate boundary conditions which correctly match the viscous clashing region with the inviscid bulk

We seek a similarity solution to equation (7.74) as $|X|$ tends to infinity, i.e. as the solution leaves the viscous clashing region and enters the inviscid bulk, in order to find the more appropriate boundary conditions for the numerical scheme (7.88). From equation (7.85) we see that we must balance $\frac{P}{t}$, $\frac{Q}{X}$ and $\frac{P}{X^2}$ as $Q \sim P^{\frac{3}{2}}$ and $|X| \to \infty$.

One choice could be $\frac{Q}{X} \sim \frac{P}{X^2}$, but this results in $P \sim X^{-2}$. This is a contradiction. As X increases, the solution should leave the inviscid region, so P should tend to large values, making $\nu^{\frac{1}{2}}P = O(1)$. Another choice is to balance $\frac{P}{t} \sim \frac{Q}{X}$. We wish this balance to hold true for all time, so t is order one. Therefore $P \sim X^2$ and $Q \sim X^3$.

Hence the solution of equation (7.74) is required at large X and order-one time with $P \sim X^2$ and $Q \sim X^3$. In this limit $C \sim P^{\frac{1}{2}}$ must be taken since this is appropriate in the inviscid region. Therefore we seek the solution to

$$P_t \mp P^{\frac{1}{2}} P_X = 0. \tag{7.89}$$

(As we shall see, the solution to this equation does in fact lead to the required $P \sim X^2$ and $Q \sim X^3$ behaviour.)

Put $P = r^2$ so

$$r_t \mp r r_x = 0. \tag{7.90}$$

Let $r = (t-t_0)^m f(\eta)$ with $\eta = \frac{(X-X_0)}{(t-t_0)^n}$. Balancing terms from the partial differential equation for r yields $r \sim \frac{X}{t}$. Therefore,

$$\frac{X}{t} \sim \frac{(t-t_0)^m (X-X_0)}{(t-t_0)^n} \tag{7.91}$$

and hence

$$n - 1 = m. \tag{7.92}$$

Finding the derivatives in terms of η in the standard way and substituting into (7.90) reveals the similarity equation

$$mf - n\eta f' \mp ff' = 0 \tag{7.93}$$

where a prime denotes differentiation with respect to η.

Now notice that the choice of $n = 1 \Rightarrow m = 0$ gives

$$f'(\mp f - \eta) = 0 \tag{7.94}$$

so $f' = 0$ or $f = \mp\eta$. For this choice of n, the $f = \mp\eta$ solution leads eventually to

$$P = \frac{(X - X_0)^2}{(t - t_0)^2} \tag{7.95}$$

which is the exact form of the expansion fan solutions we met previously (since this locally gives $C \sim \frac{X}{t}$ cf. equation (5.16)). Moreover, (7.95) is an exact solution to equation (7.89). Recall that $Q \sim P^{\frac{3}{2}}$. Thus

$$Q = -\frac{(X - X_0)^3}{(t - t_0)^3} \tag{7.96}$$

is the large X solution to equation (7.74) which matches into the expansion fan solutions which are obtained for colliding grains in the inviscid bulk. We have chosen the negative root so that initially Q is positive on the left of the chute and Q is negative on the right of the chute. This ensures that a clashing region occurs.

Therefore, if we wish to find a solution to equation (7.85) that matches into an expansion fan then the appropriate boundary conditions are:

$$Q\left(X = X_L, 0\right) = -\frac{(X_L - X_0)^3}{(t - t_0)^3}, \tag{7.97a}$$

$$Q\left(X = X_R, 0\right) = -\frac{(X_R - X_0)^3}{(t - t_0)^3}. \tag{7.97b}$$

In the computation we have arbitrarily chosen $X_0 = 0$ and $t_0 = 1$, a choice which will be discussed later in this section. Furthermore, X_L and X_R are the locations of the left-hand and right-hand edge of the viscous colliding region.

Therefore we now solve equation (7.85) by the numerical scheme (7.88) subject to the boundary conditions (7.97). We choose $X_L = -15$ and $X_R = 15$. Also, a grid size of $(\delta X, \delta t) = (10^{-2}, 10^{-5})$ is used again and the viscosity has the value $\nu = 0.001$.

Figure 7.22 shows solutions for $\rho(x,t)$ at various times (n.b. we show the plots in terms of the global co-ordinates $\rho(x,t)$, not the local coordinates $P(X,t)$). As time

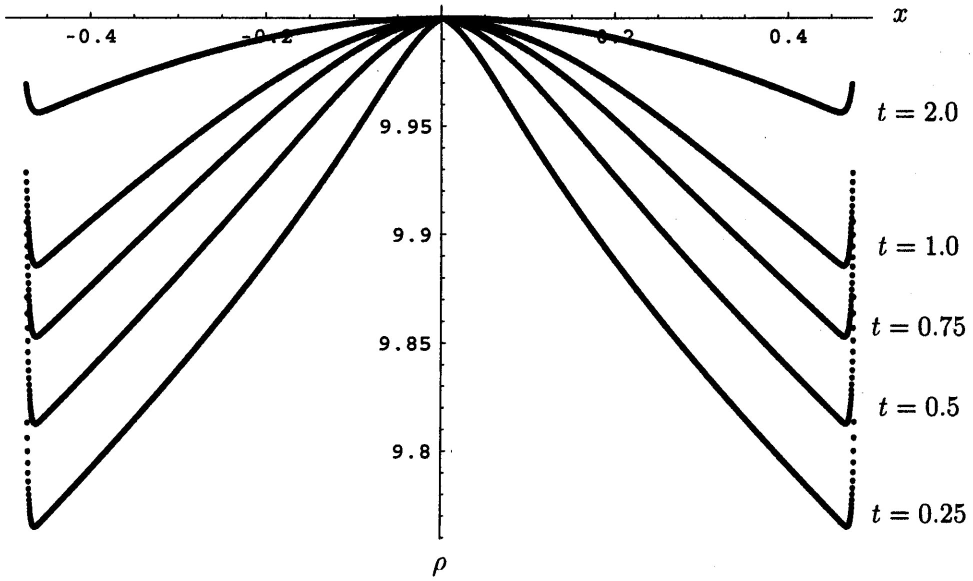

Figure 7.22: A solution is plotted for the initial condition in which grains do not continually collide, but instead match into an expansion fan. The hump spreads and increases over time and appears to be heading to a constant equal to the maximum (jamming) density.

increases, the hump spreads across the chute and the density increases. It appears as though the hump is tending to a constant equal to the maximum (jamming) density. At both sides of the plot there is a 'lip' that rises to a significantly higher density.

The presence of the 'lips' may appear peculiar at first, but it seems likely to be a consequence of imposing the arbitrary boundary conditions (7.97) on the problem. We recall that in the computation we set $t_0 = -1$, the idea being that the time-marched solution would tend toward the asymptotic form (7.95). The time-marched solution does indeed appear to head toward an asymptote of the same form but with a *different value of* t_0, and it then veers away from that asymptote 'at the last moment' in order to satisfy the particular boundary condition which we have imposed. Hence the 'lips' occur at the sides of the plot.

Such a view concerning the asymptote is supported by figures 7.23, 7.24 and 7.25. First, figure 7.23 shows solutions at t=2 for various values of t_0. Each curve has roughly the same trend in the core but the 'lips' at the sides vary for each value of t_0. Figure 7.24 shows two time-marched solutions at $t = 2$, one with $(X_L, X_R) = (-15, 15)$ and the other with $(X_L, X_R) = (-30, 30)$ (computed on the same grid) and both have $t_0 = -1$, alongside two plots of the asymptote (7.95), one with $t_0 = -1$ and the other with $t_0 = 0$. Regardless of the two different boundary conditions in the numerical scheme, both time-marched solutions appear to lie very close to the asymptote with $t_0 = 0$ (as well as to each other, as a check on grid effects). Similarly, figure 7.25 shows three time-marched solutions at $t = 2$, one with $t_0 = -1$, another with $t_0 = -0.2$ and a third with $t_0 = -0.5$ (all three have $(X_L, X_R) = (-15, 15)$), alongside two plots of the asymptote (7.95), one of which has $t_0 = 0$ and the other has $t_0 = -1$. Once more, regardless of the boundary conditions in the numerical scheme, all three time-marched solutions appear to lie very close to the asymptote which has $t_0 = 0$. Thus the solutions do indeed have the asymptotic form (7.95) with a particular (small) value of t_0 that seems to be independent of the value set in the boundary condition. The bulk or core of the solution develops its asymptote by itself, in a sense, a feature which is in line with the underlying characteristics of the inviscid limit being directed outwards with slope $\frac{dX}{dt} > 0$ for $X > 0$ and $\frac{dX}{dt} < 0$ for $X < 0$ from (7.89). The 'lips' would not occur if suitably adjusted boundary conditions were imposed of course, but the latter are unknown in advance and determining the corresponding value of t_0 is nontrivial; see for example a similar problem in Li et al. [37]. For small t the behaviour is similar to that of section 6.4; viz. there is a discontinuous start with matching between several layers.

7.3.5 Interpretation of solutions and conclusion

The introduction of a local viscous $Q(\rho)$ law at the high density cusp of the fundamental diagram has produced physically sensible results. Recall that in the previous numerical simulations of chapter 3 areas of densely packed grains were observed. This behaviour has also been seen in images provided by Sortex. In the solutions found above, we observe the growth of dense regions, symmetrically and asymmet-

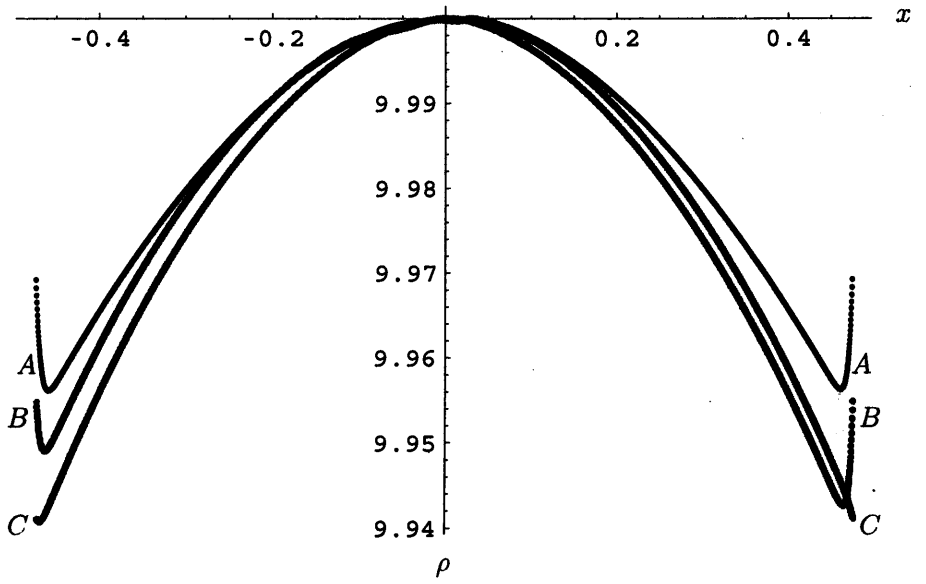

Figure 7.23: This figure shows the occurrence of the 'lips' for various values of t_0: A has $t_0 = -1$, B has $t_0 = -0.5$ and C has $t_0 = -0.2$. See the full discussion in the text.

rically, for a number of reasonable boundary conditions. Consequently, we can be fairly confident that the introduction of such a viscous law allows solutions to be found which are congruous with our understanding of the behaviour of grains involved in collisions.

The continuum model has now been seen to produce what are felt to be qualitatively sensible results for three special cases: the bulk inviscid behaviour from chapter 5, viscous separation and viscous clashing (at least for the cases investigated so far). In the last two cases, the fundamental diagram is modified as a consequence of the introduction of the introduction of the viscous dissipation term. Although this fundamental diagram cannot be entirely supported by physical arguments, physically sensible results are nevertheless obtained. The modifications therefore appear to be admissible. The next step is to develop a computational procedure for the continuum equation (6.1) for general cases which might involve any combination of the above three cases.

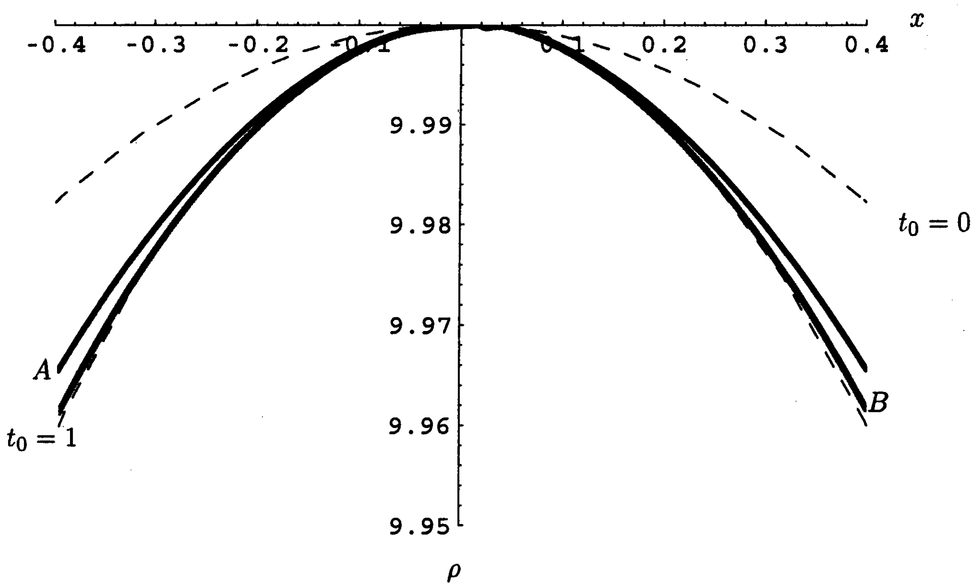

Figure 7.24: This figure shows two time-marched solutions (solid lines A and B) at t=2, alongside two asymptotes (dashed lines). Curve A corresponds to the computation which has $(X_L, X_R) = (-15, 15)$ and curve B to the one with $(X_L, X_R) = (-30, 30)$. The value of t_0 on the asymptote is shown adjacent to each curve. See the discussion in the text.

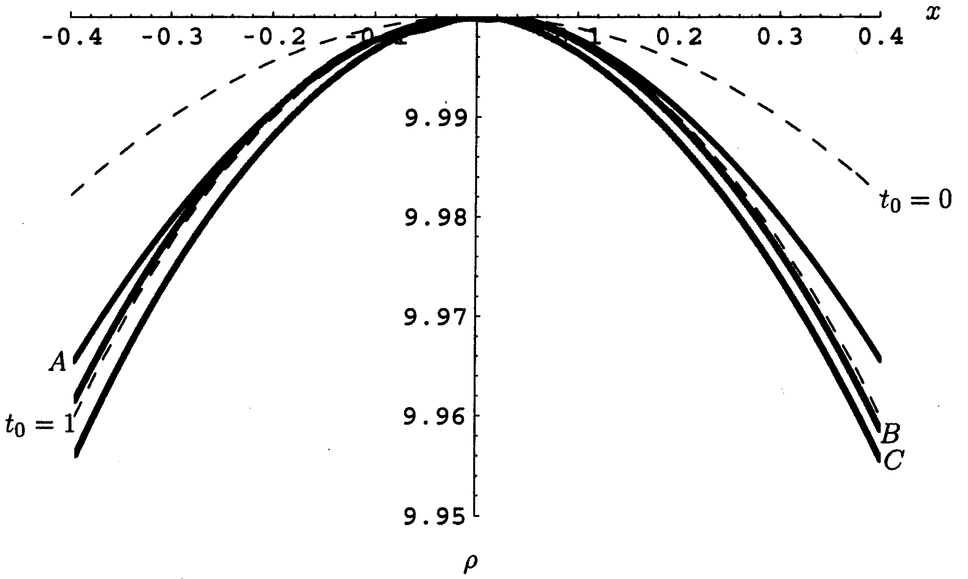

Figure 7.25: This figure shows three time-marched solutions (solid lines A, B and C) at t=2, alongside two asymptotes (dashed lines). Curve A corresponds to the computation which has $t_0 = -1$, curve B to the one with $t_0 = -0.5$ and curve C to the one with $t_0 = -0.2$. The value of t_0 on the asymptote is shown adjacent to each curve. See the discussion in the text.

7.4 A general computational procedure

The problem of branch switching can be avoided in many cases by writing the continuum equation in terms of polar co-ordinates. In so doing here, however, we choose to simplify the flux-density relationship because solving for the original fundamental diagram would lead to too complicated a function, as a first step. For simplicity we choose the fundamental diagram to be circular as an approximation to the 'proper' fundamental diagram determined in the preceding section. Although the motivation for doing so is to make the mathematics more tractable, we should obtain behaviour qualitatively similar to that of the complete model. Consequently,

$$q = a\sin(\theta) \tag{7.98}$$

and

$$\rho = a(1+\cos(\theta)) \tag{7.99}$$

where a is the radius of the circle with $a = \frac{\rho_m}{2}$ and θ is the angle, a function of position and time. Hence $\rho_t = \rho_\theta \theta_t$, $\rho_x = \rho_\theta \theta_x$, and $\rho_{xx} = \rho_\theta \theta_{xx} + \rho_{\theta\theta}(\theta_x)^2$. Note that $\rho_\theta = -a\sin(\theta)$ and $\rho_{\theta\theta} = -a\cos(\theta)$. Finally note that $c \equiv \frac{dq}{d\rho} = q_\theta \theta_\rho = -\cot(\theta)$. Therefore the continuum equation (6.1) becomes

$$\theta_t - \cot(\theta)\,\theta_x = \nu\theta_{xx} + \nu\cot(\theta)(\theta_x)^2, \tag{7.100}$$

a partial differential equation for the unknown function $\theta(x,t)$. It is assumed that $\theta(x,t)$ is a well behaved smooth function of x and t. It is tempting to think that when $\sin(\theta)$ is small boundary-layer like behaviour may occur. This is not so, however, as outlined in subsection 7.5.2.

We now solve this equation by a finite difference scheme. There are a number of different ways in which the equation can be discretized, depending on which terms are treated as unknown for the current time-step. Numerous schemes have been tried, but the one which appears to be most stable is the one in which the $\cot(\theta)$ terms and the $(\theta_x)^2$ term are evaluated at the previous time-level. Upwind or downwind differencing is chosen depending on the sign of $\cot(\theta)$ at the previous time-level.

Observe that at switching, where $\sin(\theta) = 0$, in effect the time derivative and the second derivative in x vanish from equation (7.100). This leaves, in view of the smoothness of the function,

$$\theta_x (\nu\theta_x + 1) = 0. \tag{7.101}$$

Therefore if θ is an integer multiple of π then we must impose either the condition $\theta_x = 0$ or $\theta_x = -\frac{1}{\nu}$. Which to choose? The former condition, $\theta_x = 0$, forces $\theta(x,t)$ to be maximal in x when $\sin(\theta) = 0$ and the density is either zero or at the jamming density, ρ_m. If $\theta(x,t)$ were to be at a maximum at these points then the density would approach the branch switch but would not actually be able to switch branches. In order to switch branches $\theta(x,t)$ must continually increase so that the density and the flux can 'circulate' around the fundamental diagram. Hence $\theta_x = 0$ is the inappropriate condition to impose and we must enforce $\theta_x = -\frac{1}{\nu}$. To ensure the latter does not introduce any discontinuities in the gradient, the initial condition is always chosen to satisfy it. Although this may seem as though there are too many boundary conditions, the problem is in fact not over-prescribed: see the discussion in section 7.5.1.

We employ the code to seek solutions up to large times and compare to the steady state solutions. The steady state may be regarded approximately as the density profile at the end of the chute. In section 7.5, large time solutions are sought which have $\rho = \rho_M$ at the boundaries x_L and x_R with $\rho_x|_{x_L,x_R} = 0$. This is in order to ensure that the flux $q - \nu\rho_x = 0$, which is the general condition at the boundaries (the condition we apply is actually a special case of this). If $\rho = \rho_M$ is chosen then $q = 0$ is immediately satisfied and so $\rho_x = 0$ must also hold true at the boundaries. Observe that $\rho = 0$ could also be chosen to ensure $q = 0$, but this choice is not investigated here as consequence of an argument from the inviscid model, see appendix D. The argument itself may have certain strengths and weaknesses, as discussed in the appendix, but in any case we do not study the $\rho = 0$ boundary condition in this thesis. Unfortunately, only a small number of solutions could be found despite a relatively large effort.

7.5 Steady states and solutions at large times

It is possible to examine the steady states analytically. The continuum equation can be written as

$$\rho_t + q_x = \nu \rho_{xx}. \tag{7.102}$$

Since the steady-state solution is being sought, the ρ_t term is now taken to be zero. Integrating the remaining terms once yields

$$q = \nu \rho_x - c_1 \tag{7.103}$$

where c_1 is a constant of integration which must necessarily be zero for the total flux to be zero, as mentioned below. Recall that in the present specific case $q(\rho)$ is circular and so

$$q = \pm\sqrt{\frac{\rho_M^2}{4} - \left(\rho - \frac{\rho_M}{2}\right)^2}, \tag{7.104}$$

where q is a circle of radius $\frac{\rho_M}{2}(= a)$, centred at $\frac{\rho_M}{2}$.

We consider only the case where the density profile is flat when $q = 0$, to ensure the flux is zero across the boundaries. If $\rho = \rho_M = 2a$ then $\theta = n\pi$ with n an even integer from equation (7.99). Therefore $\rho_\theta = 0$ and thus $\rho_x = 0$, provided θ_x is finite (since $\rho_x = \rho_\theta \theta_x$). The case of θ_x being infinite would result in non-zero flux at the boundaries. We have now from (7.103) that $c_1 = 0$. In other words, for zero flux at the boundaries we require $q - \nu\rho_x = 0$, since $q = 0$ also at the boundaries (so that the density is maximal there) we therefore must necessarily satisfy $\rho_x = 0$ and hence $c_1 = 0$. (For non-zero flux at the boundaries refer to subsection 6.5.2 in chapter 6, which deals with steady states for one-way flows away from the chute walls). Therefore,

$$\nu\rho_x = \pm\sqrt{\frac{\rho_M^2}{4} - \left(\rho - \frac{\rho_M}{2}\right)^2}. \tag{7.105}$$

Integrating, we can find that

$$\rho = a\left(1 + \sin\left(\frac{x - x_0}{\nu}\right)\right) \tag{7.106}$$

if the positive root is taken, or

$$\rho = a\left(1 + \cos\left(\frac{x - x_1}{\nu}\right)\right) \tag{7.107}$$

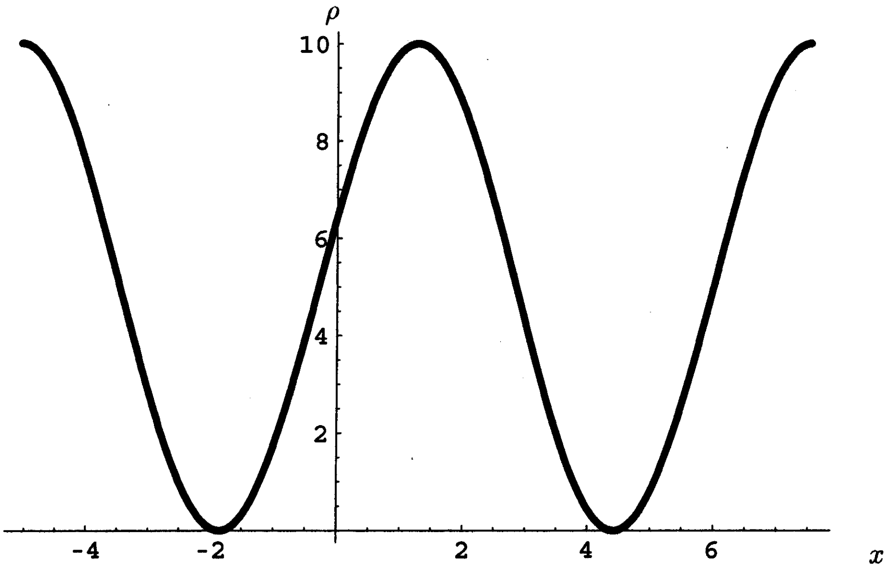

Figure 7.26: In the above figure, the solution is plotted together with the initial condition. The solution is shown at $t = 0.5, 1.0, ..., 4.5, 5.0$ and all curves appear to coincide with each other and with the initial condition. The initial condition is therefore seen to persist for all time, as one might expect.

if the negative root is taken, where x_0 and x_1 are constants of integration. The positive and negative roots correspond respectively to $q > 0$ and $q < 0$ and hence to the two branches of the fundamental diagram. Also $\rho =$ constant is a solution. Owing to the fact that $q = 0$ at $\rho = \rho_M$ and at $\rho = 0$ we see that $\rho = \rho_M$ and $\rho = 0$ could also be valid solutions. This is discussed further in subsection 7.5.2.

Steady states are now sought by time-marching, utilizing the finite difference scheme outlined at the beginning of the chapter. In each example, the viscosity takes the value $\nu = 1$. In the first instance, to test the code, the steady state is chosen to be the initial condition; it is found to persist for all time, as one might expect, see figure 7.26. This offers some encouragement about the accuracy of the numerical scheme. Next, an initial condition is chosen which resembles the steady state, but is slightly perturbed, or kinked, in two locations either side of the branch switch. Figure 7.27 shows the initial condition. Figure 7.28 shows the solution at $t = 0.01, 0.05, 0.1, 0.2, 0.5$ and 1. There is an artificial shift in the origin

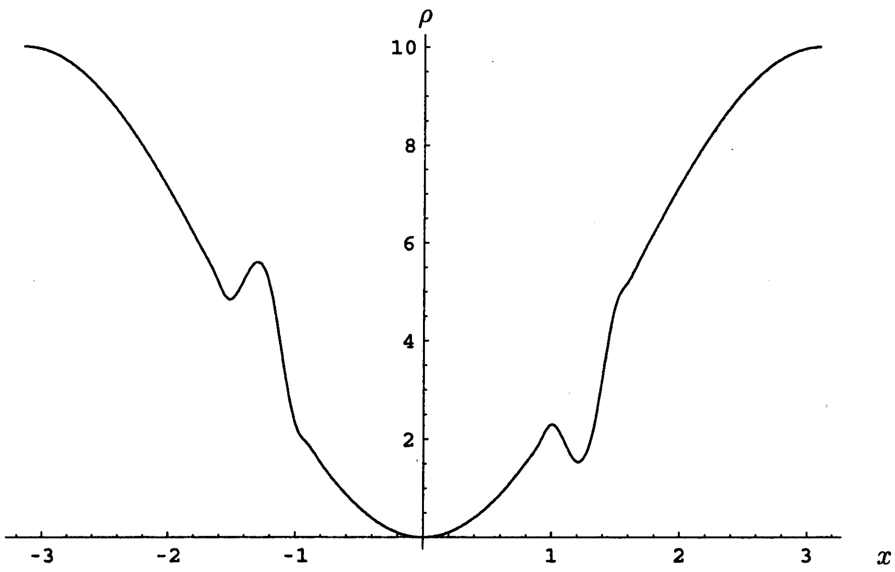

Figure 7.27: The initial condition shown here resembles the steady state except for being slightly kinked, although smooth. See also figure 7.28.

of each solution so that a proper comparison can be made. The kink is seen to disappear as time increases and then a steady state seems to appear. The apparent steady state resembles the sinusoidal steady state found in the analysis (7.106), (7.107). The solution at $t = 0.1$ has been found on three grid sizes in order to investigate the numerical accuracy. Figure 7.29 shows this solution on grids of size $(\delta x, \delta t) = (\sqrt{2} \times 0.01, 0.000001), (\sqrt{2} \times 0.01, 0.000002)$ and $(\sqrt{2} \times 0.01, 0.0000005)$. Some slight differences in solution can be seen to the right of the origin, but in general the agreement is quite close. Hence we can be reasonably confident in the accuracy of the numerical scheme. Unfortunately, it has not been possible to find any other steady states of this sort, in spite of a concerted hunt for them. One reason for this seems to be that a steady state with conserved mass will not evolve unless the initial condition starts with a precise mass. This is elaborated on immediately below.

The total mass M is given by

$$M = \int_{x_L}^{x_R} \rho dx \tag{7.108}$$

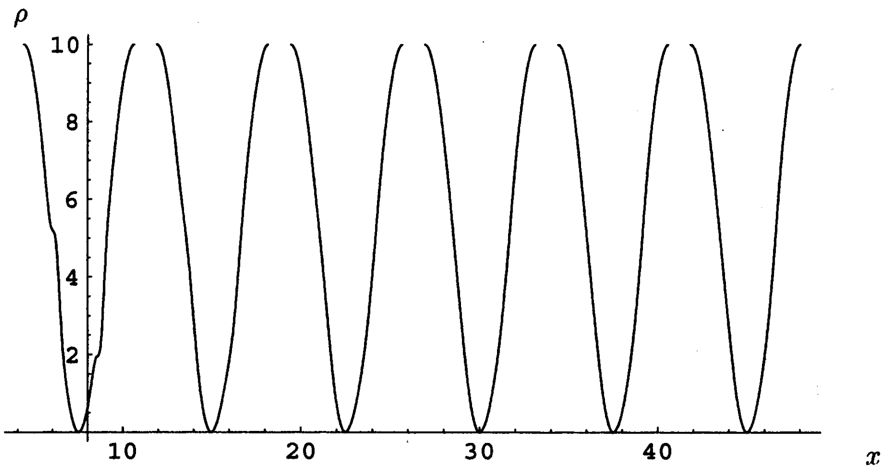

Figure 7.28: The solution that develops from the initial state of the previous figure is shown at $t = 0.01, 0.05, 0.1, 0.2, 0.5$ and 1. The kink disappears and a steady state appears to be reached which resembles the sinusoidal steady state found analytically. There is an artificial origin shift in each solution to aid ease of comparison.

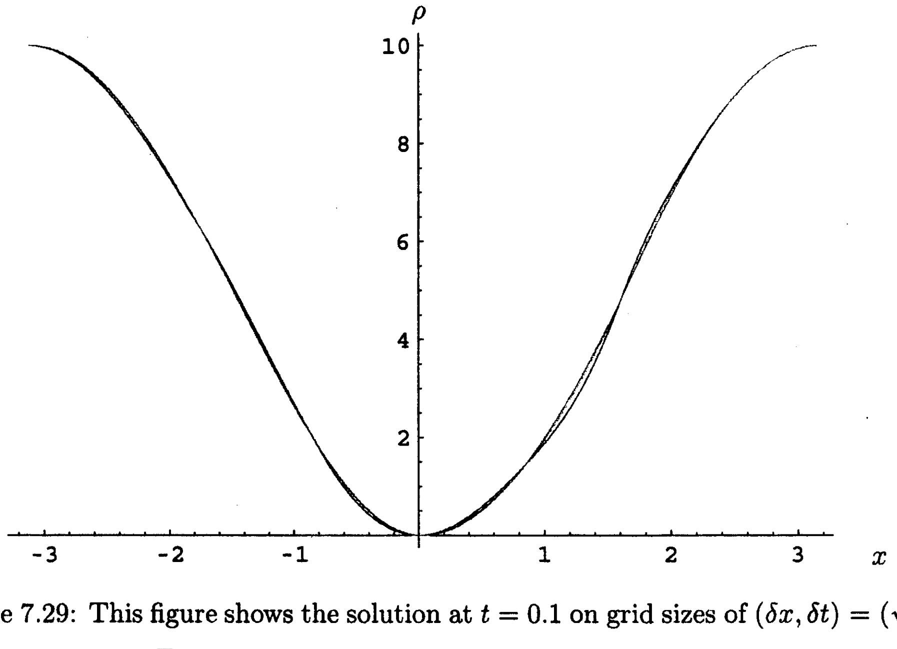

Figure 7.29: This figure shows the solution at $t = 0.1$ on grid sizes of $(\delta x, \delta t) = (\sqrt{2} * 0.01, 0.000001), (\sqrt{2} * 0.01, 0.000002)$ and $(\sqrt{2} * 0.01, 0.0000005)$. There is generally good agreement between each solution.

if there are walls located at $x = x_L$ and $x = x_R$. For the steady state with $\rho_x = 0$ at the walls we know that

$$q = \nu \rho_x, \tag{7.109}$$

from (7.103), and

$$q = \pm\sqrt{\frac{\rho_m^2}{4} - \left(\rho - \frac{\rho_m}{2}\right)^2}. \tag{7.110}$$

It is possible to split the domain into two regions, one region with $q < 0$ and $\rho \in [\rho_m, 0]$ on $x \in [x_L, 0]$ and the other with $q > 0$ and $\rho \in [0, \rho_m]$ on $x \in [0, x_R]$. Integrating (7.109) produces

$$\int_{x_L}^{0} dx = -\nu \int_{\rho_m}^{0} \frac{d\rho}{\sqrt{\frac{\rho_m^2}{4} - \left(\rho - \frac{\rho_m}{2}\right)^2}} \tag{7.111}$$

and

$$\int_{0}^{x_R} dx = \nu \int_{\rho_m}^{0} \frac{d\rho}{\sqrt{\frac{\rho_m^2}{4} - \left(\rho - \frac{\rho_m}{2}\right)^2}}. \tag{7.112}$$

This results in

$$[x]_{x_L}^{0} = -\nu \left[\frac{2}{\rho_m} \sin^{-1}\left(\frac{2}{\rho_m}\left(\rho - \frac{\rho_m}{2}\right)\right)\right]_{\rho_m}^{0} \tag{7.113}$$

and

$$[x]_{0}^{x_R} = \nu \left[\frac{2}{\rho_m} \sin^{-1}\left(\frac{2}{\rho_m}\left(\rho - \frac{\rho_m}{2}\right)\right)\right]_{0}^{\rho_m}. \tag{7.114}$$

Evaluating the above two expressions yields

$$x_L = -\frac{\nu\pi}{\rho_m} \tag{7.115}$$

and

$$x_R = \frac{\nu\pi}{\rho_m}. \tag{7.116}$$

Therefore the period of the steady-state is very precise, namely $\frac{2\nu\pi}{\rho_m}$. Hence the mass is precisely defined as

$$M = \int_{-\frac{\nu\pi}{\rho_m}}^{\frac{\nu\pi}{\rho_m}} \rho dx. \tag{7.117}$$

Next consider that

$$\frac{\partial}{\partial t}\int_{x_L}^{x_R} \rho dx + q(x_R) - q(x_L) = \nu \rho_x|_{x=x_R} - \nu \rho_x|_{x=x_L}, \tag{7.118}$$

from integrating equation (6.1). Now $q(x_R) = q(x_L) = \nu\rho_x|_{x=x_R} = \nu\rho_x|_{x=x_L} = 0$ because there is no flux across the walls. Therefore

$$\frac{\partial}{\partial t}\int_{x_L}^{x_R} \rho dx = 0. \tag{7.119}$$

Therefore if the mass in the initial condition is not equal to the steady state mass M, then a steady state with conserved mass may not be able to evolve - an issue that remains unresolved. Perhaps this is why so few steady states have been found.

Finding steady states that are significantly different from each other which start with this precise mass, satisfy the boundary conditions and which also satisfy the $\theta_x = -\frac{1}{\nu}$ condition seems to be a difficult problem. Some other solutions have been found, but these are seemingly discontinuous solutions of the sort discussed in subsection 7.5.2 below. Although these may well exist, we seek smooth solutions of the kind demonstrated in sections 7.2 and 7.3 i.e. those that are smooth through the branch switch.

7.5.1 Remarks on the boundary conditions

We note that both the gradient and the value of the density are fixed at each wall in the above cases. The problem at first sight seems over-prescribed because there seem to be four boundary conditions for a second-order problem. This is not the case, however. The restriction occurs because we must force $\theta_x = -\frac{1}{\nu}$ whenever $\theta = n\pi$ and θ must take these values at the boundaries for the density to be maximal there. Consequently, since θ_x is finite, $\rho_x = 0$ also holds at the walls. (The alternative case, with θ_x infinite and $\rho_x \neq 0$, leads to non-zero flux at the walls). To demonstrate that the problem is not over-prescribed we show in the current subsection that a solution that smoothly marches forward in time does exist.

Let $\rho = \rho_m - (t - t_0)\hat{f}(\eta) + \dots$ as $t \to t_0^+$ with $\eta = \frac{x}{(t-t_0)^{\frac{1}{2}}}$. Substituting into the continuum equation with the local form of $c \sim \pm c_0(\rho_m - \rho)^{-\frac{1}{2}}$ (since ρ is close to ρ_m) yields the nonlinear ordinary differential equation

$$\nu\hat{f}'' - \left(\pm\frac{c_0}{\hat{f}^{\frac{1}{2}}} - \frac{\eta}{2}\right)\hat{f}' - \hat{f} = 0 \tag{7.120}$$

for $\hat{f}(\eta)$ (this happens to be the same equation as (7.1) studied in section 7.2). This must be solved subject to

$$\hat{f}(0) = 0, \tag{7.121a}$$

and

$$\hat{f}'(0) = 0 \tag{7.121b}$$

so that $\rho = \rho_M$ and $\rho_x = 0$ at the boundaries.

Near the wall, the solution of (7.120) expands in the form

$$\hat{f} = f_n\eta^n + f_m\eta^m + \dots \tag{7.122}$$

for small η with $0 < n < m$. Substituting into equation (7.120), and manipulating a little, produces

$$\begin{aligned}\nu n(n-1)f_n\eta^{n-2} + \nu m(m-1)f_m\eta^{m-2} - \Bigg(&\pm\frac{c_0 n f_n}{f_n^{\frac{1}{2}}}\eta^{\frac{n}{2}-1} \pm \frac{c_0 m f_m}{f_n^{\frac{1}{2}}}\eta^{m-\frac{n}{2}-1} \\ &\mp\frac{c_0 n f_m f_n}{2f_n^{\frac{3}{2}}}\eta^{m-\frac{n}{2}-1} \mp \frac{c_0 m f_m^2}{2f_n^{\frac{3}{2}}}\eta^{2m-\frac{3n}{2}-1} - \frac{n}{2}f_n\eta^n - \frac{m}{2}f_m\eta^m\Bigg) \\ &- f_n\eta^n - f_m\eta^m = 0 + \dots\end{aligned} \tag{7.123}$$

Let $n = 2$, to obtain what we might expect to be the most general result,

$$\begin{aligned}2\nu f_2 + \nu m(m-1)f_m\eta^{m-2} - \Bigg(&\pm\frac{2c_0 f_2}{f_2^{\frac{1}{2}}} \pm \frac{c_0 m f_m}{f_2^{\frac{1}{2}}}\eta^{m-2} \\ &\mp\frac{c_0 f_m f_2}{f_2^{\frac{3}{2}}}\eta^{m-2} \mp \frac{c_0 m f_m^2}{2f_2^{\frac{3}{2}}}\eta^{2m-4} - f_2\eta^2 - \frac{m}{2}f_m\eta^m\Bigg) \\ &- f_2\eta^2 - f_m\eta^m = 0 + \dots .\end{aligned} \tag{7.124}$$

Therefore, balancing the $O(1)$ terms reveals that

$$2\nu f_2 \mp 2c_0 f_2^{\frac{1}{2}} = 0; \tag{7.125}$$

hence

$$f_2 = \left(\frac{c_0}{\nu}\right)^2 . \tag{7.126}$$

The possible remaining balances for m are $m = 0, 1$ or 2. The first two would violate the ordering chosen earlier, however, and the last would only add to the f_2 term. Therefore, if $\hat{f}'(0) = 0$, the above argument implies that we must have the *exact* solution

$$\hat{f} = \left(\frac{c_0}{\nu}\right)^2 \eta^2 \tag{7.127}$$

of (7.120) and so

$$\rho = \rho_m - \left(\frac{c_0}{\nu}\right)^2 x^2 + \dots . \tag{7.128}$$

Thus the wall-layer here is trivial as it is, in effect, identical to the solution in the core at small x.

In fact, in the core, we have a regular time expansion where

$$\rho = \rho_0(x) + t\rho_1(x) + t^2\rho_2(x) + \dots . \tag{7.129}$$

The leading order term is prescribed by the wall layer near $x = 0$ and is, at small x,

$$\rho_0 = \rho_m - \frac{c_0^2}{\nu^2} x^2. \tag{7.130}$$

We also expand the wave-speed as

$$c = \hat{c}_0(x) + t\hat{c}_1(x) + \dots \tag{7.131}$$

for small x, where $\hat{c}_0(x)$ can be determined from the fundamental diagram. Placing these expansions in the continuum equation (6.1) gives

$$\rho_1 + 2t\rho_2 + (\hat{c}_0 + t\hat{c}_1)(\rho_0' + t\rho_1') = \nu\rho_0'' + \nu\rho_1''t + \dots . \tag{7.132}$$

Hence, at leading order,

$$\rho_1 + \hat{c}_0\rho_0' = \nu\rho_0'' \tag{7.133}$$

which can easily be solved to obtain, for small x,

$$\rho_1 + \frac{2c_0^2}{\nu^2}\hat{c}_0 x = -\frac{c_0^2}{\nu}. \tag{7.134}$$

We found earlier that the wall-layer is trivial, since the solution there is exact and all terms are $O(1)$. Consequently, to avoid a contradiction, we must satisfy

$\rho_1, \rho_2, ..., \rho_n, ... = 0$. (Otherwise, at some point in time a balance would be required between the x^2 term and an $O(t^n)$ term, and a wall layer would have to be introduced). Therefore

$$\hat{c}_0 = \nu x^{-1}, \tag{7.135}$$

in order to prevent a non-trivial wall layer.

We recall that $c = \frac{dq}{d\rho}$, so $\hat{c}_0 + t\hat{c}_1 = \frac{dq_0}{d\rho_0} + t\frac{dq_1}{d\rho_1}$ and hence $\hat{c}_0 = \frac{dq_0}{d\rho_0}$. As $x \to 0$ the wall is approached. At the wall $\rho = \rho_m$. The fundamental diagram has infinite gradient at maximum density. Therefore, as $x \to 0$, $\hat{c}_0 \to \infty$. Consequently the behaviour of $\hat{c}_0$ determined in equation (7.135) is entirely acceptable and so a viscous wall-layer is avoided.

In summary, having $\rho_x = 0$ enables a solution to develop which does not have any viscous wall-layers and thus is regular in x, t locally. (In principle a steady state might evolve at large times). In that sense, the problem appears not to be over-prescribed.

7.5.2 More remarks on the steady state solution

Observe that $\rho = 0$ and $\rho = \rho_M$ are perfectly valid special solutions to the steady equation (7.103). There therefore seems to be an entire set of solutions to (7.103) where (7.106) can be used for any part and either of the special solutions can be used for any other part. It appears at first that these solutions could then be placed together, ensuring that the function is continuous, allowing any number of steady solutions to be 'stitched together' in this manner.

Solutions of this sort, however, do not form an acceptable steady state (in the sense of a steady state being a large-time limit) as the solution would not stay intact at the matching points if it were marched forward in time. The reason is as follows. In section 7.2.3 we saw that local to a minimum if a region with local curvature λx^2 say matches with a region μx^2 say, with $\mu \neq \lambda$, then there exists an intermediate region with $x = kt^{\frac{1}{2}}$ with k non-zero. (An example is $\lambda \neq 0$ and $\mu = 0$, corresponding to a solution of form (7.106) matching with $\rho = 0$). Thus as time increases to order one values and beyond a $t^{\frac{1}{2}}$ spatial growth will occur at the point of matching. This can only be avoided if $k = 0$ for which $\lambda = \mu \neq 0$ necessarily, eliminating the possibility of the stitching-together of solutions as described above. The same line of argument applies at a maximum.

7.6 Concluding remarks

In chapters 5, 6 and 7 we have attempted to develop a continuum model for the flow, including colliding and separating grains.

Chapter 5 in particular deals with the inviscid (bulk) model and we initially found solutions with discontinuous input, these being cases that yield relatively easily to analysis. In chapter 6, we attempted to extend the number of solutions to other cases. To obviate problems associated with the discontinuities present in the model, we added an artificial viscous dissipation term so that the governing equation is parabolic. We focused in this chapter solely on problems in which grain movement is uni-directional so that no branch-switching occurred. Hence we used a finite difference scheme to obtain numerical solutions that imitate those found in chapter 6. Following this, an asymptotic solution valid at asymptotically small times was obtained. Some steady state solutions were then presented.

Finally, in the present chapter 7 we extended the work still further to encompass a two-way flow in which grains can move to and fro. In order to find such solutions, the fundamental diagram is modified so its curvature is convex outwards at the endpoints. It was determined that such an alteration still allows physically reasonable descriptions of separating and clashing grains to develop. A general computational procedure was then employed to find solutions in terms of polar co-ordinates and the unknown function $\theta(x,t)$, thus avoiding concerns about the multi-valued fundamental diagram since $\theta(x,t)$ is single-valued. Again some steady state solutions were found, as these might correspond to the density profile of grains as they exit the chute, but it was difficult to find very many such solutions. In fact, a steady state with conserved mass may not always be able to evolve, an issue that remains unresolved.

Chapter 8

Air effects

Air effects in the full chute flow have so far been entirely neglected in both the computational simulations and the continuum modelling. However, air effects are potentially of great significance, as we saw for the single grain in chapter 2, and so they are examined in this chapter.

As discussed throughout the thesis, the ideal situation for Sortex is for a uniform ordered array of grains to fall down the chute in a manner such that each grain is aligned with an ejector. Ideally, the grains would be evenly spaced and uniformly oriented. We wish to determine in the current chapter whether such an array of grains is stable to the effects of the air flow. If the idealised array is unstable to air effects then a chute design that would produce a uniform grain distribution must also tackle problems associated with the unstable aerodynamics. Therefore a study of the air effects between grains and the air effects on arrays of grains is crucial to the industrial setting.

Some of the specific situations discussed in order to gain insight into possible behaviour are, for example, air effects between two flat grains, effects between two grains with curvature included, effects between unbounded arrays of grains and effects between arrays of grains bounded by chute walls. As we found in chapter 2 that the grain-based Reynolds number is $Re_g = O(150)$, i.e. a moderate Reynolds number not clearly in the low or high regimes, we therefore discuss in the current chapter both viscous and inviscid effects, as described below.

First, lubrication effects are considered. These are significant when the separation between grains is relatively small and may be important during collisions, for example. We start with a study of the viscous effects between only two grains. It is found that grains cannot actually touch when viscous effects alone are included (other physics must be included to describe collisions, such as molecular forces). Next, the viscous air effects are investigated for an array of grains and the subsequent stability of the grain array is considered.

Lubrication theory has been seen to be crucial in other similar situations. For example, Ishikawa and Pedley [25] examined such effects on micro-organisms known as 'squirmers'. The orientation of the squirmers changes dramatically as they approach each other in the limit when viscous effects dominate. An engineering example is given by Korobkin and Ohkusu [31]. They studied the impact of two circular plates, one of which is floating on a thin liquid layer. As the plates come together the air flow is of major importance and air cushion effects perhaps explain some of the dynamic responses in the system. Smith, Li and Wu [52] have also investigated air cushioning effects in the gap between an almost inviscid fluid and a solid wall and once more the important physics is seen to depend predominantly on the lubrication effects in the air.

Hinch and Leal [20], [33] have examined the rheology of particle suspensions in Newtonian fluids. Their work relates in particular to effects of Brownian motion, especially rotary Brownian motion, on the suspensions of spheroids. As Brownian motion is pertinent only to the dynamics of small particles (when the dynamics of the fluid at the molecular level cannot be neglected) we anticipate that such effects are not directly relevant here.

Hinch and Leal have also co-authored research with Russel and Tieffenbruck [49] on the motion of rods falling vertically near a wall and this is more directly relevant to the current chapter. They employed slender body theory and a mixture of analysis, numerics and experiment to study the dynamics of a falling rod at low Reynolds number. Essentially, they demonstrate that two motions can occur, dependent on the initial angle of inclination of the rod, one type being a 'glancing' motion and the other a 'reversing' motion. Their research also notes that contact cannot occur between the rod and the wall when lubrication theory is applied to the case of close approach.

Second, inviscid air effects are studied. Initially we examine again the effects between only two grains. The absence of viscosity modifies the grain dynamics, as might be expected. This is followed by an investigation of the inviscid effects on an array of grains without walls. Surprisingly, the dynamics is somewhat similar to the viscous case.

Recent research on air effects of interest here include those by Andersen, Pesavento and Wang [3], [4]. They investigate the dynamics of freely falling particles in a quasi-two-dimensional flow at large Reynolds number. This has application to cards falling through air. They find that the cards exhibit fluttering or tumbling motions with a possibly chaotic transition between the two motions. Interestingly they find that a card falling with its edge downward is always an unstable configuration, whereas a card falling with its broadside downward is stable.

Other aerodynamic effects could be investigated, such as the motion of the grains near the walls of the chute. This may have similarities to the study of fluid motions between cars and the ground by Jones and Smith [27]. They studied the boundary layer equations in the limit when lubrication theory is valid and also in an inviscid limit in the presence of a moving wall.

Research on impacting spheres, the hydrodynamics of spheres moving in the presence of wall and particle-wall collisions and so forth can be found in, for example, the theoretical studies by Eames et al. [13], Leweke et al. [35] and the experimental work by Joseph [28] and co-workers and references therein.

Finally, it is pertinent to mention here that other aspects of the aerodynamics in the food-sorting process have been subject to a number of studies [51], [56], [63]. These include the swirl-flow effects and turbulent boundary layer through the ejector ducts, and the flow from the ejector nozzle arrays.

8.1 Viscous air effects between two grains

We first examine the effects due to the air between only two grains when their separation is small relative to their length. Initially the grains are simply modelled as two flat plates. Throughout the rest of this chapter we consider only two-dimensional grains for simplicity. Following this, a more realistic shape that includes some curvature is studied.

However, the problem is formulated in the same way in both cases, and is illustrated in figure 8.1. Suppose there are two grains separated by a small gap. Let the upper surface of the lower grain be located at $y = f$ and the gap height between the grains be $h = h(x,t) = g(x) + \tau(t)$. Observe that writing $h(x,t)$ in this way restricts the grains to certain types of motion. For example, this does not allow the orientation of the grains to change. The lower surface of the upper grain is located at $y = f + h$. In the gap the force acting on the grains is due to the pressure of the air, p. Outside of the gap the air is at atmospheric pressure, p_0, and for convenience p_0 is taken to be the zero pressure level. If the lower grain has mass m_1 and the upper grain a mass m_2 then

$$m_2\left(\ddot{f} + \ddot{\tau}\right) = \int_{-a}^{a} p dx \tag{8.1}$$

and

$$m_1\ddot{f} = -\int_{-a}^{a} p dx \tag{8.2}$$

from Newton's second law, where a dot denotes differentiation with respect to time. The length of each grain is $2a$ with one end placed at $x = -a$, the other at $x = a$ and the centre of the grain at $x = 0$. We further assume that there is no normal pressure variation within the gap so

$$\frac{\partial p}{\partial y} = 0. \tag{8.3}$$

Finally, as we have assumed the gap between grains is relatively small, lubrication theory is a valid approximation. (The reduced Reynolds number, αRe must be small, where $Re = \frac{U^*H*}{\nu^*}$ is the air-flow Reynolds number, based on separation distance, and $\alpha = \frac{H^*}{L^*}$ represents a slope factor. Note that U^* is a typical velocity in the

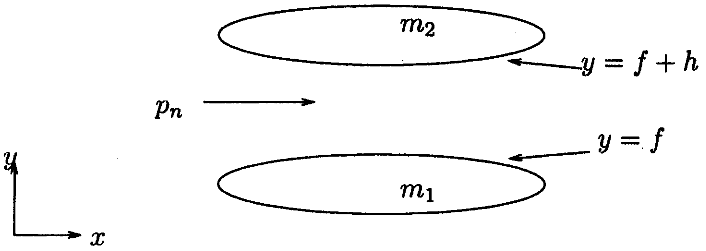

Figure 8.1: A schematic diagram showing the formulation of the air effects problem for two grains. The upper surface of the lower grain is located at $y = f$, the height of the gap is h and the pressure in the gap is p. Separation between grains is assumed to be small so that lubrication theory is valid.

gap, H^* is the height of the gap, $L^* >> H^*$ is the length of a grain and ν^* is the viscosity of the air). Of course, in three dimensions the air between two rice gains that collide in the configuration shown could escape sideways not lengthways, and the diameter of the rice would be an important length scale, but here we keep to the two-dimensional model. Thus

$$\left(h^3 p_x\right)_x = \gamma h_t \tag{8.4}$$

(see [44], for example) where γ is a constant proportional to the viscosity of the air.

Derivation of Reynolds' equation

Equation (8.4) is in fact Reynolds' equation. The derivation of this equation is sketched out here.

Consider a gap between a grain and a flat wall where the height of the gap is small relative to the length of the grain. The grain approaches the wall with a downward velocity of V and we assume that there is no horizontal motion of the grain. Furthermore, the wall is stationary. The grain has a typical length of $l(= 2a)$ and its surface is located at $y^* = h^*(x, t)$. (An asterisk denotes a dimensional quantity). The height of the air gap is scaled as $l\delta$ with $\delta << 1$.

We assume that the pressure and viscous forces balance and that there is no pressure variation in the vertical direction. Using the Navier-Stokes and continuity equations for the air, and noting that conservation of mass suggests $u_2^* \sim \frac{V}{\delta}$, where u_2^* is the horizontal velocity component of the air, allows us to write

$$u_x + v_y = 0, \tag{8.5}$$

$$-p_x + u_{yy} = 0, \tag{8.6}$$

and

$$0 = -p_y \tag{8.7}$$

after suitable non-dimensionalisation. The boundary conditions state that there is no slip along the wall and the shear forces in the air match those at the grain's surface, i.e.

$$u = v = 0 \text{ on } y = 0 \tag{8.8a}$$

and

$$u = 0, \ v = h_t \text{ on } y = h(x,t). \tag{8.8b}$$

Thus it is possible to solve equation (8.6) and obtain

$$u = \frac{1}{2}\frac{dp}{dx}y(y-h). \tag{8.9}$$

Integrating the continuity equation from $y = 0$ to $y = h$ yields

$$\int_0^{h(x,t)} u_x dy + h_t = 0. \tag{8.10}$$

Writing the integral as

$$\int_0^{h(x,t)} u_x dy = \frac{d}{dx}\int_0^{h(x,t)} u dy - \frac{\partial h}{\partial x} u \,|_{y=h} \tag{8.11}$$

and substituting equation (8.9) for u reveals

$$\int_0^{h(x,t)} u_x dy = -\frac{d}{dx}\left[\frac{1}{2}\frac{dp}{dx}\frac{h^3}{6}\right]. \tag{8.12}$$

Finally, substituting this into equation (8.10), results in

$$\frac{d}{dx}\left[\frac{dp}{dx}h^3\right] = \gamma h_t \tag{8.13}$$

where γ is a constant. This is Reynolds' equation for a lubricating layer.

Note that in the case of a moving wall the boundary conditions must be modified to

$$u = -U, \ v = 0 \text{ on } y = 0 \tag{8.14a}$$

and

$$u = 0, \ v = h_t \text{ on } y = h \tag{8.14b}$$

where U is the speed of the (leftward) moving wall. It is assumed that U does not vary along the length of the wall.

Consequently, the solution to equation (8.6) is now

$$u = \frac{1}{2}\frac{dp}{dx}y(y-h) + \frac{Uy}{h} - U. \tag{8.15}$$

After performing the same manipulations as above, we find that an extra term is generated in Reynolds' equation:

$$(h^3 p_x)_x = \gamma h_t - \frac{\gamma U}{2} h_x. \tag{8.16}$$

8.1.1 Grains modelled as two flat plates

As mentioned above, we first simply model the grains as flat plates. This reduces $h(x,t)$ to $\tau(t)$ only, with $\tau(0) = k$ where k is a positive constant. (If, for a flat plate, we wrote $h(x,t) = g(x) + \tau(t)$, $g(x)$ would add a constant only). That is, k is the initial gap height. Consequently the equation from lubrication theory, (8.4), is now

$$\tau^3 p_{xx} = \gamma \dot{\tau}. \tag{8.17}$$

Integrating, and assuming the pressure is symmetric about $x = 0$, yields

$$p = \int_{-a}^{x} \frac{\gamma \dot{\tau}}{\tau^3} \bar{x} d\bar{x}. \tag{8.18}$$

Eliminating f from equations (8.1) and (8.2) produces

$$\ddot{h} = \left(\frac{1}{m_1} + \frac{1}{m_2}\right) \int_{-a}^{a} p dx. \tag{8.19}$$

Substituting equation (8.18) into equation (8.19) results in an equation for the height of the gap:

$$\ddot{\tau} = \left(\frac{1}{m_1} + \frac{1}{m_2}\right) \int_{-a}^{a} \left[\int_{-a}^{x} \frac{\gamma \dot{\tau}}{\tau^3} \bar{x} d\bar{x}\right] dx. \tag{8.20}$$

Performing each integration, we obtain an ordinary differential equation for τ:

$$\tau^3\ddot{\tau} + \lambda\dot{\tau} = 0 \tag{8.21}$$

where

$$\lambda \equiv \frac{2a^3}{3}\left(\frac{1}{m_1} + \frac{1}{m_2}\right)\gamma. \tag{8.22}$$

Although it is possible to solve equation (8.21) to find $\tau(t)$, an analysis of the phase plane $(\dot{\tau}, \tau)$ provides more easily, perhaps, insight into the possible dynamics. The boundary conditions for equation (8.21) are

$$\tau(0) = k \tag{8.23a}$$

$$\dot{\tau}(0) = \alpha \tag{8.23b}$$

where α is the rate of change of the gap height at $t = 0$ and is a (positive or negative) constant.

Phase plane analysis

Integrating equation (8.21) once with respect to time gives

$$\dot{\tau} = \frac{\lambda}{2\tau^2} + A \tag{8.24}$$

where A is a constant of integration. From (8.23a) and (8.23b) it is easy to find that

$$A = \alpha - \frac{\lambda}{2k^2} \tag{8.25}$$

so

$$\dot{\tau} = \frac{\lambda}{2}\left(\tau^{-2} - k^{-2}\right) + \alpha. \tag{8.26}$$

Note that physically we require $\tau \geq 0$. Also observe that $\dot{\tau} = 0$ when $\tau = \sqrt{\frac{k^2}{\lambda(\lambda - 2k^2\alpha)}}$. Consequently trajectories that cross the τ axis exist only when $2k^2\alpha < \lambda$, otherwise τ is always positive.

It is now possible to determine the phase plane. Figure 8.2 shows a sketch of the phase plane. The dynamics depend upon the initial conditions, but from the phase plane we see that qualitatively there are only four different types of behaviour.

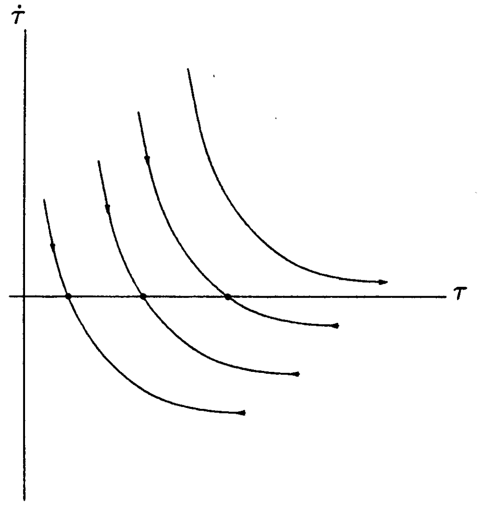

Figure 8.2: A sketch of the phase plane shows the different dynamical behaviours as described in the text. The circles highlight the equilibrium points and the arrows show the direction of movement along each trajectory. Grains can separate to a fixed distance, collapse to a fixed distance or separate indefinitely depending on the initial condition.

First, if $\alpha = 0$ then the initial condition will be located exactly at one of the equilibrium points. Therefore the grains will remain stationary for all time.

Second, if the initial condition has $\alpha > 0$, then one of two events can occur. If $2k^2\alpha < \lambda$ then the grains will move apart to a constant separation. This corresponds to moving along a trajectory in the phase plane to an equilibrium point. Since $\frac{d\dot{\tau}}{d\tau}$ is always negative (which can be seen from equation (8.26) with $\tau > 0$) the value of τ at an equilibrium point will always be greater than the initial value of τ (provided α is positive). Alternatively, if the trajectory has no root (i.e. if $2k^2\alpha > \lambda$) and $\alpha > 0$ then the grains will continue to separate for all time. This is sensible: if the initial value of the separation speed is sufficiently large the grains will continue to separate. This can be justified by examining equation (8.26); as $\tau \to \infty$, $\dot{\tau} \to \alpha - \frac{\lambda}{2k^2}$ which is positive since $2k^2\alpha > \lambda$. Viz. there exists an asymptote for $\dot{\tau}$ at large times, namely $\alpha - \frac{\lambda}{2k^2}$.

Finally, if the initial condition has $\alpha < 0$ then $2k^2\alpha < \lambda$ is always satisfied and the trajectories will always have a root. Owing to the fact that $\frac{d\dot{\tau}}{d\tau}$ is always negative the value of τ at an equilibrium point (viz. at the root) will be less than the initial value of τ if $\alpha < 0$. Therefore in this case grains will move toward each other but never meet. They will come to rest at a finite positive separation. This is because viscous forces will dominate at small gap heights and the pressure response will not allow the grains to touch. This is the expected response - see for example [52].

Thus we have determined all the different dynamic behaviours for two grains when they are modelled as flat plates. If α is sufficiently large and positive at $t = 0$ then the grains will continually separate. If α is small and positive the grains will separate to a constant distance. If α is initially negative then the grains will move toward each other, but they can never touch.

At first sight it may seem rather worrying that the inclusion of air effects does not allow grain-grain impacts, especially in light of all the prior computational and continuum modelling. However, other workers [44] have found that if appropriate physics is included when grain separation is small enough, for example molecular forces such as the Van der Waals force, grain impacts can occur.

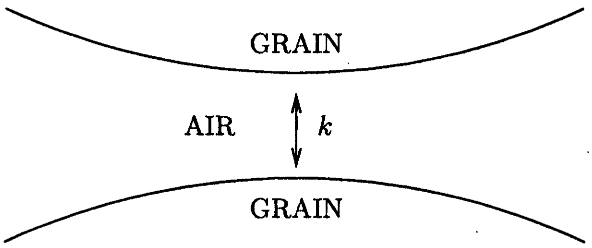

Figure 8.3: Schematic diagram showing the initial gap height between two grains when curvature is included.

8.1.2 Viscous air effects for more realistic grain shapes

The previous analysis was done with the rather crude assumption that each grain is a flat plate. We now wish to investigate whether more realistic shapes, especially those with non-zero curvature, have any important effect on the dynamics.

We now have

$$h(x,t) = g(x) + \tau(t) \tag{8.27}$$

with $g(x) \neq 0$. To introduce some curvature into the model, we choose $g(x) = x^2$ as a representative initial profile of the gap height. The equation for the pressure (8.18) now becomes

$$p = \int_{-a}^{x} \frac{\gamma \dot{\tau} \bar{x}}{(q + \tau)^3} d\bar{x}. \tag{8.28}$$

The initial conditions on $\tau(t)$ are

$$\tau(0) = k \tag{8.29a}$$

and

$$\dot{\tau}(0) = \alpha \tag{8.29b}$$

where $k > 0$ so that initial gap height is as depicted in figure 8.3 and the initial rate of change of the gap height is α, which can be positive or negative.

Evaluating

$$p = \int_{-a}^{x} \frac{\gamma \dot{\tau} x_1}{(x_1^2 + \tau)^3} dx_1 \tag{8.30}$$

we find that the pressure is

$$p = \frac{\gamma \dot{\tau}}{4} \left(\frac{1}{(a^2 + \tau^2)^2} - \frac{1}{(x^2 + \tau)^2} \right). \tag{8.31}$$

Hence, an ordinary differential equation for τ is

$$\ddot{\tau} = \left(\frac{m_1 + m_2}{m_1 m_2}\right) \int_{-a}^{a} \frac{\gamma \dot{\tau}}{4} \left(\frac{1}{(a^2+\tau^2)^2} - \frac{1}{(x^2+\tau)^2}\right) dx \tag{8.32}$$

The integral on the right hand side can be written as

$$\int_{-a}^{a} \left(\frac{1}{(a^2+\tau)^2} - \left[\frac{1}{\tau(\tau+x^2)} - \frac{x^2}{\tau(\tau+x^2)^2}\right]\right). \tag{8.33}$$

The first two terms can be integrated immediately, and the third is evaluated by parts with $u = x$ and $v' = \frac{x}{(\tau+x^2)^2}$. Consequently,

$$\ddot{\tau} = \left(\frac{m_1 + m_2}{m_1 m_2}\right) \left(\frac{\gamma \dot{\tau} a}{4(a^2+\tau)^2} - \frac{\gamma \dot{\tau}}{4\tau^{\frac{3}{2}}} \tan^{-1}\left(\frac{a}{\sqrt{\tau}}\right)\right). \tag{8.34}$$

Equation (8.34) is an ordinary differential equation for $\tau(t)$ subject to initial conditions (8.29a) and (8.29b). However, rather than solving explicitly for $\tau(t)$, we choose to examine the dynamics by phase plane methods.

First, integrating (8.34) yields

$$\dot{\tau} = \left(\frac{m_1 + m_2}{m_1 m_2}\right) \left(-\frac{\gamma a}{4(a^2+\tau)} - \frac{\gamma}{4}\left(\frac{1}{a}\ln\left(1+\frac{a^2}{\tau}\right) - \frac{2}{\sqrt{\tau}}\tan^{-1}\left[\frac{a}{\sqrt{\tau}}\right]\right)\right) + C \tag{8.35}$$

where we have used the standard formula for the integral of $\tan^{-1} x$ as given by Abramawitz and Stegun [1]. From equations (8.29a) and (8.29b) C is easily determined to be

$$C = \alpha - \left(\frac{m_1 + m_2}{m_1 m_2}\right) \left(-\frac{\gamma a}{4(a^2+k)} - \frac{\gamma}{4a}\ln\left(1+\frac{a^2}{k}\right) + \frac{\gamma}{2\sqrt{k}}\tan^{-1}\left(\frac{a}{\sqrt{k}}\right)\right). \tag{8.36}$$

Some typical curves in the phase plane are shown in figure 8.4. Note that the $\tau < 0$ region is unphysical in this section, since this corresponds to overlapping grains. Essentially, there are two types of curve: those which cross the τ axis and those which do not.

On a curve of the former type three eventualities can occur.

1. If $\dot{\tau}(0) = 0$ then the grains remain stationary.

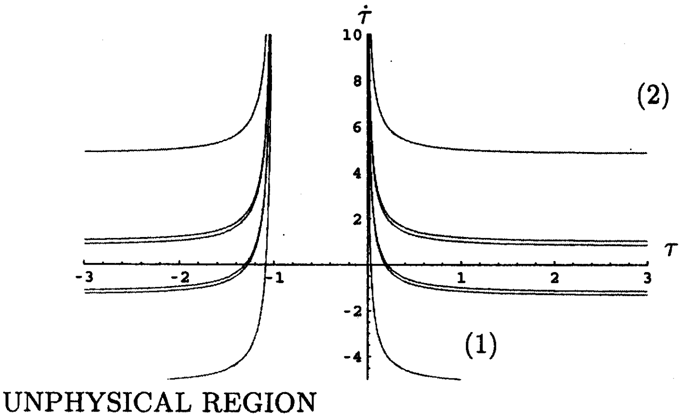

Figure 8.4: The phase plane is shown for the case of curved grains. Note that the $\tau < 0$ region is unphysical. The curves are much the same as the case for flat grains, and so apparently there are no extra effects owing to the curvature. There are two main types of motion; curves (1) that do not cross the τ axis, and (2) curves that do.

2. If $\dot{\tau}(0) = \alpha < 0$ then the particle separation will decrease until the particles are at a constant separation.
3. If $\dot{\tau}(0) = \alpha > 0$ then the particle separation increases until the particles are at a constant separation.

On curves which do not cross the τ axis, there is only one possible type of motion. In this case $\dot{\tau}(0) = \alpha > 0$. This means that the grains will separate forever, and at infinity will move apart at a constant velocity. This can be justified by noting, from equation (8.34), that $\dot{\tau} \to C$ as $\tau \to \infty$.

The dynamics, then, are seen to be much the same as for the case of flat grains. There is no apparent extra behaviour owing to the curvature of the grains. Perhaps this is to be expected, since in the neighbourhood of the points where grains would touch the grains are locally flat. In none of the cases do the grains touch.

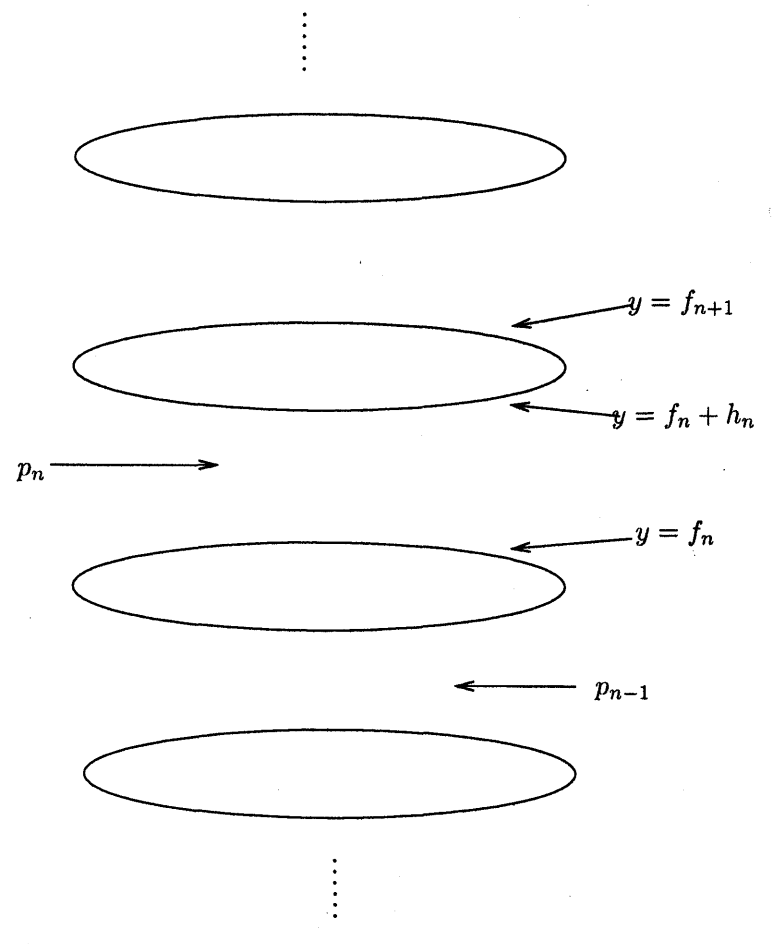

Figure 8.5: A schematic diagram showing a section of an array of grains. The upper surface of the n^{th} grain is located at $y = f_n$, the height of the n^{th} gap is h_n and the pressure in the gap is p_n. Separation between grains is assumed to be small so that lubrication theory is valid.

8.2 Viscous air effects for an array of N grains

For an array of N grains the problem formulation is much the same as the two-grains case and is depicted in figure 8.5. Once more, the force on each grain balances with the pressure difference across it. The n^{th} grain with the position of its upper surface given by $y = f_n(x,t)$, the pressure on its upper surface given by $p_n(x,t)$ and the pressure on its lower surface given by p_{n-1} thus satisfy

$$m\ddot{f}_n = \int_{-a}^{a} (-p_n + p_{n-1})\, dx \tag{8.37}$$

from Newton's second law. Here m is the mass of each grain, $2a$ is the length of each grain and x is the distance along the length of each grain. A dot denotes differentiation with respect to time, t. If h_n is the height of the gap between each grain, and is a function of x and t, then the shape of each grain is determined by

$$f_{n+1} - f_n - h_n = s(x) \tag{8.38}$$

where $s(x)$ is some representative function for the shape. However, in this section we restrict our study to the case of flat grains so that $h_n = h_n(t)$ only. Finally, assuming the gap between each grain is small, lubrication theory holds true there. Hence,

$$h_n^3 p_{n xx} = \gamma \dot{h}_n \tag{8.39}$$

where γ is a constant that is proportional to the viscosity of the air (see [44]). For the next pair of grains along in the array, equation (8.37) becomes

$$m\ddot{f}_{n+1} = \int_{-a}^{a} (-p_{n+1} + p_n)\, dx. \tag{8.40}$$

Using equation (8.38) (with $s(x)$ effectively equal to zero) we see that this can be written as

$$m\left(\ddot{f}_n + \ddot{h}_n\right) = \int_{-a}^{a} (-p_{n+1} + p_n)\, dx. \tag{8.41}$$

Substituting (8.37) into the above equation yields

$$\ddot{h}_n = \frac{1}{m}\int_{-a}^{a} (-p_{n+1} + 2p_n - p_{n-1})\, dx. \tag{8.42}$$

Therefore equations (8.39) and (8.42) yield a set of N coupled equations for the pressure in each gap, p_n, and the height of each gap, h_n.

From here, we find a symmetric steady solution and then linearly perturb about that solution. In this way, we may gain a useful insight into the physics of the problem, particularly about the physics of stability.

To find the symmetric solution, fix $\dot{f}_n$=0 and choose $p_1 = p_2 = ... = p_n = ...p_N$ so that all the pressures are equal. Thus $\dot{h}_n = 0$ from equations (8.38) and (8.40). Consequently, $h_n = k$, where k is a constant. Therefore the equation from lubrication theory reduces to

$$h_n^3 p_{n_{xx}} = 0. \tag{8.43}$$

Hence

$$p_n = \int_{-a}^{x} \left(\frac{A}{h_n^3} \right) d\bar{x} \tag{8.44}$$

where A is a constant of integration. Therefore,

$$p_{n_x} = \frac{A}{k^3} \tag{8.45}$$

and if p_{n_x} is symmetric about $x = 0$ (the centre of each grain) then $A = 0$. So p_n is then also a constant. This solution is denoted as $p_n = \bar{p}_n$ and $h_n = \bar{h}_n = k$.

To perturb about this solution, let

$$p_n = \bar{p}_n + \epsilon P_n(x,t) + ... \tag{8.46a}$$

and

$$h = \bar{h}_n + \epsilon H_n(t) + ... \tag{8.46b}$$

where $\epsilon << 1$ measures the amplitude of the small perturbations.

Substitution into (8.39) produces

$$\left(\bar{h}_n + \epsilon H_n\right)^3 \left(\bar{p}_n + \epsilon P_n\right)_{xx} = \epsilon\gamma\dot{H}_n + \text{higher order terms.} \tag{8.47}$$

At leading order we find

$$\bar{h}_n^3 \bar{p}_{n_{xx}} = 0 \tag{8.48}$$

for which we know the solution already. Then at $O(\epsilon)$

$$\left(3\bar{h}_n^2 H_n \bar{p}_{n_{xx}} + \bar{h}_n^3 P_{n_{xx}}\right) = \gamma \dot{H}_n. \tag{8.49}$$

A little manipulation leads to

$$P_n = \int_{-a}^{x} \frac{1}{\bar{h}_n^3} \left(\gamma \dot{H}_n x - 3\bar{h}_n^2 H_n \bar{p}_{n_x} + C_1\right) dx \tag{8.50}$$

where $C_1(\mathrm{t})$ is a function of t only. If the perturbed pressure is also symmetric about $x = 0$ then $C_1 = 0$.

Substituting the expressions (8.46a) and (8.46b) for the perturbed pressure and gap height into equation (8.42) results in

$$\ddot{\bar{h}}_n + \epsilon \ddot{H}_n = \frac{1}{m} \int_{-a}^{a} \left(-\bar{p}_{n+1} - \epsilon P_{n+1} + 2\bar{p}_n + 2\epsilon P_n - \bar{p}_{n-1} - \epsilon P_{n-1}\right) dx. \tag{8.51}$$

So at $O(\epsilon)$

$$\ddot{H}_n = \frac{1}{m} \int_{-a}^{a} \left(-P_{n+1} + 2P_n - P_{n-1}\right) dx. \tag{8.52}$$

Thus equations (8.50) and (8.52) yield a set of N coupled but linear equations for the perturbed pressure in each gap, P_n, and the perturbation to the height of each gap, H_n.

We now seek solutions of the form

$$H_n = \tilde{H}_n e^{qt} \tag{8.53}$$

and

$$P_n = \tilde{P}_n e^{qt} \tag{8.54}$$

with the constant q complex in general, $\tilde{H}_n$ constant and $\tilde{P}_n = \tilde{P}_n(x)$.

Placing these into equation (8.50) yields

$$\tilde{P}_n(x) e^{qt} = \int_{-a}^{x} \frac{1}{\bar{h}_n^3} \left(\gamma q \tilde{H}_n e^{qt} x - 3\bar{h}_n^2 \tilde{H}_n e^{qt} \bar{p}_{n_x}\right) d\bar{x}. \tag{8.55}$$

Substituting for the flat plate solution, with both the pressure and the perturbed pressure symmetric about the origin, results in

$$\tilde{P}_n(x) = \frac{\gamma q}{k^3} \tilde{H}_n \frac{(x^2 - a^2)}{2} \tag{8.56}$$

(after performing the integration).

Substituting the forms of P_n and H_n into equation (8.52) and integrating reveals

$$q^2\tilde{H}_n = \frac{1}{m}\int_{-a}^{a}\left(-\tilde{P}_{n+1}(x) + 2\tilde{P}_n(x) - \tilde{P}_{n-1}(x)\right)dx. \tag{8.57}$$

Hence, using (8.56) and integrating yields

$$q^2\tilde{H}_n = -\frac{2a^3\gamma q}{3mk^3}\left(-\tilde{H}_{n+1} + 2\tilde{H}_n - \tilde{H}_{n-1}\right). \tag{8.58}$$

Thus the H_n are governed by the equation

$$q^2\tilde{H}_n = \Gamma q\left(\tilde{H}_{n+1} - 2\tilde{H}_n + \tilde{H}_{n-1}\right) \tag{8.59}$$

where $\Gamma = \frac{2a^3\gamma}{3mk^3}$ which is a positive constant.

As an aside, we note that equation (8.56) is roughly $\tilde{P}_n \propto -\dot{H}_n$ (Observe $x \in (-a, a)$, hence the minus sign). Also we observe that $q^2\tilde{H}_n \propto \ddot{H}_n$. Furthermore, the right-hand-side of equation (8.57) is reminiscent of a discretized second derivative. Consequently, equation (8.57) can loosely be thought of as $\frac{\partial P_n}{\partial t} \propto \frac{\partial^2 P_n}{\partial x^2}$. It is well-known that the heat equation is stable to perturbations of the form $P \propto e^{i\mu s}$ (if $P_t = DP_{ss}$). Thus intuitively we expect the gap height and pressure to be stable to spatially oscillatory perturbations. Furthermore, this strongly hints at a possible numerical scheme for determining the pressure in each gap - see subsection 8.2.1.

To allow us to investigate the stability of some simple perturbations, we choose to write

$$\tilde{H}_n = \zeta e^{\lambda n} \tag{8.60}$$

and

$$\tilde{P}_n = \xi(x)e^{\lambda n} \tag{8.61}$$

with λ complex in general and ξ independent of n. Thus equation (8.56) becomes

$$\xi e^{\lambda n} = \frac{\gamma q}{k^3}\zeta e^{\lambda n}\frac{(x^2 - a^2)}{2} \tag{8.62}$$

and (8.59) becomes

$$q^2\zeta e^{\lambda n} = \Gamma q\zeta\left(e^{\lambda(n+1)} - 2e^{\lambda n} + e^{\lambda(n-1)}\right) \tag{8.63}$$

i.e. unforced modes exist if

$$q^2 = \Gamma q \left(e^{\lambda} - 2 + e^{-\lambda} \right) \tag{8.64}$$

which is

$$q^2 = 4\Gamma q \sinh^2 \left(\frac{\lambda}{2} \right). \tag{8.65}$$

Taking here the non-trivial solution only implies that

$$q = 4\Gamma \sinh^2 \left(\frac{\lambda}{2} \right). \tag{8.66}$$

Therefore

$$H_n = \tilde{H}_n \exp \left(4\Gamma \sinh^2 \left(\frac{\lambda}{2} \right) t \right) \tag{8.67}$$

for some λ.

If λ is real then the perturbation will always grow since $4\Gamma\sinh^2\left(\frac{\lambda}{2}\right) t \geq 0$ for all time. The case of λ being real, however, corresponds to a shift in position in each grain, since $\tilde{H}_n = e^{\lambda n}$. The gap between each grain will be consecutively larger or smaller as n increases, depending on the sign of λ, and grows without bound as n increases.

On the other hand, if λ is purely imaginary, put $\lambda = i\Lambda$. Then

$$H_n = \tilde{H}_n \exp \left(4\Gamma \sinh^2 \left(\frac{i\lambda}{2} \right) t \right). \tag{8.68}$$

We recall that

$$\sinh^2 \left(\frac{i\Lambda}{2} \right) = -\sin^2 \left(\frac{\Lambda}{2} \right), \tag{8.69}$$

therefore

$$H_n = \tilde{H}_n \exp \left(-4\Gamma \sin^2 \left(\frac{\Lambda}{2} \right) t \right). \tag{8.70}$$

Thus the perturbation now decays since $-4\Gamma\sin^2\left(\frac{\lambda}{2}\right) t \leq 0$ for all t. Observe that imaginary λ corresponds to a spatially oscillatory perturbation with Λ akin to a wavenumber (since in this case $\tilde{H}_n = e^{i\Lambda n}$). This is in full agreement with our intuitive expectations described above.

Similarly note that the perturbed pressure is

$$P_n = \tilde{P}_n \exp \left(4\Gamma \sinh^2 \left(\frac{\lambda}{2} \right) t \right) \tag{8.71}$$

or

$$P_n = \tilde{P}_n \exp\left(-4\Gamma \sinh^2\left(\frac{\Lambda}{2}\right)t\right) \tag{8.72}$$

depending on whether $\lambda \in \mathbb{R}$ or $\lambda \in \mathbb{C}$.

8.2.1 Computing an example: an array of ten grains

In the previous section it was observed that a suitable numerical scheme could be used to find the perturbed pressures in each gap based the right hand side of equation (8.57) being reminiscent of a second derivative. We elaborate on this here.

We reiterate that equation (8.56) is roughly $\tilde{P}_n \propto -\dot{H}_n$ and $q^2\tilde{H}_n \propto \ddot{H}_n$. Thus equation (8.57) can be thought of as

$$\dot{P}_n = \frac{1}{m}\int_{-a}^{a}(P_{n+1} - 2P_n + P_{n-1})\,dx. \tag{8.73}$$

If the above equation is discretized so that P_n^i represents the pressure in the n^{th} gap at the i^{th} time then

$$\frac{P_n^{i+1} - P_n^i}{\delta t} = \frac{2a}{m}\left(P_{n+1}^i - 2P_n^i + P_{n-1}^i\right) \tag{8.74}$$

where δt is a small increment in time.

Hence, given an initial condition for the pressure perturbation, it is easy to calculate the size of the perturbation in each gap a small time later. Thus it is possible to compute the perturbed pressures as a function of time. Indeed we do so, and the results are presented below.

The height perturbations are also calculated alongside the pressure. Recall that $\tilde{P}_n \propto -\dot{H}_n$. Hence we calculate H_n in discretized form as

$$H_n^{i+1} = H_n^i - \delta t P_n^i \tag{8.75}$$

and an initial condition for the height perturbations is chosen arbitrarily.

A simple case is examined first in which the perturbation to the pressure alternates between two constants: in the first gap the pressure perturbation is $P_1(0) = 1$, in the second gap $P_2(0) = 3$, in the third $P_3(0) = 1$ and so on. In figure 8.6, which shows the temporal evolution, we see that the perturbed pressures settle to positive

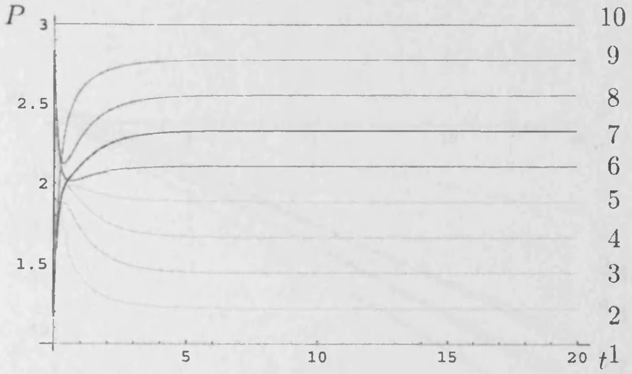

Figure 8.6: The pressure perturbations in each gap for a simple arbitrary initial condition in which the pressures are initially perturbed by alternate constants, $P = 1$ and $P = 3$. The perturbations settle to positive constant values after $t \approx 5$. The curves are labelled according to which gap the solution corresponds to. At sufficiently large t the pressures are seen to be distributed linearly in n: that result is independent of the initial condition (according to the end of this section and also another arbitrary case in figures 8.8, 8.9).

constant values after $t \approx 5$. This corresponds to all grains separating with a constant speed, as described below.

The height perturbations for this pressure perturbation are shown in figure 8.7. The initial condition for the height perturbation is $H_1(0) = 1$, $H_2(0) = 3$, $H_3(0) = 1$ and so on so that the gap height also alternates between two constants. At increased times the perturbations appear to grow linearly in time.

In each figure the curves are labelled according to which gap the solution corresponds to. In every case the pressures and gap heights at large times appear to be distributed linearly in n. This is commented on at the end of this section.

In the second example the pressure is perturbed by a small positive random value. Once again the perturbations settle to constant values, in this case at around $t \approx 15$, and the gap heights appear to grow linearly, see figures 8.8 and 8.9.

Finally, here, in figure 8.10, the pressure is perturbed alternately between $P = \pm 1$ in each gap. Again the pressure perturbations settle to constant values after $t \approx 5$

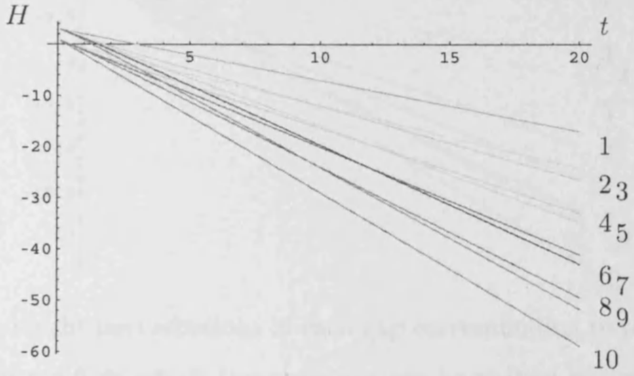

Figure 8.7: The height perturbations of each gap corresponding to the simple initial condition of figure 8.6 in which the pressures are perturbed by alternate constants, $P = 1$ and $P = 3$. The perturbations appear to grow linearly in time. The curves are labelled with the number, n, corresponding to the gap that the particular solution corresponds to. The heights are also seen to be distributed linearly in n.

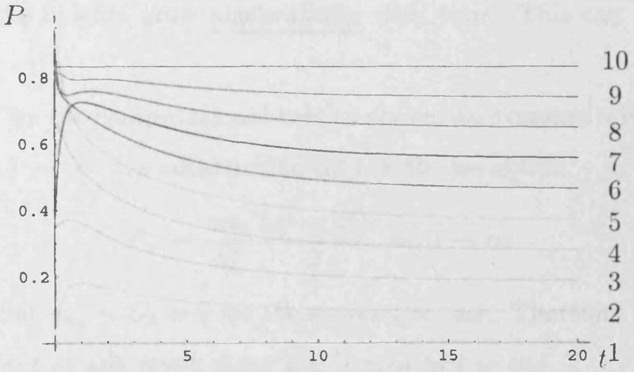

Figure 8.8: In this second example the pressure is perturbed by a small positive random value. Once again the perturbations settle to constant values, in this case at around $t \approx 15$.

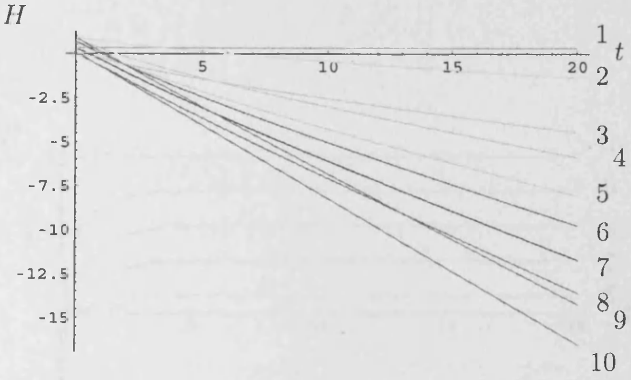

Figure 8.9: The height perturbations of each gap corresponding to the simple initial condition of figure 8.8 in which the pressures are perturbed by random amounts. Again, the perturbations appear to grow linearly in time.

and the perturbed gap heights appear to grow linearly with time, see figure 8.11.

Thus in each example we have seen that the pressure perturbations do not grow or decay exponentially, but settle to constant values after a finite time. Hence the flow disturbances do not grow exponentially nor do they stabilize to zero pressures. Similarly, the height disturbances in each gap neither grow exponentially nor decay. Another behaviour is evident, in which the pressures asymptote to non-zero constants and the heights grow algebraically with time. This can be explained as follows.

As motivated by the computational results above, we examine the possibility that $H_n(t) \to \alpha_n t$ as $t \to \infty$. On substitution into (8.50) we obtain

$$P_n \to \frac{\gamma \alpha_n}{\bar{h}_n^3} \frac{(x^2 - a^2)}{2} \quad \text{as} \quad t \to \infty \tag{8.76}$$

after recalling that $p_{nx} = C_1 = 0$ for the symmetric case. Therefore each P_n asymptotes to a constant at any given point $x \in [-a, a]$ as $t \to \infty$.

Thus the algebraic growth of $H(t)$ and the asymptotic behaviour of each P_n seen in the computations above can be reconciled with the analysis. This algebraic growth of $H(t)$ will dominate over the neutrally stable normal modes behaviour previously described. Hence the linearisation will break down as $|H| \sim \epsilon^{-1}$ and some other behaviour will be subsequently observed.

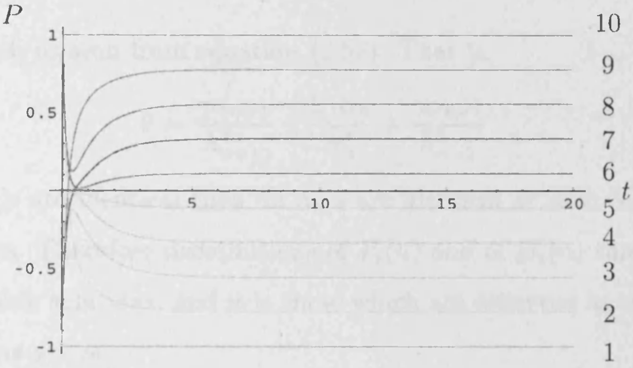

Figure 8.10: In the final example the pressure is perturbed alternately by ±1. Once more the perturbations settle to constant values, in this case at around $t \approx 5$.

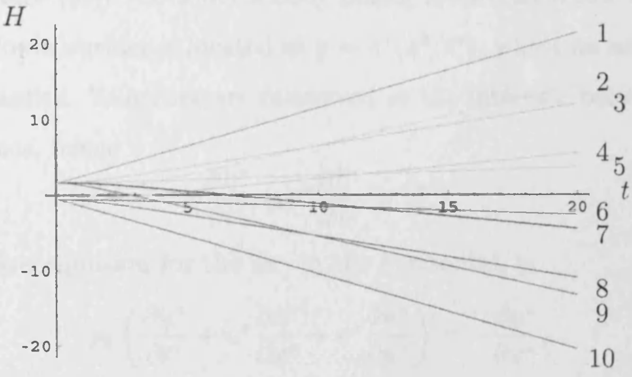

Figure 8.11: The height perturbations of each gap corresponding to the simple initial condition in which the pressures are perturbed by alternate constants, $P = \pm 1$. As in the above cases, the perturbations seem to grow linearly in time.

We remark here that if linear growth of $H(t)$ occurs then, also,

$$0 = P_{n+1} - 2P_n + P_{n-1} \tag{8.77}$$

must be satisfied, as seen from equation (8.52). That is,

$$0 = \frac{\gamma\alpha_{n+1}}{\bar{h}^3_{n+1}} - \frac{2\gamma\alpha_n}{\bar{h}^3_n} + \frac{\gamma\alpha_{n-1}}{\bar{h}^3_{n-1}}. \tag{8.78}$$

Hence, if all $\bar{h}_n$'s are identical then all α_n's are identical or each α_n is the average of its neighbours. Therefore distributions of $P_i(n)$ and of $H_i(n)$ that are linear in i are also acceptable solutions, and it is these which are observed as time increases in the computations above.

8.3 Inviscid air effects

Having examined viscous air effects, inviscid effects are now investigated. In the first instance, we restrict ourselves to the case of inviscid effects between only two grains.

The governing equations are determined as follows (see Smith, Li and Wu for some related details [52]). Consider a body falling toward a surface with downwards velocity V. Its lower surface is located at $y = h^*(x^*, t^*)$, where an asterisk denotes a dimensional quantity. Velocities are conserved at the interface between the air and the body's surface, hence

$$\frac{\partial h^*}{\partial t^*} + u^* \frac{\partial h^*}{\partial x^*} = v^*. \tag{8.79}$$

The Navier-Stokes equation for the air, in the horizontal, is

$$\rho_2 \left(\frac{\partial u^*}{\partial t^*} + u^* \frac{\partial u^*}{\partial x^*} + v^* \frac{\partial u^*}{\partial y^*} \right) = -\frac{\partial p^*}{\partial x^*}, \tag{8.80}$$

where ρ_2 is the density of the air, since viscous forces essentially vanish. In the vertical $\frac{\partial p}{\partial y} = 0$. Finally, the continuity equation is

$$\frac{\partial u^*}{\partial x^*} + \frac{\partial v^*}{\partial y^*} = 0. \tag{8.81}$$

Also note that g is the acceleration due to gravity, ρ_1 and μ_1 are respectively the density and viscosity of the falling body, μ_2 is the viscosity of the air. The typical horizontal length scale of the falling body is l, and the gap between the falling body and the surface is δl with $\delta << 1$, so the gap is small relative to the length of the grain.

We observe that, from the continuity equation, the typical horizontal velocities in the air scale as $u \sim \frac{V}{\delta}$. Therefore v^* can be non-dimensionalised as $v^* = -\frac{y^* u_x V}{\delta}$. Crucially, $v^* \sim u_x$. The other quantities can be non-dimensionalised as $t^* = \frac{\delta l}{V} t$, $x^* = lx$, $u^* = \frac{uv}{\delta}$, $y^* = l\delta h$ and $h^* = l^2 \delta h$.

Thus the kinematic condition in non-dimensional form is

$$h_t + (uh)_x = 0. \tag{8.82}$$

If we further assume that $V =$ constant and $u = u(x,t)$, and scale the pressure as $p^* = \frac{\delta^2}{\rho_2 V^2} p$ then the Navier-Stokes equation becomes

$$u_t + uu_x = -p_x. \tag{8.83}$$

If we assume that the grains are flat then $h = h(t)$ only and equation (8.82) is now

$$h_t + u_x h = 0. \tag{8.84}$$

Now let $u = xU(t)$ so equation (8.83) is

$$x\dot{U} + xU^2 = -p_x, \tag{8.85}$$

where a dot denotes differentiation with respect to t, and equation (8.84) is

$$\dot{h} + Uh = 0. \tag{8.86}$$

Therefore

$$U = -\frac{\dot{h}}{h}. \tag{8.87}$$

By symmetry, and from typical pressure responses seen in these types of fluid problems, we might expect the pressure response to be parabolic:

$$p = \bar{p} + x^2 P(t) \tag{8.88}$$

where $\bar{p}$ is a constant. Therefore equation (8.85) is

$$\dot{U} + U^2 = -2P. \tag{8.89}$$

Substituting equation (8.87) produces

$$P = \frac{\ddot{h}}{2h} - \left(\frac{\dot{h}}{h}\right)^2. \tag{8.90}$$

Consider that at $x = a$, i.e. at the end of the grains, the air is at atmospheric pressure. Therefore, from equation (8.88), we obtain

$$\bar{p} = -a^2 P(t). \tag{8.91}$$

Hence,

$$\int_{-a}^{a} p dx = \int_{-a}^{a} (x^2 - a^2) P(t) dx = -C_1 P(t) \tag{8.92}$$

where C_1 is a positive constant, namely $C_1 = \frac{4a^3}{3}$.

Newton's second law is

$$m\ddot{h} = \int_{-a}^{a} p dx, \tag{8.93}$$

since it is assumed that the only force is due to the air pressure. Hence

$$m\ddot{h} = C_1 P(t). \tag{8.94}$$

On substitution into (8.90) we discover that

$$m\ddot{h} = C_1 \left[\frac{\ddot{h}}{2h} - \left(\frac{\dot{h}}{h}\right)^2\right], \tag{8.95}$$

which is an ordinary differential equation for $h(t)$.

Putting $\dot{h} = G(h)$ yields $\ddot{h} = G\frac{dG}{dh}$. This reduces (8.95) to a first order o.d.e. for $G(h)$:

$$\left(mG + \frac{C_1 G}{2h}\right) \frac{dG}{dh} = C_1 \left(\frac{G}{h}\right)^2. \tag{8.96}$$

Rearranging yields

$$\frac{1}{G}\frac{dG}{dh} = \frac{2c_1}{h(2hm + c_1)} \tag{8.97}$$

Integrating, via partial fractions, produces

$$G = \frac{Ah^2}{\left(h + \frac{C_1}{2m}\right)^2} \tag{8.98}$$

i.e.

$$\dot{h} = \frac{Ah^2}{\left(h + \frac{C_1}{2m}\right)^2}. \tag{8.99}$$

Although it is possible to solve equation (8.99) to find $t(h)$, we prefer to deduce the dynamics by a phase plane analysis. First note that

$$A = \frac{\dot{h}(0)\left(h(0) + \frac{c_1}{2m}\right)^2}{h(0)^2} \tag{8.100}$$

so $A > 0$ if $\dot{h}(0) > 0$ and vice versa. Next, observe that if $h << \frac{C_1}{2m}$ then $\dot{h} \sim h^2$. Conversely, if $h >> \frac{C_1}{2m}$ then $\dot{h} \sim A$. At $h = 0$, $\dot{h} = 0$ and $\dot{h}$ is symmetric about $h = 0$. Finally, we draw attention to the fact that $h < 0$ is unphysical, since this corresponds to overlapping grains.

Therefore, the phase plane is as sketched in figure 8.12. The arrows indicate the direction of motion with increasing time. There are three possible behaviours:

1. Trivially, if $A = 0$ then the grains do not separate or coalesce,
2. If $A > 0$ then the grains separate for all time, asymptotically at a constant speed,
3. If $A < 0$ then the grains approach each other and touch at a finite time.

8.4 Inviscid air effects on many grains

The inviscid air effects on an array of many grains are now investigated. The problem is formulated in a way similar to that in section 8.2, and figure 8.5 is again a suitable schematic diagram. The equations in each air gap are now as follows: the inviscid horizontal momentum equation from the Navier-Stokes equation,

$$\frac{\partial u_n}{\partial t} + u_n\frac{\partial u_n}{\partial x} = -\frac{\partial p_n}{\partial x}; \tag{8.101}$$

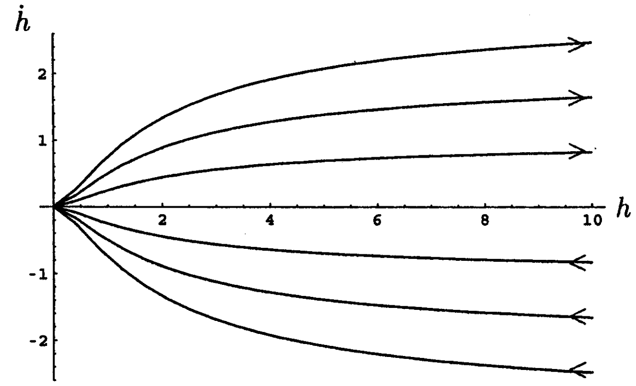

Figure 8.12: A sketch of the phase plane for two grains acting under inviscid air effects. The arrows indicate the direction of motion with increasing time. There are three possible types of motion, as described in the text.

the kinematic condition,

$$\frac{\partial h_n}{\partial t}+\frac{\partial}{\partial x}\left(u_n+h_n\right)=0; \tag{8.102}$$

Newton's second law,

$$m\ddot{f}_n=\int_{-a}^{a}\left(p_{n-1}-p_n\right)dx; \tag{8.103}$$

and a function governing the shape of each grain,

$$f_n(x,t)=f_{n-1}(x,t)+h_{n-1}(x,t)+s(x). \tag{8.104}$$

We note again that the normal pressure satisfies $\frac{\partial p}{\partial y}=0$.

The grains are assumed to be flat so that $h_n=h_n(t)$ only. (If we wrote $h(x,t)=g(x)+h(t)$, $g(x)$ would add a constant only). Thus the kinematic equation can be simplified to

$$\dot{h}_n+h_n\frac{\partial u_n}{\partial x}=0. \tag{8.105}$$

We further assume that $u=xU(t)$, this being a way to examine some simple solutions for which the equations are now separable. Therefore, the simplified Navier-Stokes equation (8.101) can be written as

$$x\dot{U}_n+xU_n^2=-\frac{\partial p_n}{\partial x} \tag{8.106}$$

and the kinematic equation produces

$$U_n = -\frac{\dot{h}_n}{h_n}. \tag{8.107}$$

Hence we arrive at

$$x\left[-\frac{\ddot{h}_n}{h_n} + \left(\frac{\dot{h}_n}{h_n}\right)^2\right] + x\left(\frac{\dot{h}_n}{h_n}\right)^2 = -\frac{\partial p_n}{\partial x}. \tag{8.108}$$

If the pressure response is also assumed to be parabolic then

$$p_n = \bar{p}_n + x^2 P_n(t), \tag{8.109}$$

where $\bar{p}_n$ is a constant. Hence

$$\frac{\partial p_n}{\partial x} = 2xP_n(t) \tag{8.110}$$

and therefore (8.108) is

$$-\frac{\ddot{h}_n}{h_n} + \left(\frac{\dot{h}_n}{h_n}\right)^2 = -P_n(t). \tag{8.111}$$

Since the pressure is atmospheric at $x = \pm a$ we find $\bar{p}_n = -a^2 P_n(t)$. Consequently $p_n = (x^2 - a^2)P_n(t)$. Therefore

$$\int_{-a}^{a} (p_{n-1} - p_n)dx = C_1 P_{n-1}(t) - C_1 P_n(t) \tag{8.112}$$

where once again C_1 is a positive constant and $C_1 = \frac{4a^3}{3}$. This yields

$$m\ddot{f}_n = C_1 P_{n-1}(t) - C_1 P_n(t). \tag{8.113}$$

From equation (8.104) we obtain

$$\ddot{f}_{n+1} = \ddot{f}_n + \ddot{h}_n \tag{8.114}$$

and from (8.103)

$$m\ddot{f}_{n+1} = \int_{-a}^{a} (p_n - p_{n+1})dx. \tag{8.115}$$

Therefore,

$$m\ddot{h}_n = \int_{-a}^{a} (-p_{n-1} + 2p_n - p_{n+1})dx, \tag{8.116}$$

after substituting for (8.103). Ultimately, this yields

$$m\ddot{h}_n = -C_1\left[P_{n-1}(t) - 2P_N(t) + P_{n+1}(t)\right]. \tag{8.117}$$

Equations (8.111) and (8.117) are two coupled ordinary differential equations for $h_n(t)$ and $P_n(t)$. Equation (8.111) is nonlinear. It is desirable to investigate the stability of the array. In order to do this, we will utilize standard linear stability analysis and the method of normal modes.

We shall denote the basic solutions (which are determined shortly) to this problem as $\hat{P}$ and $\hat{h}$. Perturbations

$$P_n(t) = \hat{P}_n(t) + \epsilon\tilde{P}_n(t), \quad \epsilon << 1, \ \tilde{P}_n(t) = O(1) \tag{8.118}$$

and

$$h_n(t) = \hat{h}_n(t) + \epsilon\tilde{h}_n(t), \quad \epsilon << 1, \ \tilde{h}_n(t) = O(1) \tag{8.119}$$

are made about these solutions.

Substituting the perturbed pressure and height into equation (8.111) and performing the appropriate expansions yields

$$-\frac{\left(\ddot{\hat{h}}_n + \epsilon\ddot{\tilde{h}}_n\right)}{2\hat{h}_n}\left(1 - \epsilon\frac{\tilde{h}_n}{\hat{h}_n}\right) + \frac{\left(\dot{\hat{h}}_n^2 + 2\epsilon\dot{\hat{h}}_n\dot{\tilde{h}}_n\right)}{\hat{h}_n^2}\left(1 - 2\epsilon\frac{\tilde{h}_n}{\hat{h}_n}\right)$$
$$= -\hat{P}_n - \epsilon\tilde{P}_n + O(\epsilon^2). \tag{8.120}$$

At leading order it is found, as we may expect, that

$$-\frac{\ddot{\hat{h}}_n}{2\hat{h}_n} + \left(\frac{\dot{\hat{h}}_n}{\hat{h}_n}\right)^2 = -\hat{P}_n, \tag{8.121}$$

which is the equation for the basic flow.

Then, at $O(\epsilon)$ we see

$$-\hat{h}_n^2\frac{\ddot{\tilde{h}}_n}{2} + \frac{\ddot{\hat{h}}_n\tilde{h}_n\hat{h}_n}{2} + 2\dot{\hat{h}}_n\dot{\tilde{h}}_n\hat{h}_n - 2\dot{\hat{h}}_n^2\tilde{h}_n = -\hat{h}_n^3\tilde{P}_n. \tag{8.122}$$

Similarly, at the same order, we find from equation (8.117) that

$$m\ddot{\tilde{h}}_n = -C_1\left(\tilde{P}_{n-1} - 2\tilde{P}_n + \tilde{P}_{n+1}\right). \tag{8.123}$$

The basic solutions $\hat{P}_n$ and $\hat{h}_n$ will be determined later. For the moment the general case is adhered to and normal modes of the form

$$\tilde{P}_n(t) = e^{qt}\tilde{\tilde{P}}_n \qquad (8.124a)$$

and

$$\tilde{h}_n(t) = e^{qt}\tilde{\tilde{h}}_n \qquad (8.124b)$$

are sought. In general, q is complex and $\tilde{\tilde{P}}_n$ and $\tilde{\tilde{h}}_n$ are constants.

Equation (8.122) is thus

$$\tilde{\tilde{h}}_n \left(-\frac{q^2\hat{h}_n^2}{2} + \frac{q\ddot{\hat{h}}_n\hat{h}_n}{2} + 2q\dot{\hat{h}}_n\hat{h}_n - 2q\dot{\hat{h}}_n^2 \right) = -\hat{h}_n^3\tilde{\tilde{P}}_n \qquad (8.125)$$

and equation (8.123) is

$$mq^2\tilde{\tilde{h}}_n = -C_1\left(\tilde{\tilde{P}}_{n-1} - 2\tilde{\tilde{P}}_n + \tilde{\tilde{P}}_{n+1}\right). \qquad (8.126)$$

Now we substitute for the basic flow solution. Observe that if $\hat{h}_n = k$, where k is an arbitrary constant then equations (8.111) and (8.117) are satisfied provided $\hat{P}_n = 0$. Therefore $\hat{h}_n = k$ and $\hat{P}_n = 0$ is an acceptable solution for the basic flow. Consequently equation (8.125) is

$$\tilde{\tilde{h}}_n \left(-\frac{q^2k^2}{2} \right) = -k^3\tilde{\tilde{P}}_n. \qquad (8.127)$$

Now we seek solutions of the form $\tilde{\tilde{h}}_n = \zeta e^{\lambda n}$ and $\tilde{\tilde{P}}_n = \xi e^{\lambda n}$ in order to investigate basic motions of the grains. Equation (8.126) is now

$$mq^2\zeta = -C_1\xi\sinh^2\left(\frac{\lambda}{2}\right) \qquad (8.128)$$

and equation (8.125) is further reduced to

$$\zeta\left(-\frac{q^2k^2}{2}\right) = -k^3\xi. \qquad (8.129)$$

It is therefore possible to determine that

$$\frac{\xi}{\zeta} = -\frac{q^2}{2k} \qquad (8.130)$$

and eliminating both ξ and ζ from (8.128) produces a quadratic equation for q:

$$mq^2 = \frac{C_1 q^2}{2k} \sinh^2 \left(\frac{\lambda}{2} \right). \tag{8.131}$$

Rather surprisingly, the only solution (apart from a special case considered below) is $q = 0$. As a consequence, the normal mode analysis fails and the perturbations seem to neither grow nor decay.

Consider this point a little further. After substituting for the basic flow solution, equation (8.122) can be written as

$$\ddot{\tilde{h}}_n = 2k\tilde{P}_n. \tag{8.132}$$

On substitution into equation (8.123) this yields

$$2km\tilde{P}_n = -C_1 \left(\tilde{P}_{n-1} - 2\tilde{P}_n + \tilde{P}_{n+1} \right) \tag{8.133}$$

i.e.

$$\tilde{P}_n = -\frac{C_1}{(2km - 2C_1)} \left(\tilde{P}_{n-1} + \tilde{P}_{n+1} \right). \tag{8.134}$$

The linearisation allows $\ddot{\tilde{h}}$ to be eliminated from (8.123) and we find that each $\tilde{P}$ is a weighted average of the pressure in the neighbouring gaps. On consideration, this is consistent with $q = 0$. If $q = 0$ then $\tilde{P}_n = \tilde{\tilde{P}}_n$, where $\tilde{\tilde{P}}_n$ is an order one constant. Thus $\tilde{\tilde{P}}_n$ could correspond to the right hand side of (8.134).

Observe that $q = 0$ also implies $\xi = 0$ through equation (8.130) (leaving ζ undefined). Hence $\tilde{P}_n = \tilde{\tilde{P}}_n = 0$ for all n. Therefore we find $\ddot{\tilde{h}}_n = 0$, so

$$\tilde{h}_n = At + B, \tag{8.135}$$

where A and B are constants of integration.

Therefore there is no exponential growth or decay of the gap height between grains. There is, rather, an algebraic growth in the gap height similar to that found for the viscous problem without walls. Physically this relates to a 'drifting' of the grains over time. This drifting would occur for finite times up to $t \sim \epsilon^{-1}$, after which some unknown behaviour would occur.

As an aside we consider the special case of non-zero q. In this instance, we find from equation (8.131) that the wavenumber λ is precisely defined as

$$\lambda = \sinh^{-1}\left(\left[\frac{2k}{m}\right]^{\frac{1}{2}}\right). \tag{8.136}$$

Hence we obtain

$$\tilde{P}_n(t) = \xi \exp\left\{\sinh^{-1}\left(\left[\frac{2k}{m}\right]^{\frac{1}{2}}\right) n + qt\right\} \tag{8.137}$$

and

$$\tilde{h}_n(t) = \zeta \exp\left\{\sinh^{-1}\left(\left[\frac{2k}{m}\right]^{\frac{1}{2}}\right) n + qt\right\} \tag{8.138}$$

for arbitrary $q \in \mathbb{C}$ with k, $m \in \mathbb{R}$.

If we write $q = \phi + i\psi$ we find

$$\tilde{P}_n(t) = \xi e^{i\psi t} e^{\sinh^{-1}\left(\left[\frac{2k}{m}\right]^{\frac{1}{2}}\right)} e^{\phi t}. \tag{8.139}$$

Similarly,

$$\tilde{h}_n(t) = \zeta e^{i\psi t} e^{\sinh^{-1}\left(\left[\frac{2k}{m}\right]^{\frac{1}{2}}\right)} e^{\phi t}. \tag{8.140}$$

We observe, therefore, that for the $q \neq 0$ case there appears to be three eventualities, as follows.

1. If $\phi = 0$ and $\psi \neq 0$ then $\tilde{h}_n(t)$ and $\tilde{P}_n(t)$ are purely oscillatory and the amplitude of the oscillations increases with n.

2. If $\phi \neq 0$ and $\psi = 0$ then $\tilde{h}_n(t)$ and $\tilde{P}_n(t)$ grow exponentially with increasing time. The growth is more rapid for increased n.

3. If $\phi \neq 0$ and $\psi \neq 0$ then $\tilde{h}_n(t)$ and $\tilde{P}_n(t)$ are again oscillatory, but the oscillations blow up as time increases. The blow up is larger for increased n.

These behaviours are different from any seen in the viscous case and are peculiar to the inviscid case.

8.5 Summary

In this chapter we have investigated some of the air effects acting upon the grains.

First, viscous effects between two flat grains were examined. It was found that the grains would be unable to collide owing to lubrication effects.

Second, viscous effects were again examined but this time some representative curvature of the grains was included. The qualitative behaviour remained unchanged. This can be understood by recalling that locally to a point of impact the grains would be flat.

Third, the viscous effects in an array of N grains were investigated in the absence of walls. A normal modes approach suggested that the array could be stable to oscillatory perturbations. However, a computation demonstrated that there is a solution that has linear growth in the perturbed height, with the perturbed pressure tending to a constant. This was found to be compatible with the analysis. The linear growth will dominate over the normal modes behaviour until a finite time of order ϵ^{-1}, after which some other unknown behaviour would come into play.

Inviscid effects were then researched. Initially, we returned to the case of only two flat plates. A phase plane analysis revealed that two non-trivial behaviours exist: either the grains separate for all time, asymptotically at a constant speed, or the grains coalesce after a finite time.

Finally, inviscid effects between an array of grains in the absence of walls were studied. Similar behaviour to the viscous case was seen to occur. That is to say, there was a linear growth in the perturbed gap height with equal pressures in each gap. This corresponded to a drifting of the grains for a finite time ($t = O(\epsilon^{-1})$), after which some other, as yet undetermined, behaviour would dominate the flow. In an aside we briefly examined a special case with behaviour that was different to the viscous case.

Some questions of interest that remain unanswered are as follows. First, for the viscous analysis when walls are present, it would be satisfying to determine analytically the value of α for which the air-grain flow regains stability. Second, in the examples in which we demonstrated that the grains 'drift' up to $t = O(\epsilon^{-1})$ the large time behaviour is undetermined. We do not know if these motions will lead ultimately to instabilities or not. Finally, only certain sorts of grain motions have been allowed in the formulation of the problems in this chapter. It would be of interest, for example, to research how changes in grain orientation would affect the stability.

Chapter 9

Concluding remarks

9.1 Overview

In this thesis we have developed a potential mathematical model for a chute flow of grains. This was motivated by a particular problem from the food-sorting industry (Sortex Ltd). As there is no existing 'grand unified theory' of chute flows, we have necessarily advanced a relatively simple and basic model for the grain flow. Nevertheless, the model has yielded some complex and interesting results of both a mathematical and practical nature.

In particular, a main new feature in this thesis is the extension of the Lighthill-Whitham theory of traffic flow to the chute flow. This involves the introduction of a multivalued flux-density relationship and also a multivalued wave-speed. The strengths and weaknesses of the fundamental diagram in this thesis have been discussed. Such a law generates many new interesting problems, and much of the thesis has been concerned with this. Problems of especial mathematical interest have been the inclusion of shocks and fans into the analytical and numerical solutions of the governing equation, the modification of the fundamental curve to include viscous branch switching, the impact that this has on solutions relating to separation and clustering of grains, and the search for general solutions and steady states of the governing equation. We mention here specifically that the problem of finding steady states computationally was not a trivial one.

Prior to developing the continuum theory for the chute flow, we investigated a basic case of one particle in a chute. Following this, a large computation of the many-grain flow was undertaken. This revealed that clustering is indeed a key feature of the grain flow.

The thesis ended with an analysis of air effects on the grain flow. We demonstrated that viscous effects prevent grains from touching, both for flat and curved grains. Then an original study of the interaction effects on an array of grains was undertaken. We observed that in the absence of the walls the array is neutrally stable and a 'drifting' of the grains occurs. This dominates over the stable normal modes behaviour. Inviscid effects were also researched. Grains are able to touch if viscosity is ignored. Surprisingly perhaps, the interaction effects within an inviscid array demonstrate a similar qualitative behaviour to that observed for the viscous case, including the finding of marginal instability.

9.2 Summary discussions of each chapter

We present here a more detailed discussion of the results from each chapter.

In chapter 2 we showed that a continuous approximation yields a fair agreement with the inherently discrete problem of one particle bouncing down a chute, when compared to results from an iterative scheme. The approximation was to take the coefficient of restitution close to unity in a narrow chute. Air effects on a single falling grain were also addressed and notably we observed that the boundary layer is of the order of the grain size.

A computational simulation of the many-grain flow was expounded in chapter 3. First, a simple code was developed by the author. This used simple ballistic laws for the particles' motion and neglected air effects. Binary collisions only were considered. Collisions were detected by an 'overlap' method. Clustering is seen to be a key feature, and is dependent on the coefficient of restitution. The results from the simulation appeared to agree qualitatively with those provided by Sortex.

More complex effects of vertical interactions between particles and effects of chute geometry, and the combination of the two, were studied with the aid of a commercially available code called PFC2D. Clustering is still a key feature for these flows, but perhaps less so for those which include vertical interactions.

Chapter 4 briefly discussed possible analytical methods that may be of use when studying chute flows. A short probabilistic analysis was presented, but appeared to generate poor results. The value of continuum modelling in other problems of a particulate nature, such as in traffic or pedestrian flows, was also addressed.

In chapter 5 the continuum modelling for the chute flow was begun in earnest. An analogy to the Lighthill-Whitham model was utilized. Most notably, our model involved the introduction of a multi-valued fundamental diagram for the flux-density relationship. This in turn generated a multi-valued wave speed for any given density. The basic features of the fundamental diagram were postulated by basic physical concerns. In particular, the fundamental curve was symmetric about the ρ-axis and the two branches met at cusps at zero and maximum density. The strengths and weaknesses of the fundamental diagram in the thesis have been discussed. In particular, we point out that the flux-density relation in this thesis may be especially relevant to colliding or separating grains, but by no means should it be expected to describe the *entire* chute flow.

We solved the resultant hyperbolic kinematic wave equation by a method of characteristics. Shocks and fans must sometimes be incorporated in the solutions. In the results presented in this chapter, only discontinuous input was considered, as this formed a basic starting point for the analysis. Some quite complex solutions were contrived which incorporated a series of shocks and fans as the solution switched branches. These were seen to describe well the clusters and voids on the chute. The chapter ended with some remarks on mass conservation and entropy.

More general solutions were sought in chapter 6 focusing solely, however, on cases which remain always on one branch of the fundamental diagram. In order to find solutions numerically, an artificial viscous dissipation term was added to change the equation from a hyperbolic to a parabolic partial differential equation. (Actually there is also some physical support for including such a term). This had the effect of 'smoothing out' the discontinuities so that problems associated with shocks and fans did not occur within the computation. This modified equation was called 'the continuum equation'.

We solved the equation by a finite difference scheme to replicate closely the evolution of expansion fans and translating shocks found in the inviscid analysis in chapter 5. The analysis was then extended from solutions with, or mimicking, discontinuous input and instead we attempted to solve the continuum equation for a smooth initial condition. We found an asymptotic solution valid at small time and compared this to the result from the finite difference scheme, a satisfactory measure of agreement being observed.

Steady state solutions for the one-way flow were then examined. We found analytically a steady state for the case of the densities at the boundaries being nearly equal. Others were sought numerically but the code appeared to be very sensitive when checked against solutions to the steady governing equation. We suspect that the sensitivity may arise from inaccuracies introduced at the change in direction of the upwind differencing.

Two-way flows, for which the grains can move to and fro across the chute, were examined in chapter 7. First, viscous branch switching was discussed. As the governing equation is now a parabolic partial differential equation, we argued that the nature of the fundamental curve should be changed in a small viscous region near the branch switches. The aim was to find solutions that can smoothly switch branches by changing the local curvature at the branch switches.

Initially, we addressed the branch switch at the zero density end of the fundamental diagram. We found a similarity equation for low densities valid at small times. This was in fact a nonlinear ordinary differential equation that corresponds to separating regions. The equation is singular at zero density, so we found a series solution locally. Runge-Kutta schemes were then employed to find the density either side of this minimum, showing that smooth solutions can indeed exist. In particular, we found that the density must always be zero in the centre of a separating region and that symmetric and asymmetric solutions can exist. This corresponds to voids forming between regions of the same or differing density. The minima in the asymmetric solutions can move in time, a property which has ramifications for the steady state solutions mentioned below. Separately, an analysis yielded solutions that are asymptotically close to a simple exact solution. Thus we demonstrated that a large region of low density can evolve, which mimics the evolution of a large void and agrees with the Runge-Kutta findings.

Following this, we examined the branch switch at maximum density. Here we introduced a small viscous layer valid to order one times and found the appropriate scalings for the density, the flux and the wave-speed. This resulted in a partial differential equation for the local density which was inverted and solved by a finite difference scheme, in order that the dependent variable in the partial differential equation was single-valued. Smooth symmetric and asymmetric solutions indicative of the evolution of high density clusters were found to exist.

Thus we demonstrated that changing the fundamental diagram to include local viscous regions allowed smooth solutions to form which incorporated branch switching. We therefore attempted to find steady state solutions and solutions at large times that have a smooth branch switch. In order to do this, we solved the continuum equation in polar coordinates for a simplified (circular) fundamental diagram, to capture the essential features of the two-way flow. A few steady states could be found analytically and numerically, but although we demonstrated that the problem is not over-prescribed it was difficult to find very many solutions that were significantly different. Some solutions can be found which join together the sinusoidal-type solution with a constant solution; however, we find that such solutions have a $t^{\frac{1}{2}}$ growth at order one times at the 'junctions' and thus do not form valid steady state solutions, in the sense of a steady state being a large-time limit. Hence they were ultimately dismissed.

Finally, in chapter 8, the effect of the air on the grain flow was researched. First we examined viscous effects between two grains in the case of the separation between grains being relatively small. We assumed that the dominating force is the pressure in the air between the grains and that lubrication theory is valid there. We found the well-known result that the viscosity prevents the grains from touching, if other effects are neglected. We included some representative curvature and the same qualitative result was seen to hold true. We then examined the viscous air effects for a large array of many grains separated by lubricating layers. A normal mode analysis revealed that such an array could be stable to spatially oscillatory perturbations. A computation however, accompanied by some analysis, demonstrated that a linear growth in the height of the gaps could occur, at least for order one times. This dominates over the stable behaviour mentioned above. Thus the grains are observed to 'drift' over time. Inviscid effects were then addressed. The governing equations in this case were a reduced form of the Navier-Stokes equations accompanied by a kinematic condition. Initially, we returned to the case of two flat grains and noted that the grains can now touch during impacts. When the stability of a large array of grains separated by small inviscid layers was investigated, we observed a behaviour qualitatively similar to that in the viscous case. That is to say, a linear growth in the perturbations was again seen for order one times, corresponding to a drifting of the grains.

9.3 Suggestions for future work

We finish the main body of the thesis with some suggestions for future work.

One extension could be to further develop the computational simulations of chapter 3. This could include research on other modifications to the chute shape, perhaps in the plane of the falling grains. Other effects to be studied could be friction between grains, friction between grains and the chute, surface roughness and so on. Non-spherical particle shapes could also be included. This would make the numerics significantly harder as spin must be included and collision detection between particles is no longer trivial. A three-dimensional simulation could also be developed. A rigorous quantitative measure of the clustering might be considered.

Some statistical methods were discussed in chapter 4. These may form problems of interest for future work. In particular, the lattice gas automata technique could be used to model the grain dynamics and the statistics of random walks could be applied.

Concerning chapter 7 the non-smooth solutions could perhaps be investigated further. Questions of interest are, for example: 'For how long spatially will the flat regions persist?' and 'How do the flat and sinusoidal regions match at large times?'. Also, the computation in this chapter could be changed to incorporate a compact difference scheme, as opposed to the standard finite difference scheme we have employed. This might obviate problems associated with the change in directional windward differencing and produce more robust solutions. Furthermore, the simplified fundamental diagram we have used in these computations could be adapted to be more realistic and perhaps more similar to the one originally described. It would be interesting to find the steady states in this case. Finally here, the relationship between mass conservation and the difficulty of finding solutions at large times could be examined further.

Concerning the final chapter, it would be of interest to find the large time behaviour of the viscous and inviscid arrays that were observed to drift with time. In particular, over a larger (nonlinear) time scale, do they remain marginally unstable or do they become strongly unstable? Chute walls could be included in the calculations for the viscous and inviscid arrays, indeed some preliminary work has been undertaken for the former case and an interesting dependence of the stability on the angle of inclination of the grains to the wall seems to exist. We hope to examine this fully in a future paper. Finally, here, different grain motions could be investigated, especially those which permit the orientation to change.

More generally, it is greatly appealing to extend the continuum model to two dimensions and thus include interactions between sets of falling particles. Chapters 5 - 7 could be repeated for such a theory where the two dimensional equations (5.7) and (6.2) would now be relevant. This model would perhaps be more applicable to the industrial setting and it would be fascinating to study the extra effects in themselves.

Appendix A

A simple test of the computational simulation

It is possible to find an exact expression for the velocity of a particle in a simplified case of the many-grain chute flow. We can compare this to the velocity found in a corresponding simulation as a way of checking whether the code is correct.

A.1 Velocity of the leftmost particle

Consider a very simple configuration of particles in the chute. Suppose that particles enter the top of the chute evenly spaced along the line $y = 0$. Furthermore, suppose that all particles have zero initial velocity with the exception of one particle at the far right-hand end of the chute (named the 'renegade' particle) which has a finite horizontal velocity component directed toward its neighbour. All particles except the renegade will initially fall vertically through the chute. The renegade will follow a parabolic trajectory for some time. At the first collision, the renegade will collide with its neighbouring particle. This particle will now have a horizontal velocity component and the horizontal velocity component of the original renegade will have been reduced. We call the leftmost particle that has a parabolic path 'the leftmost particle'. (In reality this is not *the* leftmost particle, that would be the vertically falling particle at the other far end of the chute). A plot of the leftmost particle is

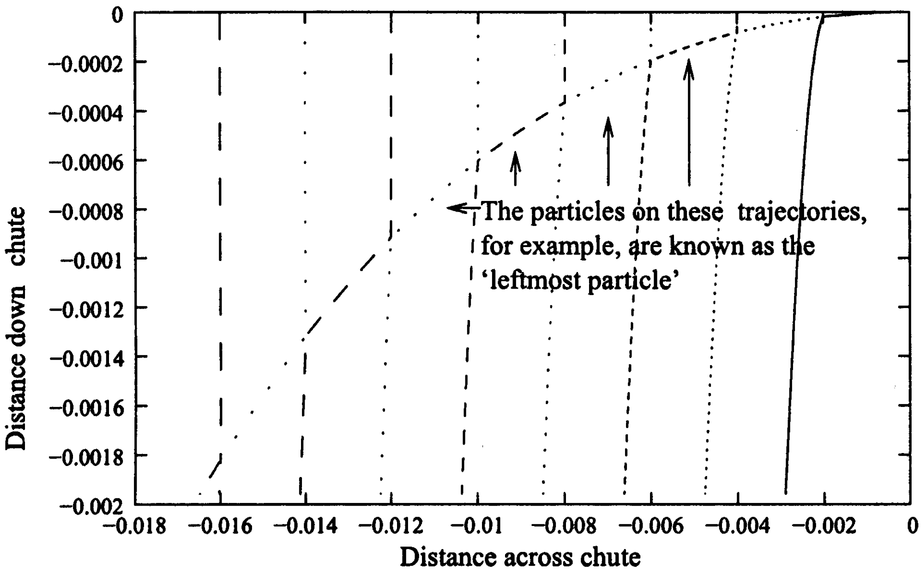

Figure A.1: The parabolic trajectories are the path of the 'leftmost particles'

shown for clarity in figure A.1.

It is possible to determine analytically the velocity of the leftmost particle at each collision. Call $\hat{u}_n$ the velocity of the leftmost particle at the n^{th} event. Then we see that

$$\hat{u}_2 = \frac{(1+\hat{e})}{2}\hat{u}_1 \tag{A.1}$$

from equation (3.10), since all other u_i's are initially zero. Thus at the n^{th} collision,

$$\hat{u}_n = \left(\frac{1+\hat{e}}{2}\right)^n \hat{u}_1. \tag{A.2}$$

We can plot this expression for the velocity of the 'leftmost particle' against the results from the simulation. To do so, we simply choose the initial conditions in the code to arrange the particles in the configuration described and record the appropriate velocity. We find that there is a very close agreement, see figure A.2. This adds some weight to the view that the code produces accurate results.

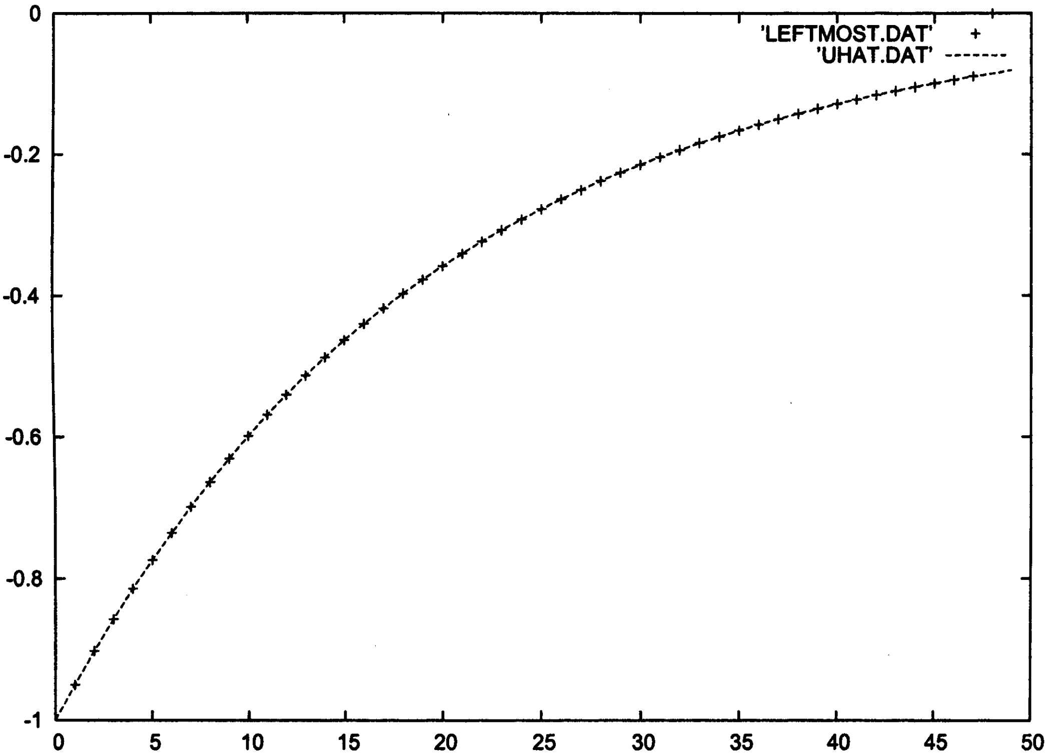

Figure A.2: Plot showing velocity of the leftmost particle against number of collisions. The points are the data from the simulation, and the line is the analytic solution found above. We see very close agreement.

Appendix B

Detailed study of clustering

In this appendix we consider clustering a little more thoroughly.

Choosing a periodic velocity distribution will provoke the clustering phenomenon as there will be regions where all the particles are moving toward a fixed point and regions where all the particles separate from a fixed point. Clusters and voids will begin to form around these points. We can locate these points simply as the roots of the horizontal velocity component: roots across which the velocity is decreasing are the points where clusters form, while roots across which the velocity is increasing are the points where voids form. If $\hat{e} = 0$ then particles will coalesce at the point where clusters form and create one large particle of ever-increasing mass. Thus it is possible to find the distance between successive coalesced particles on the chute for different initial conditions, provided $\hat{e} = 0$. Furthermore, we can also find a correction for this separation distance for non-zero $\hat{e}$. We can compare this theoretical value to one estimated from the numerics to determine whether the suggested mechanism for clustering is indeed the correct one.

Consider an initial velocity distribution of the form

$$u_i = A\cos(ki) \tag{B.1}$$

where u_i is the particle velocity for the i^{th} particle. The amplitude of the velocity is A and k is the wave number. Recall that the particles are initially evenly spaced along a horizontal line; the horizontal co-ordinate, x, of the i^{th} particle is given by

$$x_i = (i-1)d \tag{B.2}$$

where d is the particle separation. Hence,

$$u_i = A\cos\left(k\left(\frac{1-x_i}{d}\right)\right), \tag{B.3}$$

and the wavelength, λ, is

$$\lambda = \frac{2\pi d}{k}. \tag{B.4}$$

Let us also define m as

$$m \equiv \frac{\lambda}{d} = \frac{2\pi}{k}. \tag{B.5}$$

If we wish one wavelength of the velocity to exactly coincide with the particle positions we must choose $m = 1$ so that $\lambda = d$. Thus all the particles will have the same velocity and will not collide with each other. Consequently there will be no clusters. If, however, we choose $m = 2$ then $\lambda = 2d$ and so there will be pairs of particles moving toward each other, see figure B.1. Hence we expect evenly spaced clusters to form with a separation, denoted $\lambda_{cluster}$, equal to $2d$.

Furthermore, if $m = 3$, then every third particle is going rightward, and the two particles in between are going leftward. Hence the first collision is between the rightward moving particle and the neighbouring leftward moving particle. Following this we will have a coalesced particle still moving rightward heading toward the remaining leftward moving particle. These will collide to form a coalesced particle composed of the three initial particles and there will be no further collisions. In this situation the separation between clusters is $\lambda_{cluster} = 3d$.

The case for $m = 4$ is a little more involved. In this situation the velocity distribution coincides with the particles so that one particle is moving rightward, the next is stationary, the third is moving leftward and the final one is stationary again before the pattern is repeated. Thus the final state is a cluster of three particles centred on the second particle, called a triplet, followed by the fourth particle which is stationary and on its own, the singlet. See figure B.2 for clarity. Here we define $\lambda_{cluster}$ as the distance between successive triplets and so $\lambda_{cluster} = 4d$.

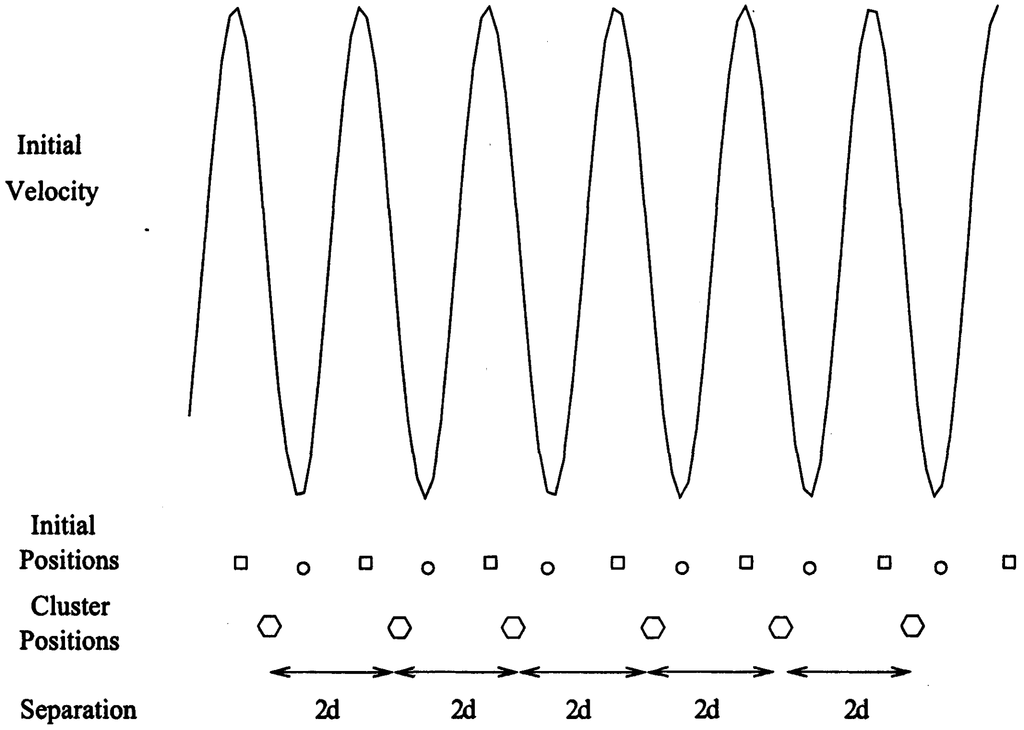

Figure B.1: Sketch showing cluster formation for $m = 2$. The particles represented by a square are moving rightward, the particles represented by a circle are moving leftward. Thus clusters form in the positions depicted by a hexagon. We expect to see the separation between clusters to equal $2d$ in this case.

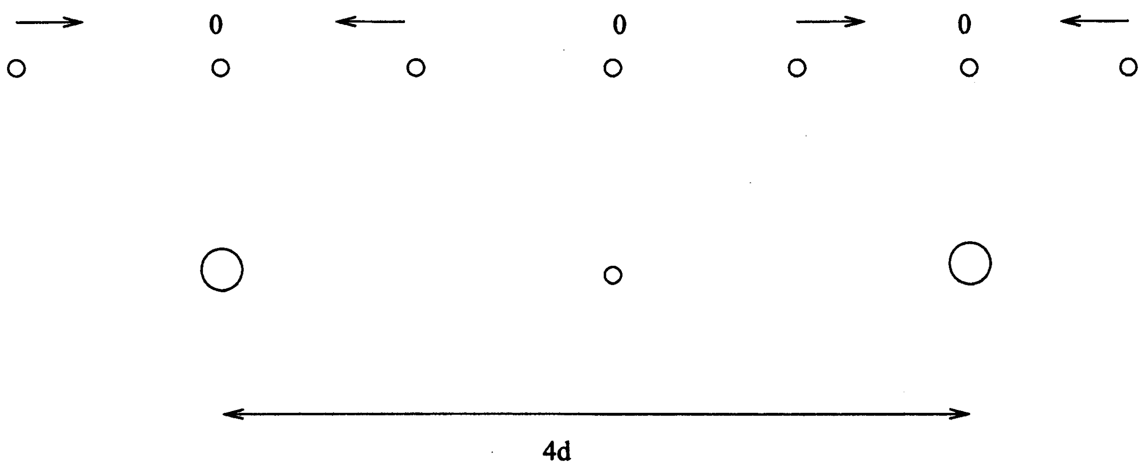

Figure B.2: Sketch showing cluster formation for $m = 4$. The top line depicts the initial particle positions and their velocities. A zero above a particle denotes that it is stationary. The triplets form in the positions depicted by the large circles. We expect to see the separation between triplets to equal $4d$ in this case.

Unfortunately it is problematic to go further than $m = 4$ since for higher values of m it becomes difficult to define clusters; the situation becomes ever more complex involving singles, pairs and triplets and so on. Consequently, we stop here and compare the theoretical value of $\lambda_{cluster}$ to the one obtained from the numerics, λ_{obs}.

To calculate λ_{obs} we measure the distance between the centres of ten clusters at the end of the corresponding simulation and find the average. It must be noted that this method is rather subjective since it is a little awkward to find the centre of each cluster. Also, in the above analytics we calculated $\lambda_{cluster}$ for $\hat{e} = 0$. It is not possible to run the computation for this value of $\hat{e}$, so instead we obtain λ_{obs} for $\hat{e} = 0.01$.

The results presented in table B.1 are quite close for each value of m. This mechanism seems therefore to be useful in describing the physical process of clustering.

Table B.1: Table of results in which predicted values of the separation between clusters, $\lambda_{cluster}$, are compared to those from the computation. We see fairly good agreement.

Comparison of $\lambda_{cluster}$ to λ_{obs}		
m	$\lambda_{cluster}$	λ_{obs}
1	-	-
2	0.0040	0.0039
3	0.0060	0.0057
4	0.0080	0.0075

B.1 Further results concerning clustering

In the computation above we obtained values of λ_{obs} for small $\hat{e}$, as opposed to $\hat{e} = 0$ which was the value used in the analysis. Now we obtain a correction to the analysis for the $m = 2$ case for non-zero $\hat{e}$.

At a collision the particle velocities are changed in accordance with equations (3.9) and (3.10). After the collision we see that two particles 1 and 2 would separate with a velocity given by

$$\bar{u}_1 - \bar{u}_2 = -\hat{e}\,(u_1 - u_2) \tag{B.6}$$

for non-zero $\hat{e}$. Rather than coalesce, the two particles will actually have separated by a distance given by s:

$$s = -\hat{e}(u_1 - u_2)t, \tag{B.7}$$

where t is the time spent in the chute. Consequently, $\lambda_{cluster}$ is reduced by this distance and the new value is $\lambda'_{cluster}$ where

$$\lambda'_{cluster} = \lambda_{cluster} - \hat{e}(u_1 - u_2)t. \tag{B.8}$$

Applying the above correction, the new value for the separation between clusters is $\lambda'_{cluster} = 0.00399$. This is only marginally closer to the computed value $\lambda_{obs} = 0.0039$. (N.B. the computed value itself is only a rough approximation anyway;

recall that it is difficult to locate the centre of the clusters when making the required measurement of λ_{obs}).

We observe that $u_1 - u_2 = 2A$, for the case of $m = 2$, where A was the amplitude of the velocity. Therefore the correction, s, is $s = 2\hat{e}At$. If the time spent on the chute is $t = O(1)$ then $s = O(\hat{e}A)$. Furthermore, consider that $\lambda_{cluster} = md = O(d)$. Therefore if $s \sim \lambda_{cluster}$ then the clustering structure will break down. Particles from one cluster will have separated so much they will have entered the neighbouring cluster. Thus the final particle distribution will look homogeneous (see figure 3.2, for example). Therefore if

$$\hat{e} \sim \frac{2d}{A} \tag{B.9}$$

then the clustering phenomenon will disappear, for the case of $m = 2$. For typical values in the computation we find that this value is around $\hat{e} = 0.4$.

Appendix C

Experimental work

In chapter 3, section 3.4, we employed nearest neighbour distributions in order to measure the clustering on the chutes. This is a naive approach, used simply as a guide. Some experimental work however was undertaken at Sortex Ltd, the purpose of which was to find a more rigorous quantitative measure of the clustering. We briefly discuss this work here. (Complete reports of this work are available from the author on request).

First, we review the work on nearest neighbour distributions. We define a quantity c as

$$c = 2\sqrt{N_A}\left(\langle\bar{n}\rangle - \frac{1}{2\sqrt{N_A}}\right) \tag{C.1}$$

where N_A is the number of particles per unit area, $\bar{n}$ is the mean nearest neighbour distance and $\langle\bar{n}\rangle$ is the average of the mean nearest neighbour distance after many trials. For a random (Poisson) distribution the mean nearest neighbour distance is the Poisson mean[48],

$$\langle\bar{n}\rangle_{\text{Poisson}} = \frac{1}{2\sqrt{N_A}}. \tag{C.2}$$

If the particles are uniformly distributed, then the mean nearest neighbour distance is simply

$$\langle\bar{n}\rangle_{\text{uniform}} = \frac{1}{\sqrt{N_A}}. \tag{C.3}$$

Therefore c can be used to quantify the clustering from a nearest neighbour distribution as follows. If the distribution is uniform then $c = 1$ from equation (C.3);

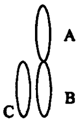

Figure C.1: Particles A and B are touching and yet C is the nearest neighbour of B. If particle B is ejected it is likely that A would be ejected too, rather than the nearest neighbour C. In this instance, finding the nearest neighbour has been fruitless.

if the distribution is random then $c = 0$ from equation (C.2); if the distribution is clustered then $\langle \bar{n} \rangle < \frac{1}{\sqrt{N_A}}$ [48] and so $c < 0$. This quantity is calculated for each nearest neighbour distribution.

We find that both for synthetic and for real data the quantity c gives ambiguous results for the clustering. Nevertheless, it seems likely from the experimental data that the particle distributions at the bottom of straight chutes are random.

Nearest neighbour distributions, moreover, would perhaps seem to be a poor clustering measure for ellipsoidal particles. When a particle is ejected, its surrounding particles and particles touching it are usually ejected as well. This is the root of the inefficiency of the machines. It could happen that two grains of rice, A and B say, are touching end-to-end along their major axes and that a third grain C is neighbouring the particles and not touching the grains. Yet this particle (C) could be found as the nearest neighbour. See figure C.1, for example. In this case it is fruitless to find the nearest neighbour, as the touching particle is perhaps more likely to be erroneously ejected.

Another measure of the clustering was consequently investigated and this is reviewed below.

The general idea for the new method is to place a grid of boxes over an image of the product feed. The number of grains in each box is counted and the standard deviation in particle number per box is found. If the feed is uniform, a small standard deviation is expected whereas if the feed is clustered, a large standard deviation is expected.

The standard deviation in particle number per box is defined as

$$s = \sqrt{\frac{1}{N-1}\sum_{n=1}^{N}(x_n - \bar{x})^2}, \tag{C.4}$$

where N is the total number of boxes, x_n is the number of particles in the n^{th} box and $\bar{x}$ is the average number of particles per box. The standard deviation is measured for twenty trials of each experiment and the signal, m, is the average:

$$m = \frac{1}{20}\sum_{i=1}^{20} s_i, \tag{C.5}$$

where, s_i, is the standard deviation at the i^{th} trial. The noise in the measurement is defined to be the standard deviation in s_i,

$$\text{noise} = \sqrt{\frac{1}{19}\sum_{i=1}^{20}(s_i - m)^2}. \tag{C.6}$$

Finally, we define a 'discriminant' between two feeds A and B as

$$d = \frac{m_A - m_B}{\text{noise A} + \text{noise B}}. \tag{C.7}$$

If trial A gives a significantly more uniform flow than trial B, in terms of uniformity of feed, then d is large and negative, and if the converse is true then d is large and positive.

The discriminant was tested first on synthetic data and in each case the expected results were seen, i.e. the discriminant correctly 'identified' the chute with the most clustering. When tested on data from experiment the discriminant was again seen to be a useful measure of clustering. Therefore we can conclude that the discriminant may be able to suggest which chutes yield the better performance in terms of uniformity of feed.

In summary, the experimental work undertaken by the author at Sortex Ltd. reveals that

1. the nearest neighbour distributions may not be a useful measure of clustering, especially for ellipsoidal particles; and

2. the discriminant d, defined above, is a useful factor in comparing chute performances.

Appendix D

Grain-wall interactions in the inviscid model

We propose an argument to find the relevant analytical solutions that incorporate shocks and fans interacting at the chute walls. The physical boundary condition must be for there to be no flux across a wall, which implies that either $\rho = 0$ or $\rho = \rho_M$ at the wall. As yet, both seem equally valid. However the argument in the current appendix forces $\rho = \rho_M$. If a particle collides with a wall then its velocity can be considered to instantaneously change direction at impact. The magnitude of the rebound velocity depends on the value of the coefficient of restitution between the grain and the wall. As the flux q is propagated along a characteristic, this must change at the wall due to the fact that the particle rebounds. Therefore the gradient of the characteristic must change. If the incoming characteristic has $q > 0$ say, then the outgoing characteristic must have $q < 0$. The magnitude of q along the outgoing characteristic is then determined by the value of the coefficient of restitution. Two cases are considered: first, the case when the coefficient of restitution $\hat{e} = 0$; second, the case when the coefficient of restitution $\hat{e} = 1$. The former case corresponds to totally inelastic collisions in which colliding grains lose all their energy upon impact and coalesce; the latter case corresponds to totally elastic collisions in which colliding grains do not lose any energy at an impact. We shall see in both cases that $\rho = \rho_M$

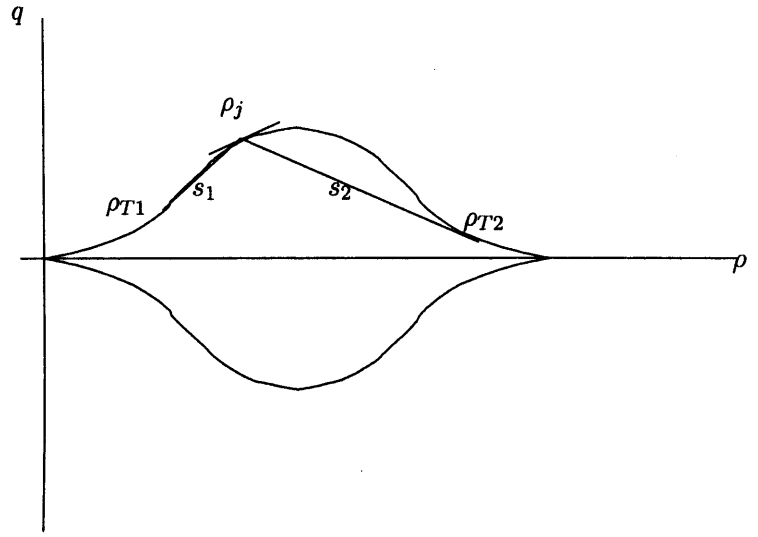

Figure D.1: A sketch of the fundamental curve and the key values for the case of clashing at walls when $\hat{e} = 0$. The two shocks are also shown.

is forced at the boundaries, consistent with the no-flux condition across the walls. In theory, intermediate values of $\hat{e}$ could also be dealt with.

D.1 Case one: $\hat{e} = 0$

If $\hat{e} = 0$, all grains will coalesce upon collision. This is analogous to a queue forming at a traffic light. Suppose we start with incoming grains flowing freely toward a wall at some value $\rho = \rho_j$. Then we start with characteristics of slope $c(\rho_j)$. At the end of this region there are no incoming particles, so there is the appropriate shock fan structure down to zero density. (There is not a continual input of grains). At the wall particles coalesce, thus $\rho = \rho_M$. Hence there is another shock-fan structure between ρ_j and ρ_M. Figures D.1 and D.2 illustrate this well.

Observe that at $t = t_3$ the two shocks merge and form a third shock between the two expansion fans. As this shock translates, it weakens over time (the gradient of the shock tends to zero). Thus, the density profile asymptotes to two expansion fans separated by a stationary shock.

Thus a picture of the evolution of the density profile can be obtained. See figures

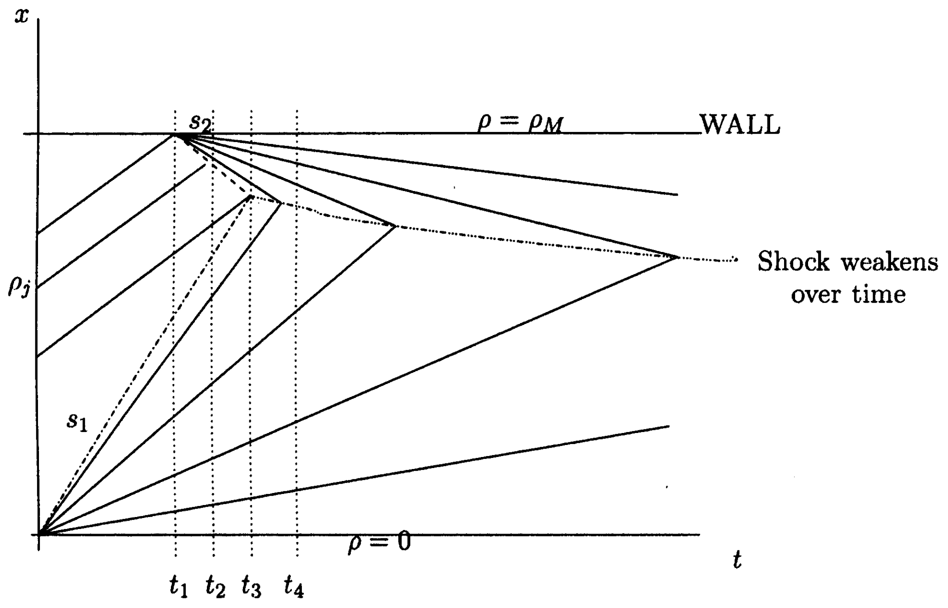

Figure D.2: The characteristics are plotted in the $x - t$ plane. The characteristics describing the incoming region of constant density can be seen adjacent to and above the shock-fan structure down to zero density. There is also a shock-fan structure after the point where the first characteristic intersects the wall, which describes the coalescing grains there. These two shocks intersect at $t = t_3$ after which a single shock separates the two fans. This shock weakens over time (viz. its gradient, and therefore its speed, decrease over time).

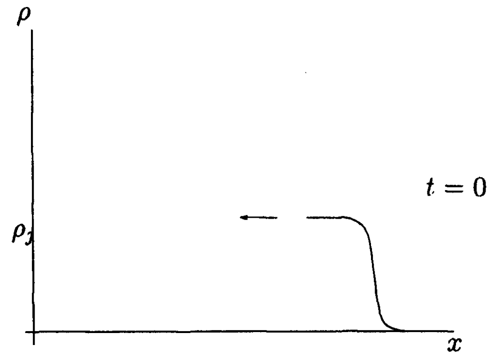

Figure D.3: Initially there is a region of constant density moving toward the wall.

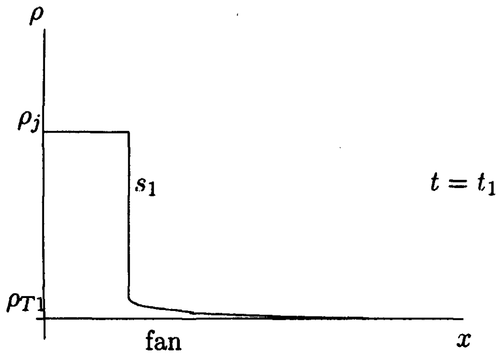

Figure D.4: At $t = t_1$ the grains just reach the wall. A leftward translating shock exists adjacent to a fan from ρ_{T1} to $\rho = 0$.

D.3 - D.7.

D.2 Case two: $\hat{e} = 1$

If $\hat{e} = 1$, an incoming grain will collide at the wall and reverse its direction. If we have an incoming particle with $(\rho, q) = (\rho_j, q_j)$ then upon a collision with a wall it will instantaneously change its direction and have $(q, \rho) = (-q_j, \rho_j)$. Thus when the incoming characteristic intersects with the wall its gradient will instantly switch from $c(\rho_j)$ to $-c(\rho_j)$. This 'reflected' characteristic will in turn intersect with the next incoming characteristic. The sign of q is different on each of these characteristics, hence the familiar shock-fan-shock structure is required to describe

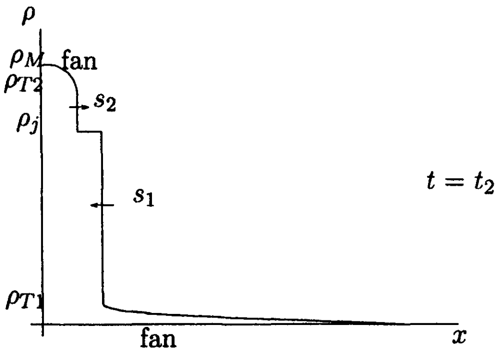

Figure D.5: As the grains coalesce at the wall, a region of maximum density is formed. A rightward and leftward moving shock expunge the region of constant density.

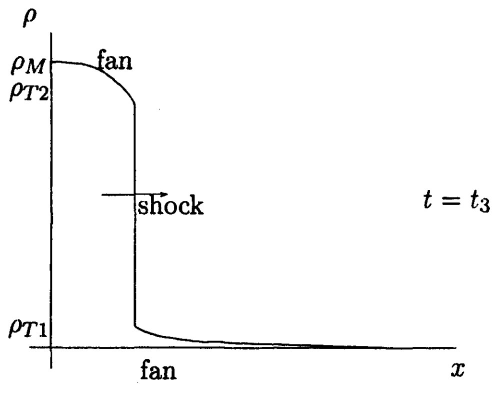

Figure D.6: The two shocks, s_1 and s_2, have merged to form one rightward translating shock. There is a high density fan next to the wall, and a low density fan next to the shock.

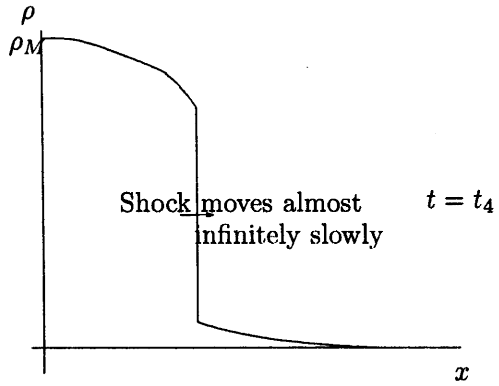

Figure D.7: Eventually the shock will come to rest. The final profile is a high density region next to the wall that protrudes on to the chute for a certain distance. Then there is a discontinuous jump to a low density region which becomes ever more sparse.

this clashing region.

As the colliding grains are moving away from the wall there will be a shock-fan structure down to zero density located at the wall. The upper shock from the shock-fan-shock structure describing the clashing of the reflected and incoming grains will then enter the expansion fan at the wall and weaken. As a consequence, the expansion fan down to zero density, which is located at the wall, will vanish and be replaced entirely with the $q > 0$ half of the expansion fan from the clashing region. See figures D.8 and D.9.

Now note that in reality the characteristics $(*)$ and $(**)$ will be infinitesimally close for the incoming $c(\rho_j)$ particles. As they coincide this case becomes identical to the $\hat{e} = 0$ case because the shock-weakening and vanishing of the fan at the wall, described above, happen instantaneously. This is made clear in figure D.10.

Therefore, by examining two extreme cases, we have seen that the correct condition at chute walls is for the density to be maximal, i.e. $\rho = \rho_m$ at boundaries. For values of $\hat{e}$ in between zero and one, we assume that this is still the case. This appears to be reasonable since the cases of fully inelastic and fully elastic collisions yield the same result.

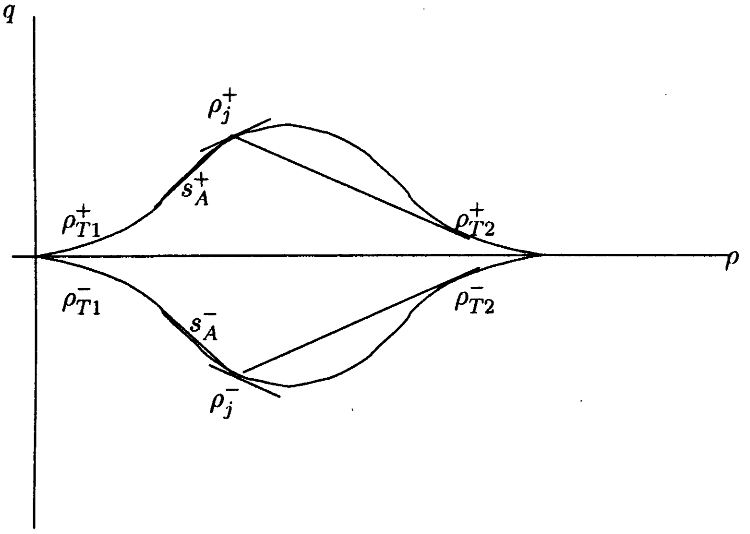

Figure D.8: A plot of the fundamental curve and the key values for the case of clashing at walls when $\hat{e} = 1$. The shocks are also shown.

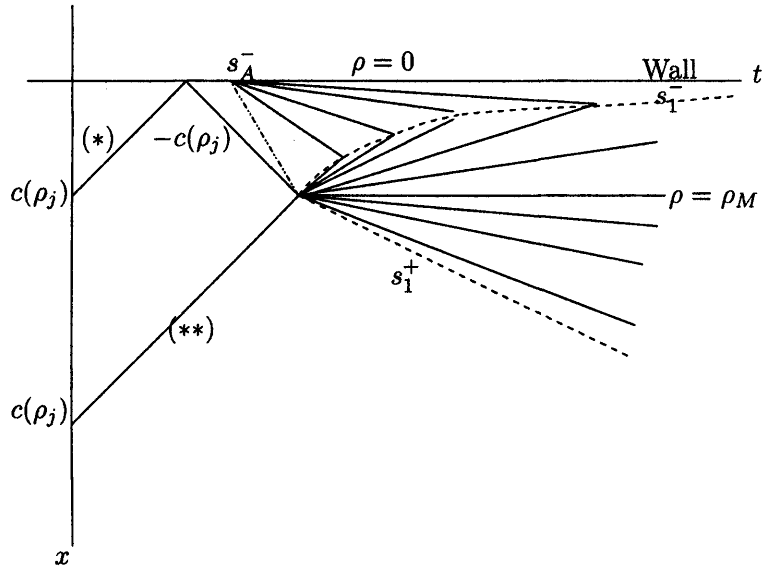

Figure D.9: The characteristics are plotted in the $x - t$ plane.

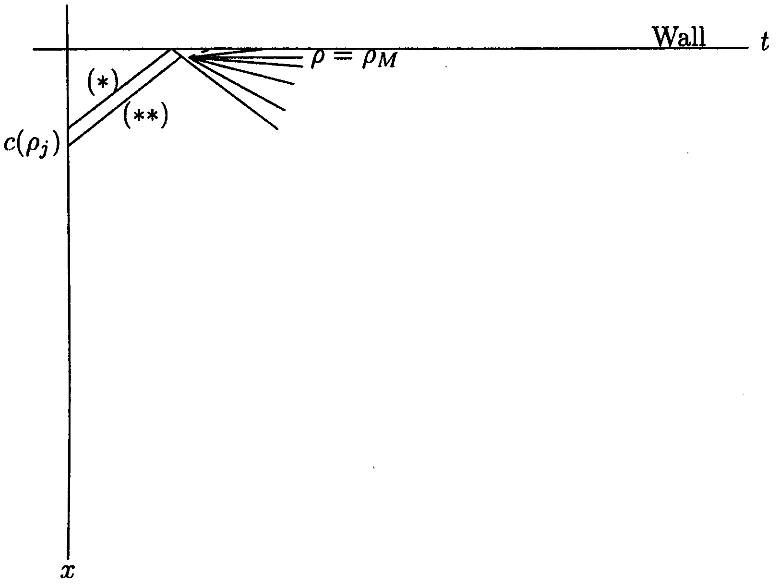

Figure D.10: In reality the characteristics (*) and (**) will coincide, so the picture above (figure D.9) is in fact identical to the $\hat{e} = 0$ case, as seen here.

Recall that in the above examples the density of the incoming grains satisfied $\rho < \rho_F$. As a consequence, the characteristic describing this region intersects the wall. However, if we had chosen $\rho > \rho_F$ the characteristic for the incoming grains would not have intersected with the wall. There would seemingly be a region devoid of characteristics adjacent to the wall. The solution in this case is to introduce an expansion fan and treat the wall as another incoming region of grains by a method of images. Hence there would be a horizontal characteristic running alongside the wall once again describing a stationary region of maximum density.

Appendix E

One method of solving the ordinary differential equation for the $O(t^{\frac{5}{4}})$ correction to the density in the inner-layer.

In chapter 6.4, section 6.4.2, we mention a method to find the complementary functions of

$$\nu g_2'' + \frac{\eta}{2} g_2' - \frac{5}{4} g_2 = \gamma \eta^{\frac{1}{2}}. \tag{E.1}$$

The method is to seek a solution to the homogeneous equation in the form of a complex integral.

Such a solution has the form

$$g_{2_{CF}} = \int_C e^{w\eta} \phi(w) dw \tag{E.2}$$

where C is an arbitrary contour and $\phi(w)$ is an unknown function [24]. On differentiation with respect to η we find that

$$g_{2_{CF}}' = \int_C w e^{w\eta} \phi(w) dw$$

and

$$g_{2_{CF}}'' = \int_C w^2 e^{w\eta} \phi(w) dw.$$

Substituting into the homogeneous form of the ordinary differential equation (E.1), in order to find the complementary function, reveals that

$$\nu \int_C w^2 e^{w\eta}\phi(w)dw + \frac{\eta}{2}\int_C w e^{w\eta}\phi(w)dw - \frac{5}{4}\int_C e^{w\eta}\phi(w)dw = 0. \qquad \text{(E.3)}$$

Integrating the second term by parts yields

$$\nu \int_C w^2 e^{w\eta}\phi(w)dw + \left[\frac{w\phi}{2}e^{w\eta}\right]_C - \frac{1}{2}\int_C e^{wn}\frac{d}{dw}(w\phi)dw - \frac{5}{4}\int_C e^{w\eta}\phi(w)dw = 0. \qquad \text{(E.4)}$$

If we choose a contour such that $\left[\frac{w\phi}{2}e^{w\eta}\right]_C = 0$ then the ordinary differential equation

$$\nu w^2\phi - \frac{1}{2}\frac{d}{dw}(w\phi) - \frac{5}{4}\phi = 0 \qquad \text{(E.5)}$$

must also be satisfied. That is,

$$\phi' + \left(\frac{7}{2w} - 2w\right)\phi = 0, \qquad \text{(E.6)}$$

where a prime denotes differentiation with respect to w. Utilizing an integrating factor of $I = e^{\frac{7}{2}\ln(w)-w^2}$ we obtain

$$\phi = Aw^{-\frac{7}{2}}e^{w^2}, \qquad \text{(E.7)}$$

where A is a constant of integration. Now consider $\left[\frac{w\phi}{2}e^{w\eta}\right]_C = \left[\frac{Aw^{-\frac{5}{2}}}{2}e^{w^2+w\eta}\right]_C = 0$. If C is the semi-infinite contour $w \in [0, i\infty)$ or $w \in (-i\infty, 0]$ then

$$g_{2_{CF1}} = \frac{A}{2}\int_0^{i\infty} w^{-\frac{7}{2}}e^{w^2+w\eta}dw \qquad \text{(E.8a)}$$

and

$$g_{2_{CF2}} = \frac{B}{2}\int_{-i\infty}^{0} w^{-\frac{7}{2}}e^{w^2+w\eta}dw \qquad \text{(E.8b)}$$

are complementary functions of (E.1), where we take only the finite part (FP) of the integrals, i.e.

$$g_{2_{CF1}} = \frac{A}{2}\int_0^{i\infty}\left\{w^{-\frac{7}{2}}e^{w^2+w\eta} - w^{-\frac{7}{2}}e^{w^2}\left[1 + w\eta + \frac{w^2\eta^2}{2}\right]\right\}dw \qquad \text{(E.9a)}$$

and

$$g_{2_{CF2}} = \frac{B}{2}\int_{-i\infty}^{0}\left\{w^{-\frac{7}{2}}e^{w^2+w\eta} - w^{-\frac{7}{2}}e^{w^2}\left[1+w\eta+\frac{w^2\eta^2}{2}\right]\right\}dw, \tag{E.9b}$$

where the principal parts of the integrand in (E.8a), (E.8b) have been removed. We can demonstrate the validity of removing these parts by showing that (E.9a) does indeed satisfy the homogeneous version of the ordinary differential equation (E.1) as follows. (Of course, the same argument applies equally well to (E.9b)).

Differentiating the homogeneous version of (E.1) three times gives

$$G'' + \frac{\eta}{2}G' + \frac{1}{4}G = 0, \tag{E.10}$$

where $G \equiv g'''_{2_{CF}}(\eta)$. To solve for $G(\eta)$ we again seek a solution of the form

$$G = \int_C e^{\eta t} f(t)dt \tag{E.11}$$

implying

$$\int_C \left\{t^2 + \frac{\eta}{2}t + \frac{1}{4}\right\} e^{\eta t} f(t)dt = 0 \tag{E.12}$$

on substitution into (E.1). This is an exact differential of the form $\frac{d}{dt}\left\{e^{\eta t}h(t)\right\}$ if $\dot{h} = \left(t^2+\frac{1}{4}\right)f(t)$ and $h = \frac{t}{2}f(t)$. Therefore $h = t^{\frac{1}{2}}e^{t^2}$ and hence $f = 2t^{-\frac{1}{2}}e^{t^2}$. Thus

$$G = \int_C \frac{2}{\sqrt{t}}e^{t^2+\eta t}dt \tag{E.13}$$

is a solution provided that

$$\left[e^{\eta t+t^2}t^{\frac{1}{2}}\right]_C = 0. \tag{E.14}$$

One contour could be $C_1 = t \in [0, i\infty)$ (and the other $C_2 = t \in (-i\infty, 0]$) so that

$$g'''_{2_{CF1}} = \hat{A}\int_0^{i\infty} \frac{1}{\sqrt{t}}e^{t^2+\eta t}dt. \tag{E.15}$$

Now, this is a well-defined finite solution as the integral is indeed convergent; it could be integrated numerically, say, and hence $g_{2_{CF1}}(\eta)$ would be obtained. It is demonstrated next that this solution is consistent with (E.9a).

Integrating (E.15) once with respect to η gives

$$g''_{2_{CF1}} = \hat{A}\int_0^{i\infty}\left\{t^{-\frac{3}{2}}e^{t^2+\eta t} + a(t)\right\}dt, \tag{E.16}$$

where $a(t)$ corresponds to a constant of integration. We must take care to ensure that the integral is still convergent so, without loss of generality, we write

$$g''_{2_{CF1}} = \hat{A} \int_0^{i\infty} \left\{ t^{-\frac{3}{2}} e^{t^2+\eta t} - t^{-\frac{3}{2}} e^{t^2} + \hat{a}(t) \right\} dt. \tag{E.17}$$

Similarly, we carefully integrate twice more to find

$$\begin{aligned} g_{2_{CF1}} = \hat{A} \int_0^{i\infty} \Bigg\{ & t^{-\frac{7}{2}} e^{t^2+\eta t} - \frac{\eta^2}{2} t^{-\frac{3}{2}} e^{t^2} + \frac{\hat{a}(t)\eta^2}{2} \\ & -\eta t^{-\frac{5}{2}} e^{t^2} + \hat{b}(t)\eta - t^{-\frac{7}{2}} e^{t^2} + \hat{c}(t) \Bigg\} dt. \end{aligned} \tag{E.18}$$

i.e.

$$g_{2_{CF1}} = \bar{A} \int_0^{i\infty} \left\{ t^{-\frac{7}{2}} e^{t^2+\eta t} - t^{-\frac{7}{2}} e^{t^2} \left[1 + \eta t + \frac{\eta^2 t^2}{2} \right] \right\} dt + \bar{a}\frac{\eta^2}{2} + \bar{b}\eta + \bar{c}, \tag{E.19}$$

where $\bar{a}$, $\bar{b}$ and $\bar{c}$ are constants which must be chosen so that the homogeneous version of equation (E.1) is satisfied. To determine their value, then, we integrate (E.10) three times to give in turn:

$$g_2'''' + \frac{\eta}{2} g_2''' - \frac{1}{4} g_2'' = \tilde{a}, \tag{E.20a}$$

$$g_2''' + \frac{\eta}{2} g_2'' - \frac{3}{4} g_2' = \tilde{a}\eta + \tilde{b}, \tag{E.20b}$$

and

$$g_2'' + \frac{\eta}{2} g_2' - \frac{5}{4} g_2 = \tilde{a}\frac{\eta^2}{2} + \tilde{b}\eta + \tilde{c}, \tag{E.20c}$$

where $\tilde{a} \propto \bar{a}$, $\tilde{b} \propto \bar{b}$ and $\tilde{c} \propto \bar{c}$. The right hand side of each must be equal to zero in order for the homogeneous equation to be satisfied. Therefore $\bar{a} = \bar{b} = \bar{c} = 0$. Thus

$$g_{2_{CF1}} = \bar{A} \int_0^{i\infty} \left\{ t^{-\frac{7}{2}} e^{t^2+\eta t} - t^{-\frac{7}{2}} e^{t^2} \left[1 + \eta t + \frac{\eta^2 t^2}{2} \right] \right\} dt, \tag{E.21}$$

which is exactly the same as (E.9a). Hence the finite parts of (E.8a), (E.8b), namely (E.9a) and (E.9b), are indeed valid complementary functions of the ordinary differential equation (E.1).

Appendix F

The local wavespeed-density relation at the large-density endpoint of the viscous fundamental diagram

In chapter 7, equation (7.77) gives the local wavespeed-density relation $C(P)$ at the large-density endpoint of the viscous fundamental diagram. It is asserted that it is possible to choose $A = 2$ and $B = \frac{2}{3}$ without loss of generality. The truth of the assertion is demonstrated here.

Put $P = \alpha\tilde{P}$, $C = \beta\tilde{C}$, $t = \gamma\tilde{t}$ and $X = \delta\tilde{X}$. Substituting into (7.74) yields

$$\frac{1}{\gamma}\tilde{P}_{\tilde{t}} + \frac{\beta}{\delta}\tilde{C}\tilde{P}_{\tilde{X}} = \frac{1}{\delta^2}\tilde{P}_{\tilde{X}\tilde{X}}, \tag{F.1}$$

and into (7.77) yields

$$\beta\tilde{C} = \pm\left(-\frac{A}{2}\tilde{P}^{-\frac{1}{2}}\alpha^{-\frac{1}{2}} - \frac{3B}{2}\tilde{P}^{\frac{1}{2}}\alpha^{\frac{1}{2}}\right). \tag{F.2}$$

In order to obtain (7.78) we must therefore choose

$$\gamma^{-1} = \beta\delta^{-1} = \delta^{-2} \tag{F.3}$$

in (F.1), and

$$\frac{A}{2\beta\alpha^{\frac{1}{2}}} = 1 \text{ and } \frac{3B\alpha^{\frac{1}{2}}}{2\beta} = 1 \tag{F.4}$$

in (F.2). Therefore equations (F.3) and (F.4) give four equations for the four unknowns α, β, γ and δ and hence $\alpha = \frac{A}{3B}$, $\beta = \frac{3}{2}\left(\frac{B}{A}\right)^{\frac{1}{2}}$, $\gamma = \frac{4A}{9B}$ and $\delta = \frac{2}{3}\left(\frac{A}{B}\right)^{\frac{1}{2}}$. Therefore 'without loss of generality' means essentially putting

$$P = \frac{A}{3B}\tilde{P}, \tag{F.5a}$$

$$C = \frac{3}{2}\left(\frac{B}{A}\right)^{\frac{1}{2}}\tilde{P}, \tag{F.5b}$$

$$t = \frac{4A}{9B}\tilde{t}, \tag{F.5c}$$

and

$$X = \frac{2}{3}\left(\frac{A}{B}\right)^{\frac{1}{2}}\tilde{X}. \tag{F.5d}$$

Appendix G

Recommendations to Sortex Ltd

In the main body of this thesis, we have developed a mathematical model of a chute flow of grains. This model has necessarily started from first principles, as there is no existing 'grand theory of everything' for granular phenomena. Consequently, the results obtained thus far are of limited practical use, as it would be unreasonable to include all the effects of geometry, the air, ellipsoidal shapes etc. into one model or simulation at this stage. A model of such complexity would perhaps be required to accurately describe the flow for engineering purposes. As we have seen, the mathematics of even the one-dimensional model yields some complex behaviours, and a steady state (which can loosely be thought of as the density profile at the end of the chute) is difficult to compute even here. If other effects were to be included, the problem would perhaps become increasingly complex, if not intractable. It would be very interesting, nonetheless, to try to progressively develop the model further in the future.

Four results of practical engineering/industrial importance arising from this thesis are described below.

1. In chapter 3 an investigation of chute shaping effects shows that, of the geometries studied, there is no noticeable improvement on the performance of a straight chute.

2. The creation of clusters and voids (see chapters 3, 5, 7 and appendix B) in the

flow of the grains appears to be a common phenomenon in the model results as well as in the industrial chute settings, encouraging further modelling aimed at cluster eradication.

3. A study of the air effects in chapter 8 demonstrates that a uniform flow distribution of grains arranged in a manner that would be ideal for reducing the ejection problem is almost certainly unstable.

4. Although designing a chute that would align the grains in such a fashion would seem to be of limited promise, design alterations of the air effects can be considered in future work with a view to stabilising the grain flow instead, enabling the efficiency of the machines to be increased.

Bibliography

[1] M. Abramowitz and I. A. Stegun, 'Handbook of Mathematical Functions with Formulas, Graphs and Mathematical Tables', National Bureau of Standards, Washington DC, 1964

[2] M. Alam, 'Streamwise structures and density patterns in rapid granular Couette flow: a linear stability analysis', J. Fluid Mech. **553**, 1 (2006)

[3] A. Andersen, U. Pesavento and Z. Jane Wang, 'Unsteady aerodynamics of fluttering and tumbling plates', J. Fluid. Mech, **541** 65 (2005)

[4] A. Andersen, U. Pesavento and Z. Jane Wang, 'Analysis of transitions between fluttering, tumbling and steady descent of falling cards', J. Fluid. Mech, **541** 91 (2005)

[5] R. Barlow, 'Statistics : a guide to the use of statistical methods in the physical sciences', Wiley (1989).

[6] H. Ahn, C. E. Brennen and R. H. Sabersky, 'Analysis of the fully developed chute flow of granular materials', J. Appl. Mech **59**, 109 (1992)

[7] W. Brilon and M. Ponzlet,'Application of traffic flow models'in 'Workshop on Traffic and Granular Flow' 41 (1995), Eds. D. E. Wolf, M. Schreckenberg, A. Bachem

[8] C. S. Campbell, 'Rapid granular flows', Annu. Rev. Fluid Mech. **22**, 57 (1990)

[9] P. Constantin, E. Grossman and M. Mungan 'Inelastic collisions of three particles on a line as a two-dimensional billiard', Physica D **83**, 409 (1995).

[10] P. G. Drazin, 'Solitons', London Mathematical Society Lecture Note Series, Cambridge University Press, (1983)

[11] Y. Du, H. Li and L. P. Kadanoff, 'Breakdown of hydrodynamics in a one-dimensional system of inelastic particles', Phys. Rev. Letts. **74**, 1268 (1995)

[12] I. Eames, J. C. R. Hunt and S. E. Belcher, 'Inviscid mean flow through and around groups of bodies', J. Fluid Mech **515**, 371 (2004)

[13] I. Eames, J. C. R. Hunt and S. E. Belcher, 'Fluid displacement by a sphere moving away from a wall', J. Fluid Mech., **324**, 333 (1996)

[14] C. F. Gerald and P. O. Wheatley, 'Applied Numerical Analysis', Addison Wesley (1994)

[15] B. J. Glasser and I. Goldhirsch, 'Scale dependence, correlations, and fluctuations in rapid granular flows', Physics of Fluids, **13**, 407 (2001)

[16] J. M. N. T. Gray and K. Hutter, 'Pattern formation in granular media', Continuum Mech. Thermodyn. **9**, 341 (1997)

[17] H. Greenberg, 'An analysis of traffic flow', Oper. Res. **7**, 79, (1959)

[18] E. L. Grossman, T. Zhou and E. Ben-Naim, 'Towards granular hydrodynamics in two dimensions', Phys. Rev. E **55**, 4200 (1997)

[19] H. Ehrentraut and A. Chrzanowska, 'Induced anisotropy in rapid flows of non-spherical granular materials' in 'Dynamic response of granular and porous materials under large and catastrophic deformations', 344, Springer (2003)

[20] E. J. Hinch and L. G. Leal, 'The effect of Brownian motion on th rheological properties of a suspension of non-spherical particles', J. Fluid Mech., **52**, 683 (1972)

[21] R. L. Hughes, 'A continuum theory for the flow of pedestrians', Transportation Research Part B, **36**, 507 (2002)

[22] R. L. Hughes, 'The flow of human crowds', Annu. Rev. Fluid Mech **35**, 169 (2003)

[23] H. E. Huppert, 'Quantitative modelling of granular suspension flows', Phil. Trans. R. Soc. Lond. A **356**, 2471 (1998)

[24] E. L. Ince, 'Ordinary differential equations', 438, Dover (1944)

[25] T. Ishikawa and T. J. Pedley, 'An active suspension', Mathematics Today, **41.3**, 84 (2005)

[26] J. T. Jenkins, 'Boundary conditions for rapid granular flows: Flat, frictional walls', J. Appl. Mech. **59**, 120 (1992).

[27] M. A. Jones and F. T. Smith, 'Fluid motion for car undertrays in ground effect', J. Eng. Math, **45**, 309 (2003)

[28] G. G. Joseph, R. Zenit, M. L. Hunt and A. M. Rosenwinkel, 'Particle-wall collisions in a viscous fluid', J. Fluid Mech., **443**, 329 (2001)

[29] L. P. Kadanoff, 'Built upon sand: Theoretical ideas inspired by granular flows', Reviews of Modern Physics, **71**, 435 (1999)

[30] D. L. Koch and R. J. Hill, 'Inertial effects in suspension and porous-media flows', Annu. Rev. Fluid Mech **33**, 619 (2001)

[31] A. A. Korobkin and M. Ohkusu, 'Impact of two circular plates one of which is floating on a thin layer of liquid', J. Eng. Math **50**, 343, (2004)

[32] L. D. Landau and E. M. Lifshitz, 'Fluid Mechanics', Course of theoretical physics, volume 6, Pergamon Press Ltd., (1959)

[33] L. G. Leal and E. J. Hinch, 'The rheology of a suspension of nearly spherical particles subject to Brownian rotations', J. Fluid Mech., **55**, 745 (1972)

[34] R. J. LeVeque, 'Finite Volume Methods for Hyperbolic Problems', Cambridge texts in applied mathematics (2002)

[35] T. Leweke, M. C. Thompson and K. Hourigan, 'Vortex dynamics associated with the collision of a sphere with a wall', Phys. Fluids **16**, 74 (2004)

[36] L. Li, 'Numerical Study of Nonlinear Evolution Equations Using Compact Differencing', Ph.D Thesis, University of London, (1997)

[37] L. Li, J.D.A. Walker, R.I. Bowles, F.T. Smith, 'Short-scale break-up in unsteady interactive layers: local development of normal pressure gradients and vortex wind-up', J. Fluid Mech **374**, 335 (1998).

[38] M. J. Lighthill and G. B. Whitham, 'On kinematic waves II. A theory of traffic flow on long crowded roads', Proc. R. Soc. Lond. A, **229**, 317, (1955)

[39] M. Y. Louge, 'Computer simulations of rapid granular flows of spheres interacting with a flat frictional boundary' Phys. Fluids **6**, 2253 (1994).

[40] N. Mitarai and H. Nakanishi, 'Hard-sphere limit of soft-sphere model for granular materials: Stiffness dependence of steady granular flow', Phys. Rev. E **667**, 021301 (2003)

[41] R. Monetti, A. Hurd and V. M. Kenkre, 'Simulations for dynamics of granular mixtures in a rotating drum', Granular Matter **3**, 113 (2001)

[42] J. V. Morgan 'Numerical Methods Macroscopic Traffic Models', PhD Thesis, University of Reading (2002)

[43] K. Nagel, 'Particle Hopping versus Fluid-Dynamical Models for Traffic Flow' in 'Workshop on Traffic and Granular Flow' 41 (1995), Eds. D. E. Wolf, M. Schreckenberg, A. Bachem

[44] H. Ockendon and J. R. Ockendon, 'Viscous Flow', 64-82, Cambridge Texts in Applied Mathematics (1995)

[45] N. Ovenden, Personal Communication, September 2003.

[46] Pars, 'Introduction to dynamics', Cambridge University Press, 157, 323-328, (1953).

[47] J. Rajchenbach, 'Granular flows' Adv. Phys. **49**, 229 (2000)

[48] J. C. Russ, 'Computer-assisted microscopy: the measurement and analysis of images', pp 260-264, Plenum Press (1990).

[49] W. B. Russel et al., 'Rods falling near a vertical wall', J. Fluid Mech. **83**, 273 (1977).

[50] J. T. Jenkins and S. B. Savage, 'A theory for the rapid flow of identical, smooth, nearly elastic, spherical particles', J. Fluid Mech. **130**, 187 (1983).

[51] F. T. Smith and L. Li, 'Swirl-flow effects in a duct bending through a substantial angle', **43**, 315 (2002)

[52] F. T. Smith, L. Li, G. X. Wu, 'Air cushioning with a lubrication/inviscid balance', J. Fluid Mech, **482**, 291 (2003)

[53] H. Sigurgeirsson, A. Stuart and W. L. Wan, 'Collision detection for particles in a flow', J. Comp. Phys. **172**, 766 (2001).

[54] C. Thornton and S. J. Antony, 'Quasi-static shear deformation of a soft-particle system', Powder Technology, **109**, 179 (2000)

[55] D. Volfson, L. S. Tsimring and I. S. Aranson, 'Partially fluidized shear granular flows: Continuum theory and MD simulations', (2003)

[56] P. Westwood, 'Flow from Ejector Nozzle Arrays for Sorting Machines', Ph.D thesis, University of London (200)

[57] G. B. Whitham, 'Linear and nonlinear waves', Wiley (1974)

[58] G. B. Whitham, 'Lectures on wave propagation', 1-20, Springer-Verlag (1979)

[59] B. Willetts, 'Aeolian and fluvial grain transport', Phil. Trans. R. Soc. Lond. A **356**, 2471 (1998)

[60] D. R. Williams, 'Driven Granular Media and Dissipative Gases: Phase Transitions and Instabilities', Aust. J. Phys, **50**, 425 (1997)

[61] H. J. Wilson and R. H. Davis, 'The viscosity of a dilute suspension of rough spheres', J. Fluid Mech. **421**, 339 (2000)

[62] H. J. Wilson and R. H. Davis, 'Shear stress of a monolayer of rough spheres', J. Fluid Mech. **452**, 425 (2002)

[63] P. Wilson, 'On the Core Flow and Turbulent Boundary Layer in a Curved Duct', Ph.D thesis, University of London (2003)

[64] D. E. Wolf, M. Schreckenberg and A. Bachem, 'Workshop on Traffic and Granular Flow' (1995)

[65] T. Zhou and L. P. Kadanoff, 'Inelastic collapse of three particles', Phys. Rev. E **54**, 623 (1996).